



**HAL**  
open science

# Étude numérique dans une décharge capillaire nanoseconde et dans la décharge contrôlée par barrière diélectrique surfacique: Cinétiques, Transport et Réponses de fluide

Yifei Zhu

► **To cite this version:**

Yifei Zhu. Étude numérique dans une décharge capillaire nanoseconde et dans la décharge contrôlée par barrière diélectrique surfacique: Cinétiques, Transport et Réponses de fluide. Plasma Physics [physics.plasm-ph]. Université Paris Saclay (COMUE), 2018. English. NNT: 2018SACLX027. tel-01803404

**HAL Id: tel-01803404**

**<https://pastel.hal.science/tel-01803404>**

Submitted on 30 May 2018

**HAL** is a multi-disciplinary open access archive for the deposit and dissemination of scientific research documents, whether they are published or not. The documents may come from teaching and research institutions in France or abroad, or from public or private research centers.

L'archive ouverte pluridisciplinaire **HAL**, est destinée au dépôt et à la diffusion de documents scientifiques de niveau recherche, publiés ou non, émanant des établissements d'enseignement et de recherche français ou étrangers, des laboratoires publics ou privés.

# Numerical Study of Nanosecond Capillary and Surface Dielectric Barrier Discharges: Kinetics, Transport and Fluid Responses

Thèse de doctorat de l'Université Paris-Saclay  
préparée à École Polytechnique

Ecole doctorale n°572 École Doctorale Ondes et Matière (EDOM)  
Spécialité de doctorat : Physique des plasmas

Thèse présentée et soutenue à Palaiseau, le 04 Mai, 2018, par

**YIFEI ZHU**

Composition du Jury :

|  |                    |
|--|--------------------|
| Jean Paillol<br>Université de Pau et des Pays de L'adour                             | Président          |
| Victor Soloviev<br>Moscow Institute of Physics and Technology                        | Rapporteur         |
| Nicolas Naudé<br>Université Paul Sabatier  | Rapporteur         |
| Anne Bourdon<br>École polytechnique  | Examineur          |
| Natalie Babaeva<br>Joint Institute for High Temperatures Russian Academy of Sciences | Examineur          |
| Svetlana M Starikovskaia<br>École polytechnique                                      | Directeur de thèse |

*To my parents, Guifei ZHU and Min ZHANG*

致我的父母：朱贵飞先生与张敏女士

“谁言寸草心，  
报得三春晖。”

——《游子吟》



# Contents

---

|  |           |
|--|-----------|
| <b>Acknowledgements</b>  | <b>5</b>  |
| <b>Abstract</b>  | <b>7</b>  |
| <b>1 Literature review</b>   | <b>11</b> |
| 1.1 Nanosecond pulsed discharges (NPD): main features and applications | 11        |
| 1.1.1 Nanosecond capillary discharge (nCD)                             | 13        |
| 1.1.2 Nanosecond surface dielectric barrier discharge (nSDBD)          | 16        |
| 1.2 Simulation of NPD: challenges and progress                         | 20        |
| 1.2.1 Kinetics and fast gas heating                                    | 20        |
| 1.2.2 Dynamics and fluid coupling                                      | 23        |
| 1.3 Simulation of nCD and nSDBD: a comparative view                    | 29        |
| <b>2 Problem formulation</b>   | <b>39</b> |
| <b>3 Mathematical model and numerical codes</b>                        | <b>41</b> |
| 3.1 Elementary kinetics theory and approximations                      | 42        |
| 3.1.1 Boltzmann equation   | 42        |
| 3.1.2 Fluid model for plasma   | 42        |
| 3.1.3 Drift-diffusion approximation                                    | 43        |
| 3.1.4 Electron energy distribution function                            | 45        |
| 3.2 0D actinometry model for nCD and ZDPlaskin code                    | 46        |
| 3.2.1 Discharge geometry and high voltage pulse                        | 46        |
| 3.2.2 Governing equations  | 46        |
| 3.2.3 Sensitivity analysis   | 47        |
| 3.3 2D model for nCD and nonPDPsim code                                | 48        |
| 3.3.1 Governing equations  | 48        |
| 3.3.2 Code and numerical schemes                                       | 50        |
| 3.3.3 Domain, boundary and initial values                              | 53        |
| 3.3.4 Modifications and validations                                    | 55        |

|          |   |            |
|----------|---|------------|
| 3.4      | 2D model for nSDBD and PASSKEy code . . . . .   | 58         |
| 3.4.1    | General experimental schematics of nSDBD . . . . .  | 59         |
| 3.4.2    | Governing equations . . . . .   | 59         |
| 3.4.3    | Code and numerical schemes . . . . .  | 61         |
| 3.4.4    | Domain, boundary and initial values . . . . .   | 68         |
| 3.4.5    | Benchmark verifications . . . . .   | 69         |
| 3.5      | A modified COMSOL model for validation and comparison . . . . .   | 74         |
| 3.5.1    | COMSOL and modelling of NPD: capabilities and drawbacks . . . . .   | 74         |
| 3.5.2    | Weak formulations and artificial stabilization . . . . .  | 75         |
| 3.5.3    | Verification and Validation . . . . .   | 78         |
| 3.6      | Conclusion . . . . .  | 81         |
| <b>4</b> | <b>Study of nCD: kinetics and optical actinometry</b>   | <b>83</b>  |
| 4.1      | Experimental measurements: techniques and results . . . . .   | 83         |
| 4.2      | Kinetics schemes . . . . .  | 87         |
| 4.2.1    | KIN1: full kinetic scheme . . . . .   | 87         |
| 4.2.2    | KIN2: reduced kinetic scheme . . . . .  | 91         |
| 4.3      | Calculated results for the selected species and discussion . . . . .  | 94         |
| 4.3.1    | Calculated results and density of O-atoms . . . . .   | 94         |
| 4.3.2    | Rate analysis for the species measured experimentally . . . . .   | 96         |
| 4.3.3    | Comparison of data for low current in the discharge: under-<br>lining the role of high electron density . . . . . | 99         |
| 4.4      | Conclusions . . . . .   | 101        |
| <b>5</b> | <b>Study of nCD: ionization wave and afterglow</b>  | <b>103</b> |
| 5.1      | Adjustment of experimental conditions and kinetics scheme . . . . .   | 104        |
| 5.2      | Discharge stage: propagation in different modes and tubes . . . . .   | 105        |
| 5.2.1    | Fast ionization wave mode and streamer mode . . . . .   | 105        |
| 5.2.2    | Streamers in tubes with different radius . . . . .  | 110        |
| 5.3      | Afterglow stage: energy deposition and evolution of species . . . . .   | 114        |
| 5.3.1    | Electrical characteristics and specific energy deposition . . . . .   | 114        |
| 5.3.2    | Long-lived plasma and de-excitation of excited species . . . . .  | 117        |
| 5.3.3    | Temporal-Spatial evolution of species . . . . .   | 120        |
| 5.4      | Conclusion . . . . .  | 124        |
| <b>6</b> | <b>Study of nSDBD: discharge, fast gas heating and fluid responses</b>  | <b>125</b> |
| 6.1      | Experimental techniques of measurement . . . . .  | 126        |
| 6.2      | Kinetics scheme . . . . .   | 127        |
| 6.3      | Streamer velocity and electric current . . . . .  | 129        |
| 6.4      | Electron density and electric field . . . . .   | 135        |

|          |   |            |
|----------|---|------------|
| 6.5      | Time-resolved emission of excited species . . . . . | 141        |
| 6.6      | Fast gas heating and fluid responses . . . . .      | 146        |
| 6.7      | Influence of dielectric parameters . . . . .        | 156        |
| 6.8      | Influence of ambient pressures . . . . .            | 160        |
| 6.9      | Conclusion . . . . .                                | 167        |
| <b>7</b> | <b>General conclusions</b>                          | <b>170</b> |
| 7.1      | Contributions of the present work . . . . .         | 170        |
| 7.2      | Perspectives and future work . . . . .              | 173        |
|          | <b>Bibliography</b>                                 | <b>175</b> |



# Acknowledgements

---

I would like to express my deepest gratitude to my supervisor, Prof. Svetlana M. Starikovskaya. I will never forget her encourage and education. Being an international student, my first half year being abroad was rather a tough period, but she always stood by my side, with patience and confident, guided me into the fantastic world of plasma physics. When I started to write a code from zero in the second year, I kept her words in mind: “When you want something, all the universe conspires in helping you to achieve it.” It was her firm support and rich knowledge of physics that drive me to finish my thesis. I am grateful to her. She provided me with great opportunities to get exposure to the plasma community all around the world, from France to Russia, from Europe to America... I fortunately got inspiring comments and feedbacks from the world’s top researchers. She is always passionate, hardworking and eager about contributing to this society and guiding her students. During the evenings and weekends, she was still revising papers, thinking of scientific solutions. It was her working so hard that made it possible for me to complete my degree.

I would also like to express my thanks to Prof. Mark Kushner and Dr. Natalie Babaeva for their guidance in using nonPDPsim code. Thanks to Dr. Anne Bourdon, for her four months of tutorial on the basics of numerical simulations, she helps to put me in a good starting point.

A great deal of credit is due to my dissertation committee: Prof. Victor Soloviev, Dr. Nicolas Naude, Dr. Natalie Babaeva, Dr. Anne Bourdon, Prof. Jean Paillol and Prof. Yun Wu for serving on my committee.

I wish to thank my Russian colleagues, Sergey Shcherbanev, Nikita Lephkin, thanks also to Orel Inna. I appreciate a lot the friendship we built during these years collaboration and discussions. Their hard works provide high quality experimental results which make validation of simulations much easier, and they helps me both in life and in science career. Thank you so much!

Thanks to my current and former lab mates: Andrey Klochko, Brian Baron, Georgy Pokrovskiy, Shiyong Huang, Zixian Jia, and Chenyang Ding, their compan-

ionship was invaluable. Special thanks go to Dr. Yue Liu, who has contributed much valuable information to my study and benefit me a lot during these years discussions. Furthermore, I am thankful for instructions on the use of the cluster by the informatics team, and administrative work by the secretary team. Thanks to Prof. Yun Wu and Prof. Yinghong Li and Mr. Yehong Shi in my Chinese institute for their firm and long term support and help of my administrative, academical and financial issues during my study abroad.

Thanks to my girl friend Xi Lin from Laboratoire Plasma et Conversion d’Energie. She helps a lot in my life in France, always brighten my emotions. The mutual encouragement and understanding is treasurable.

Finally, I would like to thank my beloved parents, grandparents and relatives for their support and love throughout my many years of study far from home. I am deeply grateful to them.

# Abstract

---

Nanosecond pulsed discharges are characterized by high reduced electric fields (hundreds of Td) and strong nonequilibrium. They have characteristic electron energies of a few to tens of eV and specific energy deposition ranging from  $10^{-3}$  eV/mol to a few eV/mol. The energetic electrons can efficiently generate chemical active species, lead to fast gas heating. These discharges are found in a growing list of successful practical applications: gas pollution control, surface treatment, plasma assisted aerodynamics, plasma assisted biology and medicine and plasma assisted combustion.

Two particular configurations are studied in present work: (i) nanosecond capillary discharge (nCD) operated at moderate pressures and high specific deposited energy, and (ii) nanosecond surface dielectric barrier discharge (nSDBD) operated at atmospheric or higher pressures and relatively low specific deposited energy.

Nanosecond capillary discharge is an experimental tool to analyse nanosecond plasma in some limit extreme conditions. Recent nCD experiments revealed that, plasma kinetics changes dramatically at high specific energy deposition. One of the aims of the present work, is to study numerically the effects of the changed kinetics to the classical actinometry measurement technique, and the spatial-temporal evolution of plasmas during discharge and afterglow.

Nanosecond surface dielectric barrier discharge has been widely studied in the community of aerodynamics. However, at the moment of starting the thesis, the parameters of nSDBD plasma were not yet clearly understood, detailed comparison of numerical calculations and experiments were not available. Therefore, modelling of nSDBD and comparison with experiments performed for the same parameters is another object of the presented thesis.

The results in the thesis are presented in three parts. In the first part, numerical modelling and experiment of Ar-based actinometry are used to study the atomic oxygen density in nanosecond capillary discharge. A kinetic scheme describing consistent behavior of the set of the experimental data is developed. The main processes responsible for population and decay of the three species of interest are selected on

the basis of sensitivity and rate analysis. The role of the reactions between excited species and electrons in early afterglow for pulsed discharges at high electric fields and high values of specific deposited energy is discussed. Density of O-atoms in the ground state is obtained from the calculations.

The second part is devoted to study, analyse and predict the features of the discharge and afterglow of nCD under different specific energy deposition based on a two-dimensional self-consistent code, nonPDPsim. Propagation of the discharge have been modelled. Two modes of propagation were identified, three shapes of ionization waves are found with various tube radius. The decay rate and radial distribution of electrons and  $N_2(C^3\Pi_u)$  in the afterglow are studied with respect to specific energy deposition.

Finally, a two-dimensional parallel PASSKEy (“PARallel Streamer Solver with KinEtics”) code coupling plasma and hydrodynamics has been developed and validated to model nSDBD. Series of numerical calculations for a single pulse nSDBD in atmospheric pressure air at 24 kV voltage amplitude has been performed, the results were compared with experiments in the same conditions. Calculated and measured velocity of the discharge front, electrical current, 2D map of emission of  $N_2(C^3\Pi_u) \rightarrow N_2(B^3\Pi_g)$ , and hydrodynamic perturbations caused by the discharge on the time scale  $0.2 - 5 \mu s$  are analysed. The effect of different kinetics processes in 2D distribution of heat release is studied. The data are presented and analyzed for negative and positive polarity of voltages. A set of parametric calculations with different dielectric permittivity, the thickness of dielectric and ambient pressures are presented.

# Résumé de thèse

---

Les décharges pulsées nanoseconde sont caractérisées par un fort champ réduit (centaines Td) et une forte thermodynamique hors équilibre. Ils ont l'énergie électronique de quelques eV à quelques dizaines eV et la déposition d'énergie spécifique de  $10^{-3}$  eV/mol à quelques eV/mol. Les électrons énergétiques peuvent générer des espèces chimiques actives efficacement, à fin de chauffer le gaz plus rapidement. Ce type de décharge est largement utilisé dans certaines applications pratiques: contrôle de la pollution du gaz, traitement de surface, aérodynamique assistée par plasma, biologie et médecine assistée par plasma, et combustion assistée par plasma.

Deux configurations particulières sont étudiées dans ce travail: (i) décharge capillaire nanoseconde (nCD) fonctionnant à la pression modérée et à l'haute pression, et (ii) décharge contrôlée par barrière diélectrique surfacique de nanoseconde, fonctionnant à la pression atmosphérique ou à la pression plus élevée, et à une énergie spécifique de la déposition relativement faible.

La décharge capillaire nanoseconde est un outil expérimental pour analyser le plasma nanoseconde dans certaines conditions extrêmes. Les expériences récentes de nCD ont révélé que la cinétique du plasma change considérablement quand l'énergie spécifique de la déposition est plus élevée. L'un des objectifs du travail est d'étudier numériquement les effets de la cinétique modifiée sur la technique classique de la mesure de l'actinométrie et l'évolution spatial-temporelle du plasma dans la décharge et en post-décharge.

La décharge contrôlée par barrière diélectrique surfacique de nanoseconde a été largement étudiée dans la communauté de l'aérodynamique. Cependant, au début de travail, les paramètres de nSDBD n'étaient pas bien compris, la comparaison des calculs numériques et des résultats expérimentaux n'étaient pas disponibles. Par conséquent, la modélisation de nSDBD et la comparaison avec des résultats expérimentaux sous les mêmes paramètres est un autre objet de la thèse.

Le travail dans le manuscrit est organisé en trois parties. Dans la première partie, la modélisation numérique et les expérimentations de l'actinométrie basée sur argon sont utilisées pour étudier la densité de l'oxygène atomique dans une décharge

---

---

capillaire nanoseconde. Un schéma cinétique décrivant le comportement cohérent de l'ensemble des données expérimentales est développé. Les processus principaux, qui sont responsables de la population et de la décroissance des trois espèces intéressés sont sélectionnés à base de l'analyse de la sensibilité et du taux. Le rôle des réactions entre les espèces excitées et les électrons au début de la post-décharge pour une décharge pulsée au grand champ électrique et haute énergie spécifique de la déposition est discuté. La densité des O-atomes des atomes d'oxygène en état fondamental est obtenue par les calculs.

La deuxième partie est consacrée à étudier, analyser et prévoir des caractéristiques de la décharge et de la post-décharge de nCD sous différents énergies spécifiques de la déposition, basées sur un code auto cohérent bidimensionnel, nonPDPsim. La propagation de la décharge a été modélisée. Deux modes de propagation ont été identifiés, trois formes d'ondes d'ionisation sont trouvées en variant le rayon de tube. Le taux de décroissance et la distribution radiale des électrons et de  $N_2(C^3\Pi_u)$  dans la post-décharge sont étudiés en respectant l'énergie spécifique de la déposition.

Finalement, un modèle parallèle bidimensionnel PASSKEy (PARallel Streamer Solver with KinEtics) a été développé et validé pour modéliser le nSDBD. Une série de calculs numériques pour un seul pulse de nSDBD dans l'air à la pression atmosphérique à une amplitude de tension de 24 kV a été effectuée, les résultats ont été comparés avec des résultats expérimentaux dans les mêmes conditions. Vitesse calculée et mesurée de l'entrée de la décharge, courant électrique, carte plan 2D d'émission de  $N_2(C^3\Pi_u) \rightarrow N_2(B^3\Pi_g)$ , et perturbations hydrodynamiques provoquées par la décharge sur l'échelle de temps sont analysées de 0.2 à 5  $\mu s$ . L'effet des différents processus cinétiques dans la distribution 2D de la chaleur est étudié. Les données sont présentées et analysées pour la polarité de tension négative et positive. Un ensemble de calculs paramétriques avec différentes permittivité diélectrique, différent épaisseur des diélectriques et différente pression ambiantes sont présentés.

---

---

# Chapter 1

---

## Literature review

### 1.1 Nanosecond pulsed discharges (NPD): main features and applications

Low temperature plasma discharges operating at moderate and high pressure (much larger than tens of mbar) have received increasing attention in recent years, both in academic research groups and in industries for their ability to produce active species in well-controlled environments at low energy cost. These discharges are found in a growing list of successful practical applications such as ozone generation, polymer processing, excitation of laser and excimer lamps, pollution control, biological decontamination, medical treatment, aerodynamic flow control, and thin film coating [1–8].

A simple way to generate low temperature plasma at moderate and high pressure is to use electrodes at high-voltage separated by a gaseous gap. However, the originally cold plasma could rapidly become a high-conducting junction that evolves into a thermal plasma where heavy species tend to be in equilibrium with the electrons at a few tens of thousands degrees Kelvin (arc discharge), leading to huge amount of energy consumptions and destruction of chemical species. One way to prevent this equilibrium of temperature between heavy species and electrons is to use Nanosecond Pulsed Discharges (NPD), which are usually produced by a short duration and high peak voltage on the electrodes.

NPD are characterized by relatively high reduced electric fields (hundreds of Td) and strong nonequilibrium [9–13], thus are extremely efficient for generating

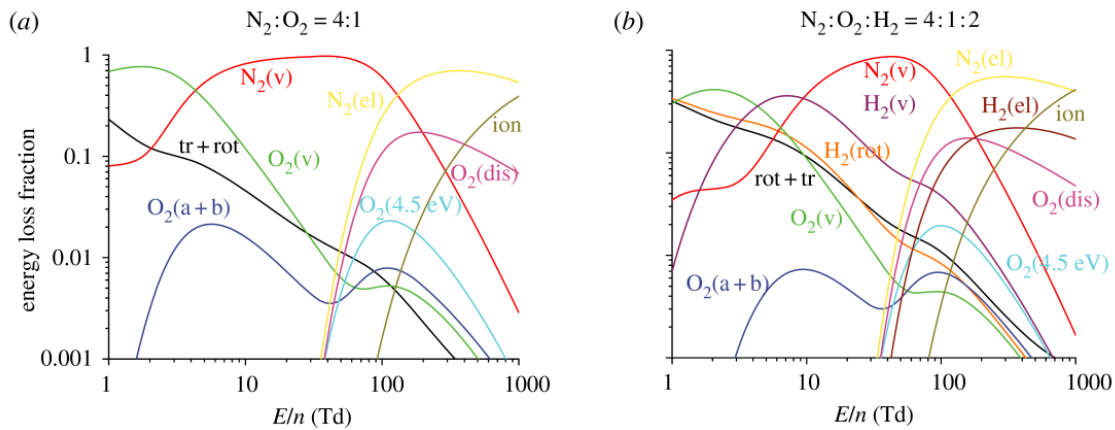


Figure 1.1: Electron energy branching through molecular degrees of freedom as a function of  $E/N$ . (a) Air; (b) hydrogen-air; (c) methane-air; (d) ethane-air stoichiometric mixtures.  $tr + rot$ : sum of translational and rotational excitation;  $v$ : vibrational excitation;  $el$ : electronic excitation;  $ion$ : ionization;  $dis$ : dissociation;  $a + b$ : sum of electronic excitation of singlet 'a' and 'b' states of molecular oxygen. The figure is taken from [8].

high reactivity. This feature can be seen from Figure 1.1, where the energy branching of electrons under different reduced electric fields for various mixtures are plotted with reduced electric field. It is shown that, for higher reduced electric field (100–1000 Td) the energy mainly goes to excitation of electronic degrees of freedom. In particular, in discharges in air at moderate and high pressures, quenching of electronically excited nitrogen molecules,  $N_2(B^3\Pi_g)$ ,  $N_2(C^3\Pi_u)$ ,  $N_2(a^1\Sigma_u^-)$ , leads to efficient  $O_2$  dissociation, including dissociation with  $O(^1D)$  production [14, 15], see Figure 1.2 (b). The high reactivity of NPD enables the possibility of applications in medical treatment, including living tissue sterilization and sterilization of non-living objects, nonthermal plasma assisted blood coagulation, plasma assisted wound healing and tissue regeneration, plasma assisted treatment of various diseases [16–23].

Another key feature of NPD is the fast gas heating (FGH), which occurs at the time scale much less than VT relaxation or VV' exchange. The heating is caused by relaxation of the electronic energy of the excited species produced under the high reduced electric field in NPD. In [11, 25] the rotational temperature of molecular nitrogen was measured and compared with synthetic spectrum calculated numerically. The measurements of fast gas heating were performed in preheated air (1000 K) at atmospheric pressure. A pulse with duration 10 ns, 5.7 kV voltage amplitude and frequency 10 kHz applied to a pip-to-pin geometry with 4 mm gap, could lead to reduced electric field value  $E/N \leq 250$  Td. The results of [11], the temperature evolution measurements during the discharge pulse are presented together with sim-

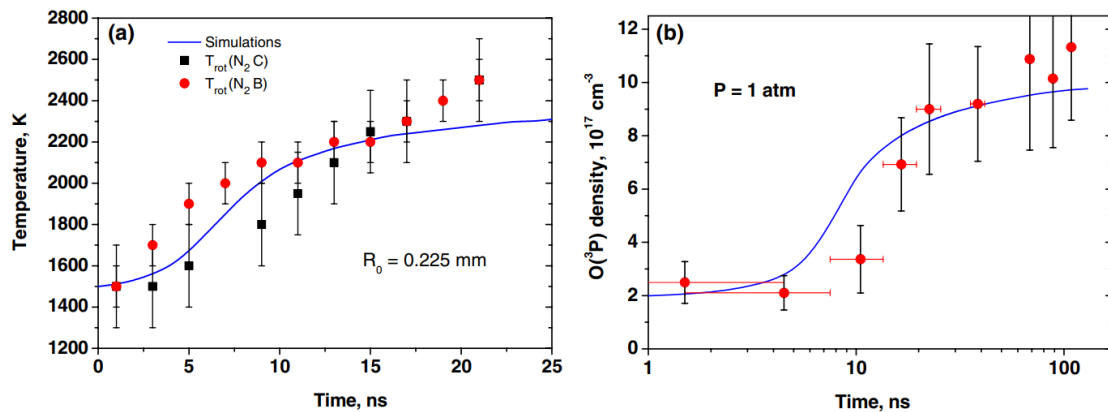


Figure 1.2: Comparison of measured (symbols) and simulated (line) temporal evolution of (a) the gas temperature (b) the ground state atomic oxygen density. The simulations were performed by Popov [24]. The figure is taken from [11].

ulation in Figure 1.2 (a). The fast rise of the temperature from 1500 K to 2200 K during the discharge pulse (20 ns) was observed.

The unique features of high chemical activity and fast gas heating in NPD, and the potential of its application for plasma assisted aerodynamics [26], plasma assisted biology and medicine [27], plasma assisted combustion [28, 29] have raised interest of researchers around the world. For analysis and applications, NPD have been implemented in various geometrical configurations and with different materials. This Thesis will focus on NPD in two configurations: (i) Nanosecond Capillary Discharges (nCD) operated at moderate pressures to study NPD in condition of high energy depositions. (ii) Nanosecond Surface Dielectric Barrier Discharges (nSDBD) operated at atmospheric or higher pressures and relatively low energy depositions, which is a widely used configuration in the community of aerodynamics.

### 1.1.1 Nanosecond capillary discharge (nCD)

Energy exchange at the conditions of high electric fields, non-uniform at high gas densities spatial distribution of discharge energy, and at high specific deposited energy is a subject of broad scientific discussions. During last decades, comprehensive high-pressure laser diagnostics, typical earlier for combustion systems and for low-pressure non-quenching plasma, is applied to high pressure discharges in complex reactive mixtures [15, 30–32]. Use of laser diagnostics demands detailed analysis of quenching coefficients for the fluorescent state, otherwise the error in the obtained data can be significant. In discharge system, related to combustion, the situation is even more complex because of a strong dependence of energy branching and so chemical composition of plasma upon the reduced electric field,  $E/N$  [33, 34].

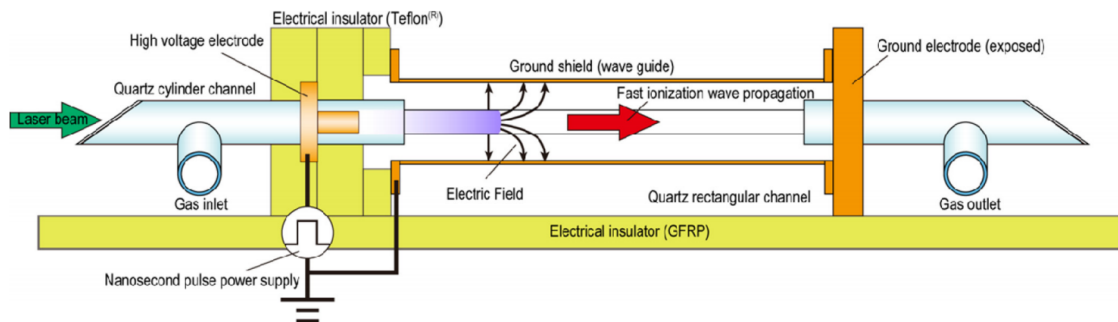


Figure 1.3: Schematic of the fast ionization wave discharge apparatus. The figure is taken from [35].

In nanosecond discharges at high electric fields, a significant amount of energy goes to the production of electronically excited species, which react quickly with other species. Experimental and numerical study of nanosecond capillary discharges at moderate (tens of mbar) pressures under conditions of spatially uniform excitation and high energy release allows analysis of some limit extreme conditions for nanosecond plasma, emphasizing possible limitations of optical measurements technique at conditions of higher pressure if a high discharge energy density is kept in the experiments. Recent TALIF measurements in nanosecond capillary discharge in air [36] at 24 – 30 mbar showed that if three subsequent discharges are initiated by a train of high-voltage nanosecond pulses 30 ns each, separated by 250 ns, with a total energy density about 1 eV/molecule, then the oxygen density increases progressively, approaching practically complete dissociation about 2  $\mu$ s after the first pulse. Gas temperature in the capillary reached 1500 – 2500 K at the time scale 1 – 2  $\mu$ s, confirming significant role of the fast gas heating due to energy release from electronically excited species [37].

The nanosecond capillary discharge is produced in a discharge cell consisting a dielectric tube surrounded by a metal cylindrical screen. The discharge cell is connected to the generator of high-voltage nanosecond pulses by coaxial transmission line. The high-voltage electrode installed inside the tube is connected to the central conductor of the coaxial line, the metal screen is connected to the shielding of the coaxial line. Thus the discharge cell is a continuation of the coaxial transmission line. The discharge can be divided into two stages: the propagation stage and the afterglow stage.

The propagation stage starts once voltage pulse arrived the HV electrode and a fast ionization wave (FIW) is formed inside the tube and propagates. A schematic view of the discharge cell for FIW generation and propagation can be found in Figure 1.3 proposed by paper [35]. In [35] the discharge is generated in a 22 mm  $\times$  13.5 mm

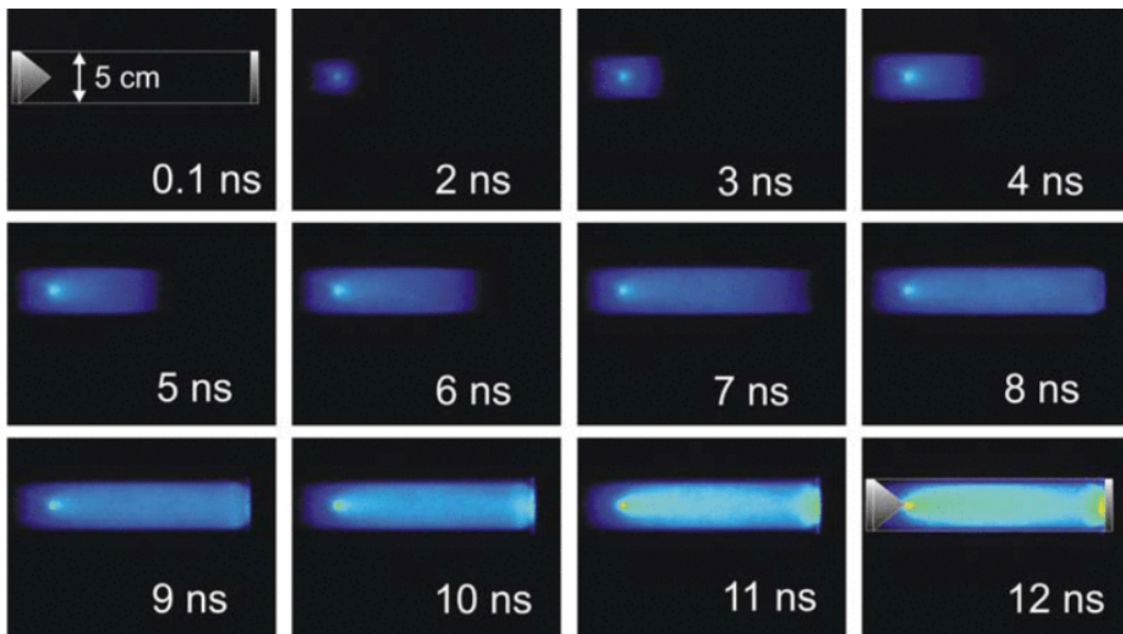


Figure 1.4: Propagation of the FIW in the tube with exposure time of 1 ns. The figure is taken from [38].

rectangular discharge cell. By reducing the diameter of the tube from tens of mm to 1.5 mm a capillary tube is achieved. The propagation stage is important, as the distribution of electric field and species formed during this stage are the key factors for analyzing nCD. Measurements of potential and electric field in the capillary tube is available based on the techniques of back current shunts and capacitive probe [39,40]. The structures of FIW depend on several factors, including tube radius, pressure, voltage polarity and frequency. Typical ICCD images of the propagation of FIW are presented in Figure 1.4.

In the afterglow stage, high energy deposition, and thus high excitation degree is achieved when the current density after the fast ionization wave propagation increases significantly. By varying the experimental conditions (voltage, tube radius and length, etc) one can adjust the energy deposited to the plasma in the tube, making nCD a useful tool for studying plasma kinetics under with regard to specific energy deposition. Several experimental techniques can be implemented for diagnostics. A widely used non-intrusive, passive, in-situ diagnostic techniques is optical emission spectroscopy (OES). Classical OES provides the spatial and temporal evolution of emission from plasma, but do not provide absolute densities of species of interest. Indirect techniques like trace-rare gases optical emission spectroscopy (TRG-OES) [41] are used for the measurement of absolute densities of ground state reactive atomic species. One of the methods belonging to this family of diagnostic techniques is optical actinometry. Actinometry was originally used as a correction

technique for measuring F-atom density, and based on the measuring of emission intensity of Ar ( $2p_1 \rightarrow 1s_2$ ) [42, 43], has later been extended for relative measurements of different radicals [44, 45] and later [46] was converted into technique to measure absolute densities of intermediate species. Classical actinometry for O-atom density measurement is usually based on the assumption that the density of the electronically excited states is small compared to the density of the ground state neutrals and will decay only by quenching with neutral species [47].

Although measurements provide temporal profiles of averaged  $E/N$ , spatial-temporal evolution of excited species and grounded atoms, a lot of information is still hidden. Rather limited experimental results have to be analyzed based on numerical simulations to reveal the full image of nCD. A global model with detailed kinetics is necessary to describe the evolution of species in absolute value, two-dimensional model based on simplified kinetics is also needed to have a self-consistent description of nCD and to provide initial conditions for global models.

### 1.1.2 Nanosecond surface dielectric barrier discharge (nS-DBD)

A special attention to surface dielectric barrier discharges (SDBD) during last 2–3 decades is explained by their potential application for active control of airflows. In a SDBD, one electrode (“top electrode”, or “exposed electrode”) is placed above the dielectric surface while the other electrode is placed below the dielectric surface [48–51]. In this asymmetric configuration an ion wind is generated from the tip of the top electrode, along the dielectric surface above the other electrode. With sinusoidal voltage amplitudes from a few kV to 20 or 30 kV and frequencies in the 1-10 kHz range, SDBDs can also generate a flow of a few  $\text{m s}^{-1}$  (up to  $10 \text{ ms}^{-1}$ ).

Nanosecond SDBD is realized when using a nanosecond voltage pulse generator (the voltage pulse can be several tens of kilovolts with rise and decay time on the order of or less than 10 ns) to drive the SDBD. Under these conditions, the corona regime that is responsible for the ion wind in sinusoidal regimes [52, 53] is no longer present and the main discharge regime is a streamer regime.

A few well-established experimental facts about nSDBD can be found in the literature. Existing measurements consists mainly of the morphology and dynamics of streamers, and the reduced electric field.

Morphology and dynamics of nSDBDs are usually measured by nanosecond ICCD imaging in UV and visible range of spectra. Figure 1.5 shows one of the typical available data providing a top view above the dielectric [9], while the fine structure of the discharge in the direction perpendicular to the dielectric is practically not studied. Only a few attempts to measure distribution of emission in the

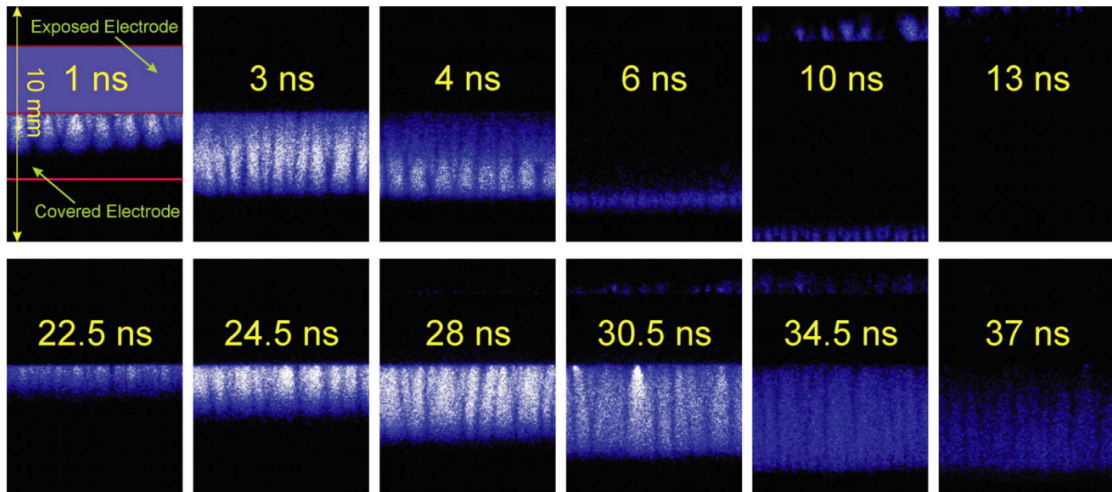


Figure 1.5: Images of surface nanosecond barrier discharge development taken with nanosecond time resolution. Camera gate is 0.5 ns. Voltage on the HV electrode is 14 kV. The half-width time of pulse is  $\tau_{1/2} = 25$  ns,  $P = 1$  bar. Cathode-directed streamer discharge [9].

direction from the dielectric to the bulk of the plasma [54,55] exist in the literature. In [54], the surface barrier discharge initiated over the ceramics or glass-ceramics by a 5 – 14 kHz sinusoidal voltage 2.2 – 2.8 kV in amplitude. A segment corresponding to about 10 mm of the discharge along the dielectric was monitored using photon counting technique. The conclusion was made that the thickness of the discharge is about 1 mm. In [55], a cross-correlation spectroscopy was used to get a 2D picture of  $N_2$  emission. The thickness of the emission layer did not exceed 1 – 2 mm. Because of the coplanar geometry of electrodes in [55], the results cannot be directly compared to nSDBD in classical airflow configuration.

Reduced electric field was derived in [56,57] from the measurements of the ratio of emission of the first negative ( $1^-$ ) and second positive ( $2^+$ ) systems of molecular nitrogen, the technique developed for the uniform plasma [58–60]. The following conclusions were made on the basis of joint experimental and numerical analysis [57]: (i) electric field in nSDBD is high but cannot be measured from optical emission without special precautions: emission of the  $1^-$  and  $2^+$  systems come from different spectral regions near the surface of the dielectric within a scale of units-tens of microns; (ii) to compare experimentally measured ratio of emission and numerical modeling, it is necessary to integrate the results of the calculations in space, “imitating” the light collection by spectral system; (iii) comparison of experiments and numerical modeling gives similar values for the negative polarity nSDBD and different values for the positive polarity streamer: there is a region of high electric

field producing “more emission” of the  $1^-$  system in the experiments.

Study of plasma parameters during discharges is difficult due to the small spatial-temporal resolution. Meanwhile, numerous investigations have been conducted based on nSDBD for plasma flow control and plasma assisted ignition/combustion applications. The features of high reactivity and fast gas heating have been implemented in these applications.

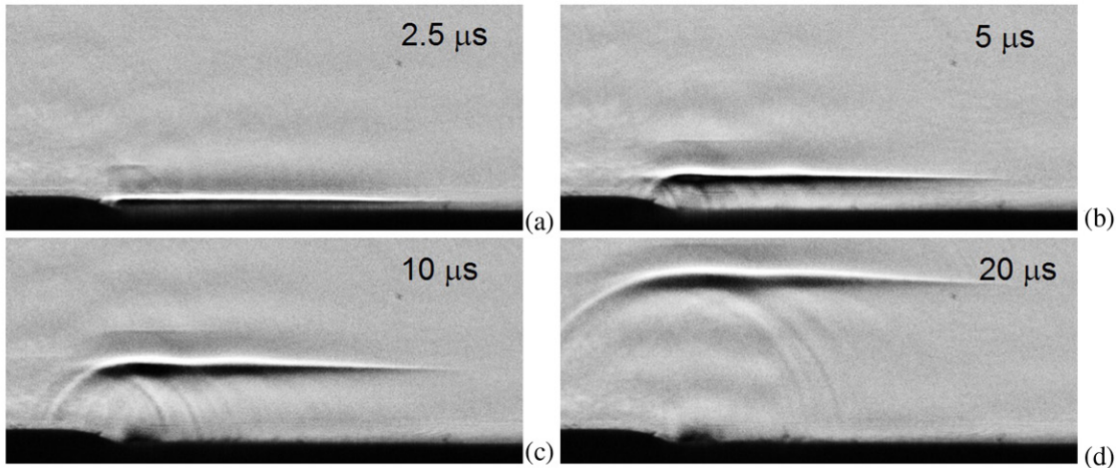


Figure 1.6: Schlieren images of quiescent air perturbations caused by a nanosecond pulse surface DBD plasma, for different delay times after the discharge pulse. Pulse peak voltage 14 kV, pulse repetition rate 200 Hz, “side view” (high voltage electrode is on the left), approximate image size  $x \times z = 25 \times 11$  mm, discharge is in a constricted mode. Delay time and polarity are shown on images; for delay time  $t \leq 25 \mu\text{s}$  schlieren images look very similar for both polarities. The figure is taken from [61].

Pioneering experiments for flow control with nSDBD are dated to the beginning of 2000th [9, 62]. Since that, an intensive study of nanosecond DBD actuators has been done by different groups [63–66]. One important conclusion of the experiments of [9, 67, 68] is that a large part of the plasma energy is released into gas heating in a short time (less than  $1 \mu\text{s}$ ), leading to the formation of a micro-shock wave, as is shown in Figure 1.6. [9, 67, 68] showed the ability of nSDBD to affect the aerodynamic properties of a flow along the surface, and that a detached flow could be reattached when a nanosecond voltage pulse was applied between the electrodes at a repetition rate of a few kHz (for spanwise as well as streamwise configurations of the DBD actuators with respect to the flow direction). Later the dynamics of near-surface electric discharges and their interaction with the airflow was considered in review [26], in which the authors distinct four types of flow perturbations: (1) low-speed near-surface gas motion generated by electrohydrodynamic interaction (ion

wind); (2) spanwise and streamwise vortices formed by both electrohydrodynamic and thermal effects; (3) weak shock waves produced by rapid energy release (fast gas heating) in pulsed nanosecond discharges; and (4) near-surface localized stochastic perturbations on sub-millisecond time. Among all the mechanisms, it was confirmed that the thermal effects are dominating for nSDBD plasma flow control.

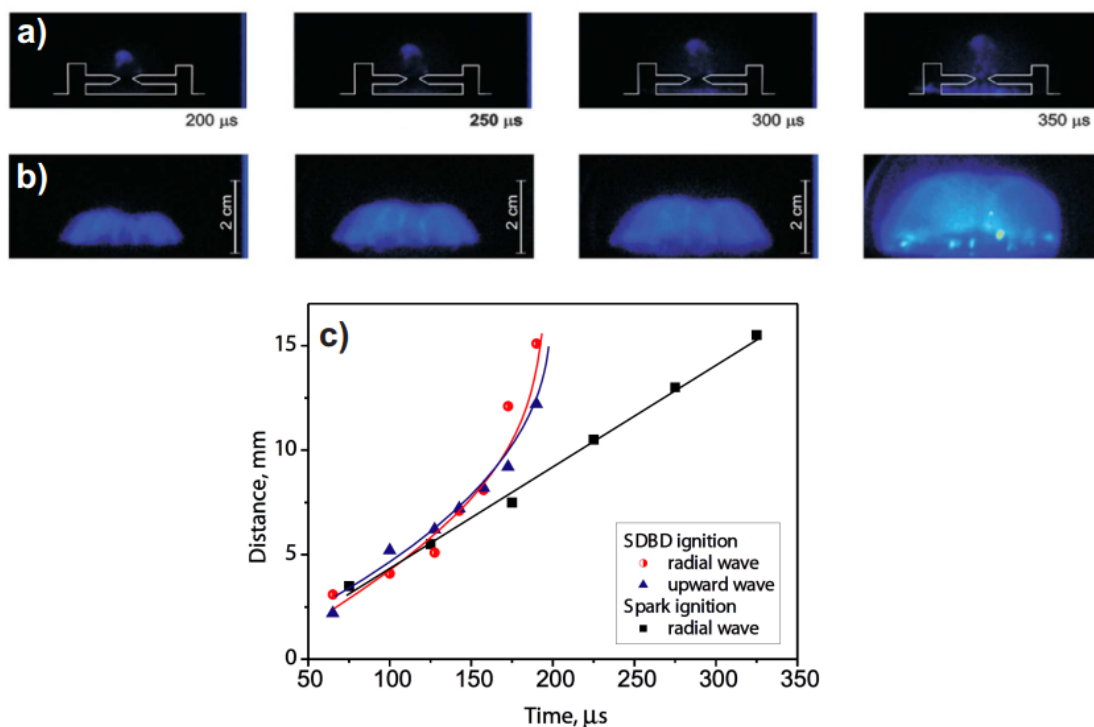


Figure 1.7: ICCD images of  $\text{C}_2\text{H}_6 : \text{O}_2 = 2 : 7$  mixture ignition by (a) a nanosecond spark discharge; (b) a nanosecond SDBD. Camera gate for both cases is  $0.5 \mu\text{s}$ . (c) Flame propagation x-t diagrams for the SDBD and for spark ignition [69].

Nanosecond SDBD as a tool for plasma-assisted ignition has been suggested for the first time in [70]. Figure 1.7 (a) and (b) show the ICCD images of the flame propagation initiated by nanosecond spark and SDBD respectively with the same energy input. During the same period the flame from the nSDBD occupies bigger volume than that of the nanosecond spark. Figure 1.7 (c) shows the x-t diagrams of combustion waves, at  $t \geq 150 \mu\text{s}$  the flame front initiated by SDBD moves significantly faster. The effects of chemical activity and fast gas heating to plasma-assisted ignition is still under dispute, recent study [71] of ignition based on nanosecond spark shows that the combining effect of chemical activity and fast gas heating is important.

For optimization of applications based on nSDBD, various parameters (voltage profile and polarities, dielectric geometric factors, permittivity, etc) have to be selected based on deep understanding of physics. The spatial distributions of essential

species and temperature rise due to fast gas heating, the fluid response with regard to discharge parameters, have to be studied both numerically and experimentally.

## 1.2 Simulation of NPD: challenges and progress

Numerical simulation is a promising way to test theoretical assumptions, validate experimental conclusions and to predict the behaviour and parameters of discharges under specific conditions. NPD is a multi-scale system, which includes various processes including chemical reactions, species transport, electromagnetic field propagation and fluid coupling. The requirements of high resolution and high performance make simulation of NPD bringing quite big challenges to the community.

The simulation of NPD can be classified according to the dimensions of interest: (i) zero or one dimensional simulations, based on detailed chemistry scheme and assumptions of global uniformity, to study the kinetics and the features of fast gas heating; (ii) two or three dimensional simulations, based on simplified kinetics scheme (usually obtained from complete kinetics modeling) and high resolution numerical schemes for transport of species and flow, to study the hydrodynamics of NPD.

### 1.2.1 Kinetics and fast gas heating

Simulation of NPD requires chemical rates of the production of charged species for calculation of electric field, and neutral species of interest. A detailed kinetics scheme of non-equilibrium plasma-chemical processes in nitrogen-oxygen mixtures is necessary to study the discharges considered in this work.

At present, several fundamental publications devoted to the analysis of kinetic processes in molecular gases and plasmas are available in the literature [14, 72–76]. Among them [14] summarized a kinetic scheme of non-equilibrium discharge in nitrogen-oxygen mixtures, which describes the main chemical transformations of particles in the cold ( $220\text{ K} < T < 500\text{ K}$ ) vibrationally unexcited gas, including about 450 processes of excitation of electronic states, destruction and ionization of heavy particles by electron impact, associative ionization, electron attachment and detachment, electron-ion and ion-ion recombination, chemical transformations of neutral particles (in ground and excited electronic states) and ion conversion. A more complete and general scheme is presented in [72], where the chemical and the vibrational kinetics, and the kinetics of ions and electronic levels in discharge and post-discharge plasma columns are analysed in detail. The complete physical interpretation of experimental data and a consistent description of the basic discharge

provides a concrete basis for specific investigations, such as nCD and nSDBD. Despite the quite complete set of data, challenges still exist, for example:

(i) Extension of the existing kinetics schemes to explain latest experimental measurements. Questions of the role of various mechanisms of excitation, ionization and chemical (ion) transformation in the nitrogen-oxygen plasma are still to be clarified, despite many efforts that have been done [34, 37, 77, 78]. New experimental results which cannot be explained by existing kinetics schemes are kept arising and introducing new challenges and new kinetics mechanisms to the community. For example, recent time-resolved OES results of the second positive system of  $N_2$  in capillary nanosecond discharge with similar parameters in molecular nitrogen [79] shown in Figure 1.8 revealed the following fact: starting from deposited energies about 0.1 eV/molecule, quenching of  $N_2(C^3\Pi_u)$  state is faster the quenching caused by collisions with  $N_2$  molecules, and depends upon the energy deposited in the discharge.

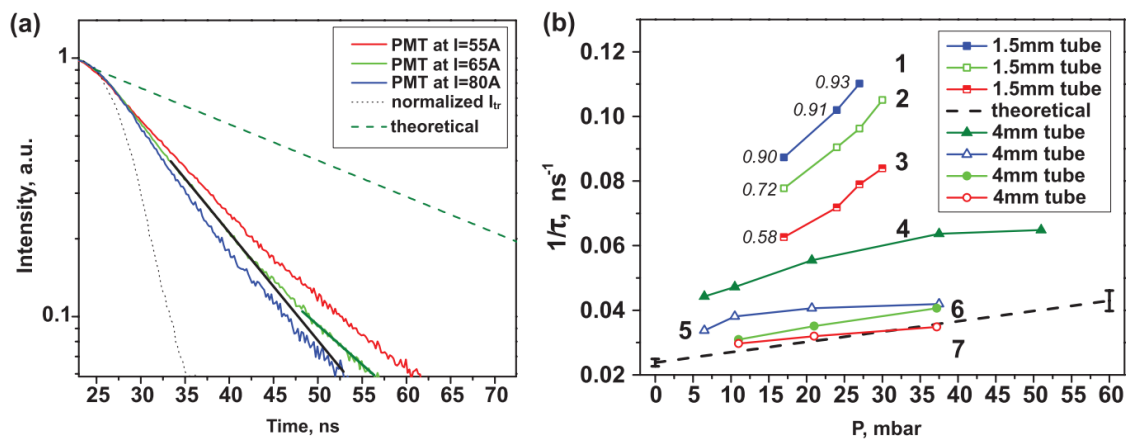


Figure 1.8: Experimental results for  $N_2(C^3\Pi_u)$  quenching in a capillary tube in pure nitrogen: (a) experimentally measured emission at 27 mbar for different discharge current; dashed line represents nitrogen emission calculated on the basis of quenching by  $N_2$  with rate constant from [14]; dot line shows a normalized waveform for electric current; (b) reverse decay time  $1/\tau$  as a function of pressure for different specific deposited energies. Dashed curve is for theoretical prediction. The figure is taken from [79].

(ii) Reduction of the dimension of kinetics for high performance numerical simulation. In non-equilibrium plasma, the number of species and reactions increases dramatically when extensive excitations and state-to-state kinetics are taken into account. Furthermore, many different time scales are involved in the chemical reactions, resulting in a stiff system of equations. These issues cause the computational load become prohibitive for spatially resolved simulations of chemically complex

plasmas. In [80, 81] the kinetics is reduced by grouping of energy levels in state-to-state kinetic models, In [82, 83] principal reaction pathways were used for kinetics reduction. A recent work [84] uses the concept of machine learning and proposes a principle component analysis method. For air discharges, in [85] a simplest kinetics scheme, including only 7 charged species and 15 reactions was proposed for predicting the development of a cathode-directed volumetric streamer discharge in air at different pressures, a good agreement between simulation and experiments have been achieved. In [86] a reduced set of air reactions was selected based on detailed reduction method, the reaction set was used to model energy release in glow mode and filamentary mode nanosecond pulsed discharge theoretically. Paper [87] introduced a reduced kinetics scheme based on sensitivity analysis in an 1D model to calculate the fluid responses induced by a plane-to-plane nanosecond dielectric barrier discharge. The main principle of kinetics reduction for nanosecond pulsed discharge, is to correctly reproduce the propagation of streamer with reactions involving charged species, and to calculate density species of interest or gas heating by including reactions responsible for the specific species or energy release.

Kinetic analysis for fast gas heating is another challenge in NPD simulation. Latest kinetics schemes validated by experiments are developed and used to study the features of fast gas heating by different groups [37, 88]. A good agreement between calculations and experiments confirms that energy relaxation from the electronic degrees of freedom of excited species is the heating source at time scale much less than those of VT relaxation, or VV' exchange. Two key parameters were defined to characterize FGH in nanosecond pulsed discharge, the fractional power of each process to total fast gas heating power  $\eta_{proc}$ , and the fractional power of FGH to total electron power  $\eta_{total}$ .

The first parameter,  $\eta_{proc}$ , was used to evaluate the contribution of each process to the fast gas heating energy release. Paper [37] concluded that the main processes leading to gas heating are: (i) dissociation of nitrogen and oxygen molecules by electron impact; (ii) quenching of the electronically excited states of nitrogen molecules by oxygen molecules; (iii) quenching of the excited atoms O(<sup>1</sup>D); (iv) ion-molecule reactions, reactions of electron-ion and ion-ion recombination. The ratio between energy release through the different channels is a function of the reduced electric field. The contribution of different processes to the fast gas heating was also calculated in [37] for air at pressure 760 Torr, see Figure 1.9 (a). At fields  $E/N \leq 200\text{--}300$  Td the dominant processes are quenching of N<sub>2</sub>(C<sup>3</sup>Π<sub>u</sub>) and N<sub>2</sub>(B<sup>3</sup>Π<sub>g</sub>) states by molecular oxygen and quenching of O(<sup>1</sup>D) atoms, total contribution more than 70%. At high reduced electric fields ionization become sufficient, and the heating due to charged particles becomes dominant.

The second parameter,  $\eta_{total}$ , was more practical for applications as it can be di-

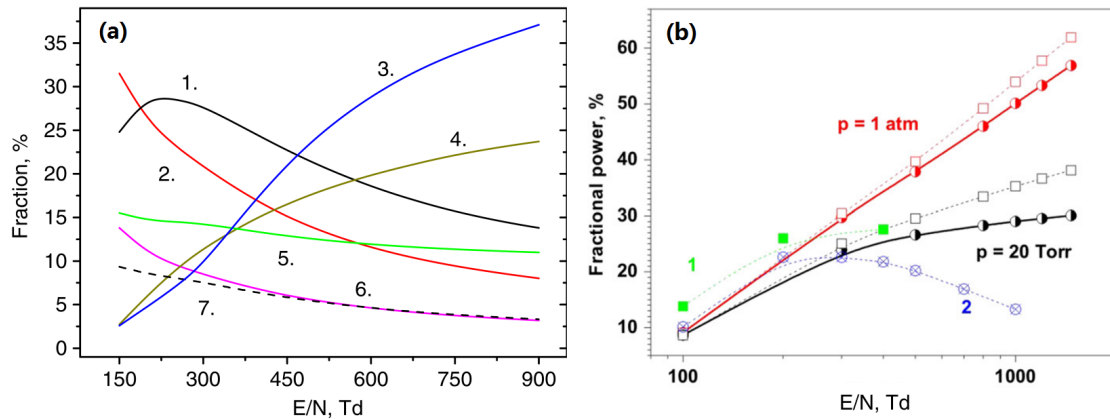


Figure 1.9: (a) Contribution of processes to fast gas heating in air at  $P = 760$  Td as function of reduced electric field. Curve 1: quenching of  $\text{N}_2(\text{C}^3\Pi_u)$  state by molecular oxygen, 2: quenching of  $\text{N}_2(\text{B}^3\Pi_g)$  state by molecular oxygen, 3: reactions involving charged particles, 4: dissociation of  $\text{N}_2$  by electron impact and following quenching of  $\text{N}(^2\text{D})$  atoms, 5: quenching of  $\text{O}(^1\text{D})$  atoms by molecular nitrogen, 6: dissociation of  $\text{O}_2$  by electron impact, 7: quenching of  $\text{N}_2(\text{A}^3\Sigma_u)$  and  $\text{N}_2(\text{a}^1\Sigma_u^-)$  states by molecular oxygen. (b) The total fractional electron power transferred into heat in dry air at 20 Torr and 1 atm as a function of the reduced electric field. The calculations were carried out for initial electron density being  $10^{15} \text{ cm}^{-3}$  (solid curves) and  $10^{14} \text{ cm}^{-3}$  (dash curves). Curve 1 corresponds to calculations [37] and curve 2 corresponds to the calculations assuming that 28% of the energy spent on the excitation of electronic  $\text{N}_2$  and  $\text{O}_2$  states is quickly transferred into gas heating. The figures are taken from [37] and [88], respectively.

rectly used to estimate the fast gas heating energy delivered into gas, by multiplying with deposited energy calculated based on measurement or simulation. In [88]  $\eta_{total}$  calculated from two groups were compared, see Figure 1.9 (b). The value of  $\eta_{total}$  was not in agreement between groups especially at high electric fields. [88] concluded that  $\eta_{total}$  increases with  $E/N$ , and can reach 50%-60% when  $E/N \geq 1000$  Td. In [37]  $\eta_{total}$  is almost constant and equal to  $30\% \pm 3$ , the difference is caused by different treatment of energy release from electron-ion recombination reactions.

## 1.2.2 Dynamics and fluid coupling

Dynamics simulation of NPD provides the spatial-temporal evolution of species and charges, making a consistent description of NPD available. The simulation of NPD in high pressure can be considered as the simulation of streamers with or without dielectrics. However, there exist multiple numerical challenges.

First, the dynamics of streamers is highly nonlinear, because the electric field

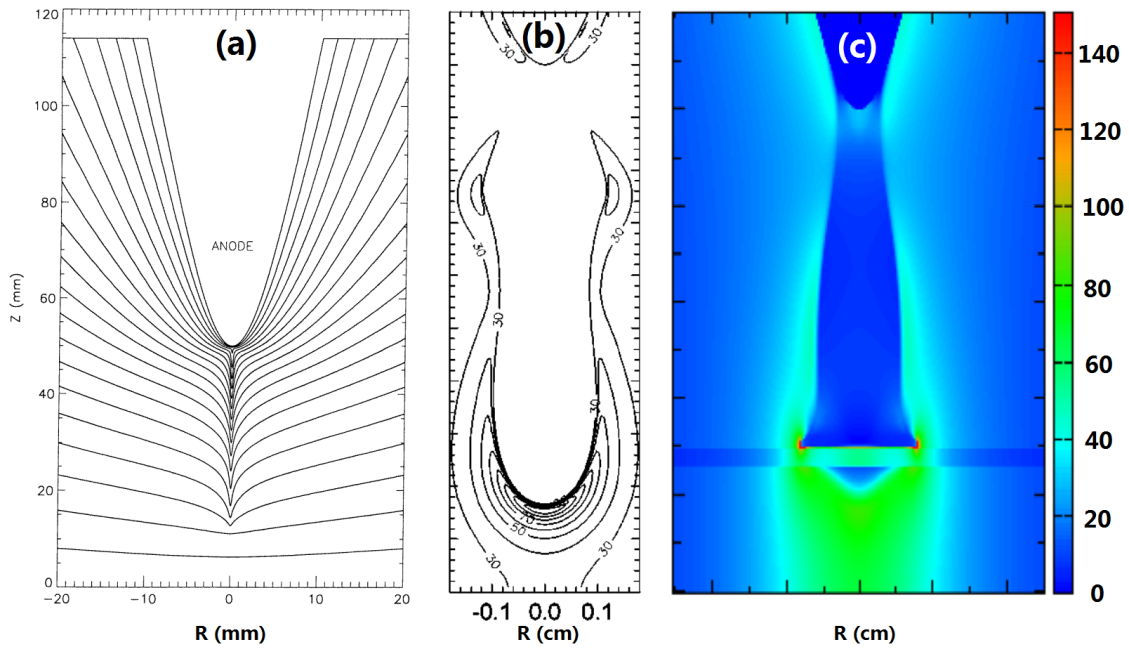


Figure 1.10: Calculated distribution of electric field distribution for streamers from different groups, (a) 1.5D model of a volumetric streamer [89]; (b) 2D asymmetric model of a volumetric streamer [90]; (c) 2D asymmetric model of a volumetric streamer in contacting with a dielectric barrier [91].

is coupled with the space charge layer at the streamer head and between streamer body and dielectric surface, therefore high resolution numerical implementations are required. Besides, since the space charge layer has a curvature, a pure 1D model is not enough to describe the propagation of streamers. In [89] a 1.5D model is proposed to study the streamer in a pin-to-plane configuration by linking a two dimensional solution of Poisson equation to one dimensional transport equations. The propagation and axial electric field were successfully modelled, see Figure 1.10 (a). However this approach fails in case of negative streamers and surface streamers. Paper [92, 93] introduced the Schaffter-Gummel (SG) method to the simulation of streamers by applying an implicit variant to simulate the pseudospark discharge and glow discharge in a 2D cylindrical geometry, and in [94, 95] the dynamics of positive and negative streamers were analysed. The SG scheme was later improved and used [96] for 2D simulations of high pressure discharges. The SG scheme is modified in [90] to improve the precision of a pin-to-plane streamer simulation, see Figure 1.10 (b). More precise and monotonic schemes were applied in recent works to improve the calculation of streamers in the vicinity of dielectrics [91], as can be seen in Figure 1.10 (c).

Second, streamer discharges are spatially multi-scale phenomena. The space charge layer at the head of the streamer is very thin and curved. It is of the order of

a few electron mean free paths, which is a few micrometers in atmospheric air. At the same time, typical propagation length of streamers is centimeters or more. This means that a streamer model has to be able to resolve at least these two length scales separated by four orders of magnitude. The most widely used approach is to use non-uniform mesh, with smaller grid size for plasma region. Some pioneering works done in [97,98] used structured adaptive mesh refinement (SAMR), see Figure 1.11, significant gain in performance was achieved with these techniques. Streamers are also temporally multiscale phenomena. The typical time development of streamers is usually tens of nanoseconds, whereas the smallest time scale to capture the dynamics can be as small as  $10^{-14}$  s for NPD in atmospheric pressure. Efforts to release the limit of time scale includes semi-implicit time stepping [99–101] and asynchronous scheme with local time stepping [102].

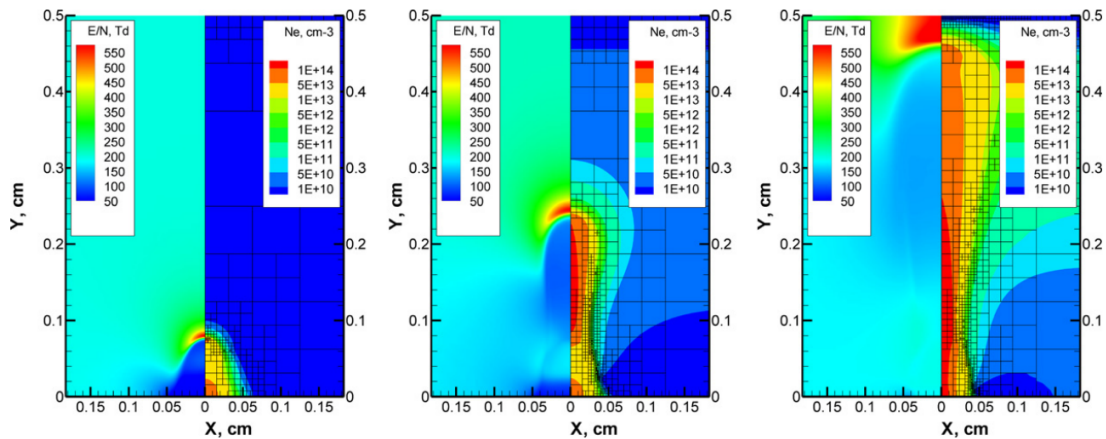


Figure 1.11: Electric field and electron density distributions for cathode-directed streamer at different time moments. Results of 2D simulation with adaptive mesh of  $10^{-4}$  cm. Blocks of  $8 \times 8$  cells are shown. Figure is taken from [97].

Third, streamers are intrinsically non-local phenomena, which makes it difficult to efficiently parallelize the numerical implementation. The non-locality of streamers is attributed to the non-locality of the electric field and photo-ionization. Once in presence of dielectrics, the boundary conditions on the interface lead to steep gradients and even discontinuities of the electric field, as well as of the charge density. To account for this non-locality, one of the solution is local energy approximation, that the kinetic and transport coefficients are taken as functions of the local mean electron energy, the latter being evaluated by the addition to the streamer model of the electron energy balance equation [104,105]. Another approach is to introduce, at evaluation of the ionization rate constant, some corrections proportional to the gradients of electron density and electric field [106–108]. More rigorous methods con-

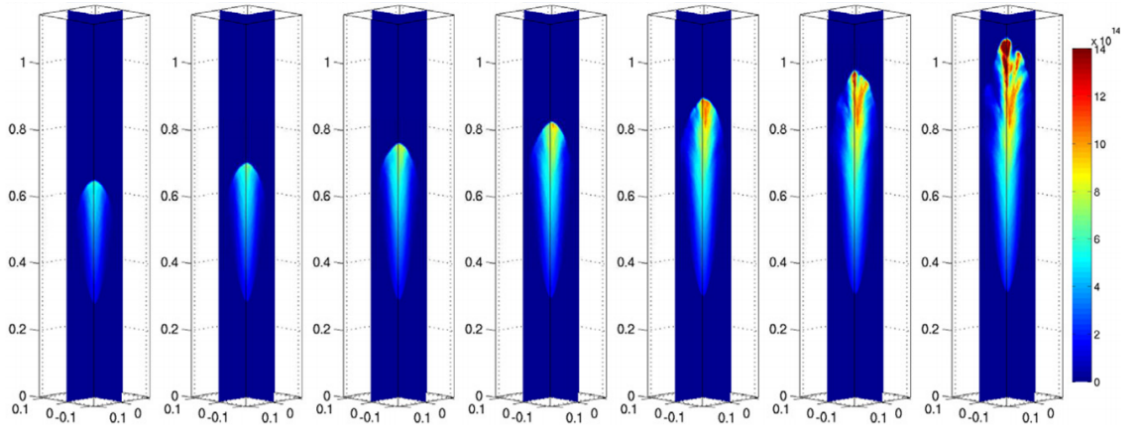


Figure 1.12: The electron density of a anode directed streamer in a hybrid model. The columns show the temporal evolution from time 0.72 to 0.9 ns in steps of 0.03 ns. The densities are plotted on two orthogonal planes intersecting with the 3D structure. Densities range from 0 (blue) to  $1.4 \times 10^{15} \text{ cm}^{-3}$  (red), as indicated by the color bar. The full height of 1.17 mm of the simulated system is shown in the lowest row, while the upper rows are truncated below 0.2 mm. The figure is taken from [103].

cerning the formation of fast (runaway) electrons, are based on hybrid approaches, see Figure 1.12, coupling of a particle model for a streamer head region with a fluid model for a channel is used in [103]. The “beam-bulk” models combining the Monte Carlo method for fast electrons, with a fluid code for bulk electrons are also used in several works [109–112]. In a number of works, mostly aimed at the simulation of runaway electron beams or study of streamer inception and branching, pure particle models, which couple particle-in-cell codes (PIC) with Monte Carlo collision codes (MCC) are used [113–116].

The coupling between dynamics of fluid and NPD is another point of interest, especially for the community of aerodynamics and combustion. Challenges in the coupling of plasma and fluid come from the large gap of timescale (ns for plasma and ms for fluid) and spatial scale of mesh size ( $\mu\text{m}$  for plasma and mm for fluid) required for plasma equations and Navier-Stokes (N–S) equation, and from the coupling with chemistry. Two approaches are usually used: (i) to solve plasma equations assuming constant gas parameters (temperature, density, ...) for energy deposition and species distribution. The calculated results from plasma equations are used in the same mesh or mapped to the mesh for N–S equations as initial conditions; (ii) to solve plasma and fluid equations simultaneously on the same mesh and the same time step during the voltage pulse, then solve pure transport-reaction equations for excited species and N–S equation for gas parameters.

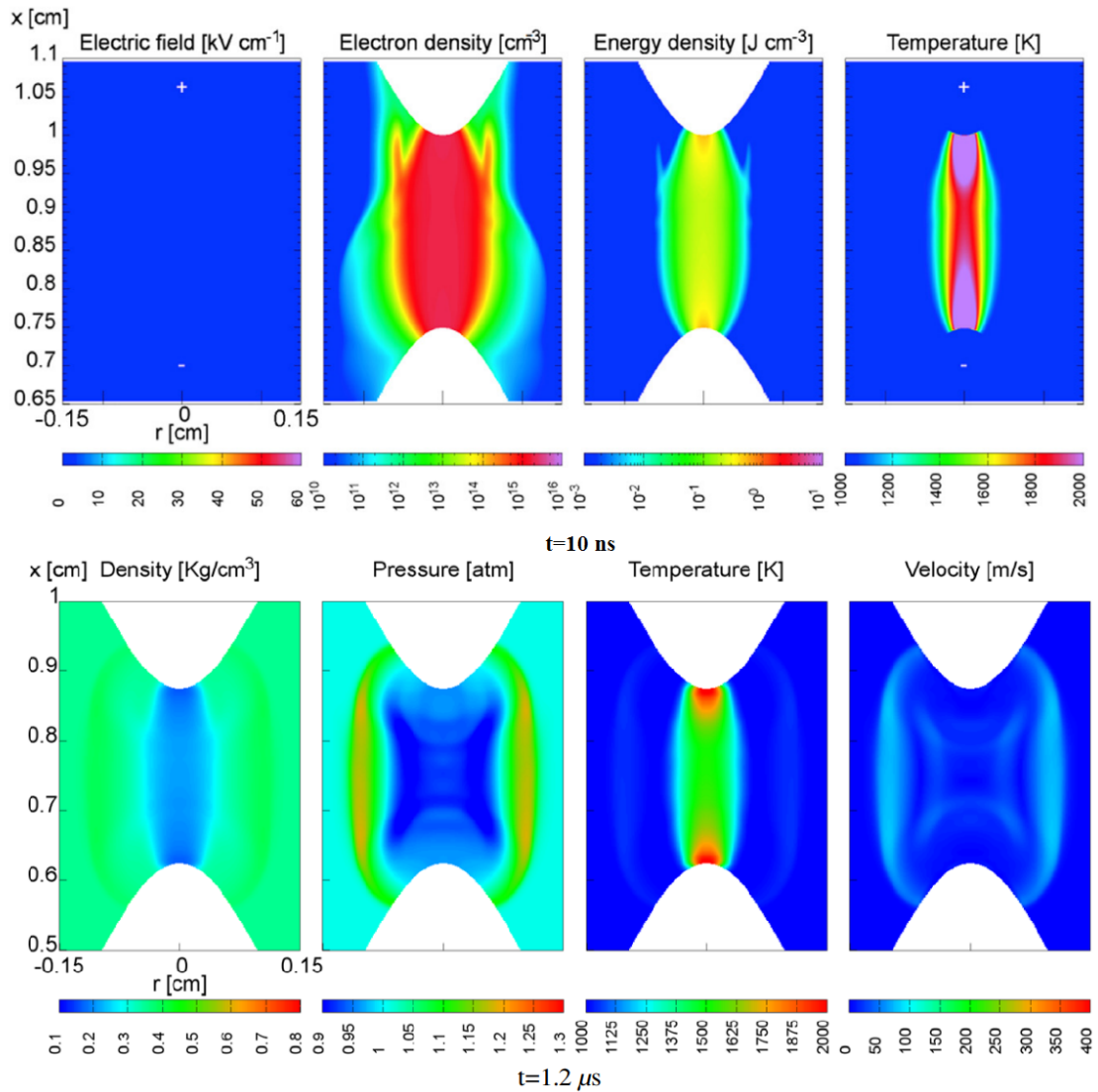


Figure 1.13: Cross-sectional views of calculation results in a pin-to-pin discharge in air, conducted at  $P=1$  bar,  $T=1000$  K. First row: calculated plasma parameters at 10 ns. Second row: fluid responses at  $1.2$   $\mu$ s in air. The figures are taken from [117].

Approach (i) makes full use of the advantages of plasma codes and CFD codes from different groups or based on different data structures and algorithms. In [117] the dynamics of formation of a nanosecond spark discharge between two point electrodes in air at atmospheric pressure at 300 and 1000 K, the induced air heating and the following hydrodynamic expansion are studied by considering the solution of plasma equations as initial conditions for fluid equations, see Figure 1.13, both discharge parameters and fluid characteristics were calculated in the same geometry, a shock wave was generated right after the discharge with gas heated in the discharge region. The disadvantage of approach (i) is that, one has to be careful if mesh mapping technique was used, as CFD meshes are usually coarser than mesh for

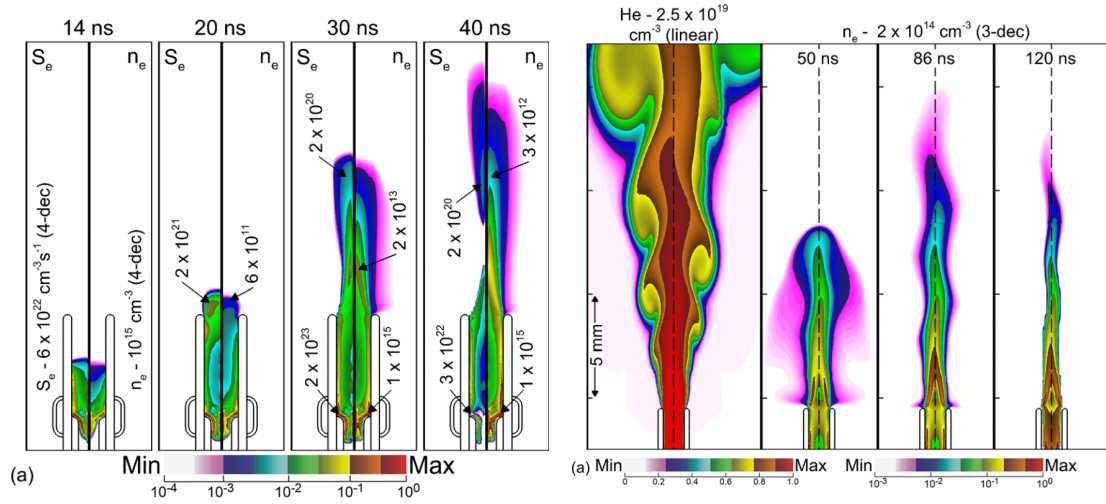


Figure 1.14: Cross-sectional views of calculation results of an atmospheric pressure plasma jet. Left 4 figures: plasma properties during and after the ionization wave, Electron impact ionization source (left half) and electron density ( $n_e$ ) (right half) during the ionization wave. Right 4 figures: characteristics of the resulting slot jet, initial eddy-dominated helium density for a flow rate of 15 slm/mm (first figure), with electron densities as the plasma propagates into the unstable flow (last 3 figures). The figures are taken from [118].

discharge, the information obtained from plasma equations may be “diluted” or “averaged” to unnoticeable level during interpolation. Also, the one direction coupling method (from plasma to fluid) does not solve influence of fluid to plasma dynamics.

Approach (ii) sacrifices the computational cost to achieve higher resolution solution for both plasma and fluid equations. This approach can be found in recent work [118], which studied the stability of a He atmospheric pressure plasma jet with a powered electrode exposed to the gas flow, see Figure 1.14. It was found that localized gas heating at the powered electrode occurs on the time scale of the voltage pulse, tens to 100 ns, which is short compared to the fluid timescales. An acoustic wave propagates from this heated, expanding gas and exits the jet. The wave disturbs the shear layer between the He and surrounding air, exciting a shear instability which grows downstream with the flow and increases the mixing of the air into He. The result is an ionization wave propagating in an eddy-dominated flow.

### 1.3 Simulation of nCD and nSDBD: a comparative view

The developing kinetics theory and innovative numerical techniques give access to high resolution simulation of nanosecond capillary discharges and dielectric barrier discharges. These two types of discharges share the common features in NPD: (i) both discharges propagate with strong electric field in the ionization head and relatively low field in the plasma channel during propagation. They can be considered as streamer propagation in different geometries; (ii) both discharges are conducted at relatively high pressure, leading to high collision frequency and rich kinetics; (iii) both discharges are accompanied with significant temperature rise due to fast gas heating in the time scale of tens to hundreds of nanoseconds. In aforementioned features, (ii) and (iii) are essential in study of nCD and nSDBD, and numerically can only be studied by models based on fluid methods currently.

Despite the aforementioned features sharing in common, nCD and nSDBD attract the interest from the community of numerical simulations in rather different aspects. The reason can be classified as different kinetics and dynamics properties.

#### (I) Kinetics properties.

In a capillary tube, the discharge process is confined within a dielectric wall. By adjusting the tube radius and applied voltage pulse, the specific deposited energy in the tube can be changed accordingly. It has been found that, the behaviour of species evolution and fast gas heating cannot always be predicted by available kinetics scheme when the specific deposited energy  $E_{dep} \geq 0.1$  eV. On the other hand, by slightly tuning down the pressure in the tube, a uniform discharge can be achieved when the streamer fills a tube. The uniformity of plasma parameters, makes nCD an attractive tool for analysing detailed kinetics of discharges at different deposited energies, using 0D or 1D global models with experimental measurements.

In [79], quenching of electronically excited nitrogen state,  $N_2(C^3\Pi_u)$ , in the afterglow of nanosecond capillary discharge in pure nitrogen is studied. On the basis of additional measurements of electron density and a 1D kinetic model, see Figure 1.15 (a), the anomalously fast quenching of the  $N_2(C^3\Pi_u)$  in the afterglow is explained by quenching in collisions with electrons. The high electron density in the afterglow is sustained by associative ionization via  $N_2(A^3\Sigma_u^+)$  and  $N_2(a^1\Sigma_u^-)$  electronically excited molecules at high specific deposited energies ( $E_{dep} = 1.0$  eV), as is shown in Figure 1.15 (b).

In [120], a 1D kinetic modelling of nCD in air at similar deposited energy ( $E_{dep} = 1.0$  eV) is conducted. The results show that, a high dissociation degree of oxygen molecules makes relaxation of the electronic energy of atoms and molecules

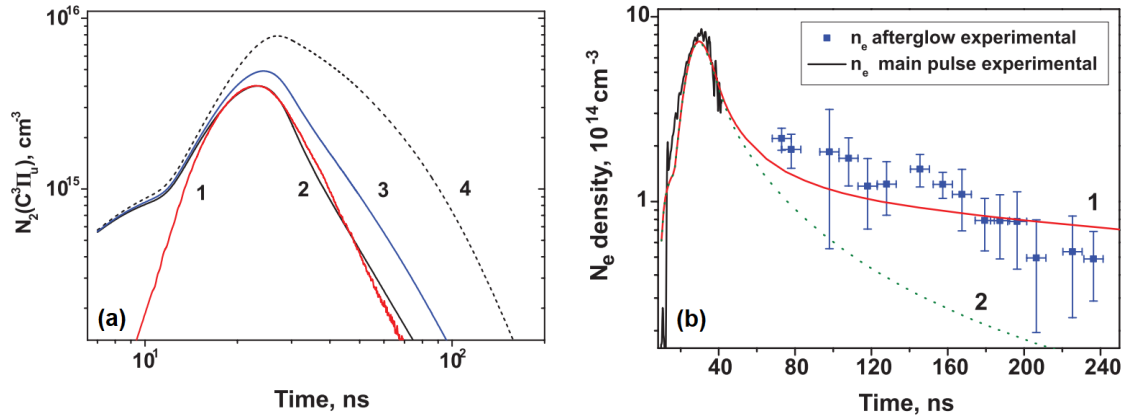


Figure 1.15: Comparison between calculations and experimental results of a capillary discharge. (a) Calculated density of  $N_2(C^3\Pi_u)$  state compared to measured emission profile. Curve 1 corresponds to measured signal in arbitrary units, curves 2-4 correspond to numerical calculations with different quenching rate constant. (b) Calculated and measured electron density in the afterglow for 27 mbar pure nitrogen. Calculations are performed with (curve (1)) and without (curve (2)) taking into account the reactions of associative ionization. The figures are taken from [79].

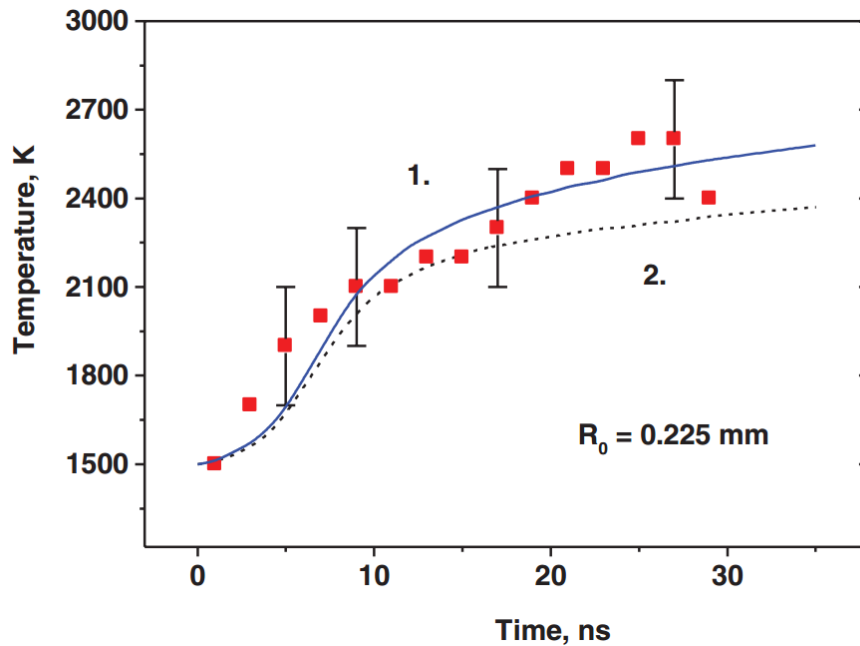


Figure 1.16: Temporal dynamics of the gas temperature at the discharge axis under the conditions of [25, 119]. The dots are for the experimental data, and the curves are for the numerical results taking into account gas heating from different reactions. The figure is taken from [120].

in reactions with O atoms extremely important. Fast gas heating in the discharge plasma due to the quenching of electronically excited N<sub>2</sub> molecules by oxygen atoms becomes noticeable, resulting in a temperature rise of 1000 K in 30 ns, see Figure 1.16.

Nanosecond SDBD, In contrast to nCD, is not an ideal tool for kinetics investigation, based on two reasons: (i) instead of a volumetric discharge in the capillary tube at moderate pressures, nSDBD operates mainly at pressures equal or higher than 1 bar, the discharge is closely attached to a plane surface. As a result, the discharge parameters are non-uniform, and it is difficult to conduct high resolution diagnostics in the thin plasma layer; (ii) the specific energy deposition for nSDBD is quite small comparing to nCD (an estimated value of maximum 0.2 eV/mol for discharges initiated by 20 kV, 2 ns voltage pulse in air:H<sub>2</sub> mixture nSDBD), the changes of kinetics are not as dramatic as in nCD discussed before. As a result, the study of kinetics concerning nSDBD is mainly based on the reduction of classical air plasma chemistry, which has been discussed in the previous section.

(II) Dynamic properties.

Capillary discharges model in most of available works are configured with an open side in the tube [121–125], which is directly related to applications. The aim of these models are to study the dynamics of plasma jet or plasma “bullets” injected into the ambient air, and the interaction between plasma and the ambient gases. Dynamics of plasma within the capillary tube during and after discharge is not well addressed in those works.

In [121], a positive streamer propagation in atmospheric-pressure helium jets injected into ambient air was modelled, two types of streamer structures were identified, depending on the jet width and the initial radial distribution of electron number density, see Figure 1.17: one with maxima of electric field and electron density at the jet axis and another with maxima of these parameters near the boundary between the jet and surrounding air. In this case, the dynamics of discharge propagation along the tube wall is not studied, but the ambient air still plays as a virtual wall.

A few modelling studies of nanosecond discharge propagating within a capillary tube operated at atmospheric pressure are available. In [126] 2D simulations were performed for Xe: Ne FIW discharges initiated by a nanosecond, high-voltage pulse and propagating in a branched channel consisting of two straight inlet and outlet sections separated by a circular loop section, shown in Figure 1.18. Qualitatively agreement of the dynamics of FIW splitting, propagation and merging between predictions and experimental observations is achieved. It was found that, with tube radius of 4 mm, for straight channels, the FIW develops along both walls while for curved channels, plasma typically hugs one side of the wall, but can shift from one

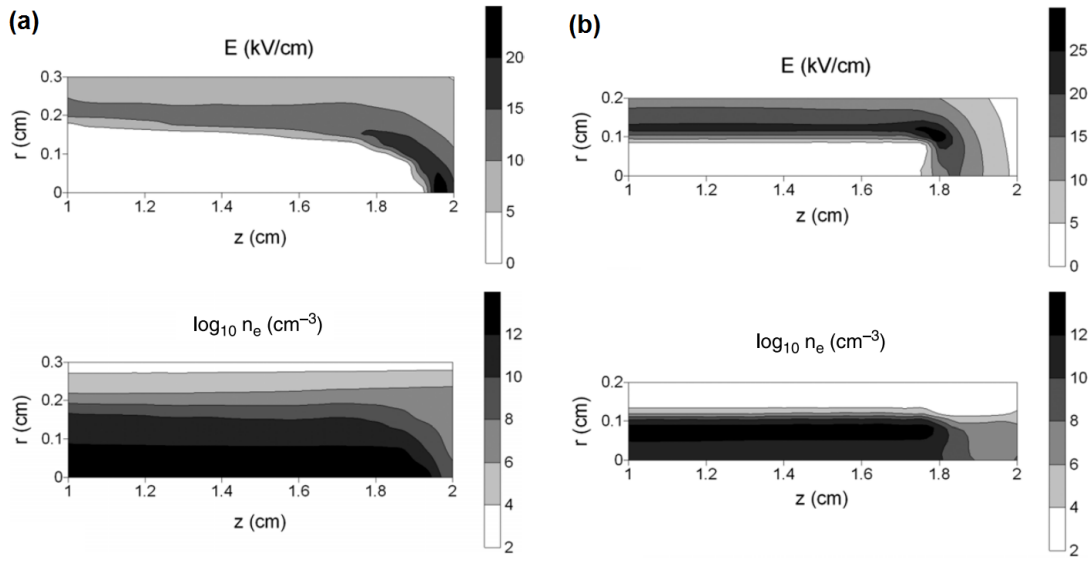


Figure 1.17: Calculation results of a atmospheric pressure helium plasma jets. Contours of electric field and number density of electrons at (a) time moment 180 ns, the jet radius 0.25 cm; (b) time moment 160 ns, the jet radius 0.1 cm. The figures are taken from [121].

side to the other during the propagation.

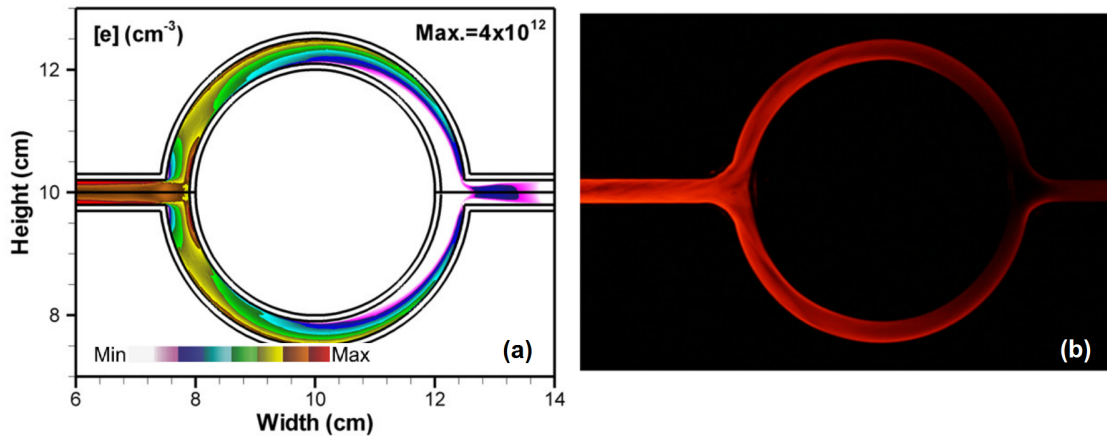


Figure 1.18: Plasma properties of a fast ionization wave front propagating in atmospheric-pressure neon. (a) Computed electron density at  $t = 320$  ns; (b) experimental time-integrated 16 ms exposure of visible neon emission. The figure is taken from [126].

Simulation of the nCD propagation operated in air was done in [127] at atmospheric pressure. Structure and dynamics of a discharge in air at atmospheric pressure initiated by a needle set in a dielectric capillary tube were studied assuming a constant voltage of 6-9 kV. Calculations reveal the influence of the tube inner

radius  $R$ , relative permittivity  $\epsilon_r$  and photoemission source on the discharge structure and dynamics. On the basis of the results presented in Figure 1.19, it can be concluded that for atmospheric pressure: (i) for a tube radius of  $100 \mu\text{m}$  and  $\epsilon_r = 1$ , the discharge fills the tube during propagation and is rather homogeneous behind the discharge front, as is shown in Figure 1.19 (a); (ii) when permittivity increases, the discharge structure becomes tubular (Figure 1.19 (b)); (iii) when the radius increases from  $100 \mu\text{m}$  to the range  $300\text{-}600 \mu\text{m}$ , the discharge structure is tubular with peak values of electric field and electron density close to the dielectric surface (Figure 1.19 (c)); (iv) photoemission increases the number of secondary electrons close to the dielectric surface, and promotes the tubular structure of the discharge. Paper [127] also indicates that, the discharge velocity increases with decrease of the tube radius and dielectric permittivity, but decreases at very high values of the photo-emission coefficient.

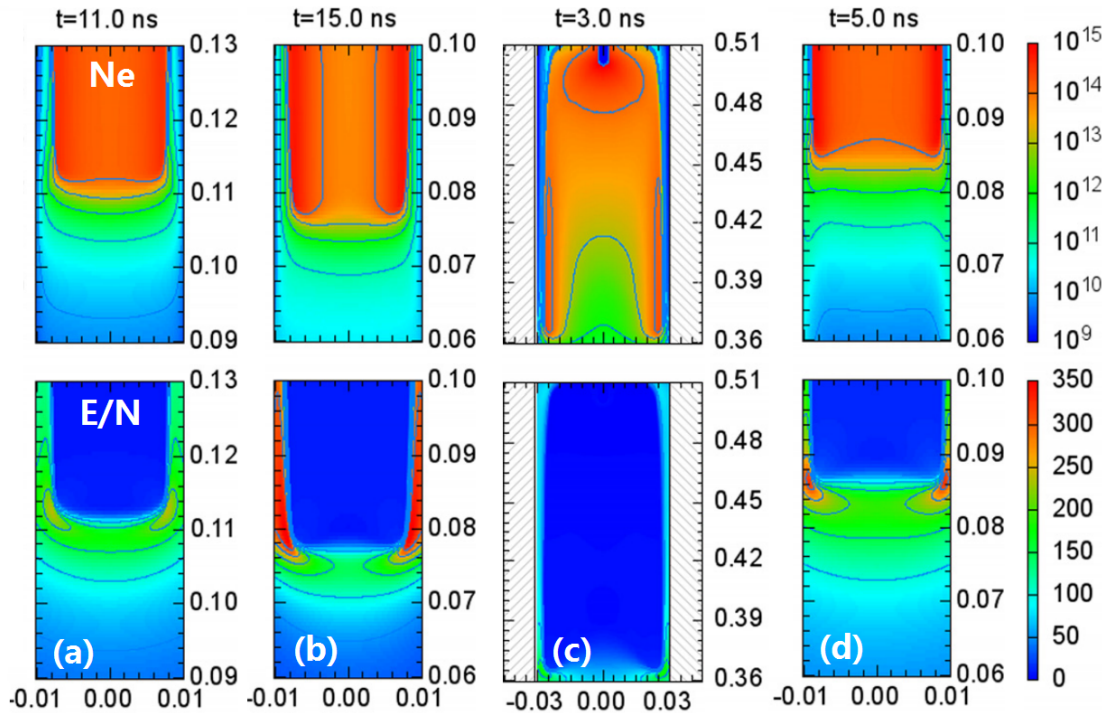


Figure 1.19: Calculated results of propagation of electron density ( $N_e$ ) and field ( $E/N$ ) in a capillary tube with different tube radius  $R$  and relative permittivity  $\epsilon_r$ . (a)  $R=0.01 \text{ cm}$ ,  $\epsilon_r=1$ ; (b)  $R=0.01 \text{ cm}$ ,  $\epsilon_r=5$ ; (c)  $R=0.03 \text{ cm}$ ,  $\epsilon_r=1$ ; (d) the same as (a) but with photo-emission source term included with coefficient  $\gamma_{photo} = 5.0 \times 10^{-4}$ . The applied voltage is  $6 \text{ kV}$  for (a)-(c) and  $9 \text{ kV}$  for (d). The figures are taken from [127].

One can find that, for practical applications, numerical studies of capillary discharges are either operated at atmospheric pressure, or conducted with an open side

tube, or ignited in rare gases. However, the potential for kinetics research drops in these conditions, as the increased pressure makes it hard to achieve global uniformity, and the low current in open tube results in only low specific energy deposition conditions.

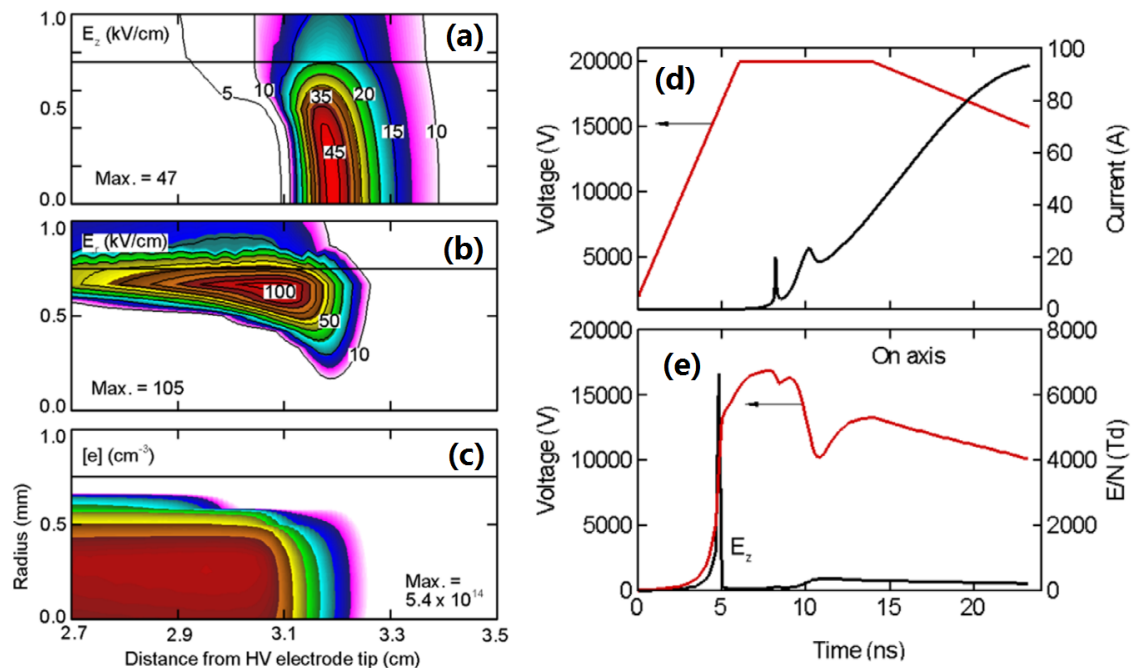


Figure 1.20: Calculated results of plasma parameters during and after an capillary discharge operated at moderate pressure 27 mbar: the instantaneous axial (a) and radial (b) electric fields, the electron density (c) at the FIW front, the HV electrode voltage and transmitted current (d), as well as the time dependences of potential and axial electric fields on tube axis (e). The figures are taken from [128].

The unique features of nanosecond capillary discharge studied in this work is related to the special geometric characteristics: a closed tube sustaining a moderate pressure and high specific energy deposition. A first trial of modelling of nCD in this condition, can be found in [128]. In this paper, air discharges initiated in a quartz capillary tube, having inner and outer diameters of 1.5 and 3.4 mm, and length of 80 mm at 27 mbar were studied by both experiment and simulation. The simulation focuses on the FIW and the plasma properties in the immediate afterglow after the conductive plasma channel has been established between the two electrodes. The FIW produces a highly focused region of electric field on the tube axis that sustains the ionization wave (see Figure 1.20 (a)-(c)) that eventually bridges the electrode gap. Results from the model predict FIW propagation speed, current rise and  $E/N$  rise agree with the experiment (see Figure 1.20 (d) and (e)). The influence of tube walls on discharge propagation and structure in this special condition, the influence

of energy deposition on spatial-temporal evolution of discharge structures in the afterglow, were not studied yet.

Comparing with nCD, more efforts have been devoted to numerical studies of nSDBD during the past decades. As a configuration designed initially for aerodynamic applications, nSDBD has attracted attention from the communities of both aerodynamics and plasma physics.

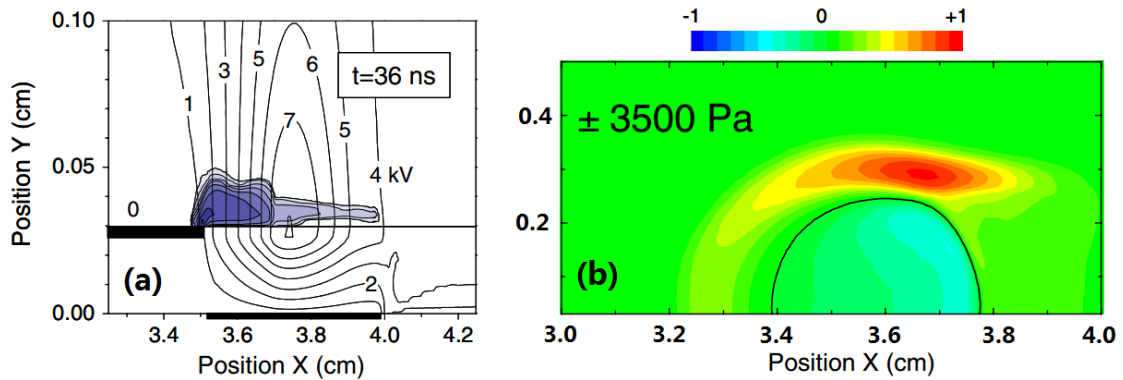


Figure 1.21: Calculation results of a coupled nSDBD model. (a) Electron density (grey scale) and potential distribution (contours) at 36 ns. The plotted contour levels are 0.01, 0.02, 0.05, 0.1, 0.2, ...,  $\times 10^{20}$   $\text{m}^{-3}$ , with a maximum value of  $2.2 \times 10^{20}$   $\text{m}^{-3}$ . The electric potential contour levels are indicated in kV. (b) Spatial distribution of the gas pressure perturbation at time  $t = 8$   $\mu$ s. The figures are taken from [98]

Pioneering simulation of nSDBD can be found in [129], in which the use of positive repetitive pulses with dc bias is demonstrated to be promising for enhancing EHD force and the ion wind for SDBD actuators. But later investigations revealed that, the nSDBD modifies flow field by thermal effects rather than by ion wind. In [98] a model coupling fluid discharge equations of 3 species with compressible Navier-Stokes equations was proposed, the thermal effects were considered using a simple gas heating model. The results shown in Figure 1.21 confirm that fast gas heating takes place in the boundary layer, leading to the generation of a “micro” shock wave in the flow field. Since then, thermal effects become one of the key interests of research. Two approaches dealing with the energy release of nSDBD have been used in the community of aerodynamics and plasma physics, respectively.

The first approach is to simplify the thermal effects by a simple line distribution of temperature boundary [130] or a phenomenological model [131–134]. Paper [131] assumes that the electric field far ahead of the wave is created by the space charge in the wavefront (see Figure 1.22 (a)), approximated as a thin charged line on the surface of the dielectric layer with thickness  $h$  and dielectric constant  $\epsilon$ , placed on top of the grounded electrode. The 2D drift-diffusion equations of a surface

nanosecond pulse discharge were reduced to a quasi-1D equation system for the near-wall electric field components parallel and perpendicular to the surface, electron and ion densities, and plasma layer thickness parameter. Providing electric field, electron density distributions and the plasma layer thickness versus the ionization wave speed, the equation system can be solved analytically. The resulting distribution of heating energy is shown in Figure 1.22 (b).

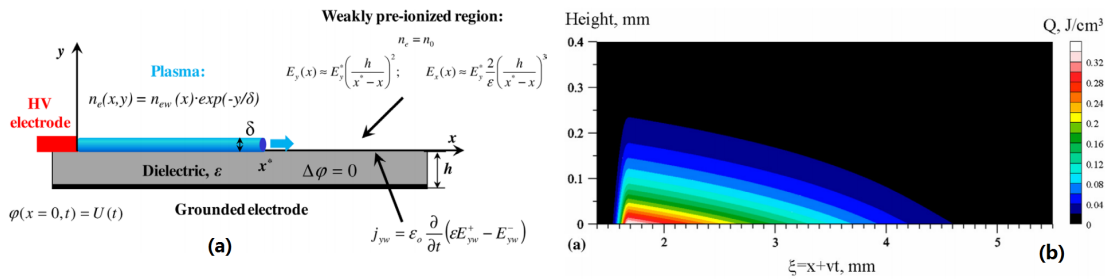


Figure 1.22: (a) A schematic view of the simplified phenomenological model. (b) Total energy coupled per unit actuator length calculated from the phenomenological model. The figures are taken from [131].

This approach was frequently used for high resolution computational fluid dynamics (CFD) [130, 132–134], due to its simplicity in implementation. However, this approach is not self-consistent, some input parameters can only be provided by approximations and experiments, and cannot capture the physics near the electrode. Currently there is no direct validation of this approach. The micro-shock waves observed in experiments were usually used as a way for validation in these works, but it is a rather rough validation, as similar shock waves can be generated within a wide range of energy density values and distributions, while the local structure of flow field modified by different distribution of gas heating energy is definitely different.

The second approach is to characterise nSDBD based on the coupled solution of Poisson equation, transport equations for charged particles, photoionization and minimum set of kinetic equations for charged species. This approach focuses more on the physical process of nSDBD. The most detailed and complete analysis of physics of a nSDBD available at present, can be found in recent cycle of publications [108, 135–137], in which the discharge development and propagation of the streamer initiated by a high-voltage nanosecond pulse have been studied. Different shapes of the discharge were reported: diffuse discharge for negative polarity, with a thin, a few microns, layer of high electric field and low electron density in the vicinity of the dielectric; and a “streamer-like” discharge for positive polarity, the thickness of the layer of the high electric field under the streamer is tens of microns,

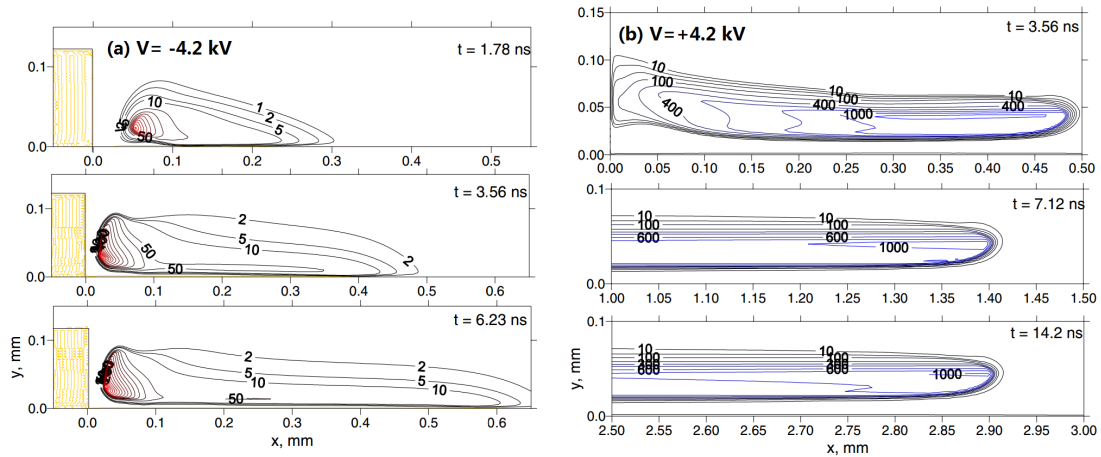


Figure 1.23: Calculation results of a surface streamer evolution. Electron density  $n_e/n_0$  contours in (a)  $-4.2$  kV and (b)  $+4.2$  kV. The figures are taken from [108].

as was shown in Figure 1.23. Specific energy distribution in the discharge was calculated on the basis of the current density and electric field. It was shown that in the negative polarity discharge, the energy is concentrated near the high-voltage electrode (cathode) whereas in the positive polarity streamer the energy is spread almost uniformly along the streamer.

Paper [110] presents a comparative numerical study of nSDBD discharge for both polarities for high ( $\varepsilon = 16$ ) value of a dielectric permittivity, voltage of 12 kV, and the thickness of the dielectric of 0.5 mm. Calculations were performed using two different approaches. Calculations using 2D fluid model was compared with the calculation with the help of a new hybrid model. The hybrid model considered bulk electrons in a fluid approximation, while electron Monte Carlo simulation (EMCS) was used to treat energetic secondary electrons in a kinetic way. The calculation confirmed qualitatively behavior of positive and negative polarity streamers obtained earlier. A consistent set of velocities, isolines of the electron density, ionization source and electric field near the streamer head has been presented. Results in Figure 1.24 show that, the positive polarity streamer does not change when using EMCS module. With negative polarity applied to the high-voltage electrode, the anode layer is formed between the streamer body and the surface. The electrons are trapped in the sheath region by the electric field and produce a thin near-surface layer ahead of a streamer that significantly accelerate the streamer propagation.

The second approach was incorporated with N-S equations in many teams to have a multi-physics modelling of nSDBD, many of which are based on existing open source or commercial software, including OpenFOAM [138, 139], COMSOL Multi-physics [13, 140–142], et al. These modelling works combined solution of plasma equations and fluid equations in the same framework to have a self-consistent de-

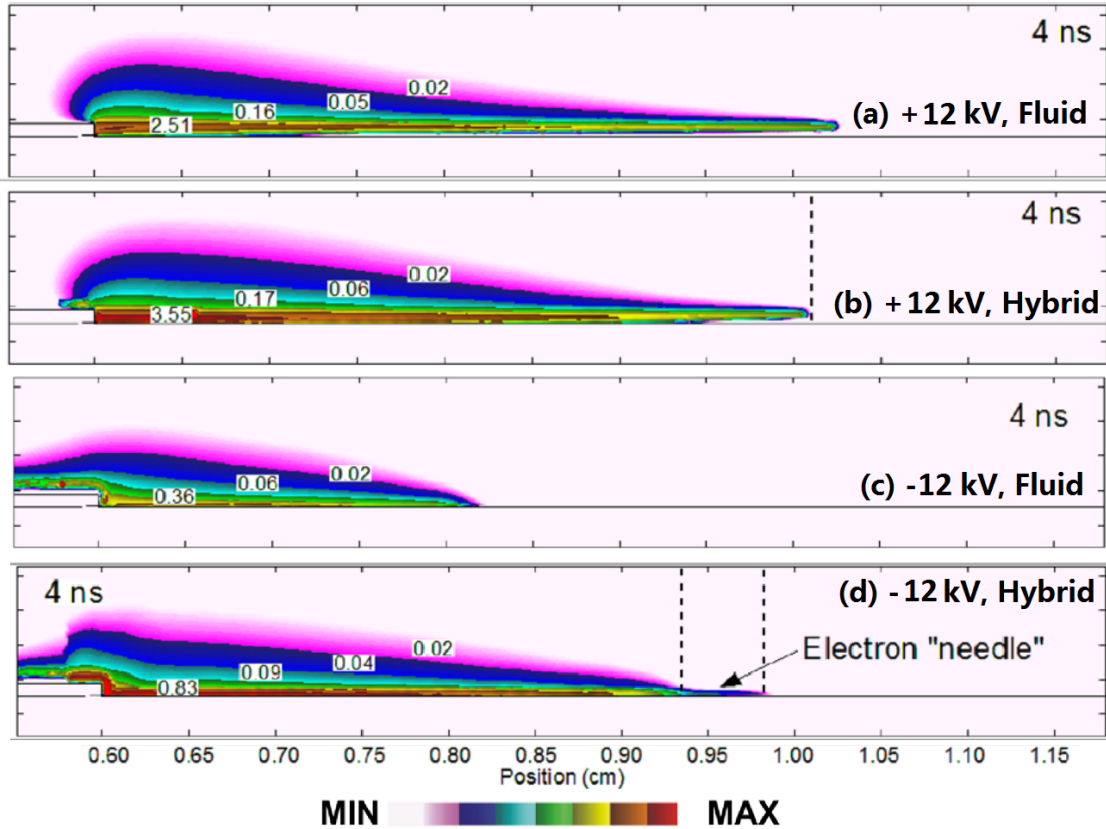


Figure 1.24: Calculated electron density  $n_e/n_0$  with different voltage polarities and approaches. (a) +24 kV, fluid method; (b) +24 hybrid method; (c) -24 kV, fluid method and (d) -24 kV, hybrid method.  $n_0$  is taken as  $10^{15} \text{ cm}^{-3}$ . The figures are taken from [110].

scription of plasma flow control. However, in these works, plasma and fluid are coupled mainly in one direction (from plasma to fluid) and separate in time sequence (calculate plasma dynamics only in ns time scale and then fluid dynamics in longer time scale). Results obtained in these models, need supports from numerical benchmarks and experimental measurements.

In conclusion of this comparative discussion, modelling of nCD is aimed at analysing kinetics of NPD at different specific energy deposition, the dynamics properties play a second role and provide necessary dataset for 0D or 1D chemical modelling as initial conditions and for reference of experimental measurements; modelling of nSDBD, on the contrary, focuses more on discharge dynamics and energy release based on existing kinetics, and the fluid responses for applications.

---

---

# Chapter 2

---

## Problem formulation

As it was mentioned in the literature review, nanosecond pulsed discharge (NPD) is characterized by high electric field, high chemical reactivity, and fast gas heating. Nanosecond capillary discharge (nCD) and nanosecond surface dielectric barrier discharge (nSDBD) are two typical types of NPD.

nCD is characterized by a high specific energy deposition when operated at moderate pressures in a closed tube. The unambiguous measurements of discharge parameters and densities of excited species make the nCD an ideal tool for kinetic study. Recent optical emission spectroscopy and TALIF measurements of nCD together with detailed kinetics models have revealed that, increase of the specific energy deposited during nanosecond discharge leads to increase of the probability of interaction of excited and/or charged species between each other, which changes the plasma kinetics dramatically. Therefore, the classical actinometry techniques have to be modified according to latest kinetics to detect O atoms in the early afterglow correctly. The spatial-temporal dynamics of nCD is important for providing initial conditions of kinetics model and for applications, and has to be modelled taking into consideration new kinetics features.

nSDBD is characterized by a relatively low specific energy deposition if operated at atmospheric pressure for applications like plasma flow control or plasma assisted combustion. The structure and dynamics of nSDBD provide necessary information of energy release and species distribution, which is important for applications of plasma assisted aerodynamics/combustion/ignition. However, the parameters of nSDBD plasma and physics of the discharge are not yet clearly understood, as the complex discharge structure and presence of dielectrics bring additional challenges to

experiments. Modelling of nSDBD, by linking together Poisson equation, transport equations, the stiff system of detailed chemical kinetics and fluid dynamics is also a challenging task due to high computational cost and complexities in multiphysics coupling, and currently no direct comparison between experiments and modelling results were found in the literatures.

The main aim of the present work is to study, on the basis of numerical modelling accompanied by experiments under the same conditions, the kinetics, transport and fluid responses of nanosecond plasma in a capillary tube and above a surface dielectric barrier. Codes based on different numerical methods have been selected or developed according to the case to be studied. Following objectives are to be achieved:

1) To analyse and update kinetics of nanosecond capillary discharge numerically based on experimental observations ( $E/N$ , current, profiles of optical emission) and to provide the basis for 2D self-consistent simulations. Based on the developed kinetics scheme, to study a possibility of optical actinometry for nanosecond pulsed discharges under high specific energy depositions in early afterglow. The calculations are performed using the GNU code for plasma kinetics, ZDPlaskin [143].

2) Based on simplified schemes from kinetics analysis, to study the spatial-temporal evolution of electric field, electrons and excited species in capillary discharges. To describe propagation of ionization waves with respect to tube radius. To study the hydrodynamic motions and the redistribution of species in the afterglow with regards to specific energy depositions. The results in turn provide initial conditions for further 0D and 1D kinetics analysis. The calculations are performed using nonPDPsim [96], a hybrid code with finite element meshes.

3) To study the characteristics of nSDBD at both negative and positive polarities. To obtain parameters of atmospheric nSDBD (propagation, current, field, density and optical emissions) and to compare them with experimental measurements. To analysis the fast gas heating and corresponding hydrodynamics responses. To predict the influence of dielectric permittivity and ambient pressure on the discharge characteristics. The calculation is based on a multi-scale, multiphysics code, Parallel Solver for Streamer with KinEtics (PASSKEy), which is developed independently during this thesis to study nSDBD with higher flexibility and reasonable cost of time.

---

---

## Chapter 3

---

### Mathematical model and numerical codes

Mathematical models for plasma simulation based on fluid method are used throughout this work, and they share the same origin: Boltzmann kinetics equation. With respect to the scale of problems to be solved, different orders of reductions are achieved, mathematical models for kinetics, transport properties and multi-physics coupling are derived in zero-dimension and two-dimension scale. All the mathematical models are closed with electron energy distribution function obtained from the two-term approximation of the Boltzmann equation.

Taking into account the differences in requirements of numerical approaches between nanosecond capillary discharge (nCD) and nanosecond surface dielectric barrier discharge (nSDBD) discussed in Chapter 1, a set of numerical codes based on different schemes are selected, modified or developed to study the specific features of each type of discharge.

The global kinetics in nCD is solved by 0D ZDPlaskin code [143] and simplified by a supplementary sensitivity analysis module developed in this work. A 2D self-consistent code nonPDPsim [96] is used to study the kinetics and spatial properties in nCD during and after the discharge. A 2D high performance/resolution PASSKEY code is developed in this work to study nSDBD coupled with fluid. Additionally, an improved COMSOL streamer code based on finite element method (FEM) is used for third-party validation and supportive calculations.

This chapter describes the mathematical theories and numerical codes used in present work. General schematics for each experiment is given with a following 0D/2D geometric modelling. Detailed measurement techniques and calculated results will be presented in upcoming chapters.

### 3.1 Elementary kinetics theory and approximations

The elementary kinetics theory of gases is the starting point to the fluid description of plasma. The following sections will illustrate the formulation of fluid models and corresponding approximations used in the models.

#### 3.1.1 Boltzmann equation

An ensemble of particles can be described by one distribution function  $f(\mathbf{v}, \mathbf{r}, t)$ , the statistical meaning of  $f(\mathbf{v}, \mathbf{r}, t)d^3rd^3v$  is the number of particles inside the phase-space volume  $d^3rd^3v$  at position  $(\mathbf{v}, \mathbf{r})$  and at time  $t$ . Then one can define the density of particles [144]:

$$n(\mathbf{r}, t) = \int f(\mathbf{v}, \mathbf{r}, t)d^3v \quad (3.1)$$

and the mean flux of the group of particles:

$$\mathbf{\Gamma} = n\mathbf{u}(\mathbf{r}, t) = \int \mathbf{v}f(\mathbf{v}, \mathbf{r}, t)d^3v \quad (3.2)$$

where  $\mathbf{u}$  is the mean particle velocity. The characteristic frequencies of collision between particles can then be defined from their cross sections by taking:

$$\nu = \frac{N}{n(\mathbf{r}, t)} \int \sigma \mathbf{v}f(\mathbf{v}, \mathbf{r}, t)d^3v \quad (3.3)$$

where  $N$  is the neutral particle density and  $\sigma$  the momentum transfer cross section. The equation governing the evolution of the distribution  $f(\mathbf{v}, \mathbf{r}, t)$  in above equations, is Boltzmann equation:

$$\frac{\partial f}{\partial t} + \mathbf{u}\nabla_r f + \frac{\mathbf{F}}{m}\nabla_v f = \left(\frac{\partial f}{\partial t}\right)_c \quad (3.4)$$

where  $\mathbf{F}$  is the force acting on the charged particles. The right hand side of Boltzmann equation is a symbolic representation of the collision processes.

It is hard to solve Boltzmann equation directly, but the velocity moments of this equation allow one to construct the fluid models.

#### 3.1.2 Fluid model for plasma

By taking the zero moment of equation 3.4, one can get the continuity equation:

$$\frac{\partial n}{\partial t} + \nabla\mathbf{\Gamma} = S \quad (3.5)$$

where  $\mathbf{\Gamma} = n\mathbf{u}$  is mean flux of particles as defined in equation 3.2,  $S$  denotes the source term for particles due to collisions, respectively. In this equation there are two unknown variables,  $n$  and  $\mathbf{u}$ .

The first moment of Boltzmann equation, momentum balance equation, is used to close the equation 3.5:

$$\frac{\partial \mathbf{u}}{\partial t} + (\mathbf{u} \cdot \nabla) \mathbf{u} = -\frac{\nabla P}{nm} + \frac{\mathbf{F}}{m} - \nu \mathbf{u} \quad (3.6)$$

where the second term on the left hand side is inertial term and the last term on the right hand side is the collision term. The isotropic pressure  $P$  can be represented as:

$$P = nk_b T \quad (3.7)$$

Equation 3.6 and 3.7 introduce additional unknown variable  $T$  to the system, which can be solved by taking the second moment of Boltzmann equation, energy conservation equation:

$$\frac{\partial n_\epsilon}{\partial t} + eE \cdot \mathbf{\Gamma} + \nabla \mathbf{\Gamma}_\epsilon = S_\epsilon \quad (3.8)$$

where  $n_\epsilon = 3nT/2$ . However, equation 3.8 again introduces new variable, the energy flux  $\mathbf{\Gamma}_\epsilon$ , which can not be simplified as  $\mathbf{\Gamma}_\epsilon = 0$  or  $\mathbf{\Gamma}_\epsilon = -k_T \nabla T$  in case of equilibrium discharges. Actually the solution of moment  $k$  of Boltzmann equation is always coupled to moment  $k+1$ , it is necessary to truncate the moment series at a finite stage by a set of approximations.

### 3.1.3 Drift-diffusion approximation

To truncate the moment of Boltzmann equation at first moment, a simplification of the moment balance equation 3.6 can be done.

First, the particle flow velocity becomes stationary in time scale of  $\tau = \nu^{-1}$ . If  $\tau$  is shorter than the propagation time scale  $\tau_s$  of streamers studied in our cases, the first term of equation 3.6 can be considered as 0:

$$\frac{\partial \mathbf{u}}{\partial t} \sim 0 \quad (3.9)$$

Second, if  $|(\mathbf{u} \cdot \nabla) \mathbf{u}| \ll \nu \mathbf{u}$ , which is common in high pressure plasma discharge, both terms of the left hand side of equation 3.6 can be neglected, and one obtains:

$$\mathbf{u} = -\frac{\nabla P}{nm\nu} + \frac{\mathbf{F}}{m\nu} \quad (3.10)$$

With equation 3.7 substitute into above equations, one can achieve the well-known drift-diffusion approximation:

$$\mathbf{u} = -\frac{k_b T}{m\nu} \frac{\nabla n}{n} + \frac{\mathbf{F}}{m\nu} = -D \frac{\nabla n}{n} + \mu \frac{\mathbf{F}}{q} \quad (3.11)$$

or in flux form:

$$\mathbf{\Gamma} = n\mathbf{u} = -D\nabla n + \mu\mathbf{E}n \quad (3.12)$$

where  $D$  and  $\mu$  is the diffusion coefficient and mobility of particles, respectively. Similarly one can write the energy flux  $\mathbf{\Gamma}_\epsilon$  for the equation 3.8 as:

$$\mathbf{\Gamma}_\epsilon = n_\epsilon \mathbf{u} = -D_\epsilon \nabla n_\epsilon + \mu_\epsilon \mathbf{E} n_\epsilon \quad (3.13)$$

As it was mentioned above, the drift-diffusion approximation is based on two assumptions: (1) inertial has much smaller influence than collisions,  $|(\mathbf{u} \cdot \nabla)\mathbf{u}| \ll \nu\mathbf{u}$  and (2) the characteristic time scale of momentum transfer is shorter than the case time scale,  $\tau = \tau_s$ . It is interesting to take electron (the fastest particle in a plasma system) in air mixture to make an estimation of the range of electric field and pressure in which these two assumptions are valid.

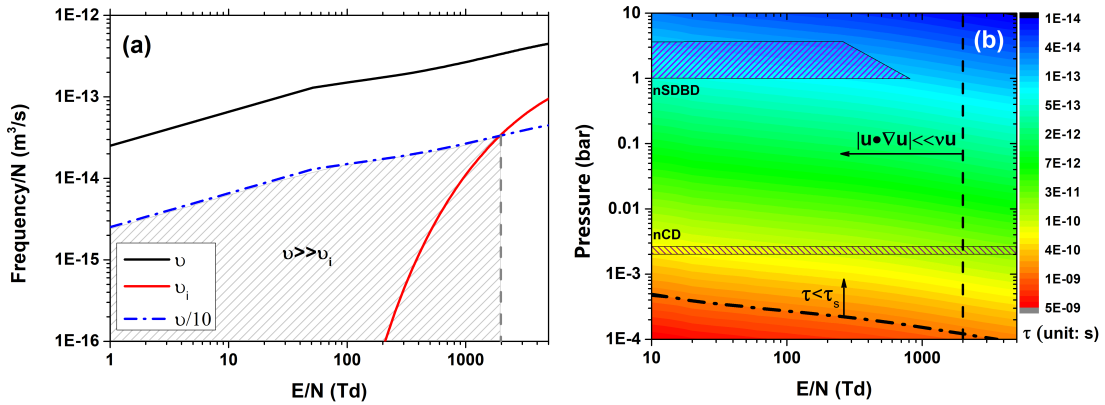


Figure 3.1: (a) Variation of effective momentum transfer frequency  $\nu$  and ionization frequency  $\nu_i$  in dry air. Region covered with gray dense lines indicate validate  $E/N$  domain for drift-diffusion approximation. (b) Characteristic time scale of effective momentum transfer in dry air at 300K in Pressure- $E/N$  plot. Shadow region denotes the region this work will study. The dash dot line and dash line indicates the estimated boundary of drift-diffusion approximation, out of which the accuracy will drop. The data for the figures are calculated using BOLSIG+ code [145].

For assumption (1),  $|(\mathbf{u} \cdot \nabla)\mathbf{u}| \ll \nu\mathbf{u}$  can be further simplified as:

$$|(\mathbf{u} \cdot \nabla)\mathbf{u}| = \alpha u^2 = \nu_i u \ll \nu u \Rightarrow \nu_i \ll \nu \quad (3.14)$$

where  $\alpha$  is the first Townsend coefficient, and  $\nu_i$  is ionization frequency. The variation of  $\nu_i$  and  $\nu$  with respect of  $E/N$  for air can be plot in Figure 3.1(a), which

shows that, the accuracy of drift-diffusion approximation will drop starting from 2000 Td, if we consider  $10 \cdot \nu_i < \nu$  as equivalent to  $\nu_i \ll \nu$ .

For assumption (2), a contour plot of  $\tau$  with respect to different pressure and  $E/N$  can be used to find the validate boundary of drift-diffusion approximation, by finding the domain where characteristic time scale of streamer propagation,  $\tau_s = 10^{(-9)}s$  is larger than  $\tau$ . In Figure 3.1(b), the given limitations based on assumption (1) and (2) are plot together as a dash dot line and a dash line. The pressure- $E/N$  domain above dash dot line and left of dash dot line is the valid region in which the accuracy of drift-diffusion approximation is ensured. According to Figure 3.1(b), this approximation is well fit for nSDBD, but for nCD in high  $E/N$  region (mainly in the ionization head), the accuracy of calculated electron flux in the head will drop, which may affect the propagation of calculated streamer in capillary tube.

The estimation of  $\nu$ ,  $\nu_i$  and  $\tau$  mentioned above are made with the help of BOL-SIG+ code based on two-terms approximation of Boltzmann equation. The two-terms approximation will be illustrated in following section.

### 3.1.4 Electron energy distribution function

The drift-diffusion approximation helps to truncate the moment of Boltzmann equation, leaving a system of PDEs consisting equations 3.5, 3.8, 3.12 and 3.13. This system can be finally closed if the transport coefficients in flux terms  $\Gamma$ ,  $\Gamma_\epsilon$  and rate coefficients in source terms  $S$  and  $S_\epsilon$  are known. However, these coefficients are rather specific for the discharge conditions. In particular, coefficients concerning electrons depend on the electron energy distribution function (EEDF), which in general is not Maxwellian but varies considerably depending on the conditions.

The EEDF and the electron swarm coefficients for the given discharge conditions can be calculated from the fundamental collision cross-section data by solving the electron Boltzmann equation [146]. A common approach to solve Boltzmann equation for EEDF and electron swarm coefficients is to expand electron distribution function in terms of Legendre polynomials of  $\cos\theta$  [145]:

$$f(v, \cos\theta, z, t) = f_0(v, z, t) + f_1(v, z, t)\cos\theta \quad (3.15)$$

where  $f_0$  is the isotropic part of  $f$  and  $f_1$  is an anisotropic perturbation. For high precision results six or more expansion terms are needed [147], but for many cases a two-term approximation already gives useful results. This two-term approximation is often used and has been extensively discussed in [148, 149].

The two-terms approximation is known to fail for high values of  $E/N$  when most collisions are inelastic and  $f$  becomes strongly anisotropic [150], but the errors in

the calculated transport coefficients and rate coefficients are acceptable for fluid discharge modelling in the usual range of discharge conditions [145].

All the codes of this work are based on two-terms approximation of Boltzmann equation, for the 0D global code, PASSKEY code and COMSOL code, BOLSIG+ is used, for nonPDPsim code an intrinsic module is called to calculate EEDF, transport coefficients and electron parameters. The specific approximations, numerical approaches for each codes, will be discussed in following sections.

## 3.2 0D actinometry model for nCD and ZDPlaskin code

Detailed analysis of plasma chemistry is the basic of any plasma diagnostics experiments or high dimensional simulations. In the present work, a zero dimensional model for optical actinometry is proposed to study the temporal evolution of  $N_2(C^3\Pi_u)$ ,  $O(3p^3p)$  and  $Ar(2p_1)$  species after the fast ionization wave in nCD. The direct aim of this 0D model, is to take a view into the kinetics in nCD, and to find a pathway into actinometry diagnosis for nanosecond pulsed discharge in case of high specific energy deposition.

### 3.2.1 Discharge geometry and high voltage pulse

A general scheme of the discharge tube of nCD is shown in Figure 3.2. The discharge is initiated inside a 70 mm long capillary quartz tube with inner and outer diameters of 1.5 and 3.4 mm. Two grounded aluminium plates enclose the capillary from above and below with a 50 mm separation. Adhesive aluminium sheets covered this construction to form a closed, grounded screen having a rectangular cross section ( $50 \times 60$  mm). The discharge tube is terminated by two metal pin-shaped high (HV) and low (LV) voltage electrodes that are connected to two cables. A 25 m long coaxial RG213 cable connects the HV electrode to a HV generator that supplies the voltage pulses (30 ns FWHM, 10 kV amplitude, and 4 ns rise time). The other cable, connected to the LV electrode, is left unterminated. Gas flows inside the capillary at a pressure of 27 mbar with a fixed flow rate, ensuring gas renewal between pulses.

### 3.2.2 Governing equations

0D model is valid assuming global uniformity for a small region. By ignoring the second term on the left hand side of equation 3.5 for each species studied in present work, we can achieve a system of ordinary differential equations (ODEs), which can be rewritten as follows:

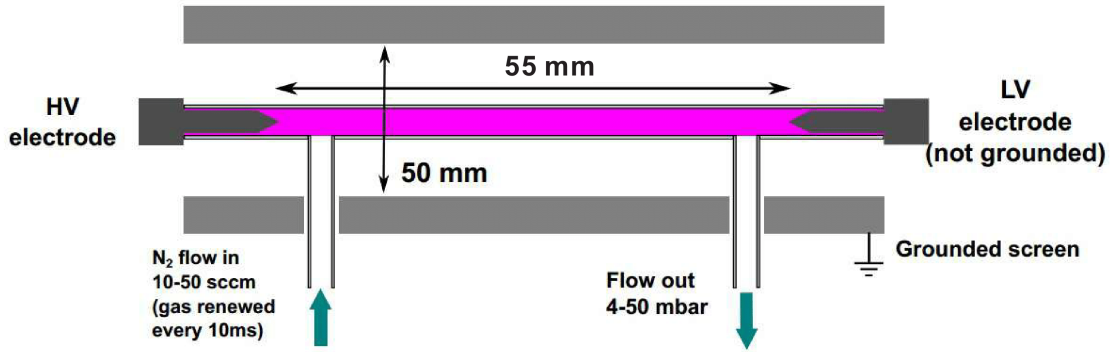


Figure 3.2: Scheme of the experimental setup of nanosecond pulsed discharges in a capillary tube.

$$\frac{d[c_i]}{dt} = F_i(c_1, \dots, c_S; k_1, \dots, k_R), c_i(t = t_0) = c_i^0 \quad (3.16)$$

here  $c_i$  is the concentration of species  $i$  and  $k_r$  are rate coefficients of the reaction  $r$ . A zero dimensional ZDPlaskin code for plasma chemistry is used for solution of the ODEs. The rates of electron impact reactions on the right hand side are calculated by BOLSIG+ library incorporated in ZDPlaskin code, the time integration is calculated by the DVODE solver [151]. The experimentally measured reduced electric field over time,  $E/N(t)$ , and the initial electron density calculated from experimental current are used as input. Detailed parameters of time steps,  $E/N(t)$ , current are presented in 4. Kinetics used are given in the Appendix.

### 3.2.3 Sensitivity analysis

The use of actinometry code starts from as "big" as possible kinetics scheme. Due to the fact that most of the reactions have minor effects for optical actionmetry on the time scale of nanoseconds, a sensitivity analysis is required to reduce the kinetics scheme and to find the key reactions.

One of the widely used methods for sensitivity analysis is Tangent Linear Method (TLM) [152]. This method is based on the fact that small changes  $\delta c_0$  in the initial conditions result in small perturbations  $\delta c(t)$  of the solution of system of equations in 3.16. Let  $\dot{c} = \delta c / \|\delta c_0\|$  be the directions of solution change, these directions propagate forward in time according to the tangent linear ODE:

$$\dot{c}' = \mathbf{F}_c(t, c) \cdot \dot{c}, t_0 \leq t \leq t_f, \dot{y}(t_0) = \dot{y}_0 \quad (3.17)$$

One can solve the sensitivity equation 3.17 for key reactions by taking the small

changes of reaction rates as  $\delta c_0$ . This method requires constructing additional source term function  $F_c$  based on the Jacobian of original  $F_i$  in equation 3.16, and will take much effort in organizing algorithms on automatic Jacobian generation, which is out of the interest in study of actinometry. Despite this fact, in the present work the concept of TLM method is kept by estimating the sensitivity of species  $i$  to reaction  $k$  by defining a sensitivity coefficient  $\varphi(t)_{i,k}$ :

$$\varphi(t)_{i,k} = \delta c_i(t, \xi r_k) / c_i(t, r_k) \quad (3.18)$$

where  $r_k$  is the reaction rate for the  $k^{th}$  reaction, and  $\delta c_i$  is the change of species concentration with rate of reaction  $k$  being  $\xi r_k$ . In the present work, the value of  $\xi$  is chosen as 1.50.

Validation of the code, the detailed kinetics, and the sensitivity analysis approach, are presented in Chapter 4 by comparison calculated current and species density with experimentally measurements.

### 3.3 2D model for nCD and nonPDPsim code

The actinometry code described in previous section was developed to analyse the experimental data in discharge and early afterglow. However although validated by measurements, this 0D code is based on the assumption of uniform discharge, the 0D results strongly depend on the accuracy of experimentally measured  $E/N$  and initial values. In other words, the actinometry code is a non-consistent kinetic model for analysis of existing experiments.

In this section, a two dimensional self-consistent capillary discharge model is built for the following interests: (1) the temporal evolution of species of interest, under different specific energy deposition; (2) spatial distribution of species densities as initial values for 0D or 1D kinetics analysis.

#### 3.3.1 Governing equations

Equation 3.5 and 3.8 can be rewritten in detail as:

$$\frac{\partial n_i}{\partial t} - \nabla \cdot \mathbf{\Gamma}_i = S_i, i = 1, 2, \dots, N_{total} \quad (3.19)$$

$$\frac{\partial n_e \varepsilon}{\partial t} = P(\varepsilon) - n_e \sum_j N_j \kappa_j - \nabla \cdot \mathbf{\Gamma}_\varepsilon \quad (3.20)$$

With drift-diffusion approximation for flux terms for charged species, neutral species and electron energy:

$$\mathbf{\Gamma}_i = D_i \nabla n_i + (q_i/|q_i|) \mu_i n_i \nabla \Phi, i = 1, 2, \dots, N_{charge} \quad (3.21)$$

$$\mathbf{\Gamma}_i = D_i \nabla n_i, i = 1, 2, \dots, N_{neutral} \quad (3.22)$$

$$\mathbf{\Gamma}_e = \frac{5}{2} \epsilon \mathbf{\Gamma}_e - \lambda \nabla T_e \quad (3.23)$$

In above equations,  $\Phi$  is electrical potential, and  $n_i$ ,  $D_i$ ,  $\mu_i$ ,  $q_i$  and  $S_i$  is the number density, diffusion coefficient, mobility, charge and source function for species  $i$ , respectively. The source function  $S_i$  includes gain and loss terms due to gas phase reactions (neutral chemistry, ion-molecule reactions and electron impact processes) and contributions associated with wall chemistry, including electron emission from surfaces.  $N_{total}$ ,  $N_{charge}$  and  $N_{neutral}$  are the number density of total species, charged species and neutral species, respectively.  $n_e$  in equation 3.20 is electron number density,  $\epsilon \equiv 3k_B T_e/2$ ,  $P(\epsilon)$ ,  $\kappa_i$ ,  $\Gamma_e$  and  $\lambda$  are the mean electron energy, power absorbed from the electric field, power lost in collision  $i$ , electron flux, and thermal conductivity, respectively. The absorbed power  $P(\epsilon)$  in equation 3.20 is computed assuming Joule heating:

$$P = \nabla \phi \cdot \sum_{i=1}^{N_{ch}} [q_i (D_i \nabla n_i + (q_i/|q_i|) \mu_i n_i \nabla \Phi)] \quad (3.24)$$

Thermal conductivity of electrons  $\lambda$  is obtained from [153]:

$$\lambda = 8n_e T_e / (\pi m_e \nu_e) \quad (3.25)$$

where  $\nu_e$  is the electron momentum transfer collision frequency.

Equation system 3.19-3.25 is closed by Poisson's equation:

$$\nabla(\epsilon \nabla \Phi) = - \sum_{i=1}^{N_{ch}} q_i n_i - \rho \quad (3.26)$$

where  $\rho$  is the charge density satisfying continuity equations for charges on surfaces and in materials:

$$\frac{\partial \rho}{\partial t} = \sum_{j=1}^n q_j [-\nabla \cdot \mathbf{\Gamma}_j + S_j] + \nabla \cdot (\sigma (-\nabla \Phi)) \quad (3.27)$$

where  $\sigma$  is the conductivity of solid materials.

The source term of photo-ionization is accounted for using a propagator method [125]. The photo-ionization source for species  $m$  at location  $\mathbf{r}_i$  due to the integral

of vacuum ultraviolet (VUV) photon emission from all other locations  $\mathbf{r}_j$  by species  $k$ :

$$S_m(\mathbf{r}_i) = \sigma_{km}^I N_m(\mathbf{r}_i) A_k \int N_k(\mathbf{r}'_j) G_k(\mathbf{r}'_j, \mathbf{r}_i) d^3 \mathbf{r}'_j \quad (3.28)$$

$$G_k(\mathbf{r}'_j, \mathbf{r}_i) = \frac{\exp(-\int_{\mathbf{r}'_j}^{\mathbf{r}'_i} \sum_l \sigma_{lk} N_l(\mathbf{r}'_n) d\mathbf{r}'_n)}{4\pi |\mathbf{r}'_i - \mathbf{r}'_j|^2} \quad (3.29)$$

where  $N_k$  is the density of the radiating species having Einstein coefficient  $A_k$ ,  $\sigma_{km}^I$  is the photo-ionization cross section for species  $m$  by photons emitted by species  $k$  and  $\sigma_{lk}$  is the total absorption cross section for photon  $k$  by species  $l$ .  $G_k(\mathbf{r}'_j, \mathbf{r}_i)$  is Green's function for the survival of the photons emitted at the location  $\mathbf{r}'_j$  to reach location  $\mathbf{r}_i$ , and also accounts for view angles and obscuration which may block the radiation. For the  $N_2 : O_2$  mixture investigated in present work, resonance radiation from  $N_2$  singlet states are the photo-ionization source in the wavelength range 98-102.5 nm. The photo-ionization cross section for  $O_2$  is adjusted and tested between  $\sigma_k = 0.1 - 1 \text{ \AA}^2$  [154], by comparing with experimental results (demonstrated in following section), the photo-ionization cross section is finally selected as  $\sigma_k = 0.6 \text{ \AA}^2$ .

In present work, only the transport of charged particles, radicals and photons are addressed, while gas heating and the hydrodynamic motion of the neutral gas resulting from temperature gradients are not taken into account due to the short time scale, the constant tube volume and the fact that few processes of interest in this stage are temperature related.

### 3.3.2 Code and numerical schemes

The code used for equations 3.21 - 3.29, nonPDPsim, is a two dimensional plasma hydrodynamics code taking into account radiation transport, developed by the group of Prof. Mark Kushner [96, 155] in Michigan University. The key features of this code for solving nCD problem, are the Scharfetter-Gummel scheme for species transport, the semi-implicit time slicing scheme for time integration and calculation based on local mean energy approximation.

#### (1) Flux discretization and Scharfetter-Gummel scheme

The flux term  $\Gamma_i$  for equation 3.19 is formulated using the Scharfetter-Gummel method [156] (SG method) on an unstructured triangular mesh. In this method, the flux  $\Gamma_{i,j+1/2}$  between density mesh points  $(i, j+1)$  separated by a distance  $\Delta x$  is given by (considering one dimension)

$$\Gamma_{i,j+1/2} = \frac{D_{i,j+1/2}}{\Delta x I_0} (n_{i,j} - e^\alpha n_{i,j+1}) \quad (3.30)$$

where  $I_0 = (e^\alpha - 1)/\alpha$ , with

$$\alpha = \frac{\mu_{i,j+1/2}\Delta x E_{j+1/2}}{D_{i,j+1/2}} \quad (3.31)$$

where  $\mu_{i,j+1/2}$  and  $D_{i,j+1/2}$  are the average mobility and diffusion coefficient of charged species  $i$  in the interval of mesh grid.

The SG method used in nonPDPsim has the advantage of calculating drift and diffusion fluxes at the same time, and keep monotonicity of the calculated flux and densities.

## (2) Time integration and time slicing scheme

First, the system of equations for charged particle transport and Poisson's equation are integrated by using an implicit Newton's method. Jacobian elements are generated for the incremental change in variable  $i$  at mesh point  $j$  due to a change in variable  $k$  at mesh point  $m$ ,  $\partial N_{ij}/\partial M_{km}$ . The mesh points for which the Jacobian elements are produced are the local point and nearest neighbours. The Jacobian element is produced by perturbing the value of the independent variable by a small amount. An example of the Jacobian element for the change in ion density  $N_{ij}$  at time  $t$  due to a perturbation of  $\Delta\Phi$  in potential  $\Phi_m$  during a time step of duration  $\Delta t$  is given in following way:

$$\frac{\partial N_{ij}}{\partial \Phi(m)}(t) = -\frac{\Delta t}{\Delta \Phi}(\nabla \cdot (\mathbf{\Gamma}_j(\Phi_m(t) + \Delta\Phi) - \mathbf{\Gamma}_j(\Phi_m(t)))) \quad (3.32)$$

The divergence operators are expressed in finite volume format,

$$\frac{\partial N_{ij}}{t} = -\nabla \cdot \mathbf{\Gamma}_{ij} = \sum_m \frac{\Gamma_{ijm} A_{jm}}{V_j} \quad (3.33)$$

where  $\Gamma_{ijm}$  is the flux from nearest neighbour cell  $m$  arriving into cell  $j$ ,  $A_{jm}$  is the area of the face between numerical cells  $j$  and  $m$ , and  $V_j$  is the volume of cell  $j$ . The discretized partial differential equation solved for equation 3.19 is,

$$\begin{aligned} N_{ij}(t + \Delta t) &= N_{ij}(t) + \Delta t \left( \sum_m \frac{\Gamma_{ijm}(N_j(t + \Delta t), \Phi(t)) A_{jm}}{V_j} \right. \\ &+ S_j(t) + \frac{\partial S_{ej}}{\partial n_e}(n_e(t + \Delta t) - n_e(t)) \\ &+ \sum_m \left( \frac{\partial N_{ij}}{\partial \Phi_m}(t) (\Phi_m(t + \Delta t) - \Phi_m(t)) \right. \\ &\left. \left. + \frac{\partial N_{ij}}{\partial N_{im}}(t) (N_{im}(t + \Delta t) - N_{im}(t)) \right) \right) \end{aligned} \quad (3.34)$$

Source functions are evaluated at time  $t$  except for those involving electron impact processes which are evaluated at time  $(t + \Delta t)$  through use of the Jacobian

element  $\partial S_{ej}/\partial n_e$ . Similar expressions are generated for potential and charge density. The values at  $(t+\Delta t)$  are obtained by solving the combined sparse matrix using a two solver-preconditioner combination based on BiCF/ILUT. After each iteration, the Jacobian elements are re-evaluated with current values of variables.

Second, following updates of charged species densities, the neutral species density are implicitly updated in a time-splicing manner, using expression:

$$N_i(t + \Delta t) = N_i(t) - \nabla \cdot (-D_i \nabla N_i(t + \Delta t)) + S_i \quad (3.35)$$

Equation 3.35 is sequentially solved for each species using the method of successive over-relaxation (SOR).

### (3) Local mean energy approximation (LMEA)

The electron transport coefficients and rate coefficients for use in solving equation 3.19-3.26 are obtained by solving Boltzmann's equation for the EEDF using the two-terms approximation. Once the electron temperature is known, the collision frequency and reaction rate coefficients are determined by interpolating from Boltzmann derived lookup table using electron temperature based on local mean energy approximation (LMEA), or electric field based on local field approximation(LFA).

LMEA is the proper method for nCD simulation for the following reason. nCD experiments were conducted under relatively low pressure (tens of Torr) and rather high energy deposition (0.1-2eV) in presence of a dielectric wall, as a consequence, between the ionization wave head and tube wall, there is a large region of high electric field and high electron gradient where the diffusion flux is larger than drift flux, and the problem of "electrons cooled by field" will arise and augmented by the field value, as is shown in Figure 3.3. The local field approximation, with its assumption that mean electron energy is only a function of  $E/N$ , will lose this physics, and lead to tremendous overestimation of electron coefficients in this case.

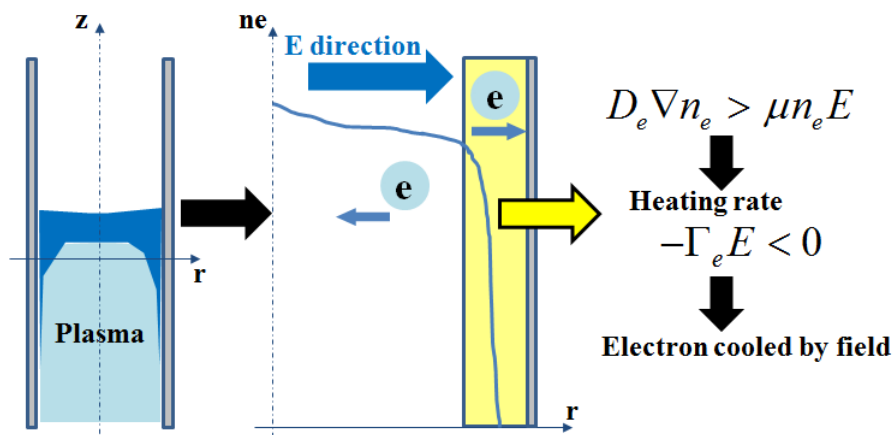


Figure 3.3: Brief illustration of the appearance of "electron cooled by field"

nonPDPsim uses the LMEA approach, and obtain electron temperature by solving the energy conservation equation 3.20 implicitly using a SOR technique, the form solved is,

$$\begin{aligned}
 T_{ej}(t + \Delta t) &= T_{ej}(t) + \frac{2\Delta t}{3k_B n_{ej}(t + \Delta t)} \\
 &\times \left[ -\frac{\partial n_{ej}(t + \Delta t)}{\partial t} k_B T_{ej}(t + \Delta t) + \Gamma_{ej} \cdot \mathbf{E}_j \right. \\
 &+ \sum_i^{max} n_{ej}(t + \Delta t) N_{ij} \Delta \varepsilon_i \\
 &\times \left( k_{ij}(T_{ej}(t)) + \frac{\partial k_{ij}(T_{ej})}{\partial T_e} (T_{ej}(t + \Delta t) - T_{ej}(t)) \right) \\
 &+ \sum_m^{max} \frac{A_{jm}}{V_j} \left( \frac{5}{2} \Gamma_{ejm}(t + \Delta t) T_{ejm}(t + \Delta t) + \lambda(t + \Delta t) \right. \\
 &\left. \left. \times (T_{em}(t + \Delta t) - T_{ej}(t + \Delta t)) \right) \right]
 \end{aligned} \tag{3.36}$$

where  $k_{ij}(T_e)$  is the rate coefficient for electron impact process  $i$  at mesh point  $j$  with change in energy  $\Delta \varepsilon_i$  and the collision partner has density  $N_i$ .  $T_{ejm}$  indicates that the upwind value of the electron temperature is used - that is, the donor-cell method is employed. During the SOR iterations (typically hundreds of iterations are required per time step), the thermal conductivities and rate coefficients are updated every 10-20 iterations. Due to the computational expense of updating the rate coefficients on a more frequent basis, a correction to the rate coefficient for changes in  $T_e$  is accounted for by the Jacobian element  $\partial k_{ij}(T_{ej})/\partial T_e$ . Convergence is determined by values of  $T_e$  only in those cells that have an electron density greater than a minimum value, typically  $10^4$ - $10^5$   $\text{cm}^{-3}$ .

### 3.3.3 Domain, boundary and initial values

According to the general schematics described in section 3.2.1 and in Figure 3.2, a simplified 2D cylindrical model is built for nCD, as is shown in Figure 3.4. The model consists of a capillary quartz with relative permittivity  $\varepsilon_r=4$ . The inner and outer diameters of the tube is 0.15 cm and 0.34 cm. The length of the tube is adjusted  $L_{real} = 8$  cm or  $L_{study} = 2$  cm, one is for direct comparison with a reference experiment, and another is for parametric study based on finer mesh, detailed kinetics and longer time scale.

Boundary conditions is assigned according to equations and materials. For transport equations, a flux in/out boundary condition is used for all the plasma-material contacting surfaces. For each species, a "disappearance" coefficient  $\alpha_i$  and "production" coefficient  $\beta_{k,i}$  are specified where  $\alpha_i$  is the probability that species  $i$  is

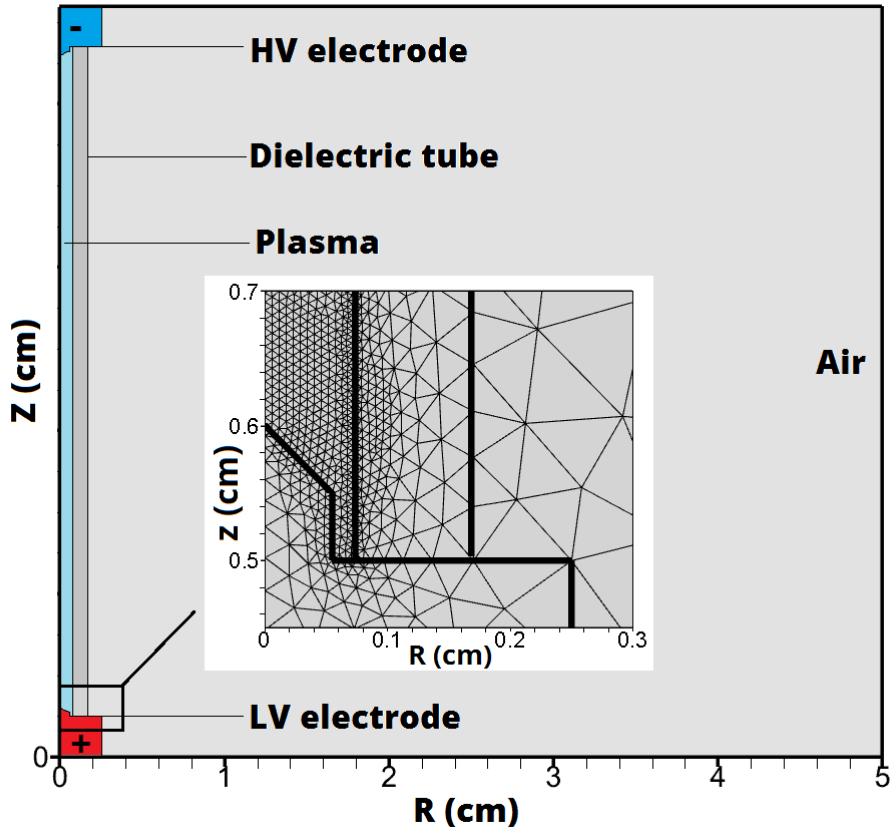


Figure 3.4: 2D cylindrical model for nCD with a zoomed region showing the distribution of mesh. Length of tube in Z axis direction ranges from  $L_{real} = 8\text{cm}$  to  $L_{study} = 2\text{cm}$ .

consumed by the surface and  $\beta_{k,i}$  is the rate of production of species  $k$  by species  $i$ . The returning flux from the surface can be written as

$$\Gamma_r = \Gamma_r^0(1 - \alpha_r) + \sum_k \Gamma_r^0 \beta_{k,r} \quad (3.37)$$

where  $\Gamma_r^0$  is the flux into the surface obtained assuming the surface density is zero and the sum is over other species. In case of nCD calculation,  $\alpha_r$  is 0, and the secondary emission coefficient  $\beta_{k,r}$  is 0.01 for all the ions.

For electron energy equation, an electron temperature of 0.05 eV is assigned to all surfaces in contact with the plasma. This adiabatic boundary condition avoids the possibility of overestimating electron density adjacent to tube wall.

For Poisson's equation, the electric potential boundary conditions are obtained from a simple circuit model. Each metal surface is connected to ground through a simple electrical circuit consisting of a resistor and power supply. The voltage

waveform of the power supply is specified in Chapter 5. Currents through each leg of the circuit are obtained by summing charged particle fluxes and displacement current obtained by time differencing the electric field at the surface. Electrically floating metal surfaces are actually represented by dielectrics having sufficiently high conductivities and permittivities that they appear to be equipotential surfaces. Surface charge is accounted for dielectric tube wall by accumulating the charge fluxes into the wall in equation 3.27.

The initial electron density was assumed to be  $n_{e0} = 10^9 \text{ cm}^{-3}$  uniformly distributed in the capillary to account for the residual electron density from prior pulses that occurs in the experiment. Initial voltage applied on the HV electrode is set as 3kV to skip the time-consuming voltage rising stage when discharge is not triggered. A corresponding plasma spot with Gaussian distribution is distributed at the tip of HV electrode ( $r=0 \text{ cm}$ ,  $z=0.6 \text{ cm}$ ) by (in unit of  $\text{cm}^{-3}$  and  $\text{cm}$  for number density and position) by

$$n_e(r, z) = 10^{13} \exp\left(- (r/0.01)^2 - ((z - 0.6)/0.01)^2\right) \quad (3.38)$$

Initial ion density is given based on quasi-neutrality. The initial electron density is distributed according to the electric field near the HV tip obtained by a one-step calculation of Poisson's equation.

### 3.3.4 Modifications and validations

The experiment of nanosecond pulsed capillary discharge is aimed at studying plasma kinetics under designed conditions. Although nonPDPsim provides an excellent two dimensional framework for nCD, additional modifications and validations for kinetics module incorporated in nonPDPsim have been done. The Boltzmann solver in nonPDPsim is used to calculate the ratio between ionization rate and electron drift velocity, these values were compared with measurements and with results produced by BOLSIG+ using the same cross sections. Two complete calculation cases are presented in this section for further validation, one in short tube for kinetics to compare with corresponding 0D model results, and another using real experimental geometry for benchmark validation.

Modification (1): update cross sections of  $\text{N}_2$  and  $\text{O}_2$  excited states based on Phelps database [157]. The species with renewed electron impact cross sections are  $\text{N}_2(v = 0 - 8)$ ,  $\text{N}_2(\text{A}^3\Sigma_u^+)$ ,  $\text{N}_2(\text{B}^3\Pi_g)$ ,  $\text{N}_2(\text{W}^3\Delta_u)$ ,  $\text{N}_2(\text{B}'^3\Sigma_u^-)$ ,  $\text{N}_2(\text{a}^1\Pi_g)$ ,  $\text{N}_2(\text{a}'^1\Sigma_u^-)$ ,  $\text{N}_2(\text{W}^1\Delta_u)$ ,  $\text{N}_2(\text{C}^3\Pi_u)$ ,  $\text{N}_2(\text{E}^3\Sigma_g^+)$ ,  $\text{N}_2(\text{sum})$  and  $\text{O}_2(4.5\text{eV})$ . Not all these species will be considered when solving transport equations and electron energy equation, but still these cross sections are necessary for getting correct solution of the two-terms approximation of Boltzmann equation for EEDF during simulation.

To check the updated cross sections mentioned above, a set of ionization coefficient,  $K_{ion}/V_{dr}$  (expressed as the ratio between ionization reaction rate constant  $K_{ion}$  and electron drift velocity  $V_{dr}$ ), are calculated under different  $E/N$  value using nonPDPsim with original cross sections and updated cross sections, respectively. The calculated results are then compared with experimental data in Figure 3.5 (a) for nitrogen and (b) for air.

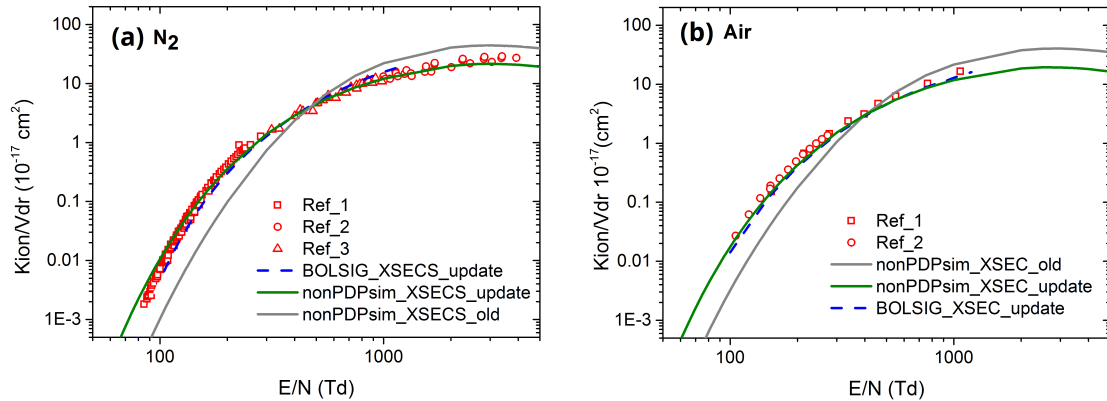


Figure 3.5: Validation of ionization coefficient of (a) pure  $N_2$  and (b) air. Grey lines are results calculated from nonPDPsim with original cross sections, olive lines are results with updated cross section data sets. Dashed lines are results from BOLSIG+ with updated cross sections. Experimental scatters are from different sources. Ref in (a) are [158–160], Ref in (b) are [161, 162]

The agreement between calculated data and experimental data with updated cross sections, shows the reliability of selected cross sections. The fact that nonPDPsim and BOLSIG+ results overlap with each other confirms the capability of nonPDPsim in evaluating EEDF based on correct cross sections.

Modification (2): add cross section for transition  $e + N_2(B^3\Pi_g) \rightarrow e + N_2(C^3\Pi_u)$ , which is one of the most important process of nCD discussed in this work. This reaction, together with the reverse reaction,  $e + N_2(C^3\Pi_u) \rightarrow e + N_2(B^3\Pi_g)$  are not available in the version of nonPDPsim used in this work, thus was added manually based on the discussion and help from the developer group of nonPDPsim. The cross section is taken from [163].

To check the added processes, a test calculation based on a short capillary tube with a length of  $L_{study}$  is conducted using nonPDPsim first. The temporal evolution of  $E/N$ ,  $N_2(C^3\Pi_u)$  and electron number density in the half length of tube on Z axis is extracted from the 2D result, as is shown in Figure 3.6 (a). Then the this temporal  $E/N$  and electron density is used in the 0D actinometry code to calculate

also  $N_2(C^3\Pi_u)$ . The profile of  $N_2(C^3\Pi_u)$  calculated by both code is shown in Figure 3.6(b). The agreement between 0D and 2D results indicate that, the study of nCD in different dimensions are consistent.

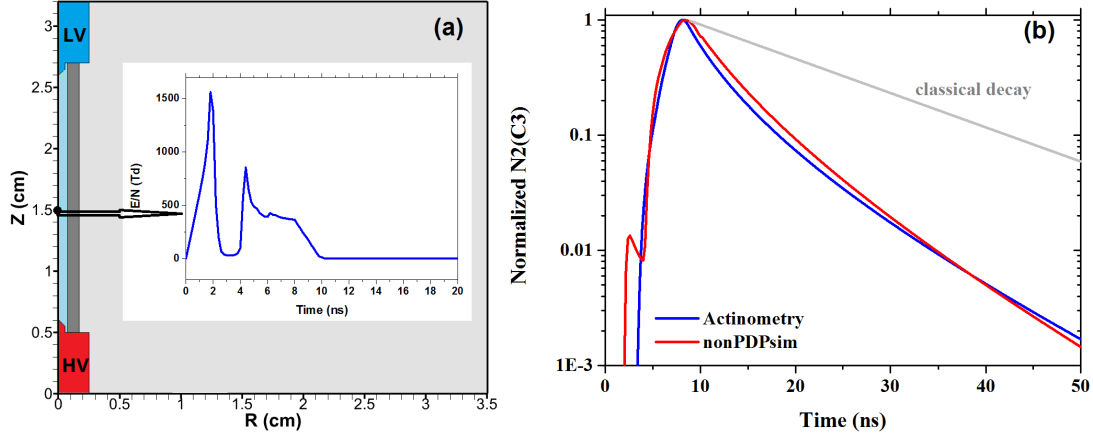


Figure 3.6: Validation of  $N_2(C^3\Pi_u)$  temporal evolution. (a) Schematic view of the observing point and probed value of  $E/N$  as the input of 0D actinometry model (b)  $N_2(C^3\Pi_u)$  temporal evolution predicted by actinometry model and by nonPDPsim in first 50 ns.

After modifications described above, an additional test case was conducted in the tube with length  $L_{exp}$ . The calculated propagation of fast ionization wave is presented by evolution of predicted axial electric potential in Figure 3.7(a) with experimental measurements in Figure 3.7(b) [39].

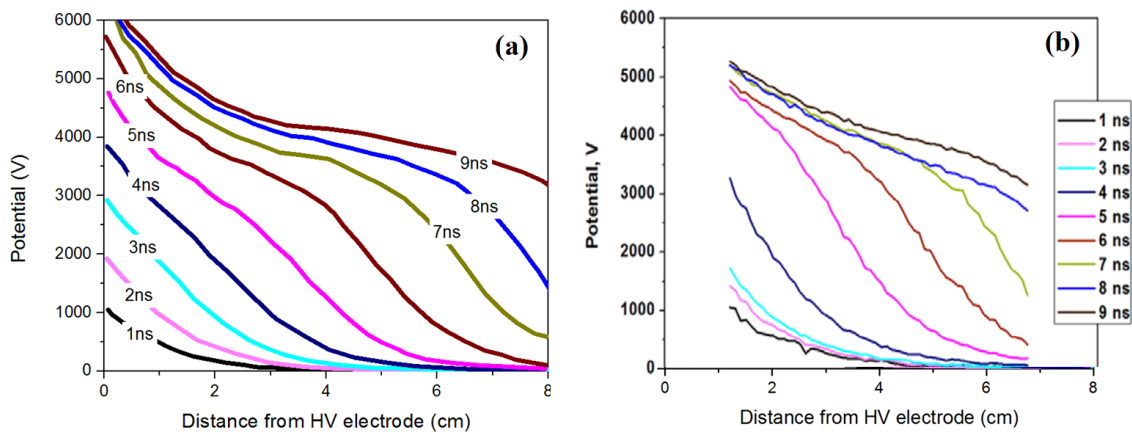


Figure 3.7: Validation of axial potential profiles of FIW during propagation stage. Results are collected from the position of the tip of capacitive probe,  $r= 1.27$  cm. (a) Model predictions (b) Benchmark results from Experimental measurements.

Figure 3.7 shows the experimental measurements and model predictions of the electric potential as a function of the axial distance  $z$  (measured from the tip of the HV electrode) at times  $t = 1-9$  ns. Values from the model are shown at the tip of the capacitive probe,  $r = 1.27$  cm to make direct comparison with experiments. Experimental curves are shown scaled to match the  $r = 1.27$  cm numerical values, in Figure 3.7(b). The FIW front speeds derived from the modelling and from the experiments, about  $1.4 \text{ mm ns}^{-1}$ , show good agreement. During the propagation of the FIW, the shapes of the potential profiles at the probe location predicted by the model are quite similar to the scaled experimental profiles. The profiles are rather smooth and lack sharp gradients.

It has to be noted here, that in nonPDPsim, the parameters for photo-ionization, the absorption cross section and length, are rather roughly estimated parameters based on specific nCD experimental results (as has been mentioned in section 3.3.1) and may vary when mixtures change. But taking into account the fact that, (i) in this work the simulation of nCD is always conducted within the same pressure, voltage profiles and mixtures conditions which have been validated in Figure 3.7, and (ii) nCD modeling focuses mainly on the evolution of species in the afterglow while discharge propagation stage provides only initial conditions for the afterglow stage, current photo-ionization parameters are reliable for cases studied in this work.

The validation of EEDF in Figure 3.5 and of Kinetics of  $\text{N}_2(\text{C}^3\Pi_u)$  in Figure 3.6, together with validation of propagation in 3.7, demonstrate the correctly resolved kinetics and transport characteristics of nCD based on nonPDPsim code, and provide a good foundation for further study of nCD in Chapter 5.

## 3.4 2D model for nSDBD and PASSKEy code

For modeling nSDBD under atmospheric pressure or even higher, there are some specific requirements to be met: (i) high mesh resolution along the entire discharge region (mesh size in  $5-10 \text{ }\mu\text{m}$  for air in 1 bar); (ii) higher order flux discretization scheme for strongly convective electron flow in high pressure streamers; (iii) accurate photoionization model based on general experimental measured photoionization functions for air; (iv) direct coupling of fluid and plasma dynamics; (iv) high performance for long time and parametric calculation based on parallelization.

To meet all mentioned requirements, a parallel code, PASSKEy (PARallel Streamer Solver with KinEtics), is developed in this work. The capability of this light weighted code in solving nSDBD problem is further discussed in section 3.4.3 and validated by both benchmarks and experiments in following sections and chapters.

### 3.4.1 General experimental schematics of nSDBD

Standard airflow configuration of the nanosecond surface dielectric barrier discharge [26] was used in the experiments. The electrode system is shown schematically in Figure 3.8 a.  $10 \text{ mm} \times W \times L$  aluminium bar,  $W$  is a width (or a span) and  $L$  is a length of ground electrode. The 0.3 mm thick PVC dielectric layer (dielectric permittivity  $\varepsilon = 3.5$ ) was glued by a silicon glue ( $\varepsilon \approx 3$ ) on the upper surface of the aluminium bar, the summary thickness of the dielectric layer was equal to 0.5 mm. For high voltage electrode, a rectangular piece of a copper foil 12 mm  $\times$   $W$  mm and 50  $\mu\text{m}$  in thickness was glued on the PVC layer, the thickness of the conductive glue did not exceed 10  $\mu\text{m}$ . The span of the electrode system,  $W$ , varied between 25 mm and 80 mm, the length was taken constant and equal  $L = 80$  mm. The experiments were carried out in atmospheric pressure air at ambient temperature without gas flow. The high-voltage pulses of positive or negative polarity (20 ns duration at FWHM, 2 ns rise time and 10 – 30 kV amplitude) shown in Figure 3.8 b were transmitted to the high voltage electrode.

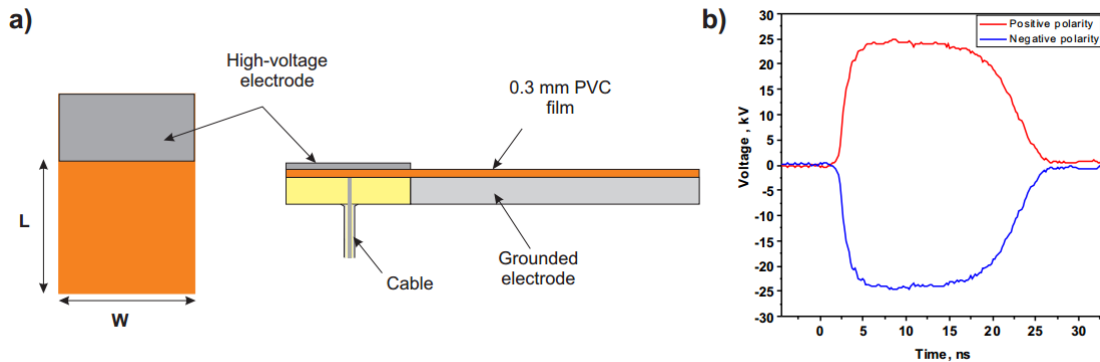


Figure 3.8: Schematic structure of nSDBD, with (a) the top and side view of nSDBD discharge setup and (b) the voltage pulsed transmitted to the electrode in both polarities.

### 3.4.2 Governing equations

PASSKEY code takes only the first moment of Boltzmann equation for charged species, and assume that neutral species do not move in time scale of nanosecond. Thus the equation system 3.19 - 3.25 can be further reduced into a series of continuity equations:

$$\frac{\partial n_i}{\partial t} - \nabla \cdot \Gamma_i = S_i + S_{ph}, i = 1, 2, \dots, N_{total} \quad (3.39)$$

$$\mathbf{\Gamma}_i = D_i \nabla n_i + (q_i/|q_i|) \mu_i n_i \nabla \Phi, i = 1, 2, \dots, N_{charge} \quad (3.40)$$

where  $\Phi$  is electrical potential, and  $n_i$ ,  $q_i$  and  $S_i$  is the number density, charge and source function for species  $i$ , respectively. The source function  $S_i$  includes gain and loss terms due to gas phase reactions,  $S_{ph}$  is the photo-ionization source term for electrons and oxygen ions.  $D_i$  and  $\mu_i$   $N_{total}$  are the diffusion coefficient and mobility of charged species. In the code,  $\nabla \cdot \mathbf{j} = 0$  for neutral species is postulated.  $N_{charge}$  and  $N_{neutral}$  are the number density of total species, charged species and neutral species, respectively. The chemical source term  $S$  is calculated with detailed kinetics. The kinetics scheme used in PASSKEY for nSDBD is shown in Chapter 6.

The photoionization model [164] describing ionization of oxygen molecules by VUV-radiation coming from electronically excited  $N_2$  in  $b^1\Pi_u$ ,  $b'^1\Sigma_u^+$ ,  $c'^1_4\Sigma_u^+$  states, is considered. The model is based on the assumption that the major contribution to the rate of photoionization comes from the radiation in the spectral range 98–102.5 nm; the radiation below 98 nm is absorbed by molecular nitrogen, and the wavelength 102.5 nm is the photoionization threshold of  $O_2$ . The photoionization source term  $S_{ph}$  is calculated by introducing three terms Helmholtz equations [165, 166]:

$$S_{ph} = \sum_j S_{ph}^j, \quad (3.41)$$

$$\nabla^2 S_{ph}^j - (\lambda_j p_{O_2})^2 S_{ph}^j = -A_j p_{O_2}^2 I, \quad (3.42)$$

$$I = \xi \frac{p_q}{p + p_q} \alpha \mu E n_e \quad (3.43)$$

where  $\alpha$  is Townsend ionization coefficient,  $\mu E$  is the absolute drift velocity of electrons,  $p$  is the ambient pressure,  $p_q$  is a quenching pressure of  $C^3\Pi_u$ ,  $p_{O_2}$  is a partial pressure of  $O_2$ .  $\lambda_j$  and  $A_j$  are fitting coefficients for photo-ionization functions obtained in experiments and taken from [165]. Quenching pressure is expressed as  $p_q = kT/\tau_0 k_q$ , where  $k$  is the Boltzmann constant,  $T$  is the gas temperature,  $\tau_0$  and  $k_q$  are the radiative lifetime of the transition and the rate constant of collisional quenching respectively.

Poisson's equation is solved without taking into account the current in the material:

$$\nabla(\epsilon \nabla \Phi) = - \sum_{i=1}^{N_{ch}} q_i n_i - \rho \quad (3.44)$$

where  $\rho$  is the charge density satisfying continuity equations for charges on surfaces:

$$\frac{\partial \rho}{\partial t} = \sum_{j=1}^n q_j [-\nabla \cdot \mathbf{\Gamma}_j + S_j] \quad (3.45)$$

Finally the system of equations is added with Euler equations:

$$\frac{\partial \mathbf{U}}{\partial t} + \frac{\partial \mathbf{F}}{\partial x} + \frac{\partial \mathbf{G}}{\partial y} = \mathbf{S} \quad (3.46)$$

$$\mathbf{U} = \begin{bmatrix} \rho \\ \rho u \\ \rho v \\ e \end{bmatrix}, \mathbf{F} = \begin{bmatrix} \rho \\ p + \rho u u \\ \rho u v \\ (e + p)u \end{bmatrix}, \mathbf{G} = \begin{bmatrix} \rho v \\ \rho u v \\ p + \rho v v \\ (e + p)v \end{bmatrix}, \mathbf{S} = \begin{bmatrix} 0 \\ 0 \\ 0 \\ S_{heat} \end{bmatrix} \quad (3.47)$$

where  $\rho$  is total density of air,  $u$  and  $v$  are the velocities in 2 dimensions, and  $e$  is the specific total energy. The reactive Euler equations are closed by the equation of state:

$$p = (\gamma - 1) \rho i \quad (3.48)$$

where  $i = e - (u^2 + v^2)/2$  is the specific internal energy.

The energy, released in fast gas heating and calculated from kinetics equations in plasma code, is used as a source term in the equation 3.47. The calculated density, pressure and temperature from Euler equations are further used for  $E/N$  calculation, Helmholtz equations and kinetics.

### 3.4.3 Code and numerical schemes

To focus on the fast and precise calculation of propagation and kinetics of nanosecond surface streamers, PASSKEy relies on an explicit time integration framework (with Poisson equation solved semi-implicitly) and hybrid parallelization. A set of numerical techniques are used for this goal, among which the following four features are the most important for the high resolution and high speed solution.

#### (1) Flux discretization and improvement of SG method

For continuity equations, the widely used SG algorithm of electron transport for gas discharges was found not accurate enough in case of high pressure gas discharges. Assuming diffusion coefficient of electrons follows Einstein relationship, the below criteria has to be followed [167]:

$$\frac{|\Delta E_k| h_k}{2T_{ek}} \ll 1 \quad (3.49)$$

where  $k$  denotes the  $k_t h$  node in the mesh grid. Equation 3.49 means, the electric potential between two adjacent nodes should be much less than the electron

temperature. This criteria can be very restrictive especially for gas discharges under relatively high pressures, and the computational cost becomes very expensive. Therefore, to apply this scheme to gas discharges with reasonable computational times, Boeuf and Pitchford have developed an implicit variant of this scheme [92,93].

Later in Ref [167] the ISG (Improved Scharfetter-Gummel) method was proposed, which actually calculates electron flux from a pair of virtual nodes in adjacent cells rather than from average values in cell centre values assuming constant electric field between virtual nodes. The two virtual nodes were placed symmetrically around the cell boundaries. The distance between the nodes, was selected to follow criteria 3.49. For the interpolation of the densities at the virtual nodes, Ref [167] has proposed a local cubic spline piecewise interpolation as the best choice.

The ISG scheme has been successfully applied to many 2D volumetric streamer simulations [168–172]. However, when it comes to modelling of nSDBD, numerical test cases based on this scheme presents significant numerical instabilities, resulting in strong oscillations of densities in region where streamer is approaching the surface. On the contrary, results based on the classical SG scheme, although incorrect and diffusive, presents quite smooth and monotonic quality. In other words, the ISG scheme proposed in [167], although improved the accuracy of original SG scheme, lost the basic advantages of monotonicity, which is rather important in modelling streamers that have interactions with walls.

The lost of monotonicity in ISG scheme is caused by the local cubic spline piecewise interpolation for values on virtual nodes. The local cubic spline piecewise interpolation cannot avoid the typical oscillations which often lead to overshoots and completely unrealistic interpolation results, especially in non-uniform grids, as is shown in Figure 3.9. Other optional choices, such as Bessel’s method or Akima’s method, either cause overshoots too, or sacrifice the smoothness of the interpolated values. In the conditions of sharply changing slopes in the given data (which is the case in the region of plasma-surface interaction), all the aforementioned interpolation schemes will fail.

Two solutions may be available for this interpolation problem. One is to reduce the interpolation order to have an upwind scheme in region of sharp gradient [174], and another is to find a proper interpolation scheme that overcomes the serious oscillations. This work used the second way, by introducing a simple method for monotonic interpolation in one dimension proposed by M. Steffen [173], which guarantees the monotonic behaviour for every situation. For each nodes, five adjacent nodes in one dimension are used to calculate the interpolated value, resulting a high order resolution in most of the computational domain. The improved ISG method, will be named NOISG (Non Oscillatory Improved Scharfetter-Gummel) scheme in following sections in this work.

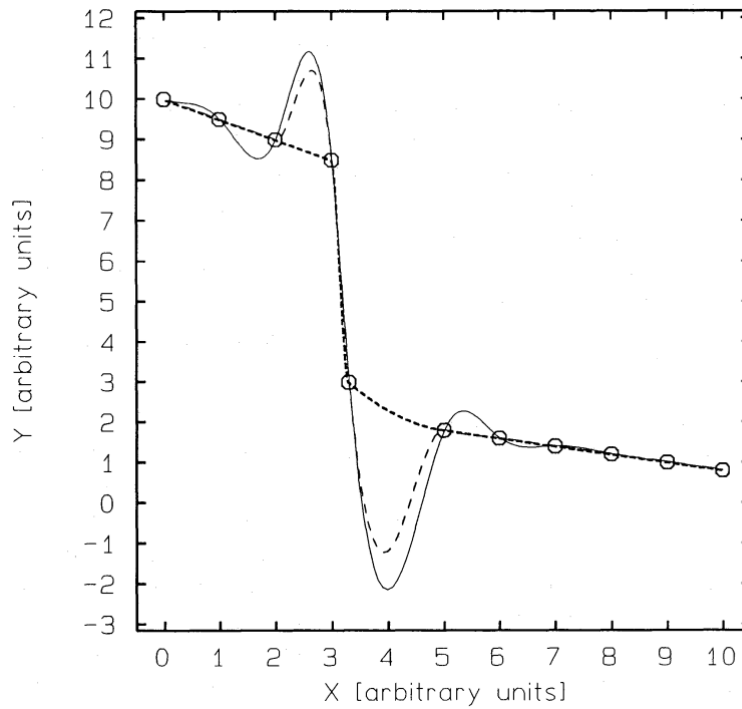


Figure 3.9: Comparison of different interpolation methods discussed in the text for the example data points indicated by circles Full-drawn: splines, long-dashed: Bessel's method, short-dashed: Akima's method. The figure is taken from [173].

For Euler equations, the well developed Z/B flux vector splitting scheme [175] is used to capture strong spatial discontinuities of solutions during simulation. It has to be noted that, the scheme proposed in [175] is given in finite difference description, some reconstruction methods can be involved to reconstruct conservative variables in the cell centre to cell interfaces, thus to improve the accuracy of the solution based on finite volume method. In this work, a simple MUSCL (Monotonic Upwind Scheme for Conservation Laws) reconstruction has been applied to conservative variables in order to build at each cell interface the left and right reconstructed values [176]. In this code the Van-Leer slope limiter [177] is chosen to keep TVD (Total Variation Diminishing). The Euler code is validated by a 1D Sod's shock tube problem in upcoming sections.

## (2) Time integration and operator splitting scheme

For the transport equations, a 1<sup>st</sup> order splitting method is used for time integration [178]:

$$V^{t+\Delta t} = \Gamma^{\Delta t} D^{\Delta t} R^{\Delta t} V^t \quad (3.50)$$

where  $V^{t+\Delta t}$  and  $V^t$  are the solution of equation 3.39 at  $t$  and  $t + \Delta t$ , respectively.

$\Gamma^{\Delta t}$  and  $R^{\Delta t}$  stands for the flux and chemistry operator respectively applied on the duration  $\Delta t$ . Different schemes are used for each operator.

For the flux  $\Gamma$ , the NOISG scheme coupled with the Strang operator for spatial splitting is used. the original 1D NOISG scheme is adapted to 2D by splitting the numerical treatment into two one-dimensional problems in the x and y directions, respectively. To improve the accuracy of the splitting method, an alternation of the order between the X and Y axes is used in two successive time steps. for chemistry, the stabilized Runge–Kutta–Chebyshev scheme [179] is used.

For the Euler equations, a dimensional splitting in X and Y directions is carried out. An alternation of the order between the X and Y axes is used in two successive time steps together with the update of flux  $\Gamma$ . This dimensional splitting method, together with a small time step (within discharge time scale) ensures the accuracy of solution of Euler equations.

All grids were integrated simultaneously with the same time step. The timestep in PASSKEy is limited strictly due to the explicit scheme. Limitations based on different characteristic time scales are introduced [180]: the drift dynamics time step  $\Delta t_c = \min \left[ \frac{\Delta x_i}{v_{x(i,j)}}, \frac{\Delta y_j}{v_{y(i,j)}} \right]$ , the diffusion dynamics time step  $\Delta t_d = \min \left[ \frac{(\Delta x_i)^2}{D_{x(i,j)}}, \frac{(\Delta y_j)^2}{D_{y(i,j)}} \right]$ , the kinetics time step  $\Delta t_I = \min \left[ \frac{n_{k(i,j)}}{S_{(i,j)}} \right]$  and the dielectric relaxation time step,  $\Delta t_{Diel} = \min \left[ \frac{\epsilon_0}{q_e \mu_{e(i,j)} n_{e(i,j)}} \right]$ . The limit from dielectric relaxation time step is removed due to the use of a semi-implicit scheme for Poisson's equation [100, 178]. Thus, the general time step  $\Delta t$  was defined as:

$$\Delta t = \min (\xi_c \Delta t_c, \xi_d \Delta t_d, \xi_I \Delta t_I) \quad (3.51)$$

where  $\xi_c = 0.1$ ,  $\xi_d = 0.1$  and  $\xi_I = 0.02$ .

### (3) Local field approximation

To reduce the calculation cost, PASSKEy does not solve mean electron energy, thus LMEA discussed in 3.3.2 is not suitable for this code. Instead, local field approximation (LFA) is assumed in the study of nSDBD in this work. This approximation implies that local equilibrium of electrons is achieved instantaneously in time in response to the electric field. All the transport coefficients and source terms are explicit functions of the norm of the local reduced electric field  $E/N$ . This is the case when the time scales of variations of the electric field and electron density are long compared to the time scale of energy relaxation. It has to be noted that, LFA is not always valid for surface streamers due to its nonlocal effect in high field regions. The lose of accuracy of LFA in streamer modelling appears in two regions, the ionization head and streamer bottom above dielectric surface.

In the ionization head, LFA may lead to underestimation of ionizations. The effects of nonlocality on positive streamers in air at atmospheric pressure were studied

by Naidis in [106], who corrected the electron source term rates calculated with the local field approximation following the work in [181]. Deviations from the LFA were studied for negative streamers in nitrogen at atmospheric pressure [182] by means of a comparison between 1D fluid and particle models. By taking into account the non-local effects, all of these authors found an increase of the ionization in the streamer head, a resulting increase of the electric field and a small increase of the streamer velocity. The discrepancies given by LFA discussed above are far smaller than an order of magnitude. For example, [182] found a relative difference between the fluid and the particle models of 10% to 20% in the ionization level behind the streamer front for homogeneous applied electric fields of 50 kV/cm and 100 kV/cm, respectively. For practical accuracy, one can obtain the main streamer characteristics by a fluid model [106]. Furthermore, recently in [113] a PIC code was used to solve the Boltzmann equation and a Monte Carlo simulation to simulate collisions, in the framework of streamer simulations in the Earth's atmosphere as applicable to sprite discharges. These authors found an excellent agreement with results obtained by a fluid model in [183] both for positive and negative streamers.

In the near-wall region where plasma bottom side is close to the dielectric surface, LFA may lead to overestimation of ionizations. As has mentioned in the work of Soloviev [108], the electrons may move against the E-field force due to the strong diffusion associated with the high concentration gradient and enter into the region of a strong E-field. In this region, the predicted ionization source is very high and the electron-ion density grows dramatically. The real ionization source cannot be so high, because the electrons lose their energy moving against the E-field force and cannot ionize gas molecules so effectively, as has been mentioned in section 3.3.2. Ref [108] used a corrected ionization electron source to overcome this problem. The modelling aim of PASSKEy in this work, is to conduct a comparative study with experiments about the characteristics of surface streamer but not the very fine region between streamer body and dielectric. To have a quantitative view, one can make a simple estimation based on the effect of "electron cooled by field". Assuming there is a sheath region where electron density  $n_e$  will drop from  $n_{emax}$  to 0 in length  $L_{sheath}$ , and the diffusion flux is larger than convection within this region:

$$D_e \nabla n_e > \mu n_e E \quad (3.52)$$

let  $n_{eavg}$  be the average electron density within the sheath, assuming Einstein relationship  $D_e = \mu T_e$ , then above equation can be simplified as:

$$\mu T_{es} \frac{n_{emax}}{L_{sheath}} > \mu E_s n_{eavg}, \rightarrow L_{sheath} < \frac{T_{es}}{E_s} \frac{n_{emax}}{n_{eavg}} \quad (3.53)$$

where  $T_{es}$  and  $E_s$  are the electron temperature and electric field in the sheath region.

If one consider  $n_{emax} = 2n_{eavg}$ , then the length of  $L_{sheath} < 2T_{es}/E_s$  can be considered as the limit length, below which the behaviour of plasma can not be resolved by LFA. One can make an estimation of the criteria length  $L_{sheath}$  with BOLSIG+ and plot it together with that of nCD to have a comparative view.

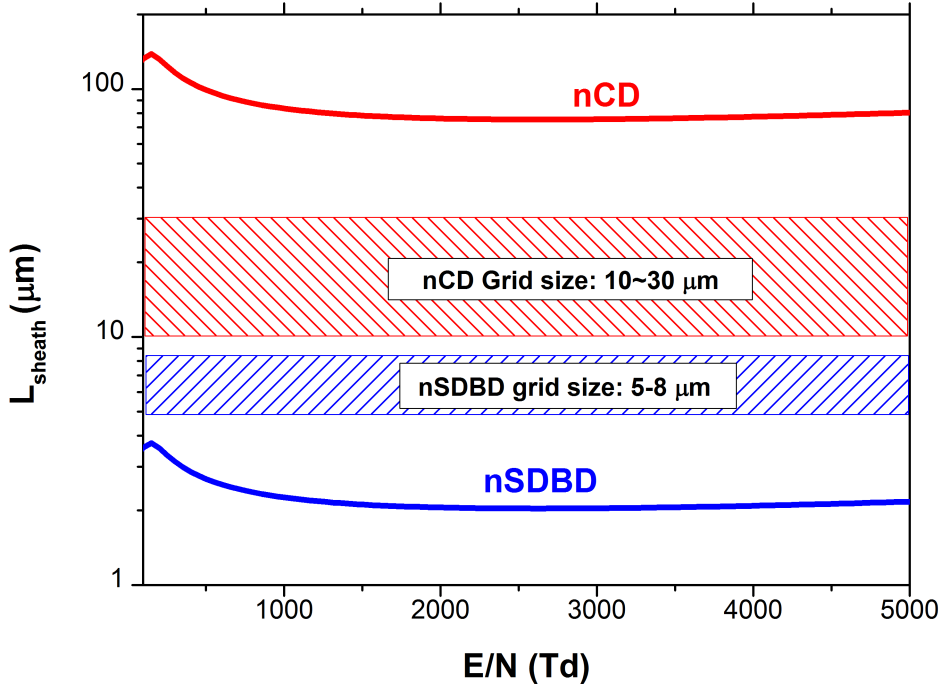


Figure 3.10: The characteristic length of region with the possibility of "electron cooled by field" in nCD and nSDBD modelling. If the mesh grid size is smaller than the line of  $L_{sheath}$ , LMEA is the best choice for a fluid model of plasma.

As has been shown in Figure 3.10, the criteria length of nCD and nSDBD are quite different due to the difference in operating pressure. The grid size used in nCD simulation by nonPDPsim, 10-30  $\mu\text{m}$ , is smaller than the criteria length, meaning that LFA is not applicable for nCD in this work. In contrast, the grid size chosen for nSDBD is larger than the criteria length, indicating that the plasma-dielectric sheath region is rather small in nSDBD in atmospheric pressure (or higher), in this work this extremely small region will not be focused and resolved, and LFA could satisfy the demand of modelling nSDBD with high performance.

#### (4) Parallelization

Despite the removal of dielectric relaxation time limit, the time step during calculation is still very small due to the high reaction rates, and computation cost grows significantly with the increase of kinetics dimension.

To accelerate the calculation, an OpenMP–MPI hybrid approach was developed in this work. OpenMP parallelization is operated on 16 CPU cores to make time integration of transport equations. LU factorization and iterations of Poisson and Helmholtz equations are with the help of intel MKL PARDISO solver. MPI parallelization is operated on different nodes according to the dimension of kinetics scheme. The suggested hybrid approach combines the advantages of both OpenMP method and MPI techniques, and avoids the drawback of intense and time consuming message exchange between different nodes in pure MPI codes.

The calculation time depends mainly on the scale of mesh and kinetics. For  $10^6$  cells and 42 kinetics reactions, the calculation of a 2 cm surface streamer propagated under the voltage pulse about 24 kV in amplitude takes 8 – 20 hours on a single HPC node (Intel Xeon E5, 2.40 GHz, 16 cores).

#### (5) Coupling between plasma and fluid equations

The aim of coupling between plasma and fluid in PASSKEy is to have a feedback from fluid to plasma and vice-verse, thus the same time step and mesh size as in plasma are used, Euler equations and plasma equations are calculated together in every time step, and coupled through the exchange of gas density, pressure, temperature and fast gas heating power source, as is shown in Figure 3.11.

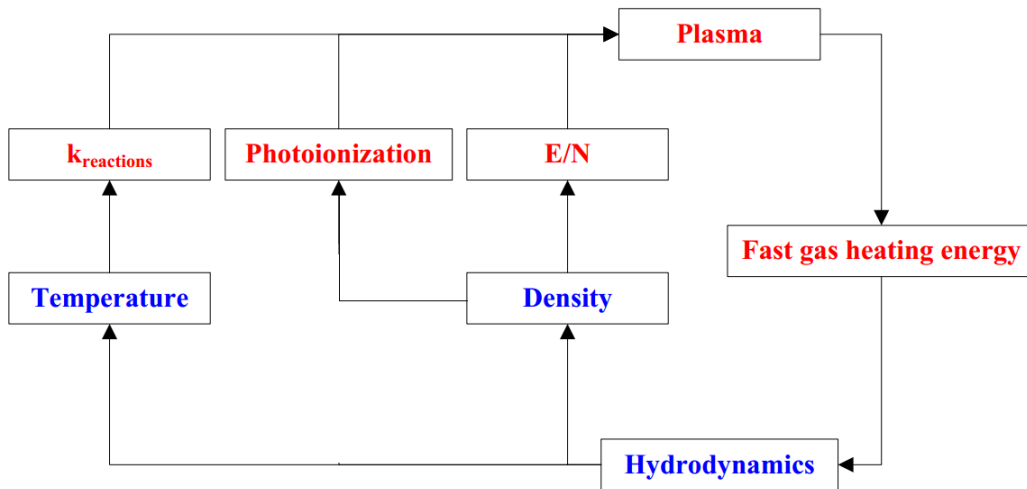


Figure 3.11: The schematic view of coupling loop between plasma and fluid equations.

In each time step, the energy released in fast gas heating is calculated together with the kinetics equations, and used as a source term for energy conservation equation 3.47 in next time step. Updated temperature are used for temperature-dependent reactions, while updated density is used to calculate  $E/N$ , and photoionization parameters in Helmholtz equations 3.42-3.43. When plasma and fluid

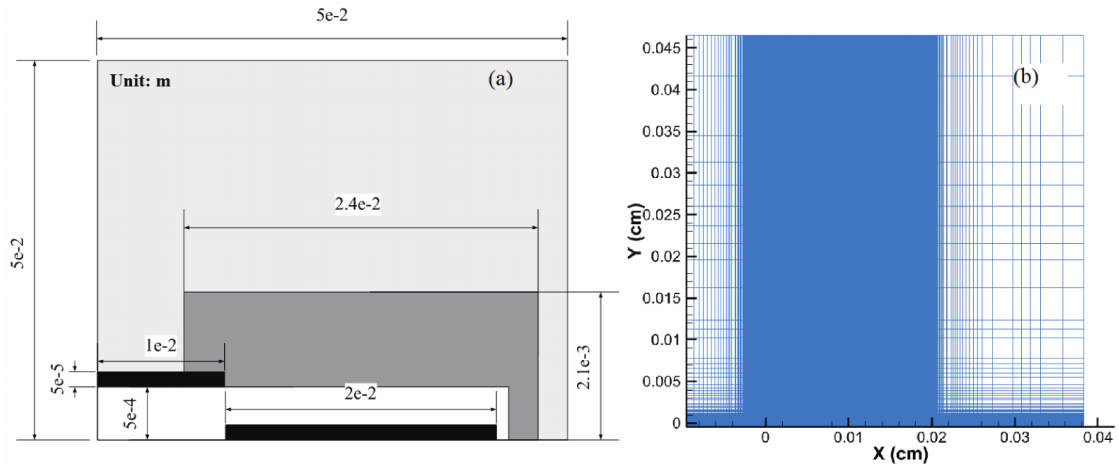


Figure 3.12: Computational domain and mesh distribution, units are meters: (a) computational domain for different equations. Transport equations: dark grey domain; Poisson’s equation and Helmholtz equation: entire domain; Euler equations: light and dark grey domain; (b) structured cartesian mesh, uniform square mesh with size of  $5 - 8 \mu\text{m}$  in dark grey domain exponentially growing in the rest of computational domain.

are calculated together, fluid velocity was not coupled into plasma equations 3.39, for the reasons (i) to reduce the non-linearity of problem (ii) the velocity of fluid in nanoseconds time scale have nothing to do with discharge features. Once the discharge stops, PASSKEy turns into a pure reaction-diffusion problem solver, the electric field is assumed to be a constant with a small value (1 Td), Poisson’s equation and drift flux of charged species are no longer solved.

The way of fluid-plasma coupling in this work takes into account the changes in reduced electric field and photo-ionization processes, which are key features in studying the characteristics of formation and propagation of nanosecond pulsed discharges.

### 3.4.4 Domain, boundary and initial values

A total computational domain of  $5 \text{ cm} \times 5 \text{ cm}$  is shown in Figure 3.12 (a). To reduce computational cost, the transport equations, Poisson’s equation, Helmholtz equations, Euler equations were solved in different sub-domains. A fine and uniform square mesh was distributed in streamer propagation region while in the rest of the computational domain the mesh size grows exponentially, as can be seen in Figure 3.12 (b).

For Poisson’s equation, classical Dirichlet boundary conditions were used for

Table 3.1: Boundary conditions for transport equations of species

| Boundary condition | flow towards boundary                    | flow away from boundary               |
|--------------------|--|---------------------------------------|
| electrons          | $\partial \mathbf{j}_e / \partial n = 0$ | $\mathbf{j}_e = -\gamma \mathbf{j}_i$ |
| ions               | $\partial \mathbf{j}_i / \partial n = 0$ | $\mathbf{j}_i = 0$                    |

the metal surfaces,  $\phi = U(t)$ . Newmann boundary conditions were written for the non-metal boundaries,  $\partial \phi / \partial n = 0$ . Surface charge is accumulated on the dielectric surface during each time step by collecting the charge flux flowing towards the dielectric on the boundary of plasma region. The accumulated charge is then stored in the edge of finite volume mesh cell, and was taken into account as additional charge when solving Poisson equation. For the Helmholtz equations,  $S_{ph} = 0$  was set on the boundary of the domain (far from plasma region).

For transport equations, boundary conditions are summarized in Table 3.1. It has to be noted that we assume secondary emission coefficient on both metal and dielectric,  $\gamma = 0$ , as calculations carried out have shown that the results do not visibly depend on  $\gamma$  ranging from 0.01 to 0.1.

For Euler equations, classical non-slip wall boundary conditions were given to the entire calculation domain, the flux is given as:

$$\mathbf{Z}_w = \begin{bmatrix} 0 & p & p & 0 \end{bmatrix} \quad (3.54)$$

To ignite the discharge, an initial cloud of seed plasma was chosen according to the electric field at starting time moment. In this calculation, the voltage (the 24 kV waveform shown in Figure 3.8(b) starts from 1.5 kV instead of 0 kV to pass the non important and time consuming voltage increasing and non discharge period. With this initial voltage, we calculated the electric field giving the range of region where ionization starts ( $E > 32$  kV/cm), and then distribute seed plasma in this region by following formula 3.55 (in unit:  $cm^{-3}$  and  $cm$ ):

$$n_e(x, y) = n_i(x, y) = 10^{12} \exp(-(x/0.002)^2 - (y/0.002)^2) \quad (3.55)$$

Several numerical tests have validated that the ranging of this Gaussian peak value from  $10^9$  to  $10^{13}$   $cm^{-3}$  does not affect the propagation of surface streamer after 0.1 ns.

### 3.4.5 Benchmark verifications

A few benchmark cases of atmospheric pressure discharges were selected, namely a case of a volumetric streamer propagation in the point-to-plane geometry with minimized discharge kinetics containing ionization and attachment [90], streamer

development taking into account detailed chemical kinetics [85], development of a nanosecond discharges at high overvoltage [184], and surface dielectric barrier discharge [57, 110, 137]. For all selected cases, the main results are correctly reproduced by the developed code. Two examples, for volumetric [90] and for surface [57, 137] streamer, are presented below.

(1) Streamer in point-to-plane geometry

Paper [90] is a classical study of a streamer propagation. The calculations [90] were done for the hyperboloid anode placed 1 cm over a plane cathode in atmospheric pressure air. Constant voltage of 13 kV was applied to the anode. The rate of collisional ionization was calculated in the approximation of local electric field,  $S_i = \mu E \alpha n_e$ , where  $\alpha$  is the first Townsend ionization coefficient. Two-body dissociative attachment and three-body attachment of electrons to oxygen molecules were taken into account. Electron mobility, the diffusion coefficient, Townsend coefficient, the reactions between charged particles were taken the same as in [90] with the aim to reproduce the calculations. Similar to [90], a small plasma spot was placed at the anode tip to initiate streamer formation.

Figure 3.13 compares the results of the calculation of the present work with the reference results taken from [90]. Calculated in the present work axial profiles of the electron density and isolines of the electric field are shown in Figures 3.13 b and 3.13 d respectively. Different computational approaches to photoionization have been used in [90] and in the present work. Both codes use classical photoionization model developed by Zheleznyak *et al* [164]. In [90], the photoionization was calculated by integration over the region containing the emission sources; the region was a restricted volume related to the streamer head. The present work uses a three-exponential Helmholtz model summarized in [165] specifically for photoionization in air. Despite the described difference, the results calculated by the PASSKEY code provide a good agreement with [90], see Figures 3.13 a and 3.13 c. The streamer is initiated in high Laplacian field close to the anode and expands along the axis of the discharge and in the radial direction until it reaches approximately a radius of 1 mm. After this, the streamer propagates along the axis of the discharge gap with almost constant radius of the channel and practically constant velocity.

(2) Surface streamer

Additional validation of the PASSKEY code was based on the calculations of the nanosecond surface discharge at atmospheric pressure. Numerous simulations of the surface streamers with rather different numerical approaches and configurations are known [57, 98, 110, 137, 185, 186]. For the moment, there is no “classical” benchmark for a case of atmospheric pressure surface streamer. In this work, papers [57, 137] were selected for comparison.

Using the same geometry and voltage waveform, the 2D map of the absolute

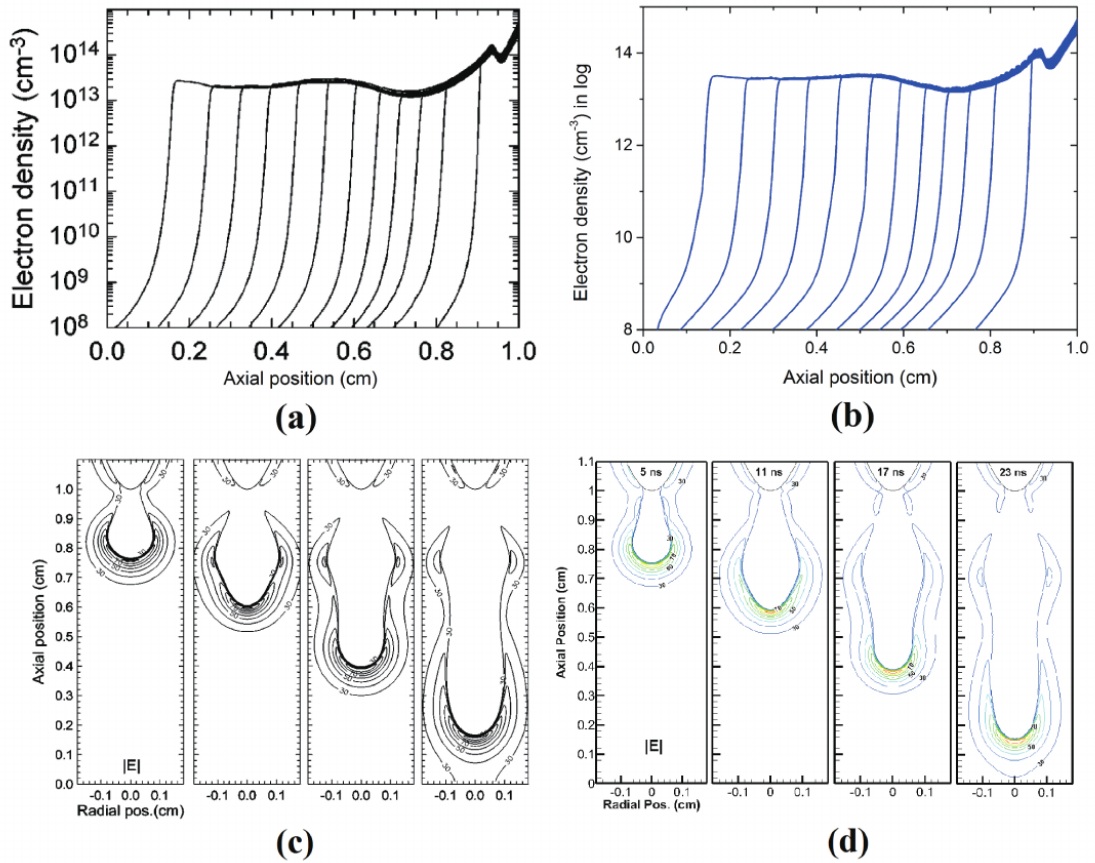


Figure 3.13: Validation of PASSKEY code developed in the present work on the benchmark describing volumetric streamer. (a,b): axial profiles of the electron density [90]. Time moments are 1–23 ns, step is 2 ns, the streamer propagates towards  $z = 0$ : (a) results of [90]; (b) PASSKEY code; (c,d): contour lines of absolute values of the electric field, in logarithmic scale, time moments are 5, 11, 17, and 23 ns. The contours are 30,40, ... kV/cm: (c) results of [90]; (d) PASSKEY code.

values of the electric field and the dependence of the electrical current upon the time were calculated. They are shown in Figure 3.14, together with results taken from the papers [57, 137]. The surface streamer starts from the edge of the high-voltage electrode, near the triple point (a point of junction of the metal, dielectric and air), and propagates along the dielectric surface. With the enhanced electric field at the ionization head, the propagation velocity of the surface streamer is much higher than the volumetric streamer.

There are two principal differences in the model developed in [57, 137] and in the present work. The detailed description of the approach [57, 137] can be found in earlier papers [135]. The photoionization in [57, 137] uses model [164] and is calculated as the integral over the region of interest. Kinetics model used in [57, 137] is

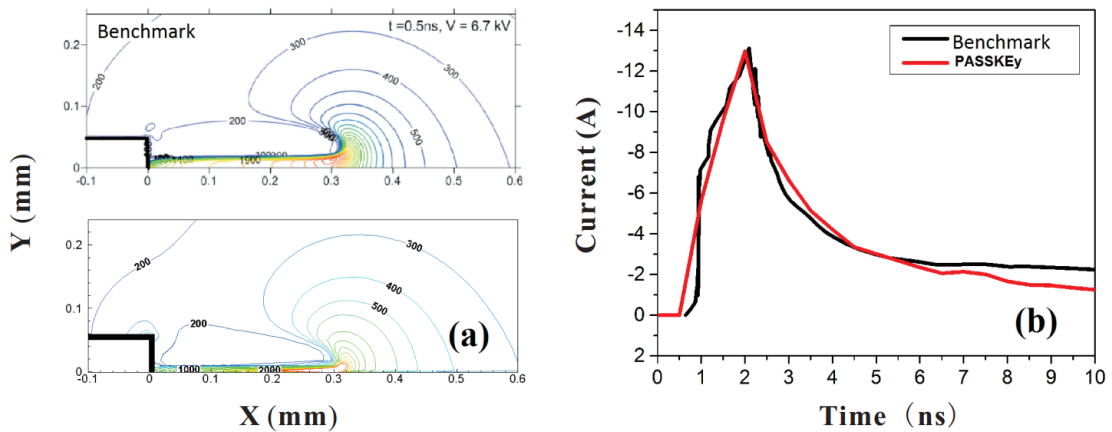


Figure 3.14: Validation of PASSKEy code developed in the present work on the benchmark describing surface streamer: (a) contour lines of electric field at first 0.5 ns, unit: Td [57]; (b) electrical current through the high-voltage electrode [137].

restricted by reactions of ionization for  $O_2$  and  $N_2$ , recombination, dissociative recombination and detachment. PASSKEy code uses the three-exponential Helmholtz model for photo-ionization [165]. kinetics model contains 38 reactions including the main set of reactions [57, 137] but also considering the reactions responsible for a fast energy release (fast gas heating) in reactions with charged and excited species.

It has to be noted that, another difference between these two models, is the treatment of flux boundary condition of the dielectric. The boundary condition used in PASSKEy has been given in Table 3.1, which is quite classical and widely used for plasma-dielectric interface in many groups [98, 110, 187, 188]. The boundary condition of the benchmark case is more sophisticated and specialized: an additional boundary flux term concerning thermal flux for electrons based on phenomenological estimations of elementary kinetics was introduced. As a result, when electric field is negative in Y direction over dielectric, the electron flux flowing away from the dielectric surface will be reduced and the charge separation will be weaker, leading to a slightly thicker region between streamer body and dielectric.

In spite of described differences between the PASSKEy code and the model presented in [57, 137], the results give a very good agreement for the streamer morphology and dynamics. The values of the electric field are similar at similar positions, and the electrical current through the high-voltage electrode is identical, indicating that the flux of species and the electric field near the boundaries are calculated correctly.

### (3) Sods' shock tube

PASSKEy uses a dimensional splitting in X and Y directions to solve 2D Euler

equations. Thus the validity of solution of Euler equations incorporated in PASSKEY can be checked in Cartesian coordinate by a 1D Sod's shock tube benchmark. The Sod shock-tube problem [189] is a particular 1D Riemann problem. The stiffness of this problem due to its strong discontinuity is very useful to test the stability and the accuracy of a compressible fluid-dynamics code [190].

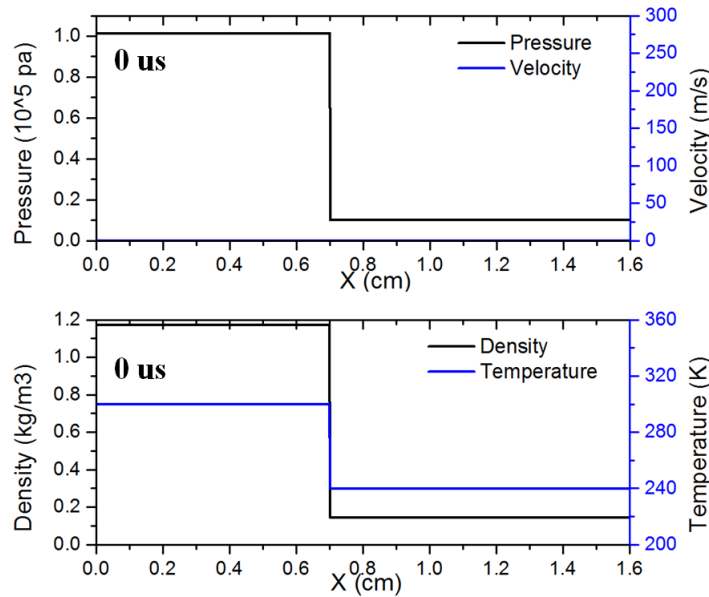


Figure 3.15: The initialization of a Sod's problem.

As for any Riemann problem, the space in the axial direction ( $X$  axis) is split into two different regions with different physical quantities separated by a discontinuity in  $x = 0$ . The Sod conditions are characterized by a high pressure, high density gas on the left region  $x < 0$  and a right region ( $x > 0$ ) with a 10 times smaller pressure and a 8 times smaller density, as is shown in Figure 3.15. The time evolution of this problem can be described by solving the Euler equations, which leads to three characteristics, describing the propagation speed of the various regions of the system, the rarefaction wave, the contact discontinuity and the shock discontinuity. If this is solved numerically, one can test against the analytical solution, and get information how well a code captures and resolves shocks and contact discontinuities and reproduce the correct density profile of the rarefaction wave.

Figure 3.16 gives the calculated results from PASSKEY together with analytical solutions. The shock wave in the tube is modelled almost exactly, the contact discontinuity of pressure, velocity, density, the rarefaction wave and the shock discontinuity copy the analytical solutions.

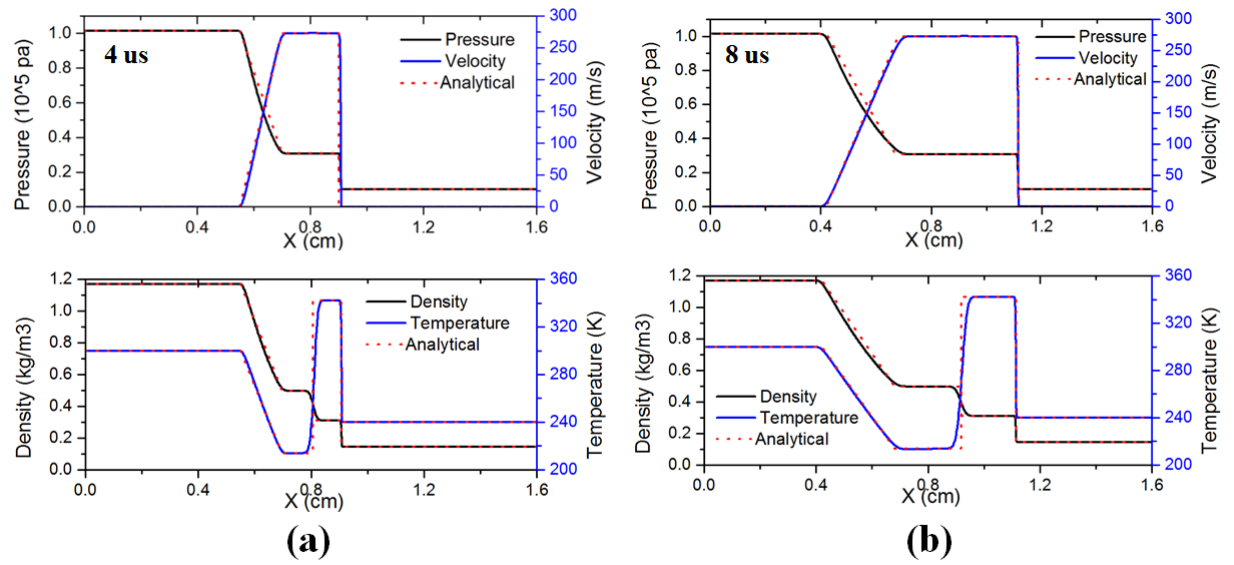


Figure 3.16: Solution of Sod's shock tube problem, calculated value and analytical solutions at (a)  $t = 4\mu\text{s}$  and (b)  $t = 8\mu\text{s}$ .

## 3.5 A modified COMSOL model for validation and comparison

In addition to the well developed academic code mentioned above, an improved FEM (Finite Element Method) model based on commercial code COMSOL Multiphysics is used for third party validations and comparison with some intermediate results. The feature of this model, is a fully implicit finite element scheme combined with the techniques of adaptive mesh and artificial stabilization.

### 3.5.1 COMSOL and modelling of NPD: capabilities and drawbacks

COMSOL has some unique advantages in simulation of plasma discharges. (i) the user-friendly interface gives a quick access to some initial results; (ii) the finite element mesh makes it possible to fit any complex geometries; (iii) the built-in plasma module assured an almost correct numerical implementation and reduced the efforts devote to programming; (iv) the capabilities of adaptive mesh refinement gives a possibility to overcome mesh number limitations; (v) the built-in post-processing toolkits are powerful in analysis; (vi) COMSOL it provides some universal PDEs (partial differential equations) interface and make the solution for PDEs flexible and

convenient.

Despite the significant advantages, COMSOL has many severe drawbacks that prevent it from being the most suitable tool in simulation of nanosecond pulsed discharges which usually appear as streamers under atmospheric pressure: (i) COMSOL incorporates a standard Galerkin method in the plasma module, which cannot capture the strong discontinuities in the convection dominating streamer head, making calculated results much more diffusive than real; (ii) the "black box" like plasma module makes it impossible to make some least adjustments in boundary conditions, and makes it hard to debug and find source of problems; (iii) the fully implicit integration scheme make calculation sensitive to any singular points in the calculated domain, making converge rather hard; (iv) the fact that FEM is based on energy conservation rather than mass conversation, make negative concentration a common phenomenon when calculating plasma kinetics; (v) the way of solving matrix by direct method, plus the weak parallelization function, results in too slow calculation speed and huge memory cost.

### 3.5.2 Weak formulations and artificial stabilization

Among the aforementioned drawbacks of COMSOL, (iii) and (iv) become dominant when plasma region is adjacent to metals or dielectrics, but for volumetric streamers these drawbacks will not destroy the results. Drawback (v) cannot be overcome from user's side. As for the items (i) and (ii), they can be solved by introducing weak formulations in PDE module with artificial stabilization techniques. This section will illustrate the construction of weak form PDEs for plasma equations in COMSOL, and the use of Streamline Upwind Petrov Galerkin method (SUPG).

Being further simplified, the equations solved in COMSOL are only Poisson's equation 3.44 for electric field, Helmholtz equations 3.41 for photo-ionization source term and continuity equations 3.39 for species. Poisson's equation and Helmholtz equation are solved simply by the validated internal modules as black boxes. For continuity equations, a manually constructed weak form PDE is used to have more flexibilities in giving boundary conditions and in introducing additional numerical techniques to improve the accuracy.

The movement of ions and neutral species are neglected, only electrons are considered as moving species. The continuity equation for electrons can be rewritten from equation 3.39:

$$\frac{\partial n_e}{\partial t} - \nabla(D_e \nabla n_e + \mu_e n_e \nabla \Phi) = S_i + S_{ph} \quad (3.56)$$

or

$$0 = \nabla(D_e \nabla n_e + \mu_e n_e \nabla \Phi) - \frac{\partial n_e}{\partial t} + S_i + S_{ph} \quad (3.57)$$

Multiplying above equation by the so called "test function"  $u(x, y, z)$ , and making volumetric integration over one cell, one can obtain

$$\begin{aligned} & \iiint_V (\nabla \cdot (D_e \nabla n_e)) u dV + \iiint_V (\nabla \cdot (n_e \mu_e \nabla \Phi)) u dV \\ & - \iiint_V \left( \frac{\partial n_e}{\partial t} \right) u dV + \iiint_V (S_i + S_{ph}) u dV = 0 \end{aligned} \quad (3.58)$$

Integrate the first two terms of equation 3.58 by part and simplify the equation:

$$\begin{aligned} & \oint_S (D_e \nabla n_e u) \cdot \mathbf{n} dS - \iiint_V D_e \nabla n_e \cdot \nabla u dV \\ & + \iiint_V (\nabla n_e \mu_e \cdot (\nabla \Phi)) u dV + \iiint_V (n_e \nabla \mu_e \cdot \nabla \Phi) u dV \\ & + \oint_S (n_e \mu_e \nabla \Phi u) \cdot \mathbf{n} dS \\ & - \iiint_V (\nabla n_e \mu_e \cdot (\nabla \Phi)) u dV - \iiint_V (n_e \nabla \mu_e \cdot \nabla \Phi) u dV - \iiint_V (n_e \mu_e \nabla \Phi \cdot \nabla u) dV \\ & + \iiint_V \left( -\frac{\partial n_e}{\partial t} + S_i + S_{ph} \right) u dV = 0 \end{aligned} \quad (3.59)$$

The final weak form equation that can be directly typed into COMSOL is

$$\begin{aligned} & - \iiint_V D_e \nabla n_e \cdot \nabla u dV - \iiint_V (n_e \mu_e \nabla \Phi \cdot \nabla u) dV + \iiint_V \left( -\frac{\partial n_e}{\partial t} + S_i + S_{ph} \right) u dV \\ & + \oint_S (D_e \nabla n_e u) \cdot \mathbf{n} dS + \oint_S (n_e \mu_e \nabla \Phi u) \cdot \mathbf{n} dS = 0 \end{aligned} \quad (3.60)$$

where the first line is the weak form PDE in the calculation domain, and second line plays the role of a natural boundary condition. In a more clear way,

$$\begin{aligned} & \iiint_V \left( (-D_e \nabla n_e - n_e \mu_e \nabla \Phi) \cdot \nabla u + \left( -\frac{\partial n_e}{\partial t} + S_i + S_{ph} \right) u \right) dV \\ & + \oint_S (D_e \nabla n_e + n_e \mu_e \nabla \Phi) u \cdot \mathbf{n} dS = 0 \end{aligned} \quad (3.61)$$

Equation 3.56 describes a typical drift-diffusion problem. If the problem is dominated by diffusion, the conventional standard Galerkin method used in COMSOL for discretizing the equation is stable. In case of convection dominated case, equation 3.56 behaves as the equation of hyperbolic type, and the conventional numerical

scheme becomes unstable, exhibiting either oscillating results in a coarse mesh or diffusive results in a fine mesh. An example of this unstable phenomena is shown in Figure 3.17 when repeating the famous pin-to-plane streamer benchmark case [90] using COMSOL based on conventional numerical scheme.

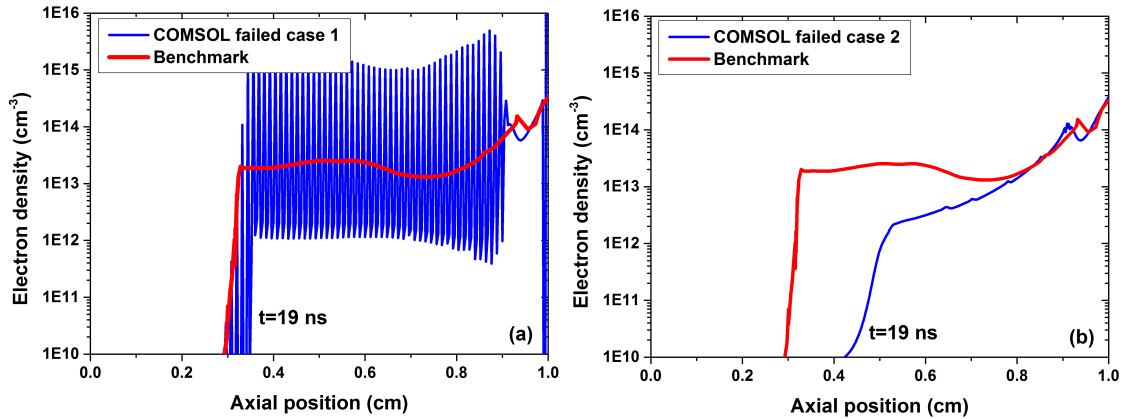


Figure 3.17: Failed cases when repeating the benchmark proposed by [90] using COMSOL with conventional methods. Two types of numerical instability appears: (a) oscillations in a coarse mesh and (b) diffusion in a refined mesh.

In Figure 3.17(a), calculated streamer repeats the streamer propagation velocity with the cost of non-physical oscillations along the streamer channel, making results non-reasonable to analyse. In the case shown in Figure 3.17(b), the mesh size is 5 times refined (tens of  $\mu m$ , which is the minimum mesh size one can achieve in COMSOL to have a acceptable calculation time and reasonable memory cost), however a diffusive streamer appears. These two example of failures clearly show that it is impossible to simulate atmospheric streamer discharge using conventional numerical scheme.

The reason for this numerical instability can also be explained by equation 3.49 discussed in section 3.4.3. For modelling high pressure streamers, the strict restriction in mesh size is impossible to met in COMSOL. Like in PASSKEY the NOISG scheme is used to overcome the numerical instability, in COMSOL one can introduce some artificial stabilization methods [191–195]. One of the widely used ways is to selectively introduce diffusion along the streamline direction, which is known as Streamline Upwind Petrov Galerkin method (SUPG) [191, 192]. This method can be applied in COMSOL by introducing artificially an additional stabilization term for each element, thus the stabilization term can be written as:

$$\sum_{e=1}^{n_{el}} \int_{\Omega^{el}} P(u_h) \tau^e R(n_{eh}) d\Omega \quad (3.62)$$

with following definitions in each cell:

$$P(u_h) = \mu_e \frac{\partial \Phi}{\partial x} \frac{\partial u}{\partial x} + \mu_e \frac{\partial \Phi}{\partial y} \frac{\partial u}{\partial y} \quad (3.63)$$

$$\tau^e = \frac{1}{2} \left( \alpha_x \frac{h}{\mu_e E} + \alpha_y \frac{h}{\mu_e E} \right) \quad (3.64)$$

$$R(n_{eh}) = \frac{\partial \Gamma_{ex}}{\partial x} + \frac{\partial \Gamma_{ey}}{\partial y} + \frac{\partial n_{eh}}{\partial t} - S_i - S_{ph} \quad (3.65)$$

where  $e$  is the index number of an element,  $n_{el}$  is the total number of finite elements,  $n_{eh}$  is the electron density in an element with size  $h$ ,  $u_h$  is the corresponding test function.  $\Gamma_{ex}$  and  $\Gamma_{ey}$  are the value of electron flux  $\Gamma = (-D_e \nabla n_e - n_e \mu_e \nabla \Phi)$  in X and Y directions.  $\alpha_x$  and  $\alpha_y$  are parameters relating to Peclet number  $Pe$  in two dimensions:

$$\alpha_x = \coth(Pe_x) - \left( \frac{1}{Pe_x} \right), Pe_x = \frac{1}{2} \frac{\mu_e \frac{\partial \Phi}{\partial x} h}{D_e} \quad (3.66)$$

$$\alpha_y = \coth(Pe_y) - \left( \frac{1}{Pe_y} \right), Pe_y = \frac{1}{2} \frac{\mu_e \frac{\partial \Phi}{\partial y} h}{D_e} \quad (3.67)$$

With equation 3.62 added in COMSOL as a weak contribution to the original weak form PDE for electrons, one can achieve a stabilized solution. Detailed validations of the improved COMSOL streamer model will be given in the next section.

### 3.5.3 Verification and Validation

As like in nonPDPsim and in PASSKEY, validation of COMSOL streamer code is done by validations with both classical simulations [85,90] and experimental results [184].

#### (1) Verification with a benchmark

To be consistent with the validation processes of PASSKEY code, the benchmark case of a positive streamer [90] described in previous section is also used here as a first test of COMSOL results. The coloured figures in Figure 3.18 (b) and (d) are calculated axial electric field and spatial distribution of electron density corresponding to benchmark shown in (a) and (c). Results from improved COMSOL streamer model no longer produce any strong oscillations, and the propagation of the streamer is accurately reproduced, with only a slightly different streamer thickness between two cases. One of the reasons of this difference, is the different implementation of photo-ionization, as has been described in previous sections.

#### (2) Validation with an experiment

A further validation of the improved COMSOL streamer code, is a direct comparison with a high voltage pin-to-plane discharge experiment [184]. Paper [184]

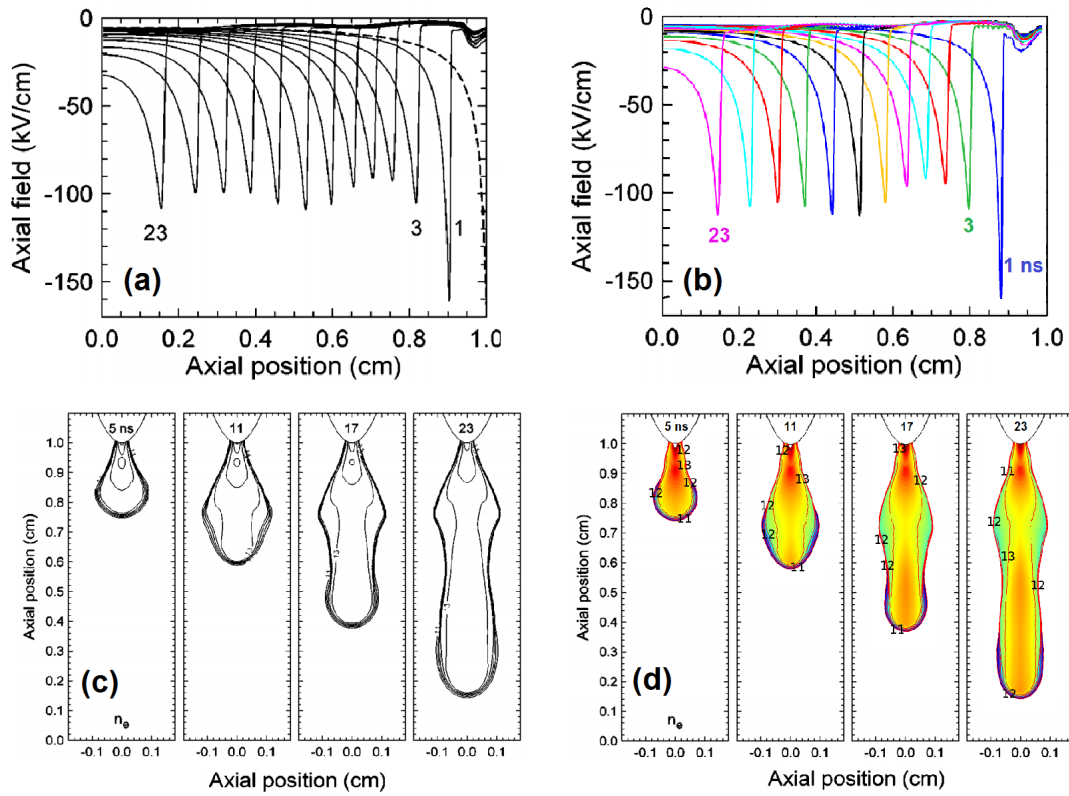


Figure 3.18: Validation of COMSOL case developed in the present work on the benchmark describing volumetric streamer. (a,b): axial profiles of the electric field [90]. Time moments are 1–23 ns, step is 2 ns, the streamer propagates towards  $z = 0$ : (a) results of [90]; (b) COMSOL; (c,d): contour lines of electron density, in logarithmic scale, time moments are 5, 11, 17, and 23 ns. The contours are  $10^{11}, 10^{11.5} \dots 10^{13} \text{ cm}^{-3}$ : (c) results of [90]; (d) COMSOL.

investigated optical properties of a pin-to-plane corona discharge induced in atmospheric pressure air under nanosecond scale high overvoltage in space and time by gated and intensified imaging. A diffuse pattern discharge like a multielectron avalanche propagating was observed both in experiment (Figure 3.19(a)) and in simulation [196], if the voltage rise time is much shorter than the characteristic time of the field screening effects, and the local field is higher than the critical ionization field in air.

Under the same experimental conditions, the aforementioned diffuse pattern discharge is reproduced using the improved COMSOL streamer code. The main optical radiation source in the experiment, the density of  $\text{N}_2(\text{C}^3\Pi_u)$  is calculated in COMSOL. To compare directly with the measurement, an Abel transformation was conducted to take into account the thickness of discharge region. Then the trans-

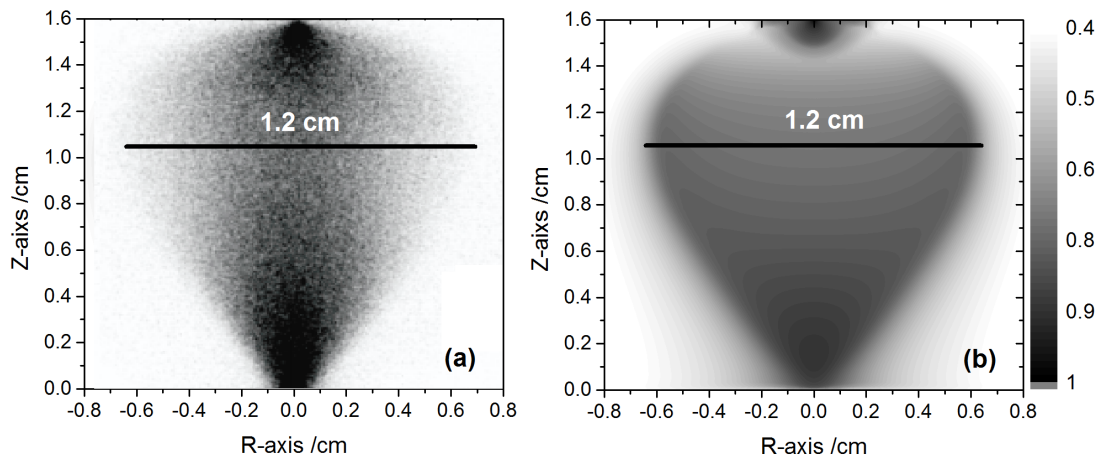


Figure 3.19: Validation of the improved COMSOL streamer code. (a) Experimental images of diffuse pattern discharge [184] (b) COMSOL results of Abel transformed  $N_2(C^3\Pi_u)$  emission.

formed data was normalized to  $[0,1]$  as is shown in Figure 3.19(b). Both experiment and calculation show intensified region in vicinity of anode and ground, with the maximum diameter of the streamer being 1.2 cm.

The validity of the results of COMSOL streamer code is confirmed by both calculations and experiments. This COMSOL code, due to its easiness in implementation and convenience in post-processing, will be used for third party validations and supportive calculations.

## 3.6 Conclusion

In this chapter, the common mathematical basis of all the numerical models used in this work have been presented. The Boltzmann equation is reduced based on the fluid approximation, and then closed by the drift-diffusion approximation and two-terms approximation. Despite the common mathematical description, according to the unique features and demands of the specific problems in this work, four codes have been used, modified, developed or improved for investigation.

A global model for actinometry in nCD have been presented. The aim of the model is to study and simplify the detailed kinetics of specific species in nanosecond pulsed capillary discharge in the afterglow. The model is based on the 0D ZDPlaskin code, and is supplied with a sensitivity analysis module and kinetics under the specific conditions of nCD. This model has been validated directly with a set of experimental measurements and will be described in chapter 4.

A 2D model for nCD have been built. The purpose of this model, is to have a self-consistent model with simplified kinetics under different experimental conditions, to study the dynamics of discharge propagation and afterglow decay, and to give initial conditions for detailed kinetics calculation. The model is built based on the 2D code nonPDPsim, with its built-in cross sections updated and accuracy of kinetics improved. The peculiarity of nonPDPsim code for nCD problem are (i) the use of local mean energy approximation to resolve the region between streamer body and capillary tube under low pressure conditions; (ii) the use of unstructured mesh to adapt to the complex geometry of capillary tube set up. The drawback of this code in modelling nCD is that, the limitations of mesh grids number due to its semi-implicit algorithm make it hard to expand the calculations into larger geometries and finer mesh. This model has been validated by comparing with the solution of BOLSIG+ code, with the results of the global actinometry model and with experimental measured potentials. Calculations of the features of nCD based on nonPDPsim will be presented in Chapter 5.

A 2D model for nSDBD has been developed. The objective of this model is to investigate the electric and fluid properties of nSDBD together with experiments with high flexibility and speed. The model is built based on a 2D in house code PASSKEy. The highlights of PASSKEy are (i) the use of the NOISG scheme to avoid the errors given by classical SG methods under atmospheric pressure; (ii) the parallelization code structure that gives higher performances and quicker results. The drawback of this code is that the local field approximation may fail under some certain conditions. This model has been successfully validated by numerical results from three independent groups. Further discussion of the results produced by PASSKEy code and corresponding direct comparisons with experimental measure-

ments, will be described in Chapter 6.

A 2D COMSOL model for volumetric streamers have been built. The purpose of this model is for third party validations and supportive calculations. This model distinguish from the standard built-in plasma module in COMSOL by utilization of an artificial stabilization method. Another unique feature of the improved COMSOL streamer model is the function of adaptive mesh refinement, which gives a possibility for COMSOL to solve larger scale problems. This model has been validated by a classical streamer model result, and by a recently conducted experiment.

---

---

# Chapter 4

---

## Study of nCD: kinetics and optical actinometry

Optical actinometry was a classical technique to measure the absolute densities of atoms. It is usually based on the assumption that the density of the electronically excited atoms under study is small comparing to the density of the ground state atoms and will decay only by quenching with neutral species [47]. The aim of this chapter, is to check if “classical” O-atoms actinometry is valid under conditions typical for short pulsed discharges with high specific deposited energy.

Kinetics modelling together with experimental values of time-resolved electrical current, longitudinal electric field, optical emission of O( $3p^3P$ ) at  $\lambda_O = 844.6$  nm, Ar( $2p_1$ )  $\lambda_{Ar} = 749$  nm and their ratio, and emission of N<sub>2</sub>( $C^3\Pi_u$ ) at  $\lambda_{N_2} = 337.1$  nm in the nanosecond capillary discharge are used to analyse the main processes responsible for O( $3p^3P$ ) and Ar( $2p_1$ ) formation in the discharge and in early afterglow.

### 4.1 Experimental measurements: techniques and results

The general scheme of the discharge tube have been shown in Figure 3.2. The experimental setup are presented in Figures 4.1.

The high-voltage electrode is connected to the central wire of the high-voltage cable. The capillary is surrounded by a rectangular metal (Al) screen 48 mm×60 mm in cross section, the screen is connected to the cable shield. The low-voltage

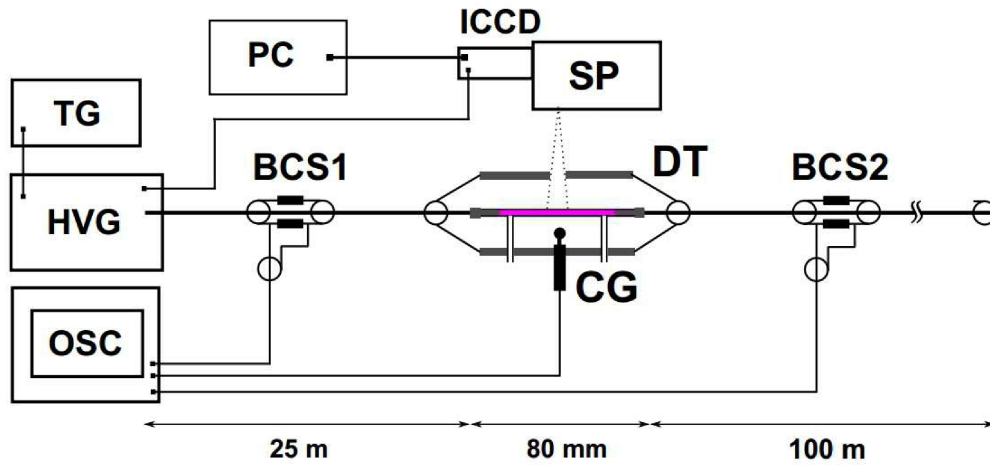


Figure 4.1: A general scheme of the experimental setup. DT is a discharge tube, HVG is a high-voltage generator, TG is a triggering generator, BCS1 and BCS2 are the back current shunts, CG is a capacitive gauge, Osc is an oscilloscope, SR is a spectrometer, ICCD is the ICCD camera, PC is a personal computer.

electrode is connected to the central wire of another coaxial RG213 cable, 100 or 200 m long (the cable can be changed) with the end load  $R = 0$  Ohm. The shield of the cable is connected to the screen. In this way, the discharge tube can be considered as a break in the cable.

Two back current shunts, BCS1 and BCS2, mounted in the high-voltage cable shield about 12.5 m apart from the high- or low-voltage electrode respectively, were used to measure the current flowing through the cable: BCS1 measured the incident pulse from the high-voltage generator and the pulse reflected from the discharge tube, while BCS2 measured the pulse transmitted through the plasma further in the long coaxial high-voltage cable. Energy deposited to the discharge tube in each pulse was calculated from the signals obtained by the back current shunts as a difference between the energies stored in the incident pulse, and the sum of the energies of charging of the capacitance of the discharge cell and the energies of the reflected and transmitted pulses:

$$W_{BCS} = \frac{1}{Z} \int_{t_0}^{t_{pulse}} (U_{refl.vac.}^2(t) - U_{refl.}^2(t) - U_{trans.}^2(t)) dt, \quad (4.1)$$

where  $t_0$  and  $t_{pulse}$  are the beginning and the end of the pulse respectively,  $U_{refl.vac.}(t)$  is a voltage waveform for the reflected pulse in vacuum without discharge,  $U_{refl.}(t)$  for the reflected pulse with discharge, and  $U_{trans.}(t)$  for the transmitted pulse.  $Z = 50$  Ohm is a wave impedance of the high-voltage cable.

The distribution of the electrical potential along the discharge gap was measured

by the capacitive gauge (CG) moving along the capillary tube in the slit in the screen. These data were further used to obtain the distribution of the longitudinal component of the electric field in time and space [40]. It should be noted that the CG technique provides only the lower limit of the electric field in the discharge front, where the field is mainly radial. Behind the front, in the region of the main energy release, the accuracy of the measurement of the electric field stays within 5 – 10 %.

A gas flow of 94.7% of synthetic air (admixtures <3.5 ppm) and 5.3% of Ar (admixtures <1 ppm) was keeping constant by two BROOKS flow controllers 5850TR series and the Edwards nXDS6i Scroll pump. Thus a regular gas exchange between the successive discharge pulses was provided each 10 ms; the frequency of the discharge pulses did not exceed 3 Hz to be sure that each new train of the discharge pulses is not influenced by the previous one. Gas pressure in the middle of the capillary was constant and equal to 28.5 mbar. It was measured by two identical pressure detectors (PFEIFFER Vacuum CMR362 range 110 mbar) installed at the equal distance from the side tubes before and after the capillary to take into account a high hydrodynamic resistance of the capillary.

Time-resolved optical emission was collected by the Thorlabs lens from the center of the discharge in the direction perpendicular to the tube axis. The spectra were taken by ACTON SP-2500i spectrograph using Pi-Max4 Princeton Instruments ICCD camera with the gate of 2 ns each 2 ns during the pulse and in afterglow. Three wavelengths were selected as the central wavelengths of the spectra:  $\lambda_{\text{O}} = 844.6$  nm for the O-atom emission ( $\text{O}(3\text{p}^3\text{P}_{1,2,0}) \rightarrow \text{O}(3\text{s}^3\text{S}_1)$  optical transition),  $\lambda_{\text{Ar}} = 749$  nm for the Ar-atom emission ( $\text{Ar}(2\text{p}_1) \rightarrow \text{Ar}(1\text{s}_2)$  optical transition) and  $\lambda_{\text{N}_2} = 337.1$  nm for the second positive system of molecular nitrogen ( $\text{C}^3\Pi_u, v'=0 \rightarrow \text{B}^3\Pi_g, v''=0$  optical transition). The integral of the emission of the appropriate atomic line or molecular band over the wavelength at each time instant was considered as an optical signal value.

The main experimental results are presented in Figure 4.2. The experiments were carried out at  $I_{max} = 120$  A maximal value of the transmitted current. The behaviour of the longitudinal electric field in the center of the gap (see Figure 4.2 a) is typical for the nanosecond discharges in the form of the fast ionization wave (FIW) [197, 198]: a sharp narrow peak with typical  $E/N$  a few kTd and duration of 0 – 2 ns corresponding to the front of the ionization wave is followed by a broad region where the electric field is still high,  $E/N \approx 100 - 300$  Td. This is an interval corresponding to maximum energy deposition (compare to Figure 4.2 b); it corresponds to the closed discharge gap and to the increasing current. The specific deposited energy is as high as 1 eV/particle (being calculated for the initial composition of the gas mixture).

The optical emission of O-atoms ( $\lambda_{\text{O}} = 844.6$  nm), Ar ( $\lambda_{\text{Ar}} = 749$  nm) and

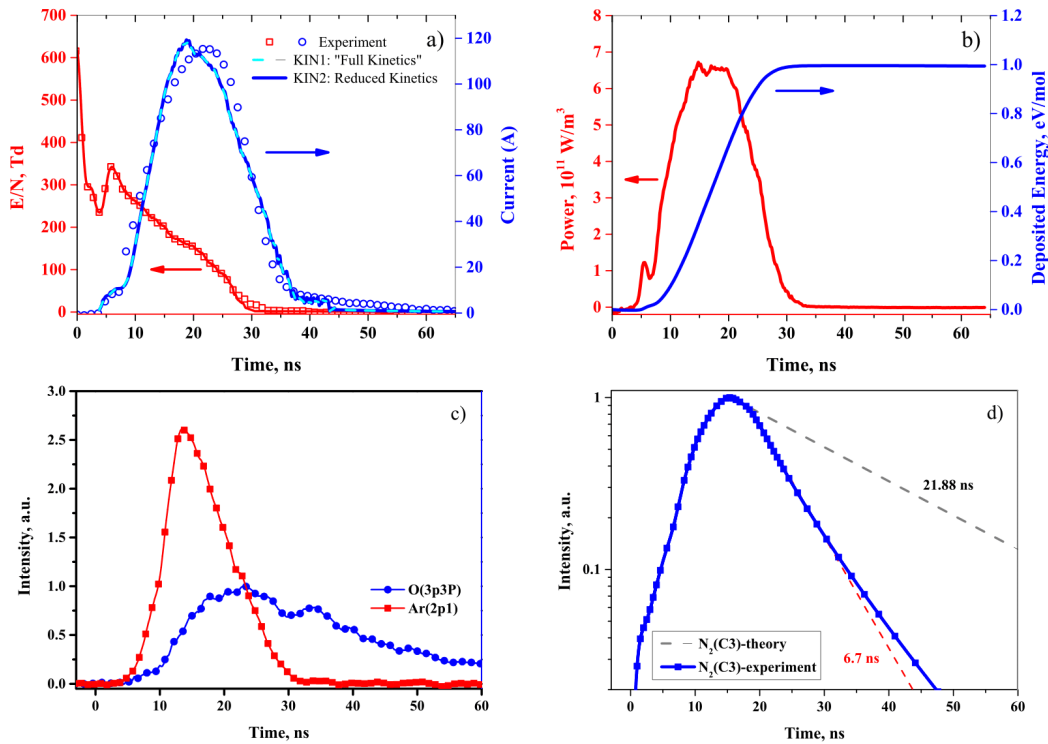


Figure 4.2: Main experimental results: (a) longitudinal electric field,  $E/N$ , in the center of the interelectrode gap and electrical current  $I_{trans}$  transmitted through the discharge tube; (b) specific deposited energy,  $\omega$ , and power deposited into plasma; (c) relative O-atoms emission ( $\lambda_{\text{O}} = 844.6$  nm) and Ar emission ( $\lambda_{\text{Ar}} = 749$  nm) curves, the maximum of emission of O-atoms is taken to be a unity; (d) optical emission of N<sub>2</sub> ( $\lambda_{\text{N}_2} = 337.1$  nm) superimposed with a theoretical decay curve according to [199].

N<sub>2</sub> ( $\lambda_{\text{N}_2} = 337.1$  nm) is presented in Figures 4.2 c, d. The curves of Ar and O emission are scaled according to the sensitivity of the spectral system at 750 and 845 nm respectively, the maximum of O-atoms emission is taken to be a unity. All the curves in Figure 4.2 are synchronized in time.

As it was mentioned in the introduction, optical actinometry is a well-adjusted technique to measure the density of atoms at relatively low electric fields and low degree of excitation/ionization. At the conditions of the present work both the electric field and the specific deposited energy are high. A simple test of a “non-usual” kinetics of a pulsed nanosecond discharge at moderate,  $P = 20\text{--}50$  mbar pressures, is the measurement of the decay of N<sub>2</sub>(C<sup>3</sup>Π<sub>u</sub>) → N<sub>2</sub>(B<sup>3</sup>Π<sub>g</sub>) emission in early afterglow,  $t \leq 100$  ns after the discharge. Mentioned pressure interval is sensitive to quenching, and any significant deviations from the well-known quenching rates [199] will indicate on the necessity to take into account a possibility of collisions of excited species

with charged, atomic and other excited species. Comparison of the experimental and theoretical decay curves for molecular nitrogen (Figure 4.2 d) shows that the difference between experimentally measured and theoretically calculated decay of  $N_2(C^3\Pi_u) \rightarrow N_2(B^3\Pi_g)$  emission is significant: 22 ns for theoretically calculated decay exceeds significantly the experimentally measured value, 6.7 ns. This means that, similar to [79], collisions between excited species and quenching by electrons should be important under given conditions.

## 4.2 Kinetics schemes

To build and to test the kinetic scheme corresponding to the experimental conditions of the present work, the following procedure has been used:

- A well-known and validated kinetic scheme for gas discharge in air was taken as a basis kinetic scheme;
- Reactions with Ar atoms were added to the basis kinetic scheme;
- Necessary reactions with participation of excited species, atomic species and electrons were added to the basis kinetic scheme. The resulting scheme will be further designated as "KIN1" scheme;
- The rate analysis and the sensitivity analysis of the KIN1 scheme were done relative to the experimentally obtained data;
- A few tens of reactions crucial for the description of the experimental results were selected from the KIN1 scheme. The resulting scheme will be designated as "KIN2" scheme;
- Role of different processes of the KIN2 scheme in the formation of  $O(3p^3P)$ ,  $Ar(2p_1)$  and  $N_2(C^3\Pi_u)$  kinetic curves were analyzed;
- Density of O-atoms in the discharge and the afterglow was calculated on the basis of the experimental data and suggested KIN2 scheme.

### 4.2.1 KIN1: full kinetic scheme

Kinetics of  $N_2:O_2$  mixtures have been intensively studied during last years. The kinetics scheme [200] suggested by Flitti and Pancheshnyi for  $N_2:O_2$  mixtures, based on air kinetics developed by Kossyi [14] and Cappitelli [72] was used as KIN1 basic scheme. Kinetics presented in paper [200] is available online [201]. ZDPlaskin software [143] with incorporated BOLSIG+ package [145] was used to solve a system

of ordinary differential equations for time-dependent densities of involved species on the period from 0 to 60 ns. Solving the problem, the gas temperature rise was neglected in the discharge and near afterglow. As far as maximum temperature rise during 50 ns is about 100 – 150 K, this should not influence the results of calculations. Another assumption was that the average value of species in the cross-section is adequately described by 0D model.

Following neutral, charged, excited molecules and atoms are taken into account in kinetics [201]:  $\text{N}_2$ ,  $\text{N}_2(v = 1 - 8)$ ,  $\text{N}_2(\text{A}^3\Sigma_u^+)$ ,  $\text{N}_2(\text{B}^3\Pi_g)$ ,  $\text{N}_2(a'^1\Sigma_u^-)$ ,  $\text{N}_2(\text{C}^3\Pi_u)$ ,  $\text{N}$ ,  $\text{N}(^2\text{D})$ ,  $\text{N}(^2\text{P})$ ,  $\text{N}^+$ ,  $\text{N}_2^+$ ,  $\text{N}_3^+$ ,  $\text{N}_4^+$ ,  $\text{O}_2$ ,  $\text{O}_2(v = 1 - 4)$ ,  $\text{O}_2(a^1\Delta_g)$ ,  $\text{O}_2(b^1\Sigma_g^+)$ ,  $\text{O}_2(\text{A}^3\Sigma_u^+)$ ,  $\text{O}_2(\text{C}^3\Delta_u)$ ,  $\text{O}_2(c^1\Sigma_u^-)$ ,  $\text{O}$ ,  $\text{O}(^1\text{D})$ ,  $\text{O}(^1\text{S})$ ,  $\text{O}_3$ ,  $\text{O}^+$ ,  $\text{O}_2^+$ ,  $\text{O}_4^+$ ,  $\text{O}^-$ ,  $\text{O}_2^-$ ,  $\text{O}_3^-$ ,  $\text{O}_4^-$ ,  $\text{NO}$ ,  $\text{NO}^+$ ,  $\text{NO}^-$ ,  $\text{O}_2^+\text{N}_2$ ,  $\text{N}_2\text{O}$ ,  $\text{NO}_2$ ,  $\text{NO}_3$ ,  $\text{N}_2\text{O}_5$ ,  $\text{N}_2\text{O}^+$ ,  $\text{NO}_2^+$ ,  $\text{N}_2\text{O}^-$ ,  $\text{NO}_2^-$ ,  $\text{NO}_3^-$ ,  $e$ . In total the scheme considered 55 species including vibrational states of  $\text{N}_2$  and  $\text{O}_2$ .

A minimum necessary number of reactions was added to describe the kinetics of excitation and de-excitation of argon. They were the reactions for  $\text{Ar}(2p_1)$  used in traditional actinometry analysis and supplementary reactions, important for  $\text{Ar}(2p_1)$ ,  $\text{O}(3p^3\text{P})$  and  $\text{N}_2(\text{C}^3\Pi_u)$  states at the conditions of high electric field and high specific energy. The following species were added to the kinetic scheme:  $\text{Ar}$ ,  $\text{Ar}^+$ ,  $\text{Ar}(2p_1)$ ,  $\text{Ar}(1s_2)$ ,  $\text{Ar}(11.55 \text{ eV})$  designating metastable  $\text{Ar}(1s_3)$  and  $\text{Ar}(1s_5)$  levels together, and  $\text{O}(3p^3\text{P})$ . The  $\text{N}_2(\text{A}^3\Sigma_u^+)$  level was considered as two separate species,  $\text{N}_2(\text{A}^3\Sigma_u^+, v = 0 - 2)$ ,  $\text{N}_2(\text{A}^3\Sigma_u^+, v > 2)$ . For electron collisions with nitrogen, oxygen and Ar, the self-consistent sets of cross sections [157], [202] and [203] respectively were used.

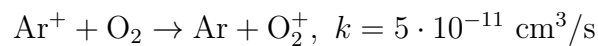
The following reactions were considered in addition to the reactions included in [200], hereinafter (R) with a number designates the corresponding reaction in the final kinetic scheme KIN2, presented in Table 4.1:

### (1) Ionization of Ar by electron impact.



### (2) Charge transfer reactions.

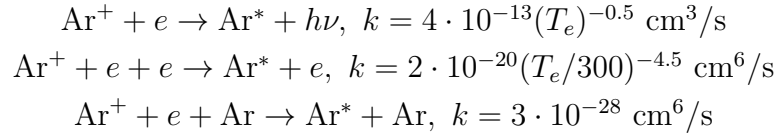
Two charge transfer reactions between  $\text{Ar}^+$  and  $\text{N}_2$  or  $\text{O}_2$  [204]



### (3) Electron-ion recombination of Ar.

Electron-ion recombination reactions is the main mechanism for loss of electrons in the early afterglow of the nanosecond discharge. Three additional electron-ion

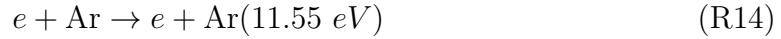
recombination reactions with participation of  $\text{Ar}^+$  ion [205] were added to the basic kinetic scheme [200]:



Here, following the paper [205],  $\text{Ar}^*$  denotes excited Ar. In the present work it is assumed that 20% of the  $\text{Ar}^*$  produced by the dielectronic recombination is  $\text{Ar}(2p_1)$ . The three body recombination reaction may be important in the afterglow, when electron temperature decreases [206].

#### (4) Excitation of Ar by electron impact.

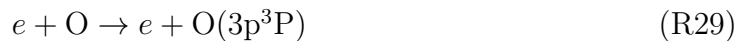
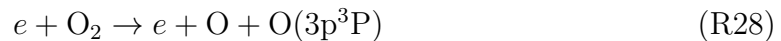
The electron impact is the main source of excited argon atoms during the discharge:



where the notation  $\text{Ar}(11.55 \text{ eV})$  refers to metastable  $1s^3$  and  $1s^5$  levels together.

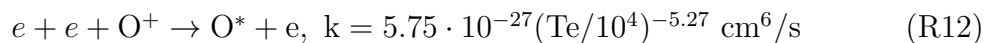
#### (5) Excitation of O-atoms by electron impact.

To predict the evolution of the studied in actinometry  $\text{O}(3p^3P)$  state, the excitation of  $\text{O}(^1D)$  and  $\text{O}(^1S)$ , which are produced from  $\text{O}_2$  molecule by electron impact and by quenching of  $\text{N}_2(\text{C}^3\Pi_u)$  have to be included together with excitation from the ground state [207–209]:



#### (6) Dissociation of $\text{O}_2^+$ and electron-ion recombination of $\text{O}^+$ ions.

Dissociation of  $\text{O}_2^+$  and three body recombination of  $\text{O}^+$  ions were considered to explain for the population of  $\text{O}(3p^3P)$  in the afterglow [210–212]:

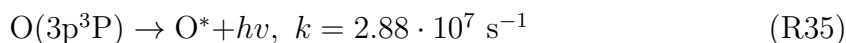
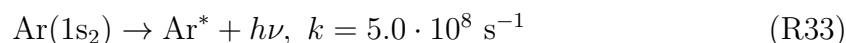
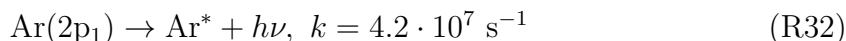


Here, following the paper [211, 212],  $\text{O}^*$  denotes excited O-atoms. Park [211] assumed that the rate constant of (R12) is the same as that of nitrogen, obtained for  $4000 \text{ K} \leq T_e \leq 20000 \text{ K}$  in using for all levels the elementary rates. In [212] the rate constant for optically thin case is obtained for  $T_e \geq 8000 \text{ K}$ , and concluding that

with the increase of electron density, the rate constant of the reaction (R12) will become similar to that proposed in [211]. In the present work, we assumed that 50% of the  $O^*$  produced by the reaction (R12) is  $O(3p^3P)$ , and used Park's expression, so the rate constant used in present work lies between the rate proposed by [211] and [212]. It should be noted that a 3-body recombination with electron as a third body is a brutto-reaction for a complex set of elementary stages [212]. In this work, we do not pretend to estimate or to derive the rate constant: uncertainty of  $T_e$  behavior in the near afterglow allows only an estimate of the behavior of the kinetic curves if the reaction (R12) is dominant.

### (7) Radiative decay of excited Ar and O-atoms.

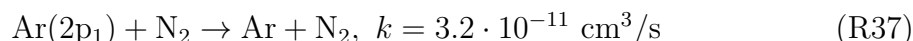
Radiative decay reactions [72] were considered as lost of excitation regardless to the lower state:



### (8) Quenching of electronically excited states.

Quenching of electronically excited states by neutrals and electrons are important processes of energy exchange in the afterglow. For example, it is responsible for the fast gas heating characteristics of nanosecond pulsed discharge and has been discussed in detailed in [37,200]. To simulate the experimental data on O-atoms actinometry, the following additional quenching processes were added to KIN1 scheme:

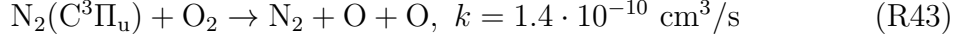
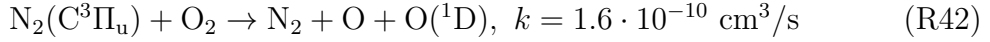
*Quenching of excited argon atoms [213–215]:*



*Quenching of excited nitrogen:*

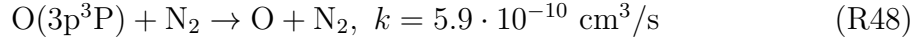
Quenching of  $\text{N}_2(\text{C}^3\Pi_u)$  in collisions with molecular oxygen is responsible for dissociation of molecular oxygen in the afterglow of short pulsed discharges. This reaction, already present in the basic kinetic scheme [200], was replaced by more detailed reaction considering different channels for products. The total rate constant of the quenching,  $3 \cdot 10^{-10} \text{ cm}^3/\text{s}$ , was taken from [199]. The possible channels of dissociation producing O,  $\text{O}(^1S)$  or  $\text{O}(^1D)$  atoms are analyzed in [37]: the ratio between the dissociation channels ( $\text{O} + \text{O}$ ), ( $\text{O}(^1S) + \text{O}$ ) and ( $\text{O}(^1D) + \text{O}$ ) is assumed to be approximately the same as in the reaction of quenching of excited metastable argon atoms  $\text{Ar}(1s_3)$  and  $\text{Ar}(1s_5)$  by oxygen, and this ratio is 0.46:0.52:0.02, according to paper [216]. The recommendation of [37] was used in the present work:





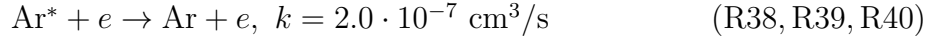
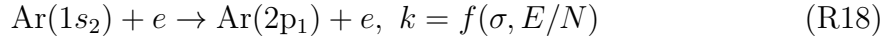
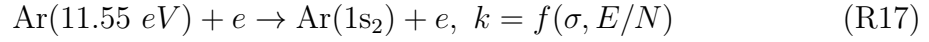
*Quenching of O(3p<sup>3</sup>P) atoms*

Rate constants of quenching of O(3p<sup>3</sup>P) atoms by N<sub>2</sub> and O<sub>2</sub> molecules were taken from the papers using two-photon absorption laser induced fluorescence (TALIF) [217, 218] to measure O-atom density:

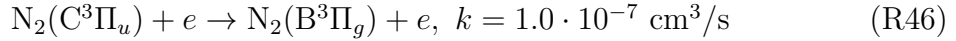
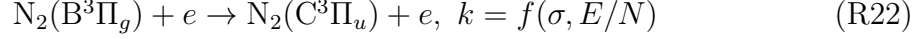


*Quenching by electrons*

Quenching of highly excited Ar states by electrons is taken into account in numerous papers [204, 205, 219, 220]. In the present work, the rate from [205] is used for quenching of Ar excited state.



Experimental observation of quenching of N<sub>2</sub>(C<sup>3</sup>Π<sub>u</sub>) state by electrons in near afterglow of nanosecond capillary discharge in nitrogen was recently reported [79]. A few reactions responsible for the quenching by electrons and for the balance of the particles on N<sub>2</sub>(C<sup>3</sup>Π<sub>u</sub>) – level were added to the scheme:



The rate of the last reaction was estimated using the cross section from [163], similar to [79].

Quenching by electrons was considered to be small for O(3p<sup>3</sup>P). This conclusion was made on the basis of comparison of the available excitation cross sections [163, 207, 208] for N<sub>2</sub>(C<sup>3</sup>Π<sub>u</sub>) and O(3p<sup>3</sup>P): for atomic oxygen, the cross-sections of excitation by electrons from the lower electronically excited states are at least 1-2 order of magnitude lower than for molecular nitrogen. The rate constant N<sub>2</sub>(B<sup>3</sup>Π<sub>g</sub>) of quenching by electron is comparable to that of N<sub>2</sub>(C<sup>3</sup>Π<sub>u</sub>), but the reaction rate is smaller comparing with quenching by molecular oxygen. These have been confirmed by several test calculations with additional quenching of O(3p<sup>3</sup>P) and N<sub>2</sub>(B<sup>3</sup>Π<sub>g</sub>) taken into account with different test rates.

## 4.2.2 KIN2: reduced kinetic scheme

KIN1 scheme contains about 700 reactions, most of which have minor effects for optical actinometry on such a short time scale. To select the key reactions describing experimentally observed data, the sensitivity analysis method described in Chapter 3 has been performed for the selected species.

Figure 4.3 a illustrates the principle of sensitivity diagrams presented in Figures 4.3 b-d. As far as the aim of the reduced kinetic scheme is to describe the behaviour of experimentally measured intensities of  $\text{Ar}(2p_1)$ ,  $\text{O}(3p^3P)$  and  $\text{N}_2(\text{C}^3\Pi_u)$ , these species were taken as the key species for comparison. For each species, the sensitivity coefficients to all reactions  $\varphi(t)$  were found according to the formula (3.18). For each reaction, the peak value of the sensitivity coefficient  $\varphi_{max}$  corresponds to the maximum deviation from the initial unchanged density calculated with KIN1 scheme. The  $\langle \varphi \rangle$  value averaged through the period of calculations was also calculated. The sensitivity coefficients equal or exceeding 10%, are presented in Figures 4.3 b-d for  $\text{Ar}(2p_1)$ ,  $\text{O}(3p^3P)$  and  $\text{N}_2(\text{C}^3\Pi_u)$  respectively.

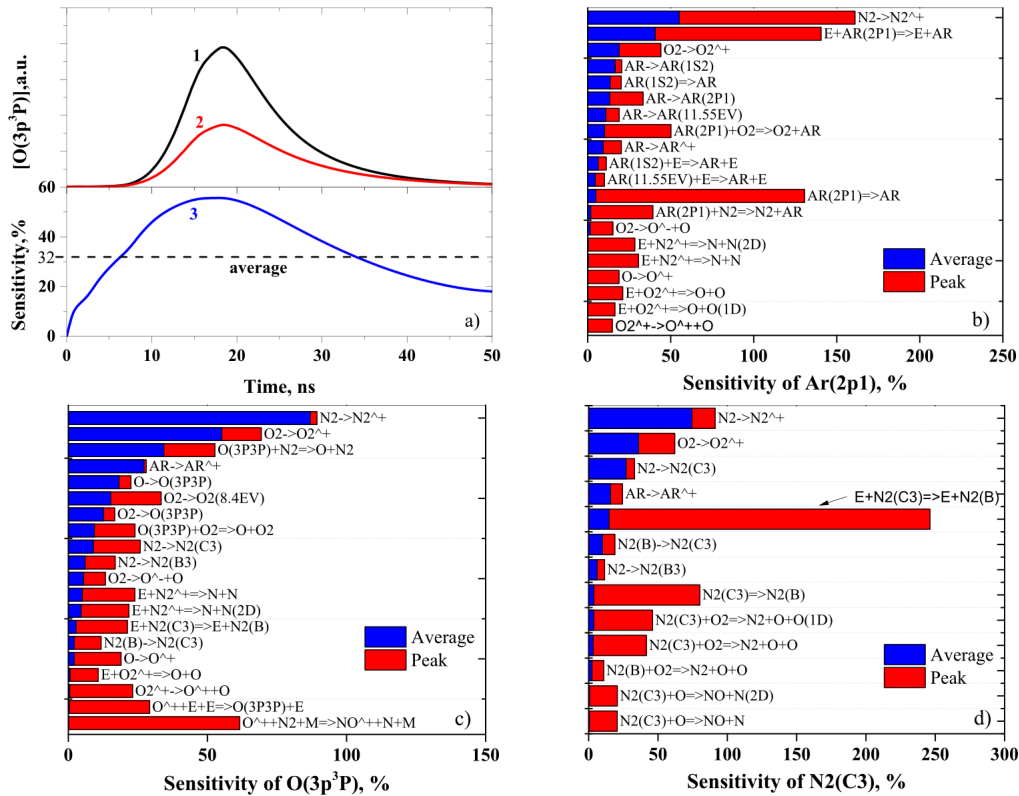


Figure 4.3: Sensitivity analysis for the key species under study: (a) an example illustrating the calculations of the sensitivity coefficient (see text for details) including the initial unchanged density calculated with KIN1 scheme (curve (1)), density calculated with one of the rates increased by 50% (curve (2)), and the corresponding sensitivity coefficient  $\varphi$  (curve (3)); sensitivity coefficients satisfying the condition  $\varphi \geq 0.1$  for (b)  $\text{Ar}(2p_1)$ ; (c)  $\text{O}(3p^3P)$  and (d)  $\text{N}_2(\text{C}^3\Pi_u)$ .

Figure 4.3 shows that only a few tens of reactions influence significantly the densities of the species of interest and so, the observed experimentally emission of

three selected excited species. Reactions can be divided into a few groups: ionization and excitation by electron impact with a typical peak values of sensitivity coefficient  $\varphi_{max} \approx 30 - 60\%$ , excitation in collisions with already excited species dominant in the afterglow and quenching by neutrals with a similar sensitivity coefficient, and reactions of quenching by electrons with a typical value of  $\varphi_{max} \approx 150 - 200\%$ .

Minimized set of reactions describing the behavior of the species of interest was finally selected on the basis of the sensitivity analysis and on the rate analysis. The resulting scheme, KIN2, consists of 48 reactions and is presented by Table 4.1.

Table 4.1: KIN2: reduced kinetics scheme

| Number | Reaction   | Rate constant <sup>*)</sup>                       | Ref.       |
|--------|--|---|------------|
| R1     | $e + \text{Ar} \rightarrow e + e + \text{Ar}^+$                                    | $f(\sigma, E/N)$                                  | [203, 221] |
| R2     | $e + \text{N}_2 \rightarrow e + e + \text{N}_2^+$                                  | $f(\sigma, E/N)$                                  | [157, 221] |
| R3     | $e + \text{O}_2 \rightarrow e + e + \text{O}_2^+$                                  | $f(\sigma, E/N)$                                  | [202, 221] |
| R4     | $e + \text{O} \rightarrow e + e + \text{O}^+$                                      | $f(\sigma, E/N)$                                  | [202, 221] |
| R5     | $e + \text{O}_2 \rightarrow \text{O}^- + \text{O}$                                 | $f(\sigma, E/N)$                                  | [202, 221] |
| R6     | $e + \text{O}_2^+ \rightarrow e + \text{O}^+ + \text{O}$                           | $f(\sigma, E/N)$                                  | [210, 221] |
| R7     | $e + \text{N}_2^+ \rightarrow \text{N} + \text{N}$                                 | $1.8 \cdot 10^{-7} (300/Te)^{0.39} \cdot 0.50$    | [72]       |
| R8     | $e + \text{N}_2^+ \rightarrow \text{N} + \text{N}(^2\text{D})$                     | $1.8 \cdot 10^{-7} (300/Te)^{0.39} \cdot 0.45$    | [72]       |
| R9     | $e + \text{O}_2^+ \rightarrow \text{O} + \text{O}$                                 | $2.7 \cdot 10^{-7} (300/Te)^{0.70} \cdot 0.55$    | [72]       |
| R10    | $e + \text{O}_2^+ \rightarrow \text{O} + \text{O}(^1\text{D})$                     | $2.7 \cdot 10^{-7} (300/Te)^{0.70} \cdot 0.40$    | [72]       |
| R11    | $e + e + \text{Ar}^+ \rightarrow \text{Ar}(2p_1) + e$                              | $2 \cdot 10^{-20} (Te/300)^{-4.5}$                | [211, 212] |
| R12    | $e + e + \text{O}^+ \rightarrow \text{O}(3p^3\text{P}) + e$                        | $5.75 \cdot 10^{-27} (10000/Te)^{-5.27}$          | [211, 212] |
| R13    | $\text{O}^+ + \text{N}_2 + \text{M} \rightarrow \text{NO}^+ + \text{N} + \text{M}$ | $6.0 \cdot 10^{-29} (300/T)^{2.0} \cdot \text{M}$ | [72]       |
| R14    | $e + \text{Ar} \rightarrow e + \text{Ar}(11.55\text{eV})$                          | $f(\sigma, E/N)$                                  | [222, 223] |
| R15    | $e + \text{Ar} \rightarrow e + \text{Ar}(1s_2)$                                    | $f(\sigma, E/N)$                                  | [222, 223] |
| R16    | $e + \text{Ar} \rightarrow e + \text{Ar}(2p_1)$                                    | $f(\sigma, E/N)$                                  | [224]      |
| R17    | $e + \text{Ar}(11.55\text{eV}) \rightarrow e + \text{Ar}(1s_2)$                    | $f(\sigma, E/N)$                                  | [225, 226] |
| R18    | $e + \text{Ar}(1s_2) \rightarrow e + \text{Ar}(2p_1)$                              | $f(\sigma, E/N)$                                  | [225, 226] |
| R19    | $e + \text{N}_2 \rightarrow e + \text{N}_2(\text{A}^3\Sigma_u)$                    | $f(\sigma, E/N)$                                  | [157, 221] |
| R20    | $e + \text{N}_2 \rightarrow e + \text{N}_2(\text{B}^3\Pi_g)$                       | $f(\sigma, E/N)$                                  | [157, 221] |
| R21    | $e + \text{N}_2 \rightarrow e + \text{N}_2(\text{C}^3\Pi_u)$                       | $f(\sigma, E/N)$                                  | [157, 221] |
| R22    | $e + \text{N}_2(\text{B}^3\Pi_g) \rightarrow e + \text{N}_2(\text{C}^3\Pi_u)$      | $f(\sigma, E/N)$                                  | [163]      |
| R23    | $e + \text{O}_2 \rightarrow e + \text{O} + \text{O}$                               | $f(\sigma, E/N)$                                  | [202, 221] |
| R24    | $e + \text{O}_2 \rightarrow e + \text{O} + \text{O}(^1\text{D})$                   | $f(\sigma, E/N)$                                  | [202, 221] |
| R25    | $e + \text{O}_2 \rightarrow e + \text{O} + \text{O}(^1\text{S})$                   | $f(\sigma, E/N)$                                  | [202, 221] |
| R26    | $e + \text{O} \rightarrow e + \text{O}(1\text{S})$                                 | $f(\sigma, E/N)$                                  | [208]      |
| R27    | $e + \text{O} \rightarrow e + \text{O}(1\text{D})$                                 | $f(\sigma, E/N)$                                  | [208]      |

|     |   |                       |       |
|-----|---|-----------------------|-------|
| R28 | $e + \text{O}_2 \rightarrow e + \text{O} + \text{O}(3\text{p}^3\text{P})$                           | $f(\sigma, E/N)$      | [207] |
| R29 | $e + \text{O} \rightarrow e + \text{O}(3\text{p}^3\text{P})$  | $f(\sigma, E/N)$      | [208] |
| R30 | $e + \text{O}(^1\text{S}) \rightarrow e + \text{O}(3\text{p}^3\text{P})$                            | $f(\sigma, E/N)$      | [209] |
| R31 | $e + \text{O}(^1\text{D}) \rightarrow e + \text{O}(3\text{p}^3\text{P})$                            | $f(\sigma, E/N)$      | [209] |
| R32 | $\text{Ar}(2\text{p}_1) \rightarrow \text{Ar} + h\nu$   | $4.2 \cdot 10^7$      | [213] |
| R33 | $\text{Ar}(1\text{s}_2) \rightarrow \text{Ar} + h\nu$   | $5.0 \cdot 10^8$      | [213] |
| R34 | $\text{N}_2(\text{C}^3\Pi_u) \rightarrow \text{N}_2 + h\nu$   | $2.45 \cdot 10^7$     | [72]  |
| R35 | $\text{O}(3\text{p}^3\text{P}) \rightarrow \text{O} + h\nu$   | $2.88 \cdot 10^7$     | [217] |
| R36 | $\text{Ar}(2\text{p}_1) + \text{O}_2 \rightarrow \text{Ar} + \text{O}_2$                            | $7.6 \cdot 10^{-10}$  | [213] |
| R37 | $\text{Ar}(2\text{p}_1) + \text{N}_2 \rightarrow \text{Ar} + \text{N}_2$                            | $3.2 \cdot 10^{-11}$  | [213] |
| R38 | $\text{Ar}(2\text{p}_1) + e \rightarrow \text{Ar} + e$  | $2.0 \cdot 10^{-7}$   | [219] |
| R39 | $\text{Ar}(1\text{s}_2) + e \rightarrow \text{Ar} + e$  | $2.0 \cdot 10^{-7}$   | [219] |
| R40 | $\text{Ar}(11.55\text{eV}) + e \rightarrow \text{Ar} + e$   | $2.0 \cdot 10^{-7}$   | [219] |
| R41 | $\text{N}_2(\text{B}^3\Pi_g) + \text{O}_2 \rightarrow \text{N}_2 + \text{O} + \text{O}$             | $3.0 \cdot 10^{-10}$  | [37]  |
| R42 | $\text{N}_2(\text{C}^3\Pi_u) + \text{O}_2 \rightarrow \text{N}_2 + \text{O} + \text{O}(^1\text{D})$ | $1.6 \cdot 10^{-10}$  | [37]  |
| R43 | $\text{N}_2(\text{C}^3\Pi_u) + \text{O}_2 \rightarrow \text{N}_2 + \text{O} + \text{O}$             | $1.43 \cdot 10^{-10}$ | [37]  |
| R44 | $\text{N}_2(\text{C}^3\Pi_u) + \text{O} \rightarrow \text{NO} + \text{N}$                           | $1.4 \cdot 10^{-10}$  | [37]  |
| R45 | $\text{N}_2(\text{C}^3\Pi_u) + \text{O} \rightarrow \text{NO} + \text{N}(^2\text{D})$               | $1.4 \cdot 10^{-10}$  | [37]  |
| R46 | $\text{N}_2(\text{C}^3\Pi_u) + e \rightarrow \text{N}_2(\text{B}^3\Pi_g) + e$                       | $1.0 \cdot 10^{-7}$   | [79]  |
| R47 | $\text{O}(3\text{p}^3\text{P}) + \text{O}_2 \rightarrow \text{O} + \text{O}_2$                      | $9.3 \cdot 10^{-10}$  | [217] |
| R48 | $\text{O}(3\text{p}^3\text{P}) + \text{N}_2 \rightarrow \text{O} + \text{N}_2$                      | $5.9 \cdot 10^{-10}$  | [217] |

\*) Rate constants are given in  $\text{s}^{-1}$ ,  $\text{cm}^3 \cdot \text{s}^{-1}$ ,  $\text{cm}^6 \cdot \text{s}^{-1}$

## 4.3 Calculated results for the selected species and discussion

### 4.3.1 Calculated results and density of O-atoms

Experimentally measured electric field presented in Figure 4.2 a was taken as an input to the model. Initial density of electrons was calculated according to experimental current value and  $E/N$  according to the formula  $n_e(t_0) = I(t_0)/(q\mu E(t_0)\pi r^2)$ , where  $t_0$  is the initial time moment,  $I(t_0)$  and  $E(t_0)$  are the electron current and the electric field at  $t_0$  moment respectively,  $q$  is unit charge,  $\mu(E/N)$  is the electron mobility calculated from Boltzmann solver, and  $r$  is the inner radius of the capillary tube. The electrical current calculated on the basis of the experimentally measured electric field is presented in Figure 4.2 together with the measured current. The

good agreement between the results of calculations and the measurements is clearly seen. It should be noted that the mean electron energy in the afterglow ( $t > 30$  ns) is not available from the experimental data. To provide the agreement between experimental data on Ar( $2p_1$ ) and O( $3p^3P$ ) emission, the  $E/N$  in early afterglow was artificially set linearly decreasing from 3 Td to 1 Td with the rate of 0.05 Td/ns, corresponding to the mean electron energy between 0.26 eV and 0.18 eV.

The maximum of energy is deposited to the plasma in the period  $10 < t < 25$  ns, corresponding to the current flowing through the capillary discharge when the interelectrode gap is closed by plasma current and to the electric field decreasing after the closing of the discharge gap. On the waveform of the electric field this point is seen as the second maximum,  $E/N \approx 350$  Td, at 6.5 ns.

The normalized densities of Ar( $2p_1$ ), O( $3p^3P$ ) and N<sub>2</sub>(C<sup>3</sup>Π<sub>u</sub>) calculated by KIN1 and by KIN2 kinetic schemes are compared with corresponding normalized emission curves in Figure 4.4 a-c. Both KIN2 and KIN1 reproduce the production and loss of Ar( $2p_1$ ) and N<sub>2</sub>(C<sup>3</sup>Π<sub>u</sub>) (Figure 4.4 a,b) reasonably well. The discrepancy between the KIN1 and the KIN2 description is negligible at  $t < 40$  ns, does not exceed 10 – 15 % for Ar( $2p_1$ ) and does not exceed 3 – 5% for N<sub>2</sub>(C<sup>3</sup>Π<sub>u</sub>) at  $t < 40$  ns. For O( $3p^3P$ ), calculations by KIN1 and KIN2 schemes give the same results at  $t < 40$  ns but diverge progressively at  $t > 40$  ns giving the difference by a factor of 1.2 at the end of the interval of calculations. It should be noted that the experimental data on O( $3p^3P$ ) emission are the most noisy: the signal-to-noise ratio is about 10 because of decrease of the sensitivity of the spectral system in the near IR region. In spite of the noise, a dip of the kinetic curve of excited oxygen at decaying phase of the electric current,  $t \approx 30$  ns, when longitudinal electric field drops to the values below the threshold of experimental measurements, is clearly seen. Similar dip but a few times more intense is observed in numerical modeling.

The last plot, Figure 4.4d, presents the the calculated density of Ar( $2p_1$ ), together with the densities of Ar( $2p_1$ ) and O( $3p^3P$ ) obtained from the experimentally measured emission taking into account Einstein coefficients for the appropriate transitions, the maximum of [O( $3p^3P$ )] is taken to be unity. It is clearly seen that the data of numerical calculations match well the experimental data.

So, the KIN2 kinetic scheme (i) provides a good agreement between experimentally observed and calculated temporal behavior of densities/emission of Ar( $2p_1$ ), O( $3p^3P$ ) and N<sub>2</sub>(C<sup>3</sup>Π<sub>u</sub>); (ii) provides a good agreement between experimentally observed and calculated ratio of densities/emission intensity of Ar( $2p_1$ ) and O( $3p^3P$ ).

Figure 4.5 presents the calculated kinetic curves for N<sub>2</sub>, O<sub>2</sub>, Ar, O-atoms in the ground state, Ar( $2p_1$ ), O( $3p^3P$ ), N<sub>2</sub>(C<sup>3</sup>Π<sub>u</sub>), and electron density. The electron density, reaching about  $2 \cdot 10^{15}$  cm<sup>-3</sup> in the time interval corresponding to maximum energy release in the discharge, is in reasonable correlation with calculations of the

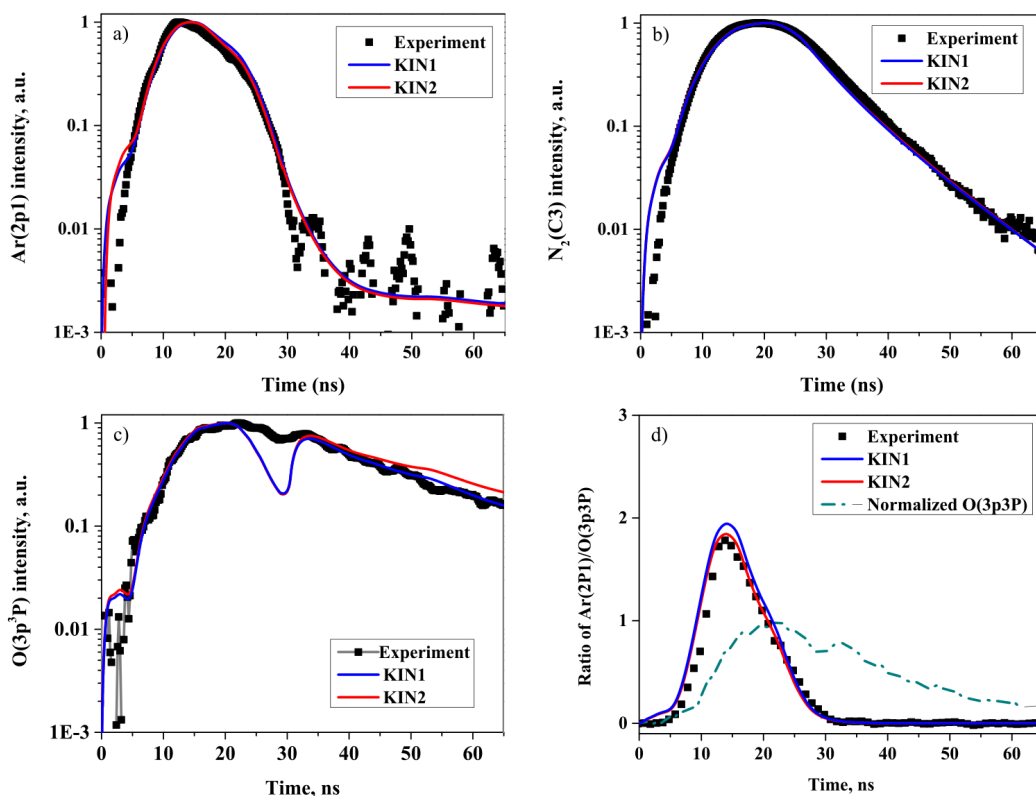


Figure 4.4: Comparison of calculated normalized density and experimentally measured normalized emission intensity for (a) Ar(2p<sub>1</sub>), (b) N<sub>2</sub>(C<sup>3</sup>Π<sub>u</sub>) and (c) O(3p<sup>3</sup>P); (d) the calculated relative density of Ar(2p<sub>1</sub>) to O(3p<sup>3</sup>P), together with experimentally measured values, the maximum of [O(3p<sup>3</sup>P)] is taken to be unity.

FIWs in capillary tubes in air [39] and measurements and calculations of the electron density in capillary discharge in pure nitrogen [79]. Atomic oxygen density at  $t = 20$  ns is equal to  $[O] = 3 \cdot 10^{16} \text{ cm}^{-3}$ , that is approaches Ar density (a few percent). In early afterglow, 65 ns after the start of the discharge,  $[O] = 7.5 \cdot 10^{16} \text{ cm}^{-3}$ . The data are in reasonable agreement with TALIF measurements [36] of O-atoms on the interval  $0.2 - 2.2 \mu\text{s}$  in nanosecond capillary discharge in air. In nanosecond discharge in air with somewhat lower electrical current, about 80 A, the density of O-atoms increased from  $(5 - 7) \cdot 10^{16} \text{ cm}^{-3}$  at  $0.2 \mu\text{s}$  to about  $2 \cdot 10^{17} \text{ cm}^{-3}$  at  $2.2 \mu\text{s}$ .

### 4.3.2 Rate analysis for the species measured experimentally

To understand which reactions influence experimentally observed data in a capillary nanosecond discharge, the rates of production and decay of three selected species of interest, Ar(2p<sub>1</sub>), O(3p<sup>3</sup>P) and N<sub>2</sub>(C<sup>3</sup>Π<sub>u</sub>), have been analyzed.

Only three main reactions are responsible in KIN2 for Ar(2p<sub>1</sub>) behavior (see

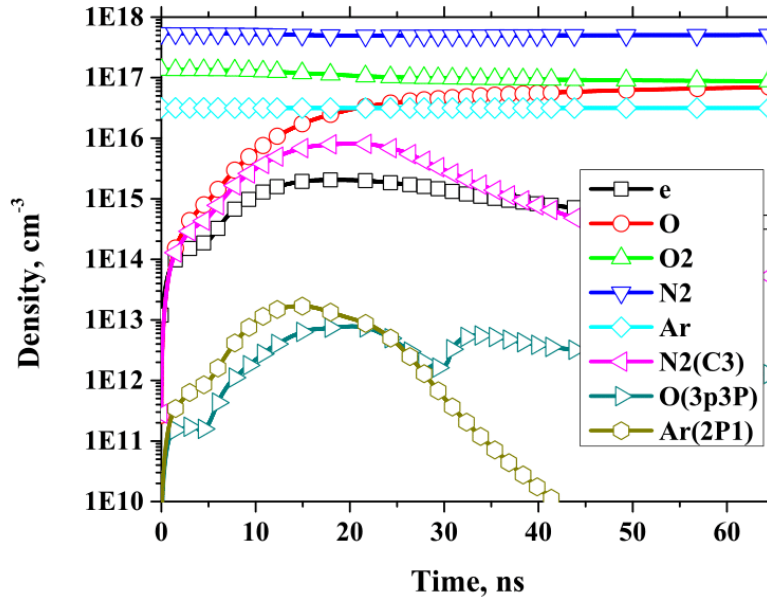


Figure 4.5: Time evolution of calculated main components, including actinometry species, electrons and O-atoms.

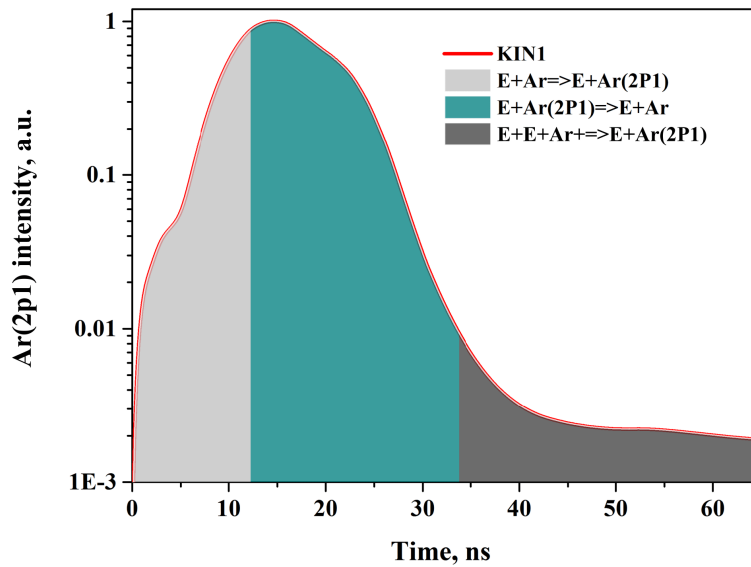


Figure 4.6: Dominating reactions for production and loss of  $\text{Ar}(2p_1)$ .

Figure 4.6). On the stage of the high electric fields and increasing current,  $t < 12$  ns, this is the reaction of direct excitation by electron impact, (R16). When electron density increases and electric current flows through the discharge, 12 – 34 ns, the dominant reaction is quenching of  $\text{Ar}(2p_1)$  by electrons, (R38). And finally, in the afterglow the slowing down of the decay of  $\text{Ar}(2p_1)$  is determined by the decay of the

electron density and simultaneous production of  $\text{Ar}(2p_1)$  caused by the electron-ion recombination (R11).

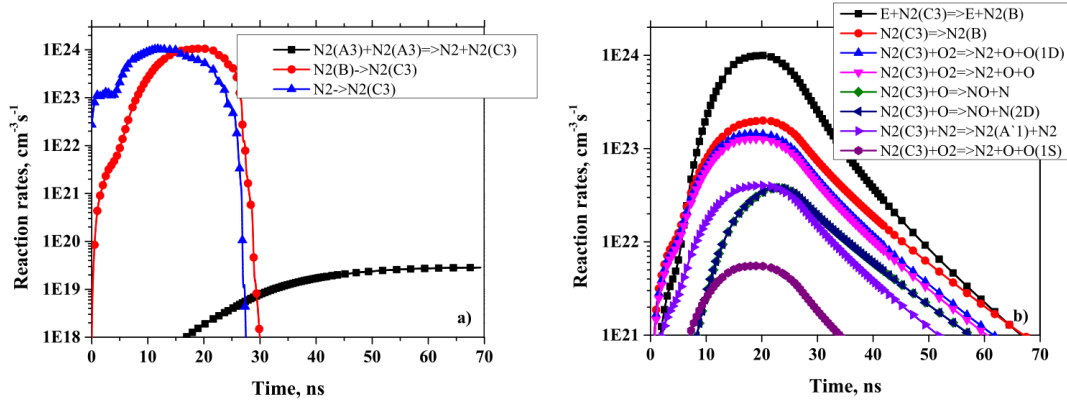


Figure 4.7: Rates of the main reactions of (a) production and (b) loss of  $\text{N}_2(\text{C}^3\Pi_u)$ .

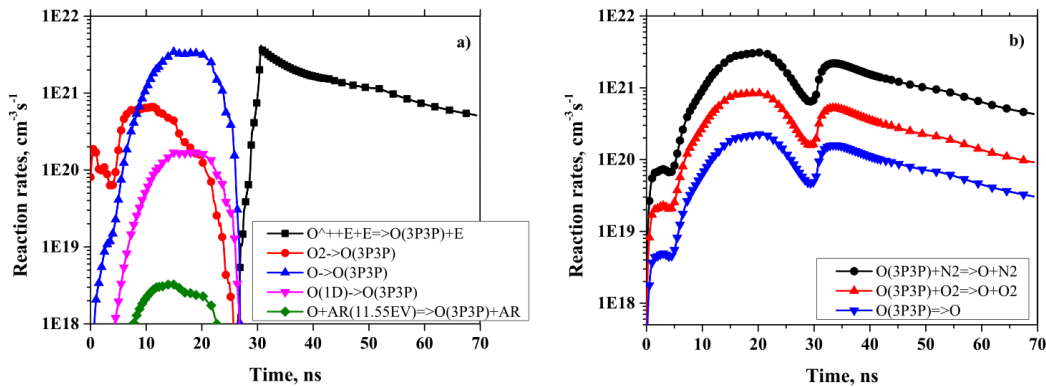


Figure 4.8: Rates of the main reactions of (a) production and (b) loss of  $\text{O}(3p^3P)$ .

Production and of decay of excited molecular nitrogen and atomic oxygen is more complicated. For these species, the highest reaction rates are plotted in Figures 4.7 and 4.8, separately for production and decay of the excited state density.

For  $\text{N}_2(\text{C}^3\Pi_u)$ , the main population process during first 15 ns of the discharge is a direct excitation by electron impact. Later, at high electron densities and still high electric field, population by electron impact from  $\text{N}_2(\text{B}^3\Pi_g)$  state becomes important. In the afterglow, the pooling reaction with nitrogen lower metastable states is responsible for some (but significantly lower than in the discharge) additional population. Decay of  $\text{N}_2(\text{C}^3\Pi_u)$  is caused, first, by quenching in collisions with the electrons, then by radiative losses and quenching in collisions with molecular oxygen. It should be noted that the rate of the two last processes together is only a few

times lower than the rate of quenching by electrons. This means that the dominant role of quenching by electrons will disappear if the electron density is an order of magnitude lower.

The main processes of O(3p<sup>3</sup>P) atoms production in the beginning of the discharge (0 – 10 ns) is dissociation of molecular oxygen by direct electron impact; after 10 ns this process is changed by direct excitation of atomic oxygen to O(3p<sup>3</sup>P) state. When the electric fields drops, at  $t > 28$  ns, the 3-body recombination of O<sup>+</sup> ion with electron as a third body becomes important. The process responsible for O(3p<sup>3</sup>P) decay is the collisional quenching on the main mixture components, N<sub>2</sub> and O<sub>2</sub>.

To summarize, for Ar(2p<sub>1</sub>) and O(3p<sup>3</sup>P) states, the “tail” of the emission,  $t > 30$  ns is mainly due to reactions of 3–body recombination with electron as a third body. The reaction rates for this kind of process at low  $T_e$  are not well-known but depends strongly upon  $T_e$ : the rate constants drop by 3–5 orders of magnitude at  $T_e$  increase already at  $T_e = 1$  eV. In the discharge, at  $t < 30$  ns, the emission of Ar(2p<sub>1</sub>) is due to reactions of production by direct electron impact, the decay is because of quenching by electrons; the emission of O(3p<sup>3</sup>P) is due to reactions of production in dissociative excitation in the beginning of the discharge and, at 10 – 25 ns, is due to excitation by direct electron impact, the decay is because of quenching by N<sub>2</sub>. The ratio of densities of Ar(2p<sub>1</sub>) and O(3p<sup>3</sup>P) excited atoms, an important data set for comparison, is measured and calculated in the period 0 – 30 ns, when the 3–body recombination is not active yet.

### 4.3.3 Comparison of data for low current in the discharge: underlining the role of high electron density

With two different lengths of the capillary tube, 55 mm and 70 mm, it was possible to get, at almost the same in amplitude electric field, the electrical current different by a factor of two. These data were used to trace a trend in actinometry experiments to verify the validity of the suggestions done for numerical modeling, at high electric field and high energy density. The data are summarized in Figure 4.9. Shorter discharge tube provides higher current, the maximum value is equal to  $(I_1)_{max} = 120$  A against  $(I_2)_{max} = 60$  A in the longer tube (Figure 4.9 a). As a result, the specific energy density was about  $\omega_1 = 1$  eV/molecule in the shorter tube and  $\omega_2 = 0.5$  eV/molecule in the longer tube. Figure 4.9 b compares the electron densities: the maximum electron density is 2.5 times higher for  $\omega_1 = 1$  eV/molecule energy density .

Plots of emission of O(3p<sup>3</sup>P) for  $\omega_1$  and  $\omega_2$ , superimposed with calculated for these cases density of O(3p<sup>3</sup>P) in arbitrary units, are presented in linear scale. The

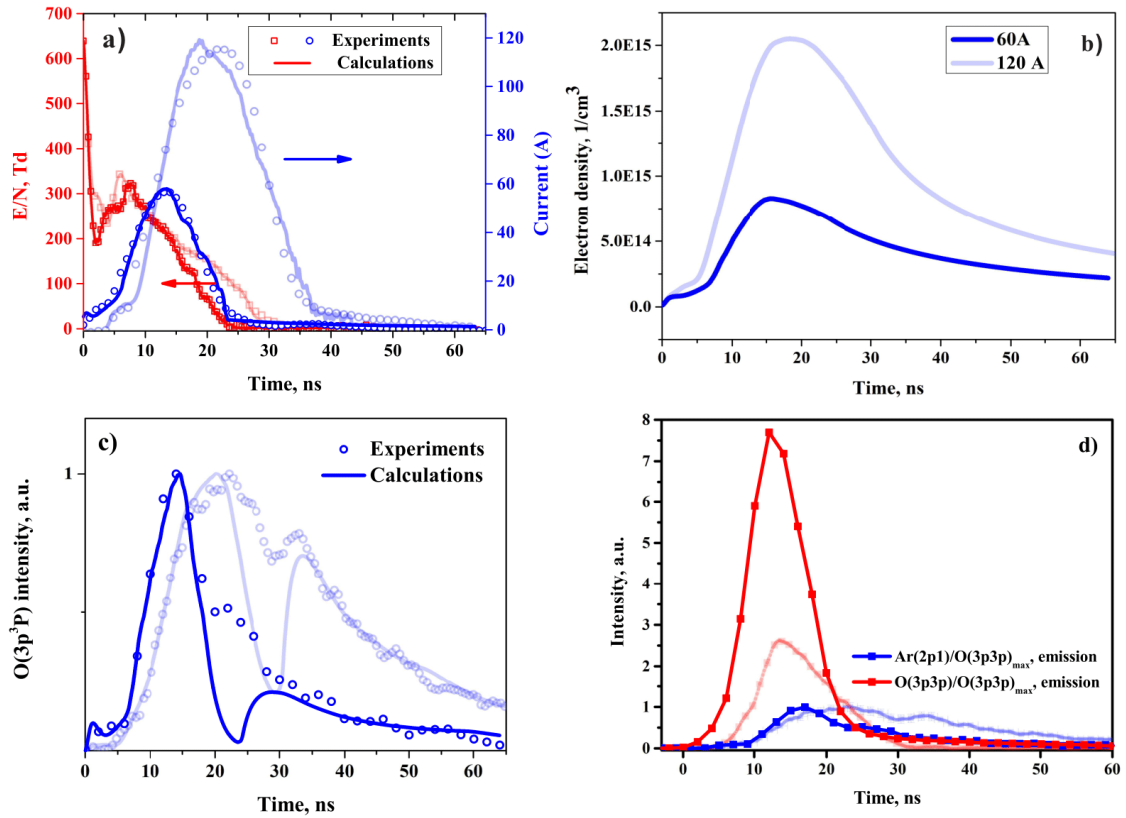


Figure 4.9: Comparison of experiments and calculations for two different currents: (a) longitudinal electric field,  $E/N$ , in the center of the interelectrode gap and electrical current  $I_{trans}$  transmitted through the discharge tube for two cases; (b) electron density; (c) calculated normalized density and experimentally measured normalized emission intensity for  $O(3p^3P)$ ; (d) the calculated density of  $Ar(2p_1)$ , together with the densities of  $Ar(2p_1)$  and  $O(3p^3P)$  obtained from the experimentally measured emission, the maximum of  $[O(3p^3P)]$  is taken to be unity. Lines and scatters in solid color are for the case with  $I_{max} = 60$  A, those with light and transparent color are for the case with  $I_{max} = 120$  A discussed in previous sections.

dip on the experimental curve is clearly seen at  $t = 27$  ns for  $\omega_1 = 1$  eV/molecule. For  $\omega_2 = 0.5$  eV/molecule, similar but less pronounced dip appears at  $t = 20$  ns. It follows from analysis of Figure 4.9 a, that for both cases, the reduced electric field at the position of the dip is the same and equal  $E/N \approx 60$  Td. For both cases, numerical modeling reproduces the dip only qualitatively — in our opinion, because of non-known dynamics of  $T_e$  in early afterglow and because of the uncertainty in the rate constants — but it is obvious that the role of electrons in population of the excited oxygen atom becomes less pronounced with decrease of the specific energy density. Finally, the density of  $Ar(2p_1)$  relative to the density of  $O(3p^3P)$  (the maximum density of excited oxygen is taken as unity) is adequately reproduced for

both values of  $\omega$ . At lower  $\omega$ , and so lower electron density, (i) the density of excited Ar is less influenced by quenching, and so is almost 3 times higher; (ii) the “tails” of the kinetic curves for both excited species decay faster, according to the idea that the reason of the observed long decay is a reaction strongly depending upon electron density. Thus, further decrease of specific energy density should lead to decay of role of 3-body recombination and to higher Ar( $2p_1$ ) intensity comparing to the intensity of O( $3p^3P$ ).

Summarizing the performed kinetic analysis, will formulate the simplified kinetic equations for the [Ar( $2p_1$ )] and [O( $3p^3P$ )]. At the developed discharge stage, when the main production of O( $3p^3P$ ) is due to excitation from the ground state of O atom and when the reaction of recombination are not important yet ( $10 \text{ ns} < t < 25 \text{ ns}$  for the case of  $\omega_1 = 1 \text{ eV/molecule}$ ), the balance between production and decay of the excited atoms can be written in the following way:

$$d[\text{Ar}(2p_1)]/dt = k_{16}n_e[\text{Ar}] - k_{38}n_e[\text{Ar}(2p_1)] \quad (4.2)$$

$$d[\text{O}(3p^3P)]/dt = k_{29}n_e[\text{O}] - k_{48}[\text{O}(3p^3P)][\text{N}_2] \quad (4.3)$$

Selecting in the left hand side the terms containing the densities of atoms in the ground state, will obtain

$$\frac{k_{29}n_e[\text{O}]}{k_{16}n_e[\text{Ar}]} = \frac{d[\text{O}(3p^3P)]/dt + k_{48}[\text{O}(3p^3P)][\text{N}_2]}{d[\text{Ar}(2p_1)]/dt + k_{38}n_e[\text{Ar}(2p_1)]} \quad (4.4)$$

and finally,

$$[\text{O}] = [\text{Ar}] \cdot \frac{k_{16}}{k_{29}} \cdot \frac{d[\text{O}(3p^3P)]/dt + k_{48}[\text{O}(3p^3P)][\text{N}_2]}{d[\text{Ar}(2p_1)]/dt + k_{38}n_e[\text{Ar}(2p_1)]} \quad (4.5)$$

The equation (4.5) can be considered as actinometry equation for the peculiar case of nanosecond discharge at high electric fields and high specific energy density. Atomic oxygen density can be found in the discharge period as a function of time at the conditions of known (i) absolute values and waveforms of the electric field and current; (ii) waveforms and relative intensities of [Ar( $2p_1$ )] and [O( $3p^3P$ )] emission. To check the validity of the equation (4.5), the analysis of the reaction rates at different stages of the discharge development is necessary.

## 4.4 Conclusions

In this chapter, the atomic oxygen density in nanosecond capillary discharge was studied experimentally by means of Ar-based actinometry and using numerical modeling. Nanosecond discharge was generated in synthetic air with additions of Ar flow-

ing through the quartz capillary 1.5 cm in diameter and 5.5 cm in length, the pressure in the center of the capillary was equal to 28.5 mbar. Under these conditions, the specific energy, deposited in the discharge was equal to  $\omega \approx 1.0$  eV/molecule.

Measurements of the electric field show that a sharp narrow peak with typical  $E/N$  a few kTd and duration of 0 – 2 ns corresponding to the front of the ionization wave is followed by a broad region where the electric field is still high,  $E/N \approx 100 - 300$  Td. Typical values of electrical current are also high, tens of A, the maximum of measured electrical current was equal to 120 A. Significant part of energy, about 90%, is delivered to plasma at  $E/N \geq 100$  Td.

It was shown that under conditions of high energy deposition and high electric fields, kinetics with participation of electronically excited species, including other electronically excited atoms/molecules or charged species as reagents, is important. Kinetic scheme containing 48 reactions and describing consistent behavior of the waveforms and the absolute values of electrical current, electric field, ratio of intensities of Ar( $2p_1$ ) and O( $3p^3P$ ) as well as the waveforms of emission of Ar( $2p_1$ ), O( $3p^3P$ ) and N<sub>2</sub>( $C^3\Pi_u$ ), has been suggested and verified for conditions of different  $\omega$  values. Calculated atomic oxygen density at  $t = 20$  ns is equal to  $[O] = 3 \cdot 10^{16}$  cm<sup>-3</sup>, that is approaches Ar density (a few percent).

It was shown that additional population of the considered Ar( $2p_1$ ) and O( $3p^3P$ ) levels in early afterglow is due to reactions of 3-body recombination of corresponding atomic ions with electron as the third body. In the discharge, a phase of active current ( $10 \text{ ns} < t < 25 \text{ ns}$ ) can be selected when oxygen atom density can be calculated in the analytical way knowing the discharge parameters ( $E/N(t)$ ,  $n_e(t)$ ), waveforms and relative intensities of [Ar( $2p_1$ )] and [O( $3p^3P$ )] emission.

---

---

# Chapter 5

---

## Study of nCD: ionization wave and afterglow

The global model in Chapter 4 reproduces the temporal evolution of species of interest in the early afterglow and provides a deep insight into the detailed kinetics. In this chapter, the study is extended by a self-consistent 2D model. Taking into account propagation of ionization waves, the hydrodynamics motion of species and the spatial-temporal redistribution of species, the 2D model is capable to calculate a wide range of experimental conditions and make predictive studies of nCD.

Additional adjustment of the experimental conditions and kinetics in Chapter 4 were implemented to adapt to the 2D nCD simulation, the details are specified in section 5.1. Investigations of nCD were split into two parts:

(i) The discharge stage. The ionization wave propagates and fill the tube with plasma at this stage. The propagation modes, the shape of the ionization waves, and the influence of discharge modes on the initial distribution of afterglow, are discussed in section 5.2

(ii) The afterglow stage. This stage is closely related to the specific energy deposition, and the temporal-spatial evolutions of species are strongly affected by the kinetics. Details are discussed in section 5.3.

## 5.1 Adjustment of experimental conditions and kinetics scheme

The 2D model studied in this chapter used the same experimental scheme as in Chapter 4. Following adjustments were done to expand the global model into higher dimensional case:

(i) The length of the capillary tube is reduced from  $L_{exp}=8$  cm to  $L_{study}=2$  cm as has been mentioned in section 3.3.3 in Chapter 3. This keeps the features of ionization waves and reduces the rather long calculation time for ionization propagations, thus allows one to focus more on the behaviour of the afterglow. Note that for shorter tubes, the rising time of applied voltage is also reduced to have voltage steady before the ionization wave touches the end. In this study a voltage of 20 kV with rising time 2 ns, plateau 6 ns and decay time 2 ns is given on HV electrode;

(ii) The radius of tube,  $R1=0.75$  mm was kept as in the previous chapter. In addition, another two tubes with radii  $R2=1.5$  mm and  $R3=3.75$  mm respectively were studied and discussed in section 5.2;

(iii) A simple circuit was incorporated to connect the LV electrode and ground through a resistor. The resistor is considered as a adjustable variable in this chapter as a way to have different specific energy deposition that is the key factors of study in section 5.3;

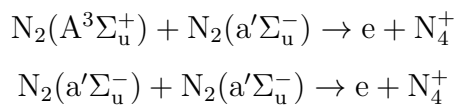
(iv) The gas mixture in the tube was replaced with synthetic air ( $N_2:O_2$ );

Corresponding to the changes of gas mixture in the capillary tube, the kinetics used in 2D nCD calculation was adjusted, three parts of the kinetic scheme can be distinguished:

(i) The kinetic scheme inherited from KIN2 scheme in Chapter 4 without reactions concerning Ar. Note that original KIN2 is a scheme validated mainly for temporal evolutions of electrons and  $N_2(C^3\Pi_u)$  and  $O(3p3P)$ ;

(ii) A kinetics of a volumetric streamer for air validated in Ref [85]. This part is important for precise description of the transport of charged species;

(iii) The reactions of associative ionization, which account for the appearance of so-called long-lived plasma in case of high specific energy deposition:



This integrated kinetics for 2D nCD model will be named KIN3 scheme in following discussions.

## 5.2 Discharge stage: propagation in different modes and tubes

The fast ionization wave propagates and fill the tube with a certain distribution of plasma during the discharge stage. The propagation and spatial distribution of electric field and electron density are the main interests at this stage. A set of numerical experiments was conducted in short capillary tubes described in the previous section. Discharges in tubes with two types of LV electrodes (grounded or floating potential) and three radii were studied numerically to have a complete image of the behaviour of ionization waves in a capillary tube.

### 5.2.1 Fast ionization wave mode and streamer mode

In a real experiment of nCD, the low-voltage (LV) electrode is connected to a long cable (a 30 m transmission line) and is not grounded. Thus the LV electrode as a metal has a floating potential, and will have conductive current flowing through that can be measured in the cable.

In a simulation by nonPDPsim code, "metal" indicates a material that has a specific potential as boundary conditions for Poisson equation, and only "metal" can be connected to the external circuit to get self-consistent voltage-current characteristics. Thus, giving experimental conditions for the LV electrode becomes a contradictory mission:

(i) If the LV electrode is defined as a dielectric (with high conductivity), it will behave like a metal with floating potential, but will not be able to be connected to an external circuit, meaning that one will lose the information of voltage-current characteristics in the simulation, and will not be able to calculate specific energy deposition which is an important factor to study nCD;

(ii) If the LV electrode is considered as a metal, it will not have the floating potential like in experiments. As a result, the discharge in the tube will not be in FIW mode but double streamers propagating in opposite directions (streamer mode).

For above reasons, two different types of LV electrodes were implemented and compared in discharge stage. One is a "metal like" dielectric that has a rather high conductivity to "simulate" metal with floating potential as close to as in experiment for FIW mode, another is a metal connecting to ground through a resistor  $R_{res}=100$  Ohm for streamer mode. The radius for cases in this section is kept as experimental one ( $R_1=0.75$  mm).

The calculated results of electron density and  $E/N$  of discharges in FIW mode

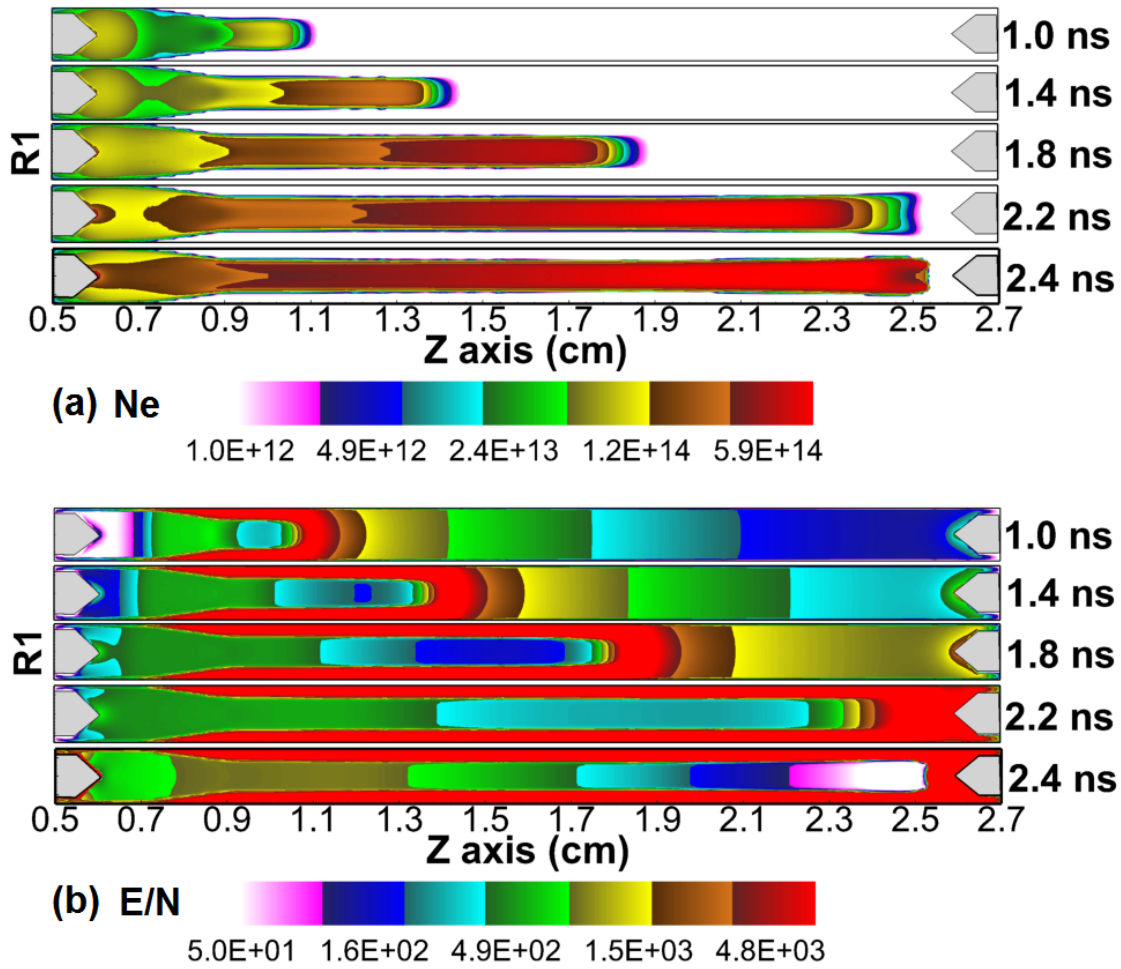


Figure 5.1: Evolution of fast ionization wave in a capillary tube. (a) electron density in unit of  $\text{m}^{-3}$ ; (b) electric field in unit of Td.

and in streamer mode are shown in Figure 5.1 and Figure 5.2, respectively.

In the FIW mode shown in Figure 5.1, the FIW is formed at HV electrode and propagates for 0.5 cm within 1 ns. In the following 1 ns the FIW velocity is accelerated from 0.7 cm/ns to 1.1 cm/ns, with density and field increasing. Once the FIW touches the end after 2.4 ns, the tube is filled with quasi-uniform plasma with high density, and quasi-uniform  $E/N$  with a relatively low value. A sheath region with low density and high  $E/N$  is formed near the dielectric wall with the thickness of about  $300 \mu\text{m}$ .

In streamer mode shown in Figure 5.2, the streamers are formed at both electrodes. The positive streamer propagates slower than that of FIW – it takes 1.6 ns for the positive streamer to propagate 0.5 cm and negative streamer 0.25 cm. Once formed, the positive streamer is accelerated to a higher velocity than FIW, reaching 1.4 cm/ns. The two streamers merge at the time moment between  $t=2.0$

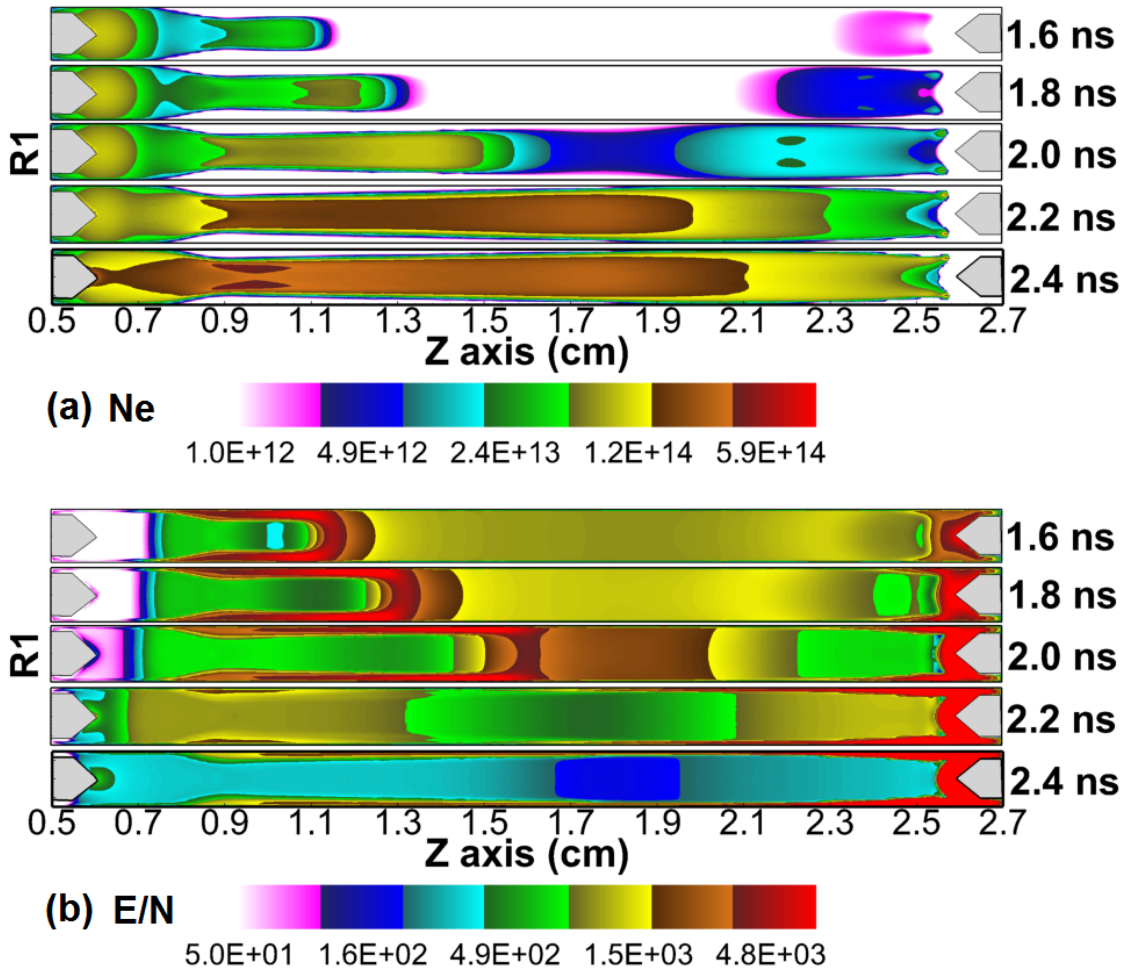


Figure 5.2: Evolution of streamers in a capillary tube. (a) electron density in unit of  $\text{m}^{-3}$ ; (b) electric field in unit of Td.

ns and  $t=2.2$  ns, leaving a quasi-uniform plasma region between HV electrode and merge position, and a density decay region from merge position to LV electrode. The thickness of the sheath region near the tube wall is as thick as in FIW mode during streamer propagation stage but decreases dramatically after all the tube is filled with plasma.

The comparison of FIW and streamer mode can be quantified in detail through axial electron density and  $E/N$  shown in Figure 5.3.

Figure 5.3 (a) and (c) are axial electron density in FIW and streamer mode, and (b) and (d) are axial fields in two modes, respectively. Significant differences are observed: (i) peak electron density and  $E/N$  in the FIW mode keeps increasing during the propagation, reaching  $N_e = 10^{15} \text{ cm}^{-3}$  and  $E/N=14000$  Td at 2.4 ns. In streamer mode, the increase of maximum electron density and  $E/N$  stops once two streamers merged. (ii)  $E/N$  in the head of FIW is 3-4 times higher than that of

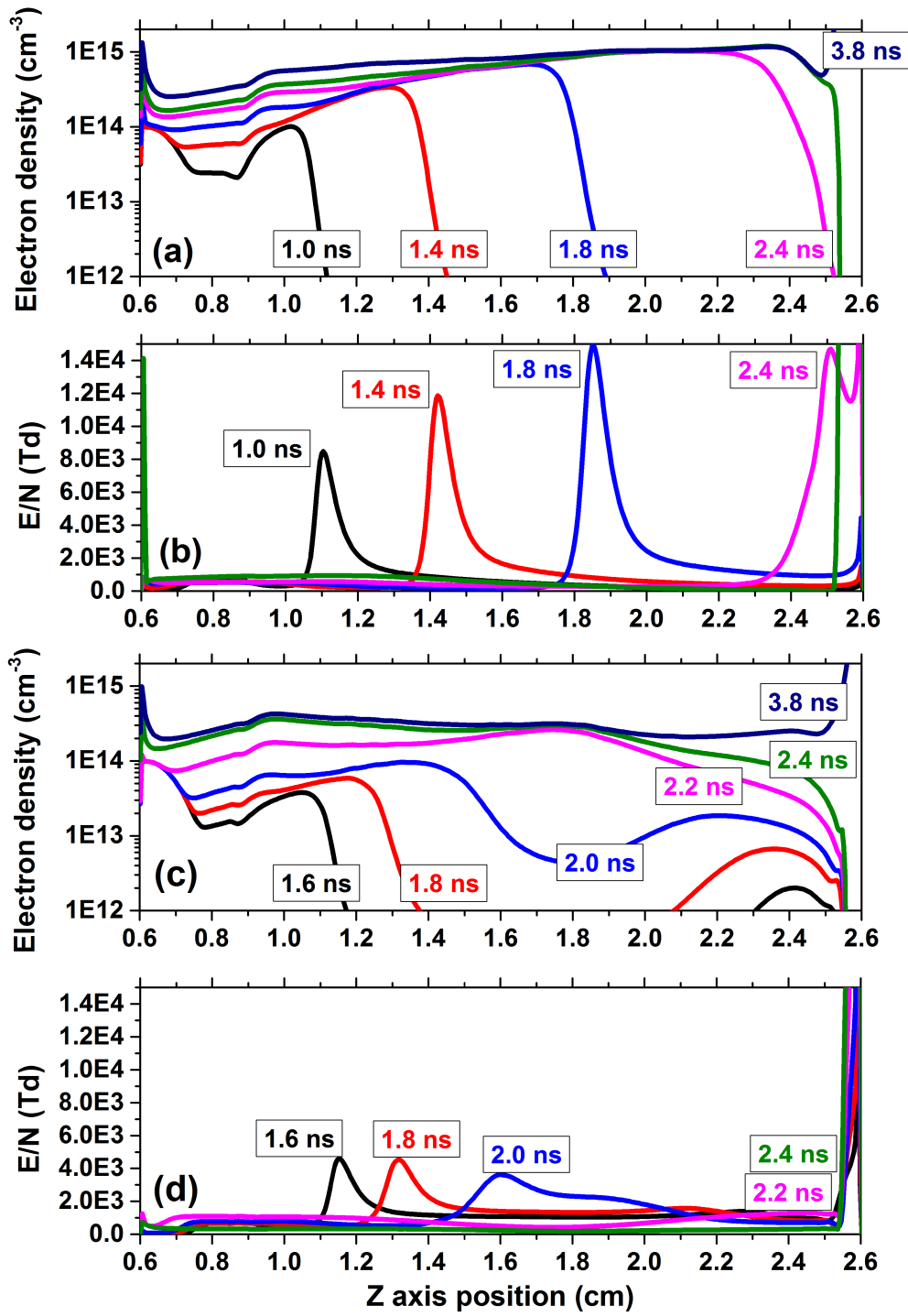


Figure 5.3: Axial distribution of electron density in (a) fast ionization wave and (c) streamers, and axial electric field in (b) fast ionization wave and (d) streamers.

streamers, electron density in the channel of FIW is also 3-4 times larger.

It has to be noted that, despite above differences during discharge propagation, there is one key similarity between FIW mode and streamer mode: in both modes,

electron density along the channel becomes almost flat after the capillary tube was filled by plasma in about 1 ns, which is confirmed by axial electron density at 3.8 ns in Figure 5.3 (a) and (c). This indicates a good uniformity of plasma in both FIW mode and streamer mode.

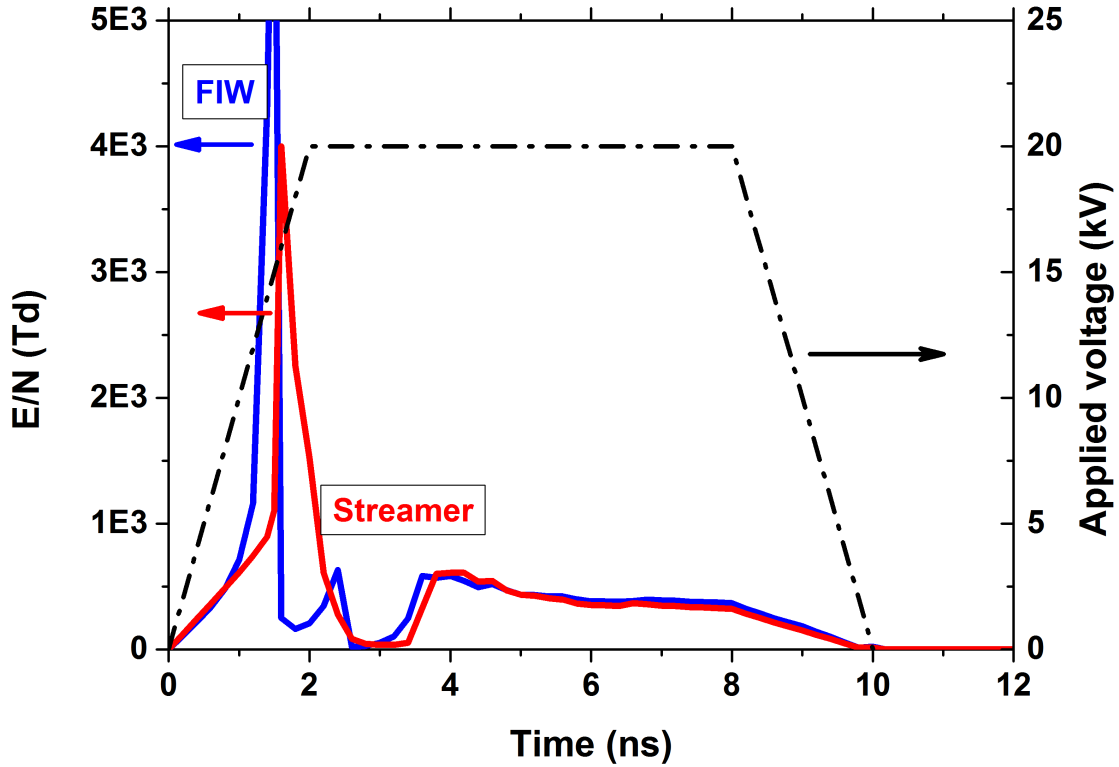


Figure 5.4: Temporal evolution of  $E/N$  at central position of the capillary tube ( $r=0$  cm,  $z= 1.5$  cm) for two modes of discharges in nCD.

The behaviour of the electric field after the ionization waves are more important for comparing FIW mode and streamer mode and describing the afterglow. By probing the calculated  $E/N$  over time at the central point of the tube ( $z=1.5$  cm,  $r=0$  cm), one can achieve Figure 5.4, in which the variations of  $E/N$  in the FIW mode and streamer mode between 0 to 12 ns are plotted together and compared directly. In FIW mode, after the rather sharp rise and drop of the field caused by the ionization front (2 ns), there is a second peak caused by the secondary electron emission neutralization of the charge when FIW approaches the end of the capillary tube. After the tube is filled by plasma (after 3 ns), the field is decided merely by the potential difference between HV electrode and LV electrode. In streamer mode the field in ionization wave head is much smaller, the secondary peak disappears, but the behaviour of field after the tube is filled, agrees well with that of FIW mode.

The similarities of plasma uniformity and electric field after the tube is filled in

both FIW mode and streamer mode, enables the flexibility of studying the kinetics and hydrodynamics of nCD based on both modes – the temporal and spatial distribution of densities will be the same in profile.

From the point of view of experiment, FIW mode is preferable as the processes of propagation is rather simple and easy to control; From the point of view of simulation, streamer mode is more preferable for following reasons: (i) there is a contradiction in calculating FIW mode and circuit properties simultaneously, as has been mentioned before. (ii) the relatively low electric field in streamer head gives higher accuracy comparing with that of FIW, the reasons are in the application range of drift-diffusion approximation discussed in 3.1.3 in Chapter 3. Thus, following numerical studies of nCD will be based only on streamer mode.

## 5.2.2 Streamers in tubes with different radius

The tube radius is an important factor affecting the plasma parameters for afterglow stage. In this section studies of streamer mode discharge in tubes with varying radius (R1=0.75 mm like in experiment, R2=1.5 mm and R3=3.75 mm additionally for simulation) were conducted.

In all three cases, ionization waves start from both electrodes, propagate in opposite directions and then merge to form quasi-neutral plasma regions. But for tubes with different radius, the detailed behaviour of ionization waves are quite different before they merge, as is shown in Figure 5.5 (a) and (b). The differences are distinctive in:

(i) Ionization wave front. When the radius of the tube increases, the radius of the ionization head  $R_s$  (can be considered as the radius of tube in capillary discharge studied in this work) also increases, as a result, charge separation in the head occurs in a larger region, leading to lower space charge density and  $E/N$ , as well as lower ionization rate. An increase of streamer propagation velocity was observed when doubling the tube radius from R1 to R2. The gain of propagation velocity can be explained according to the formulation of streamer velocity  $v_s$  proposed in Ref [169]:

$$v_s = \frac{R_s \nu_i}{\ln(n_s/n_0)} \quad (5.1)$$

where  $\nu_i$  is the ionization frequency,  $n_s$  is the electron density in the streamer and  $n_0$  the electron number density at a distance  $R_s$  from the ball-like surface of the streamer. Equation 5.1 means that streamer advancement occurs due to avalanche ionization at a distance from the tip of the order of the width of the space charge domain, streamer head radius, ionization frequency and ratio of electron density in the streamer body and at streamer tip are the three factors affecting streamer propagation velocity. In this work,  $R_s$  is controlled by the tube radius and is doubled

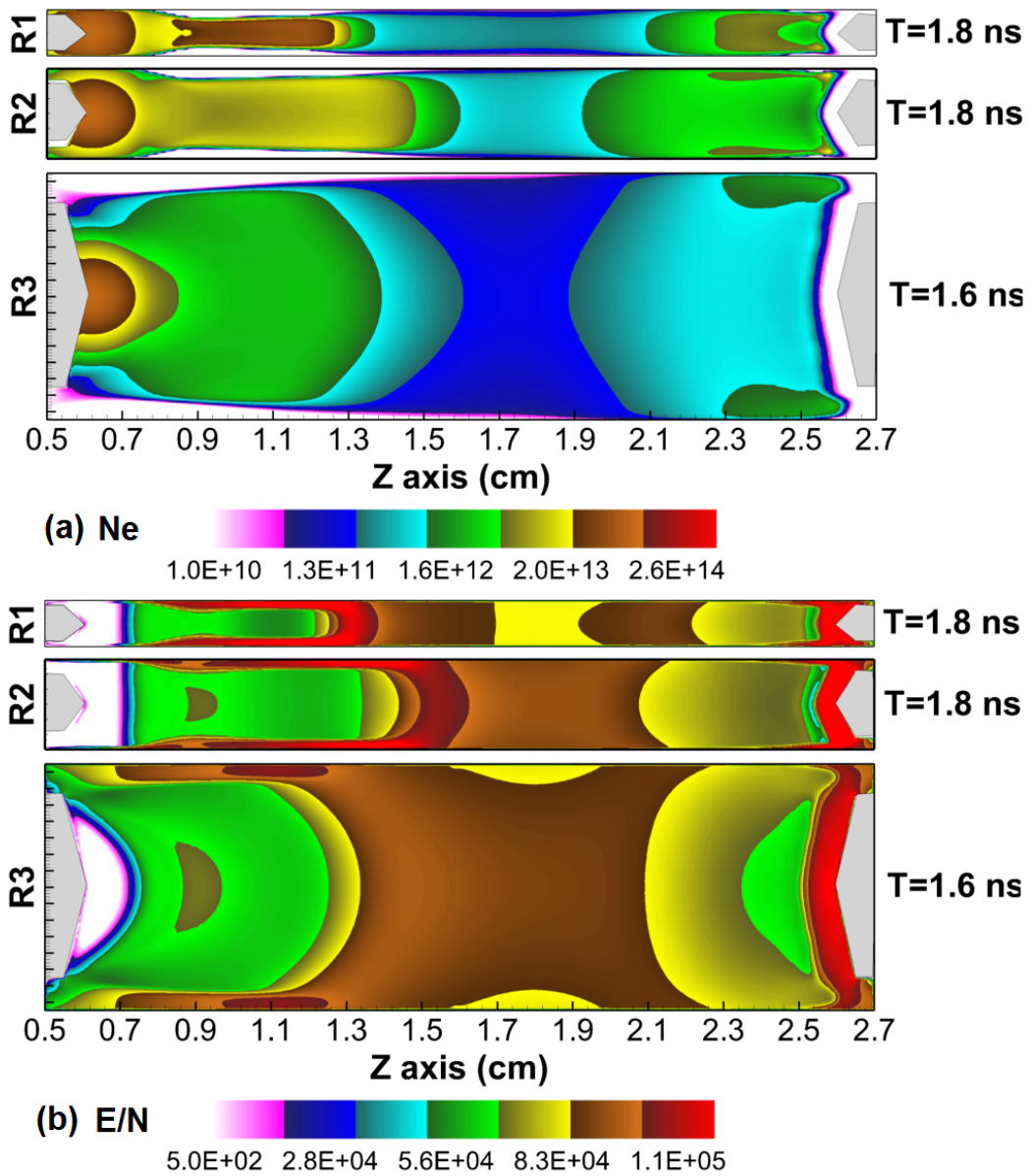


Figure 5.5: The spatial distribution of streamer parameters (a) electron density and (b) electric field in tube with different radius: R1=0.75 mm, R2=1.5 mm and R3=3.75 mm).

from R1 to R2 case.  $\nu_i$  is the function of  $E/N$ , as can be seen in Figure 5.6, the electric field in R2 case is 1.5 times R1 case. The value of  $\ln(n_s/n_0)$  decreases with the increase of tube radius (although  $n_s/n_0$  are in the same magnitude). The combination of above changes gives a 1.1 to 1.3 times gain in streamer propagation velocity when double the tube radius.

(ii) Ionization wave channel. With the increase of tube radius, the electron density in the plasma channels after ionization waves decreases. An obvious difference

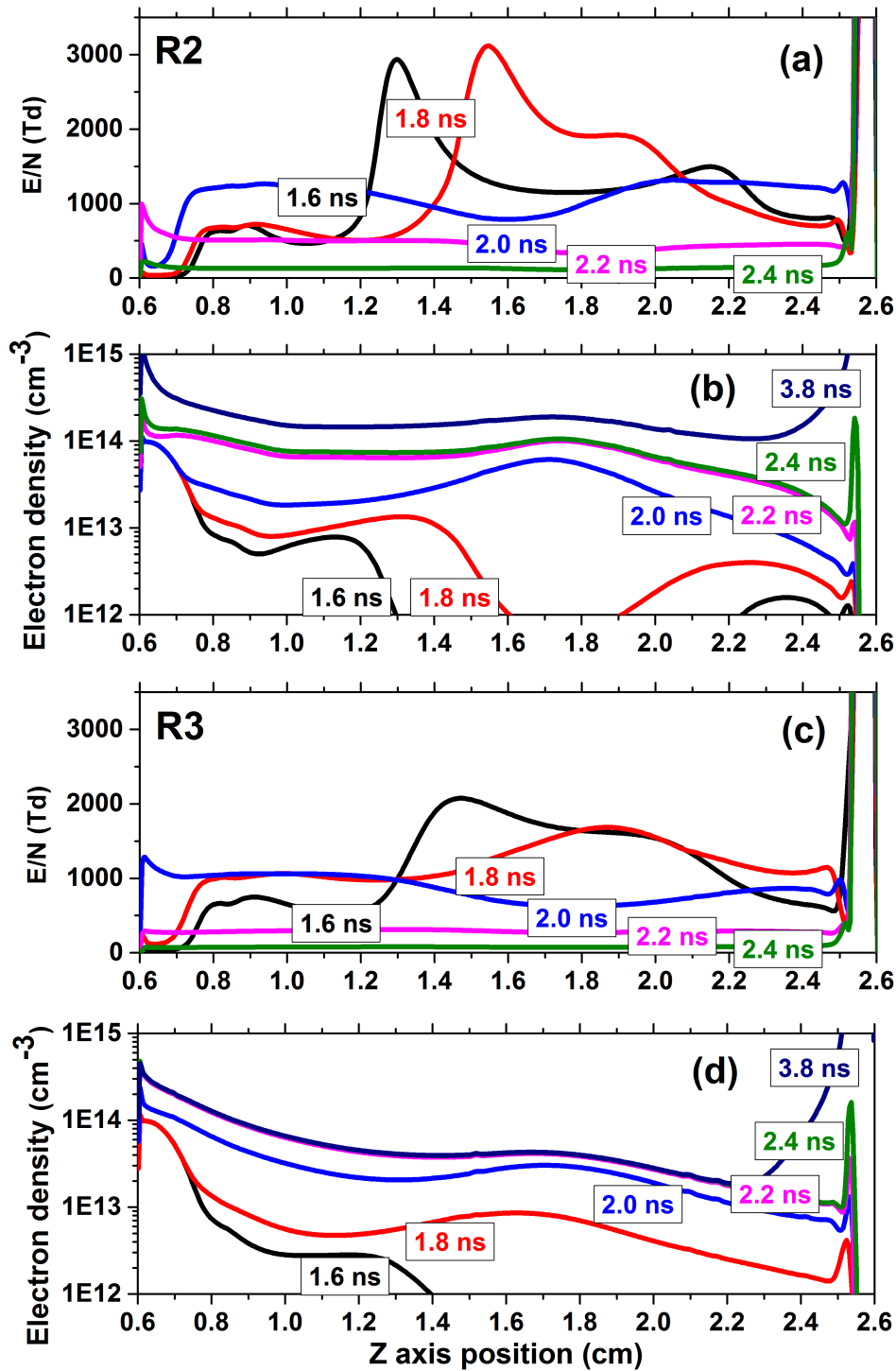


Figure 5.6: Axial distribution of electric fields in tube with radius of (a) R2 and (c) R3, and axial electron density in tubes with radius of (b) R2 and (d) R3.

is the change of the ionization wave shape. In the experimental setup  $R_1=0.75$  mm, the electron density is concentrated near the centre axis with relatively high  $E/N$  in the head. When tube radius is doubled,  $R_2=1.5$  mm, the electron density is more

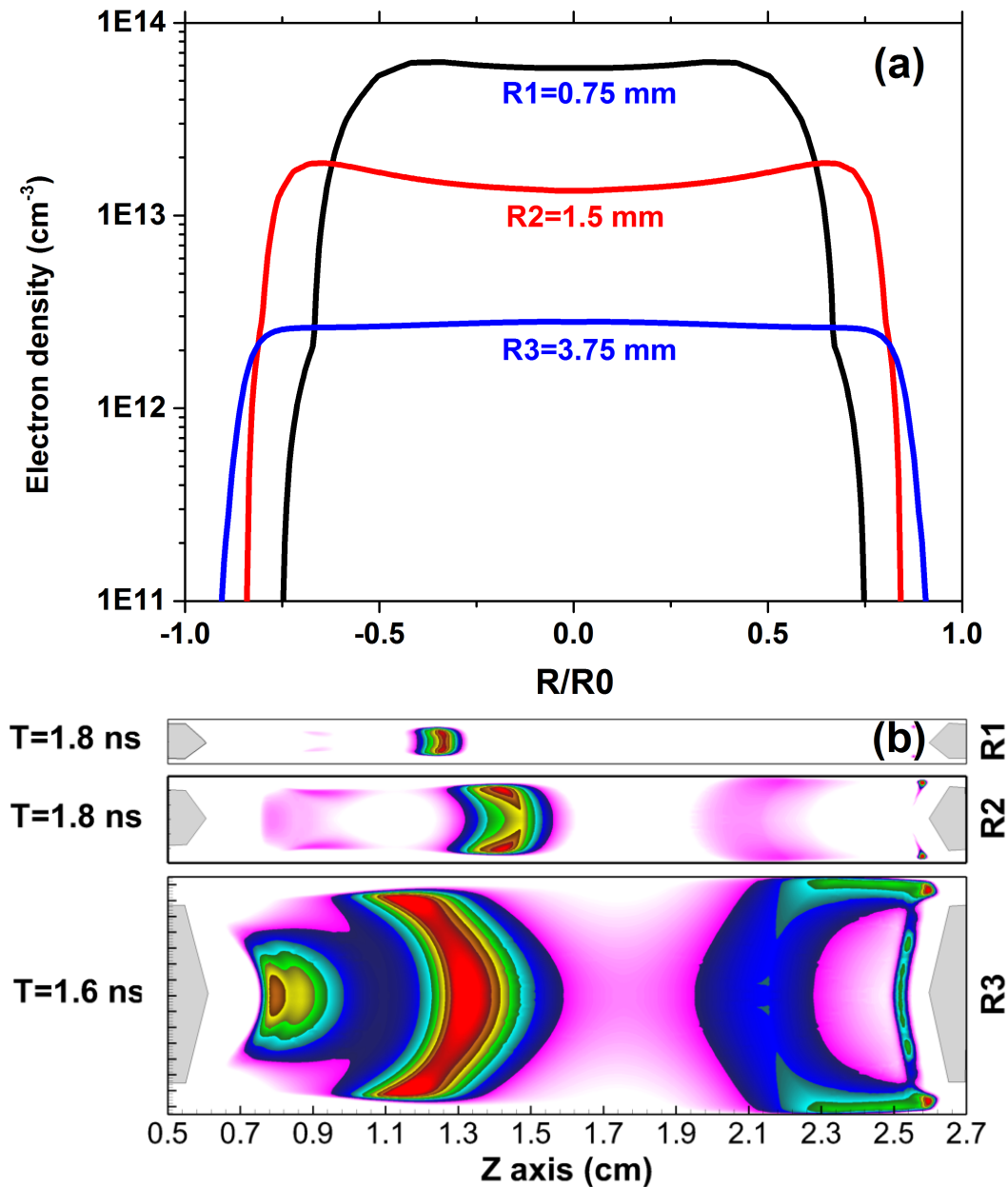


Figure 5.7: (a) The radial distributions of electron density when the streamer channels form in tubes with different radius (normalized) at  $z=1.5$  mm, at time instants  $t=1.8$  ns, 1.8 ns and 1.6 ns, respectively; (b) Electron impact source in the ionization head in tubes with different radius.

concentrated near the tube wall with lower  $E/N$  in the ionization head, leaving a hollow region in the channel. If one conducts experiments in a larger tube  $R_3=3.75$  mm, a bulk plasma is formed, the enhancement of electron density near the wall is no longer announced, and the  $E/N$  in the head is the weakest among all the cases.

This difference is quantified in Figure 5.7 (a) in which the radial distributions of electron density in the streamer channel are plotted together in normalized radius with corresponding electron impact source term plotted in Figure 5.7 (b). One can clearly see that (i) plasma occupies the largest region of tube in R3 case, with electron density distributed uniformly. Electron source is high in both in the centre and near the wall; (ii) with reduced tube radius R2, a sheath region grows in size, and higher electron density appears near the tube wall. The intensive electron source in the centre disappears; (iii) further decrease of radius leads to the "merge" of the two density peaks, forming a uniformly distributed plasma channel located in the centre of the tube. In this case, the near-wall electron source are also merged.

This section focuses on the discharge propagation stage of nCD. The influence of LV electrode potential and tube radius to the propagation of ionization waves were quantified. The similarities between streamer mode and FIW mode after the ionization propagation stage were emphasized. Suggested approach gives a possibility of studying afterglow of nCD based on simulation results of the streamer mode even though experimentally the afterglow is initialized by the FIW mode.

### 5.3 Afterglow stage: energy deposition and evolution of species

The 2D study of afterglow of nCD focus mainly on the behaviour of species of interest (electrons and  $N_2(C^3\Pi_u)$ ) with respect to deposited energy. Different values of specific energy deposition were achieved by adjusting the resistance in the external circuit. Temporal-spatial behaviour of electrons and  $N_2(C^3\Pi_u)$  are discussed under different specific energies.

#### 5.3.1 Electrical characteristics and specific energy deposition

Once the ionization wave reach the end of LV electrode, or two streamers merge, the tube becomes a conductive channel with electrical current flowing through. This current is coupled to the external circuit, changing the potential of LV electrode. This prevents the calculated plasma in the tube from transitioning into an arc, and triggers the process of energy deposition. By adjusting the resistance in the circuit module from 20  $\Omega$  to 12700  $\Omega$ , a set of voltage-current characteristics and different magnitudes of energy deposition and  $E/N$  values were achieved.

Figure 5.8 shows the U-I characteristics calculated with different resistance in the circuit. Current started to grow at 4 ns for each case, leading to a drop of gap voltage (here "voltage" means the potential drop from HV electrode to LV electrode). At

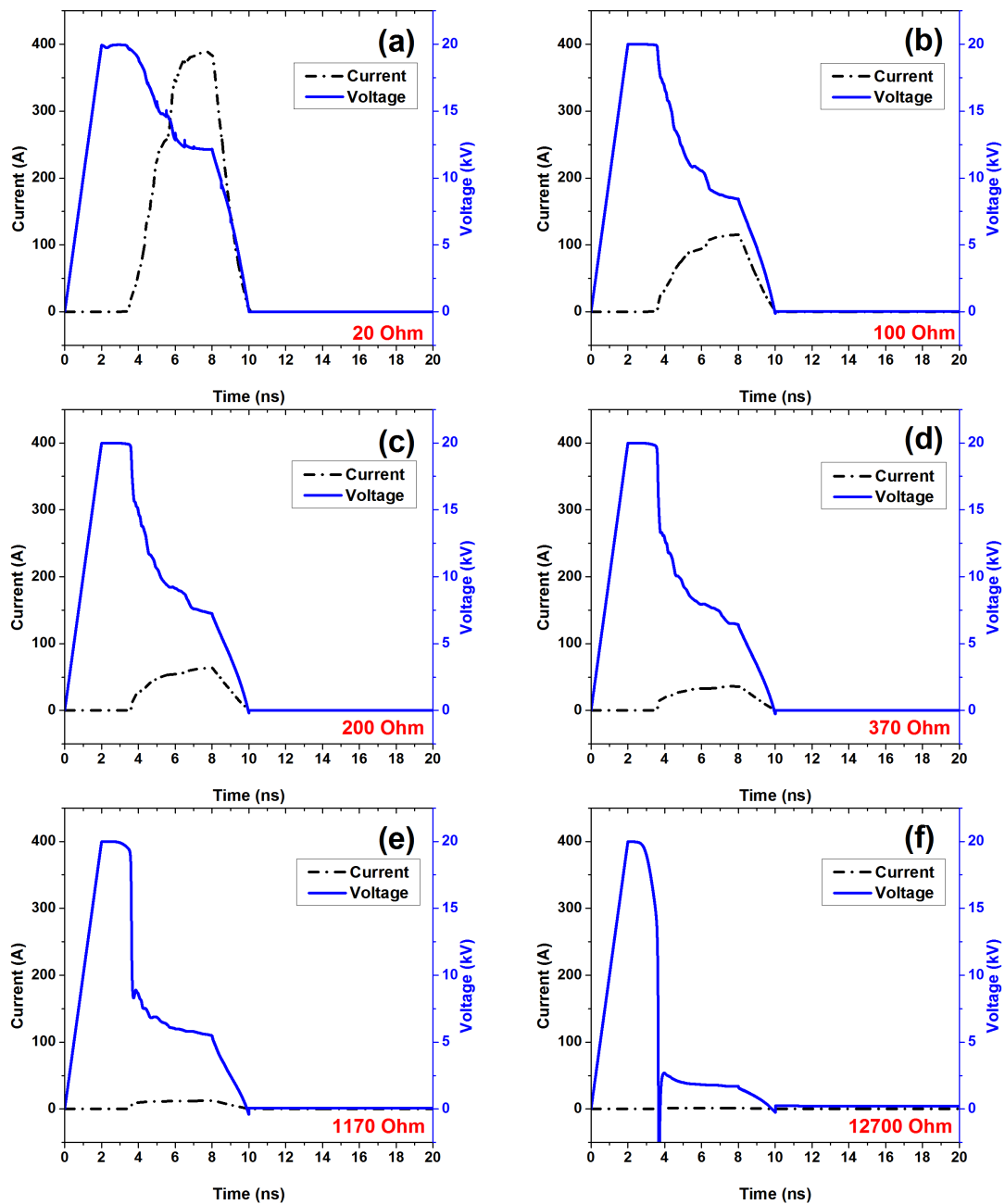


Figure 5.8: Calculated U-I characteristics of discharges in short capillary tubes with varying resistance in the external circuit.

10 ns both current and voltage dropped to zero. The increase of resistance leads to a significant drop of maximum current value. When the resistance reaches as high as  $12.7 \text{ k}\Omega$ , the current caused by the charge flux flowing from tube into the external circuit is strongly suppressed, and lead to a transient reverse of the polarity, as can be seen in Figure 5.8 (f).

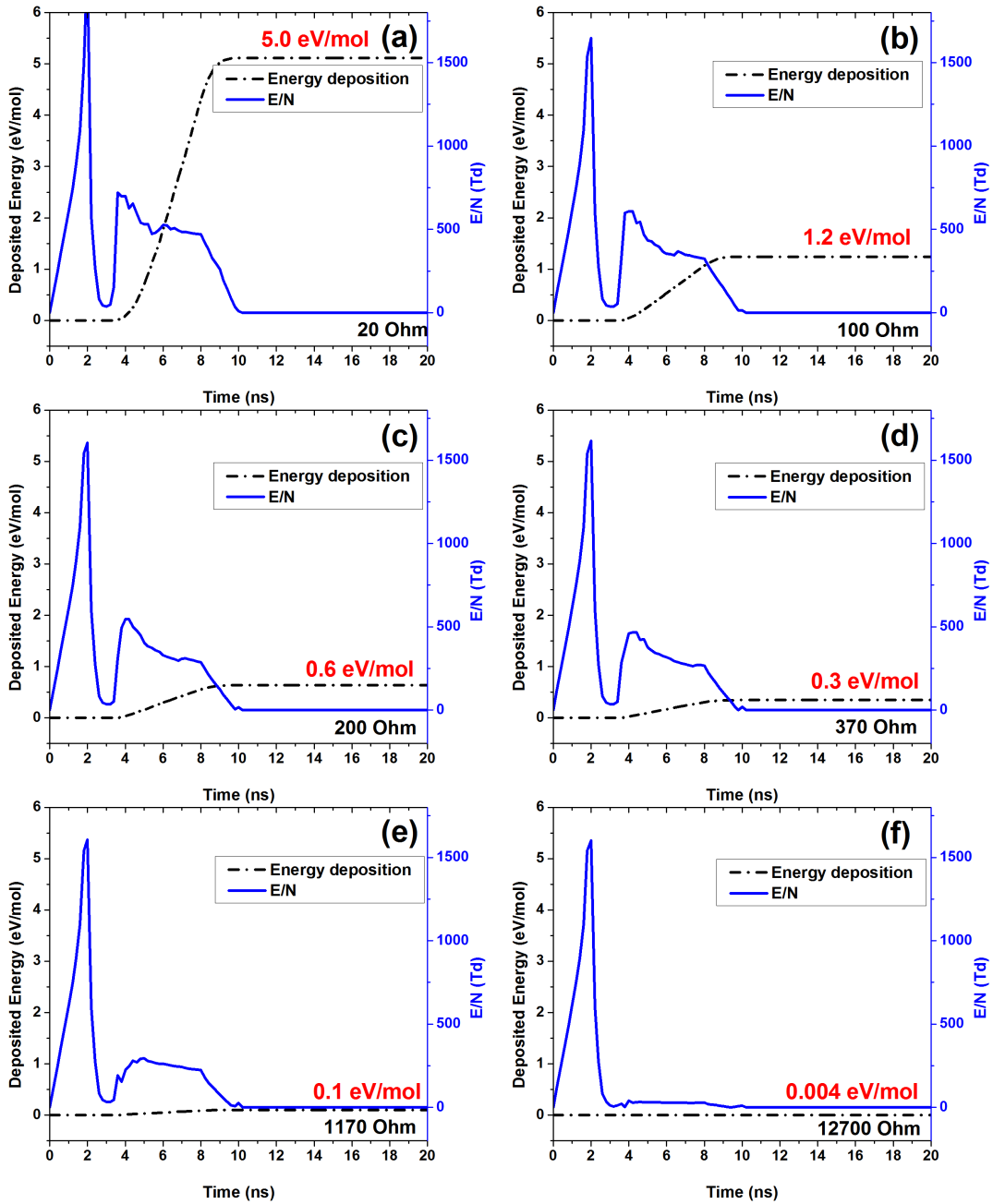


Figure 5.9: Calculated reduced electric field and deposited energy in short capillary tubes with varying resistance in the external circuit.

$E/N$  and specific energy deposition  $W_{dep}$  are the key factors that relate 2D nCD model with 0D global model discussed in Chapter 4. In this 2D self-consistent model,  $E/N$  is obtained by probing the variation of  $E/N$  in the central position of the tube throughout the calculation, and  $W_{dep}$  is calculated through U-I characteristics given in Figure 5.8. In Figure 5.9  $E/N$  and  $W_{dep}$  for each case was plotted together. In

this study, a set of resistance was tested among which 6 cases were chosen to have  $E/N$  ranging from 600 Td to 50 Td, and  $W_{dep}$  from 5.0 eV/mol to 0.004 eV/mol. These calculated  $E/N$  help to analyse the kinetics and would become input of 0D global model in the future, while  $W_{dep}$  can be used to judge about the condition of discharge and to analyse the kinetics in the afterglow in following sections.

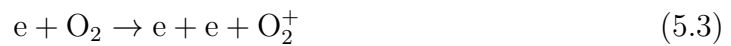
### 5.3.2 Long-lived plasma and de-excitation of excited species

Both 0D calculation and experiments have found that, in case of high  $W_{dep}$  (i) electron density reaches the maximum during the discharge, but only slightly decays in the afterglow in case of high energy deposition, this slow decay processes indicates the existence of long-lived plasma; (ii)  $N_2(C^3\Pi_u)$  density, after reaching the maximum, decays much faster than the classical predicted value.

Previous calculations and experiments for studying long-lived plasma and depopulation of excited species were mostly based on global kinetics model or fixed experimental setups. In this work the 2D self-consistent model enables the possibility of studying electron and  $N_2(C^3\Pi_u)$  density as the “marker” of kinetics, with respect to varying  $W_{dep}$ .

The absolute density of electrons is plotted in Figure 5.10 (a) together with normalized density in Figure 5.10 (b).

At  $t < 10$  ns, before afterglow period, electrons are mainly produced by ionizations:



and consumed by three body attachment, dissociative attachment and recombinations (mainly with  $O_2^+$ ) [14]:



Once  $E/N$  approaches to zero, the electrons start to decay. A quick decay process was observed in the first 50 ns for cases with  $W_{dep} > 0.1$  eV/mol, in this stage the decay rate increases with  $W_{dep}$ . This fast decay is mainly due to high electron density produced by high  $E/N$  during discharges and quick process of three body attachment at low  $E/N$  condition in the early afterglow. Starting from  $t = 50$  ns, the density of electrons decays in a much slower rate. The decay for cases with higher  $W_{dep}$  is fast in early afterglow stage, becomes even slower. In this stage, associative ionization become an important electron source:

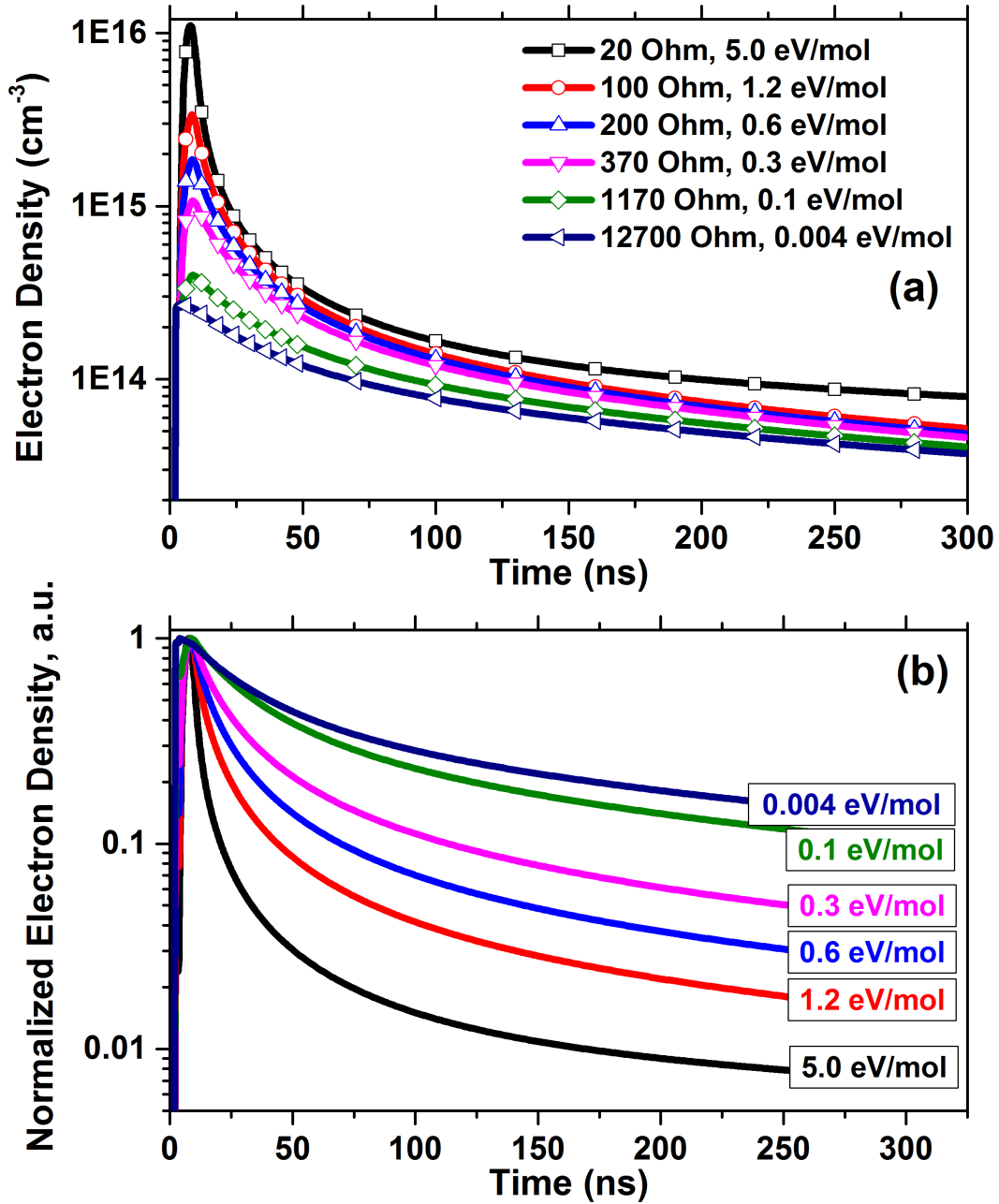
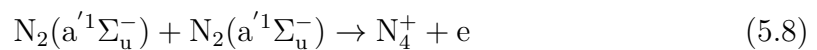
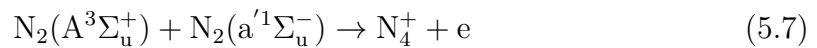


Figure 5.10: The temporal evolution of (a) absolute electron density and (b) normalized electron density during and after discharge under different specific energy deposition.



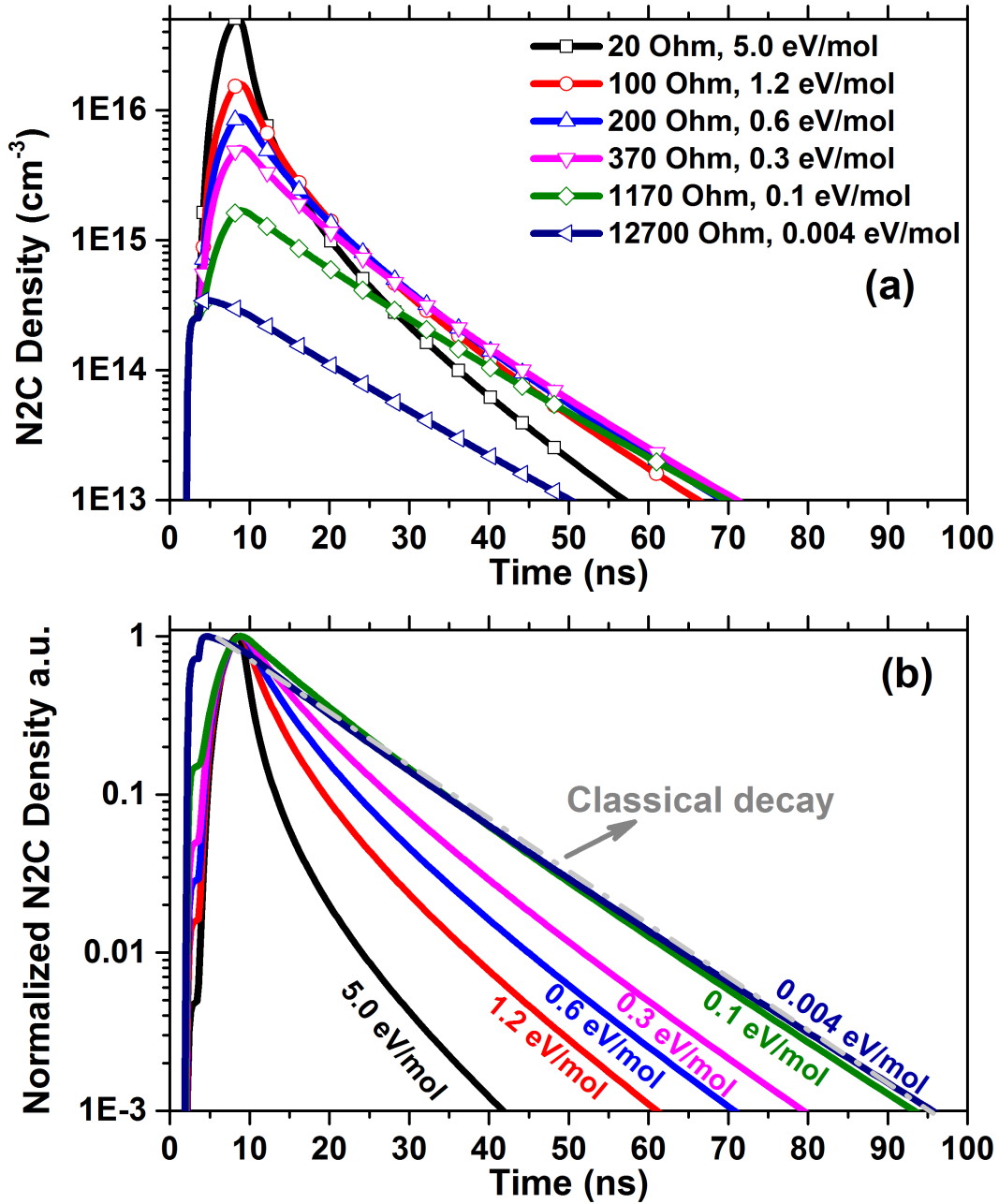


Figure 5.11: The temporal evolution of (a) absolute  $N_2(C^3\Pi_u)$  density and (b) normalized  $N_2(C^3\Pi_u)$  density during and after discharge under different specific energy deposition.

The density of  $N_2(A^3\Sigma_u^+)$  and  $N_2(a^1\Sigma_u^-)$  are much higher in high  $W_{dep}$  cases, leading to higher associative ionization rates, thus lower electron density decay rates especially for case  $W_{dep}=5.0$  eV/mol shown in Figure 5.10.

The mechanism of production and loss of  $N_2(C^3\Pi_u)$  have already been discussed

in Chapter 4. The role of electron quenching process was announced in the actinometry experiment conducted under condition  $W_{dep} \approx 1.0$  eV/mol.

In Figure 5.11, the kinetic curves for  $N_2(C^3\Pi_u)$  density under different magnitudes of  $W_{dep}$  are plotted together in absolute values and normalized values, respectively. The role of electron quenching can be clearly seen by comparing absolute density of  $N_2(C^3\Pi_u)$ . In conditions of higher  $W_{dep}$ , despite high  $N_2(C^3\Pi_u)$  production rate during discharge process, the density  $N_2(C^3\Pi_u)$  decays much faster in the afterglow and soon becomes lower than cases with smaller  $W_{dep}$  within 100 ns.

The direct comparison of normalized  $N_2(C^3\Pi_u)$  density shows the transition: starting from  $W_{dep}=0.1$  eV/mol, the decay rate of  $N_2(C^3\Pi_u)$  in the afterglow deviates from the exponential curve calculated analytically by classical approximation based on radiative decay and quenching of  $N_2(C^3\Pi_u)$  by neutral molecules.

In other words, kinetics of electrons and  $N_2(C^3\Pi_u)$  in the afterglow of nCD is strongly connected to specific energy deposition  $W_{dep}$ : classical kinetics with excitation by electron impact and quenching by neutral molecules is valid at  $W_{dep} \leq 0.1$  eV/mol, with the increase of  $W_{dep}$ , the decay rate of electrons decreases while for  $N_2(C^3\Pi_u)$  the decay rate increases significantly.

### 5.3.3 Temporal-Spatial evolution of species

After the tube is filled with plasma, the loss mechanisms of electrons and  $N_2(C^3\Pi_u)$  lead to the redistribution of species in the afterglow. This redistribution of species are mainly caused by kinetics and can be observed by analysing the radial distribution of species in the centre cross section ( $z=1.5$  cm) of the tube.

A direct comparison of radial distribution of species under different  $W_{dep}$  is shown in Figure 5.12 (a) for electrons and (b) for  $N_2(C^3\Pi_u)$  at  $t=50$  ns in absolute density. The radial electron density grows in accordance with the increase of  $W_{dep}$  within the range of one magnitude, and reaches  $3.5 \times 10^{14}$  cm<sup>-3</sup> at  $W_{dep}=5.0$  eV/mol. The radius of channel also increases. Although density of  $N_2(C^3\Pi_u)$  also varies within one magnitude, its radial profiles are rather different comparing with those of electrons. The profile of  $N_2(C^3\Pi_u)$  copies that of electrons with  $W_{dep}=0.004$  eV/mol, 0.1 eV/mol and 0.3 eV/mol, and reaches the maximum density of  $6.0 \times 10^{13}$  cm<sup>-3</sup> at  $W_{dep}=0.3$  eV/mol. Further increase of  $W_{dep}$  leads to a change of the profiles starting from  $W_{dep} \geq 0.6$  eV/mol: (i) the density decreases along the entire radial direction; (ii) the drop of density is more significant in the central region, resulting in peak density position located on the edge of the channel. Both (i) and (ii) are caused by electrons: the growth of density accelerates the decay of  $N_2(C^3\Pi_u)$ , while profiles of electron density make decay of  $N_2(C^3\Pi_u)$  faster in the centre region and slower on the edge.

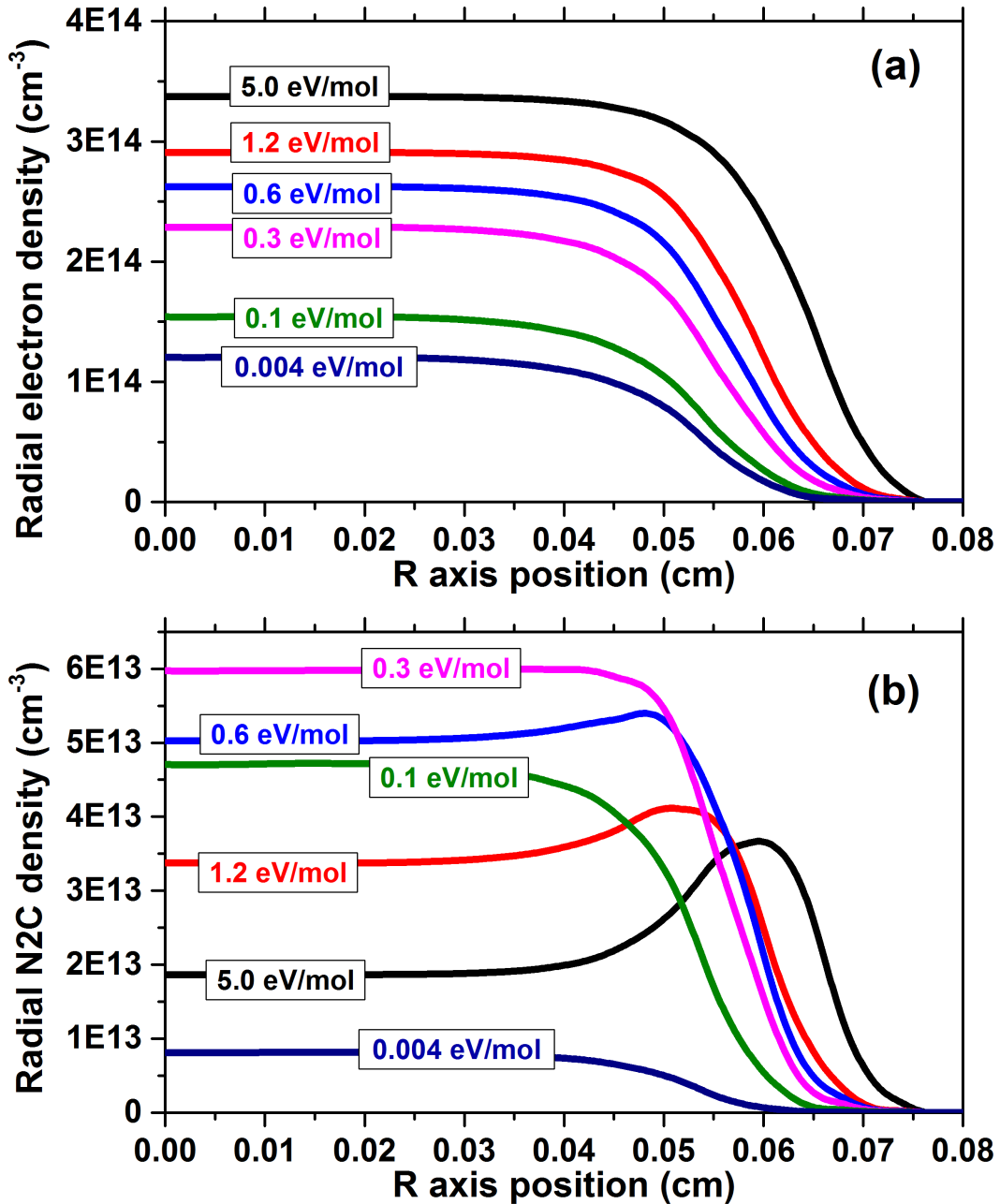


Figure 5.12: The radial distribution of (a) absolute electron density and (b) absolute  $N_2(C^3\Pi_u)$  density at  $Z= 1.5$  cm position,  $t= 50$  ns.

Detailed temporal-spatial evolution of radial electrons and  $N_2(C^3\Pi_u)$  under three typical  $W_{dep}$  are plotted in Figure 5.13, in which the transition of density distribution from classical profile to the profile under high  $W_{dep}$  is demonstrated.

Figures 5.13 (a),(c) and (e) show the evolution of electron density. The density profiles are almost the same for each case before afterglow. In the afterglow, the

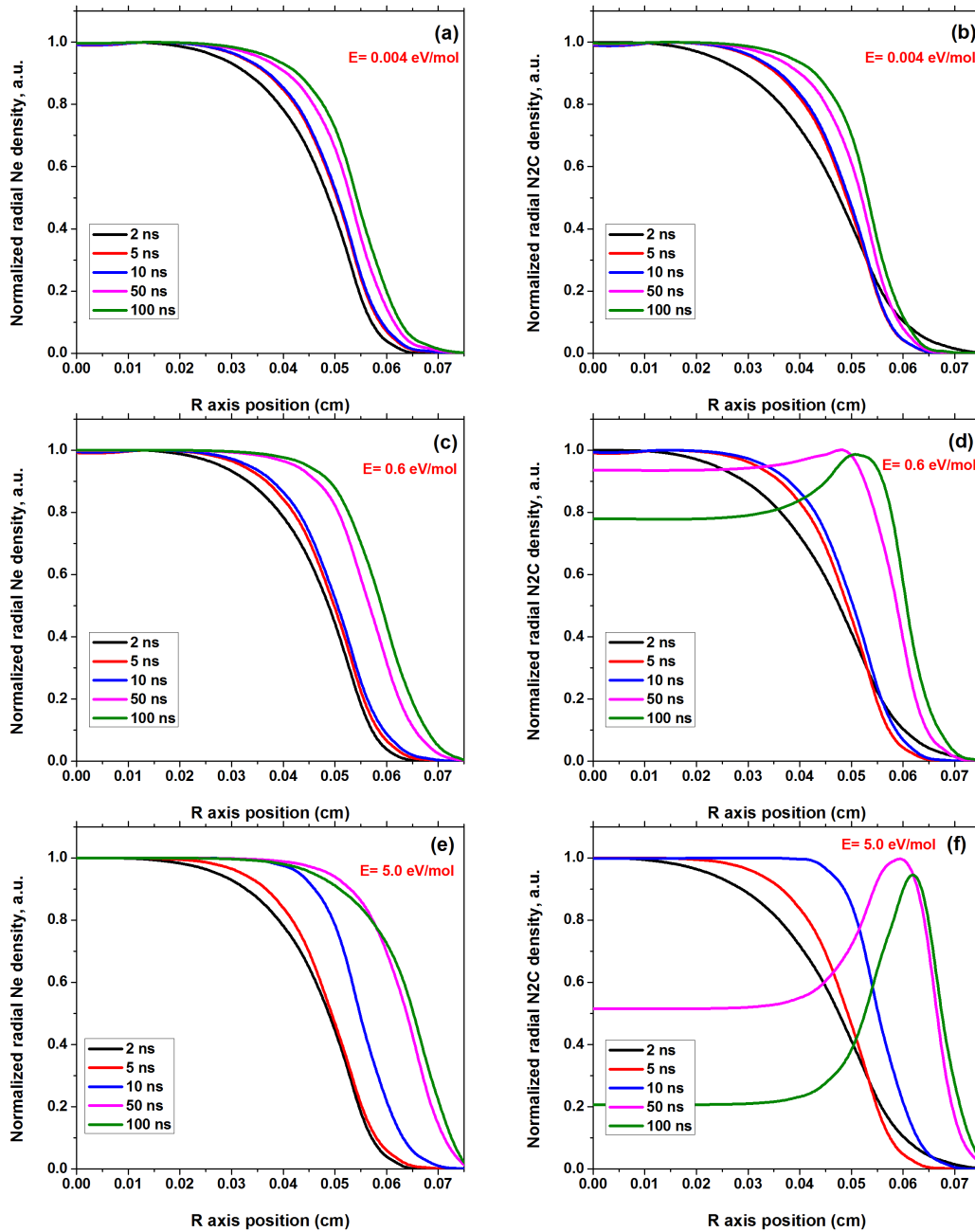


Figure 5.13: The evolution of radial distribution of absolute electron density (left) and absolute  $N_2(C^3\Pi_u)$  density (right) at  $Z=1.5$  cm position at discrete time moment under different specific energy deposition.

shape of profiles keeps the same, with a "plateau" near the centre and a sharp drop on the edge. The channel width increases with the increase of  $W_{dep}$  in the afterglow. The possible reasons for the growth of the channel width in the model is the increased diffusion of electrons on the edge, and the increased rates of associative

ionizations under higher  $W_{dep}$ .

Figures 5.13 (b),(d) and (f) show the evolution of  $N_2(C^3\Pi_u)$  density profiles. At low  $W_{dep}$  in (a), the profile copies that of electrons, the distribution of  $N_2(C^3\Pi_u)$  emission in experiment can be considered as the distribution of electrons. With the increase of  $W_{dep}$ ,  $N_2(C^3\Pi_u)$  is strongly quenched in the region of the plateau where the electron density is maximal. Further increase of  $W_{dep}$  makes the quenching stronger, leading to an obvious hollow region in the centre plateau. Experimentally this distribution indicates another emission profile, which may give an impression that discharge were attached to the tube walls.

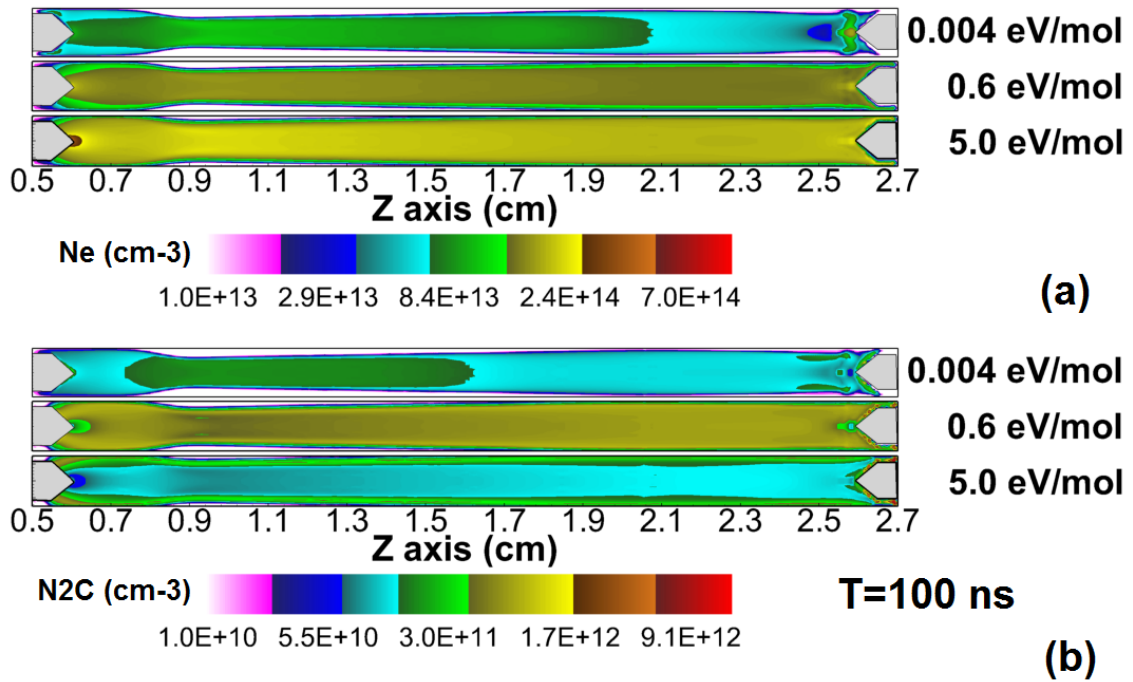


Figure 5.14: 2D distribution of electrons and  $N_2(C^3\Pi_u)$  at  $t=100$  ns under different specific energy deposition.

To have a direct comparison of the profiles in the entire tube for the cases discussed in Figure 5.13, the 2D distribution of electrons and  $N_2(C^3\Pi_u)$  at  $t=100$  ns are plotted in Figure 5.14. The following features of nCD in the afterglow are confirmed again in a 2D scale: (i) the electron density grows with the increase of  $W_{dep}$ ; (ii) the  $N_2(C^3\Pi_u)$  density grows if  $W_{dep} \leq 0.6$  eV/mol and drops at higher  $W_{dep}$ ; (iii) the radii of electron and  $N_2(C^3\Pi_u)$  channels grow with increase of  $W_{dep}$ ; (iv) the radial profiles of electrons remain the same, while radial distribution of  $N_2(C^3\Pi_u)$  density changes, with higher  $N_2(C^3\Pi_u)$  density located closer to the tube wall.

## 5.4 Conclusion

Based on the simplified KIN3 kinetics, a 2D self-consistent model was used to study, analyse and predict the features of discharge and afterglow stage of nCD under different specific energy deposition.

Propagation of ionization wave and filling of the discharge tube with plasma have been modelled. Two modes of propagation were identified, depending on whether or not the LV electrode is grounded: fast ionization wave (FIW) mode and streamer mode. In streamer mode, two ionization waves appears and propagate in opposite directions, while in FIW mode, there is only one ionization wave propagating from HV electrode to LV electrode with much higher  $E/N$  in the head and higher electron density in the channel. Despite the differences in propagation, a good uniformity of electrons can be achieved in both propagation modes.

Three shapes of ionization waves were found when tube radius was changed. At large tube radii  $R3=3.75$  mm (5 times the experimental one), a bulk plasma was formed, with electrons almost uniformly distributed in the radial direction. With reduced tube radius  $R2=1.5$  mm (2 times the experimental one) higher electron density was observed near the tube wall, leaving a hollow region in the centre. Further reduce the radius to experimental one, the two density peaks of electron merge, stronger electron density and higher electric field were observed. The propagation velocity increases with tube radius.

Based on plasma distribution initialized by streamer mode, The afterglow stage is also modelled to study the kinetics and redistribution of species with respect to specific energy deposition  $W_{dep}$ .

The decay rate of electrons increases with  $W_{dep}$  in the early afterglow due to higher electron density produced in discharge stage and strong three body attachments and recombinations. But in afterglow  $t \geq 50$  ns the decay slows down due to associative ionization. The increase of  $W_{dep}$  leads more excited species for associative ionizations. This long-lived plasma phenomenon makes the radial profile of electrons in the tube cross sections keeps almost the same during the 300 ns period studied in this work.

The decay rate of  $N_2(C^3\Pi_u)$  increases in case of high  $W_{dep}$ . Starting from  $W_{dep}=0.3$  eV/mol,  $N_2(C^3\Pi_u)$  can no longer be described by “classical” kinetics scheme due to the fast electron quenching process. The relative high electron density and strong electron quenching process lead to redistribution of radial  $N_2(C^3\Pi_u)$  profiles in the afterglow.  $N_2(C^3\Pi_u)$  density increases with specific energy deposition if  $W_{dep} \leq 0.3$  eV/mol and decreases if  $W_{dep} \geq 0.6$  eV/mol. Under high  $W_{dep}$  the loss of  $N_2(C^3\Pi_u)$  near axis makes the distribution of  $N_2(C^3\Pi_u)$  change, resulting higher  $N_2(C^3\Pi_u)$  density near the tube wall where electron density drops.

---

---

## Chapter 6

---

### Study of nSDBD: discharge, fast gas heating and fluid responses

Different from nCD as a tool focusing on plasma kinetics, nSDBD is designed mainly for applications in communities of aerodynamics and combustion. As a result, nSDBD is mainly operated at (different) high pressures. The production of active species, energy release for fast gas heating and the fluid responses are of great interest. The changes of discharge characteristics under different pressures are also significant and remain to be studied.

In this chapter, the specific 2D code PASSKEY, which have been validated in [2](#), is used to achieve maximum flexibility and to study the physics of nSDBD. The calculated results are accompanied with latest experiments conducted under the same condition for validity and direct comparison. The experimental setup have been specified in [Chapter 2](#), measurement techniques are briefly described in [section 6.1](#). The features of nSDBD are studied in 3 aspects for both negative and positive polarities:

(i) Discharge characteristics of atmospheric nSDBD: the dynamics of surface streamer and electric current ([section 6.3](#), simulation and experiment), electron density and electric field ([section 6.4](#), simulation), and time-resolved emission ([section 6.5](#), simulation and experiment);

(ii) Hydrodynamics characteristics of atmospheric nSDBD: energy distribution and fast gas heating, fluid responses including pressure perturbations and temperature evolution ([section 6.6](#), simulation and experiment).

(iii) Parametric studies of discharge characteristics: the influence of dielectric

permittivity, pressures (section 6.7, simulation) and ambient pressure (section 6.8, simulation) to the discharge characteristics are predicted and discussed.

## 6.1 Experimental techniques of measurement

Figure 6.1 b presents a general scheme of the experimental setup. The electrode system was connected to the 30 m long coaxial cable. The high-voltage pulses of positive or negative polarity (20 ns duration at FWHM, 2 ns rise time and 10–30 kV amplitude) were transmitted from the high voltage generator (commercial FID Technology pulser, FPG20–03PM/NM) to the electrodes with a frequency 2 Hz or lower. Back current shunt BCS#1 installed with the electrode was used to synchronize the opening of the ICCD camera with the high voltage profile. Calibrated back current shunt BCS#2 in the middle of the cable was used to measure the voltage on the high voltage electrode, the electric current and the deposited energy. Electrical signals were registered by LeCroy WaveRunner 600 MHz oscilloscope. ICCD images of the discharges were taken with the help of Pi-Max4 Princeton Instruments ICCD camera with Edmund Optics 50 mm focus length objective.

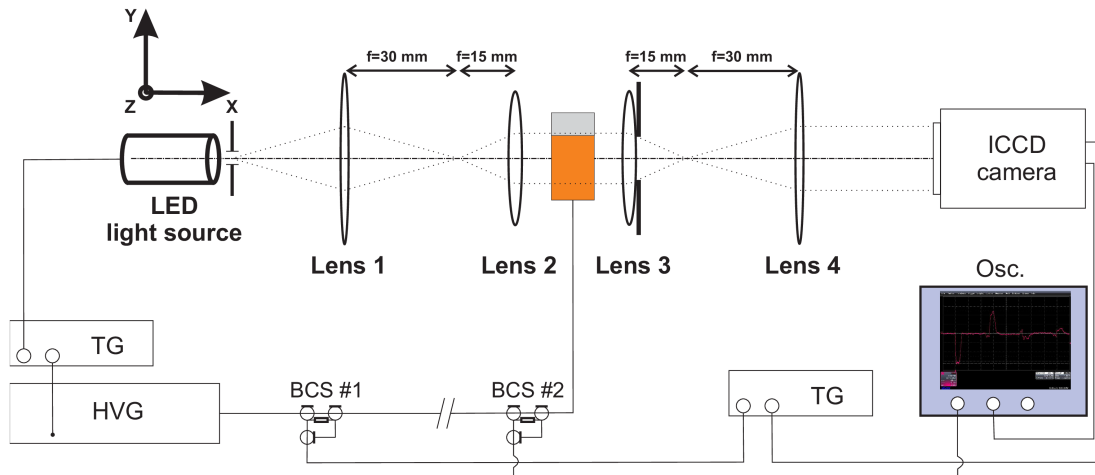


Figure 6.1: General scheme of the experiment. TG is a triggering generator, HVG is a high voltage generator, BCS is a back current shunt.

Measurements by back current shunts are based on the fact that voltage between the central wire and grounded shield is related to the electric current in the cable as  $U = IZ$ , where  $Z$  is the cable impedance. The velocity of the propagation of electromagnetic signal in the cable is limited,  $v_c = c/\sqrt{\epsilon\mu}$ , where  $c$  is the velocity of light in free space,  $\epsilon$  and  $\mu$  the dielectric permittivity and magnetic permeability of the media, respectively. Pulse coming from the high voltage generator (the incident

pulse,  $U_{inc}$ ) and pulse reflected from the discharge cell (the reflected pulse,  $U_{refl}$ ) are separated in time at the point where the back current shunt is situated. The value of the voltage on the electrode is equal to  $U(t) = U_{inc}(t) + U_{refl}(t)$  at the conditions of DBDs, where the impedance of the load is much higher than the impedance of the cable,  $U \approx 2U_{inc}$ . The waveform of the voltage on the high voltage electrode is given in Figure 6.1. In more details, the technique of the back current shunts can be found elsewhere [40, 128].

To study microstructure of the discharge, shadowgraphy images and optical emission images were obtained using the optical system where a system of quartz lenses presented in Figure 6.1 c was used instead of the objective of the ICCD. The Thorlabs green LED M505L3-C with 505 nm central wavelength and 30 nm bandwidth was used as a light source. To increase the intensity of the background light, the LED was powered by a custom-made pulsed source, the pulse duration being 15  $\mu$ s. A symmetric system of lenses provided a uniform light beam from the LED and 2 $\times$ magnified image of the discharge. A diaphragm 5 mm in diameter was installed after the lens 3; although the intensity of the light decreased, the increased depth of field significantly exceeded the length of the high-voltage electrode, and so the distortions of the emission caused by presence of adjacent streamers were minimized. A camera was placed at the 2D translation platform. A  $\Gamma$ -shape mask from the copper foil (20  $\mu$ s in thickness) was used (i) to check the depth of field; (ii) to assure that the electrode system is perpendicular to the axis of the optical diagnostic system. Spatial resolution of the system was equal to 6.4  $\mu$ m/pixel at ICCD camera gate equal to 0.5 ns; the jitter was less than 0.1 ns.

## 6.2 Kinetics scheme

In present work the kinetics scheme from [85] to model streamer propagation and part of [37] suggested by Dr. Popov for fast gas heating are selected combined with additional reactions from [72]. Following neutral, charged and excited species are taken into account:  $e$ ,  $N_2$ ,  $N_2(A^3\Sigma_u^+)$ ,  $N_2(B^3\Pi_g)$ ,  $N_2(C^3\Pi_u)$ ,  $N_2^+$ ,  $N_4^+$ ,  $O_2$ ,  $O$ ,  $O(^1D)$ ,  $O_2^+$ ,  $O^-$ ,  $O_2^-$ . The scheme includes 13 species and 38 reactions. Detailed reactions and corresponding rates are given in Table 6.1. This scheme has been successfully used in [227].

Table 6.1: Kinetics scheme for nSDBD

| No. | Reaction                            | Rate constant <sup>*)</sup> | Ref.       |
|-----|-------------------------------------|-----------------------------|------------|
| R1  | $e + N_2 \rightarrow e + e + N_2^+$ | $f(\sigma, E/N)$            | [157, 221] |
| R2  | $e + O_2 \rightarrow e + e + O_2^+$ | $f(\sigma, E/N)$            | [202, 221] |

|     |  |   |            |
|-----|--|---|------------|
| R3  | $e + N_2 \rightarrow e + N_2(A^3\Sigma_u)$                           | $f(\sigma, E/N)$                          | [157, 221] |
| R4  | $e + N_2 \rightarrow e + N_2(B^3\Pi_g)$                              | $f(\sigma, E/N)$                          | [157, 221] |
| R5  | $e + N_2 \rightarrow e + N_2(C^3\Pi_u)$                              | $f(\sigma, E/N)$                          | [157, 221] |
| R6  | $e + O_2 \rightarrow e + O + O + 0.8 \text{ eV}$                     | $f(\sigma, E/N)$                          | [202, 221] |
| R7  | $e + O_2 \rightarrow e + O + O(^1D) + 1.26 \text{ eV}$               | $f(\sigma, E/N)$                          | [202, 221] |
| R8  | $N_2^+ + N_2 + M \rightarrow N_4^+ + M + 1.057 \text{ eV}$           | $5 \cdot 10^{-29}$                        | [85]       |
| R9  | $N_4^+ + O_2 \rightarrow O_2^+ + N_2 + N_2 + 2.453 \text{ eV}$       | $2.5 \cdot 10^{-10}$                      | [85]       |
| R10 | $N_2^+ + O_2 \rightarrow O_2^+ + N_2 + 3.51 \text{ eV}$              | $6 \cdot 10^{-11}$                        | [85]       |
| R11 | $O_2^+ + N_2 + N_2 \rightarrow O_2^+ N_2 + N_2$                      | $9 \cdot 10^{-31}$                        | [85]       |
| R12 | $O_2^+ N_2 + N_2 \rightarrow O_2^+ + N_2 + N_2$                      | $4.3 \cdot 10^{-10}$                      | [85]       |
| R13 | $O_2^+ N_2 + O_2 \rightarrow O_4^+ + N_2$                            | $10^{-9}$                                 | [85]       |
| R14 | $O_2^+ + O_2 + M \rightarrow O_4^+ + M + 0.425 \text{ eV}$           | $2.4 \cdot 10^{-30}$                      | [85]       |
| R15 | $e + O_2 + O_2 \rightarrow O_2^- + O_2$                              | $2 \cdot 10^{-29} (300/T_e)$              | [85]       |
| R16 | $e + O_2 \rightarrow O^- + O$  | $f(\sigma, E/N)$                          | [202, 221] |
| R17 | $O^- + O \rightarrow e + O_2$  | $1.4 \cdot 10^{-10}$                      | [72]       |
| R18 | $O_2^- + O \rightarrow e + O_2 + O$                                  | $1.5 \cdot 10^{-10}$                      | [72]       |
| R19 | $e + N_4^+ \rightarrow N_2 + N_2(C^3\Pi_u) + 3.49 \text{ eV}$        | $2.3 \cdot 10^{-6} (300/T_e)^{0.53}$      | [72]       |
| R20 | $e + N_2^+ \rightarrow N + N + 2.25 \text{ eV}$                      | $1.8 \cdot 10^{-7} (300/T_e)^{0.39}$      | [72]       |
| R21 | $e + O_4^+ \rightarrow O + O + O_2 + 4.6 \text{ eV}$                 | $1.4 \cdot 10^{-6} (300/T_e)^{0.50}$      | [85]       |
| R22 | $e + O_2^+ \rightarrow O + O + 5.0 \text{ eV}$                       | $2.0 \cdot 10^{-7} (300/T_e)$             | [85]       |
| R23 | $O_2^- + O_4^+ \rightarrow O_2 + O_2 + O_2 + 6.5 \text{ eV}$         | $10^{-7}$                                 | [85]       |
| R24 | $O_2^- + O_4^+ + M \rightarrow O_2 + O_2 + O_2 + M + 6.5 \text{ eV}$ | $2 \cdot 10^{-25}$                        | [85]       |
| R25 | $O_2^- + O_2^+ + M \rightarrow O_2 + O_2 + M + 7.0 \text{ eV}$       | $2 \cdot 10^{-25}$                        | [85]       |
| R26 | $O^- + N_2^+ \rightarrow O + N + N + 2.25 \text{ eV}$                | $2.0 \cdot 10^{-7} (300/T_{gas})^{0.50}$  | [14]       |
| R27 | $N_2(C^3\Pi_u) + N_2 \rightarrow N_2(B^3\Pi_g, v) + N_2$             | $1.0 \cdot 10^{-11}$                      | [37]       |
| R28 | $N_2(C^3\Pi_u) + O_2 \rightarrow N_2 + O + O(^1D) + 4.83 \text{ eV}$ | $3.0 \cdot 10^{-10}$                      | [37]       |
| R29 | $N_2(C^3\Pi_u) \rightarrow N_2 + h\nu$                               | $2.45 \cdot 10^7$                         | [85]       |
| R30 | $N_2(B^3\Pi_g) + O_2 \rightarrow N_2 + O + O + 2.35 \text{ eV}$      | $3.0 \cdot 10^{-10}$                      | [37]       |
| R31 | $N_2(B^3\Pi_g) + N_2 \rightarrow N_2(A^3\Sigma_u) + N_2(v)$          | $1.0 \cdot 10^{-11}$                      | [37]       |
| R32 | $N_2(A^3\Sigma_u) + O_2 \rightarrow N_2 + O + O + 1.0 \text{ eV}$    | $2.5 \cdot 10^{-12} (T_{gas}/300)^{0.50}$ | [37]       |
| R33 | $O(^1D) + O_2 \rightarrow O + O_2 + 0.33 \text{ eV}$                 | $3.3 \cdot 10^{-11} \exp(67/T_{gas})$     | [37]       |
| R34 | $O(^1D) + N_2 \rightarrow O + N_2 + 1.37 \text{ eV}$                 | $1.8 \cdot 10^{-11} \exp(107/T_{gas})$    | [37]       |

\*) Rate constants are given in  $s^{-1}$ ,  $cm^3 \cdot s^{-1}$ ,  $cm^6 \cdot s^{-1}$ . Electron temperature  $T_e$  is taken as a function of  $E/N$  based on BOLSIG+ with cross sections indicated in the table, unit in K. Gas temperature  $T_{gas}$  is calculated from fluid module in PASSKEY, unit in K.

### 6.3 Streamer velocity and electric current

Typical time-resolved ICCD images of the nSDBD discharge taken with the 1 ns ICCD gate are presented in Figure 6.2. Here and further, the ICCD images are taken without any spectral selection of emission within the spectral range 300 – 800 nm. Camera sensitivity is the same for all the results presented in the figure. According to current knowledge about nanosecond SDBDs, the optical emission in the mentioned range corresponds mainly to the second positive system of emission of molecular nitrogen,  $N_2(C^3\Pi_u) \rightarrow N_2(B^3\Pi_g)$  transition. The quenching time of  $N_2(C^3\Pi_u)$  is determined by the collision with molecular oxygen, the rate constant being equal [228] to  $k_Q^{O_2} = 2.7 \cdot 10^{-10} \text{ cm}^3\text{s}^{-1}$ . The efficient life time of  $N_2(C^3\Pi_u)$  is 0.7 ns at atmospheric pressure, thus ICCD imaging adequately reflects the spatial structure of the discharge, and the resolution is limited by the camera gate. Two peaks of emission are observed during development of the discharge (we will also use terms "the first stroke" and "the second stroke", similar to [137]): one corresponding to the ionization wave charging the surface, on the rising front of the voltage pulse; and another, corresponding to removal of the electrical charge from the surface, on the trailing edge.

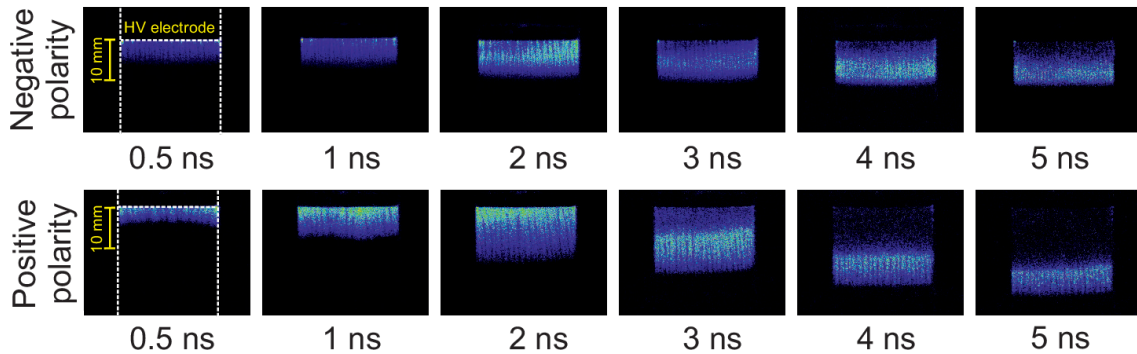


Figure 6.2: Typical time-resolved ICCD images of the nSDBD discharge (top view) of negative and positive polarities of the applied pulse. Width of the high-voltage electrode (a span of the system) is  $W = 25 \text{ mm}$ . The camera gate is 1 ns, the time delay is indicated under each frame. Single-shot images without accumulation of the signal.

Similar ICCD images are usually used to plot the  $x - t$  diagrams, presenting subsequent discharge front positions at different time instants, and to calculate the nSDBD propagation velocity. A few  $x - t$  diagrams are shown in Figure 6.3 a. The experiments were carried out in airflow geometry in quiescent ambient pressure air for the same high voltage pulse with amplitude  $U = \pm 24 \text{ kV}$ , the shape of the pulse is presented by a dashed line in Figure 6.3. The length of the grounded

electrode,  $L = 80$  mm, was always longer than the maximum length of the discharge propagation. The span of the electrode system (the length of the high voltage electrode) changed from  $W = 25$  mm to  $W = 80$  mm. For 50 mm span, the data are presented for both the rising front and the trailing edge. Two waves of emission, corresponding to two ionization fronts, are clearly seen (indicated as I and II in the figure).

The first ionization front (the first stroke) propagates differently for negative and positive polarities of the high-voltage electrode: the velocity is significantly lower for the negative polarity discharge. The second ionization front (the second stroke) propagates with a similar velocity for both polarities. The maximal length of propagation of the discharge  $L_{max}$  along the grounded electrode decreases with the length (span) of the high-voltage electrode,  $W$ . This effect is significant when passing from 25 mm to 50 mm HV electrode (the transition is indicated with arrows in Figure 6.3 a), but then the maximal propagation length changes only slowly with the HV electrode length, approaching to some asymptotic value. The  $x-t$  diagram for 50 mm span and for 80 mm span are quite similar. The  $x-t$  diagram obtained for 63 mm long HV electrode in coaxial system similar to the system described in [57] are in a good correlation with the data obtained for the airflow electrode configuration. To plot the  $x-t$  diagrams from the numerical results calculated by PASSKEY code, the position of the front of the discharge was selected as a position of the front of electron density. It is clearly seen that the results of numerical calculations are in excellent agreement with the experimental data for  $W = 50$  mm and for longer HV electrodes.

Instantaneous speed of the discharge front was calculated for all time intervals of the first stroke presented on the  $x-t$  diagram. The results are shown in Figure 6.3 b. The experimental data are given by the hollow symbols for negative polarity and by the filled symbols for positive polarity. The half-filled symbols represent the results of numerical modeling. Quantitative agreement between experimental data and calculations for both polarities is evident. It should be noted that in the calculations, a few first points were omitted: at the early stage of the discharge the velocity increases, reaches the maximum, and only the right branch of the velocity  $vs$  time was taken into account. No maximum of velocity is observed experimentally.

The velocity of the negative polarity streamer is systematically lower than the velocity of the positive polarity streamer. The velocity is about 2 – 3 mm/ns for negative and  $\sim 5$  mm/ns for positive discharge at the early stage of propagation. It drops down to 0.1 mm/ns and less for the negative polarity streamer, while the positive polarity streamer continues to propagate with a velocity progressively decaying to 0.4 – 0.5 mm/ns at the end of the pulse.

This behavior is dictated by the difference in mechanisms of the negative and

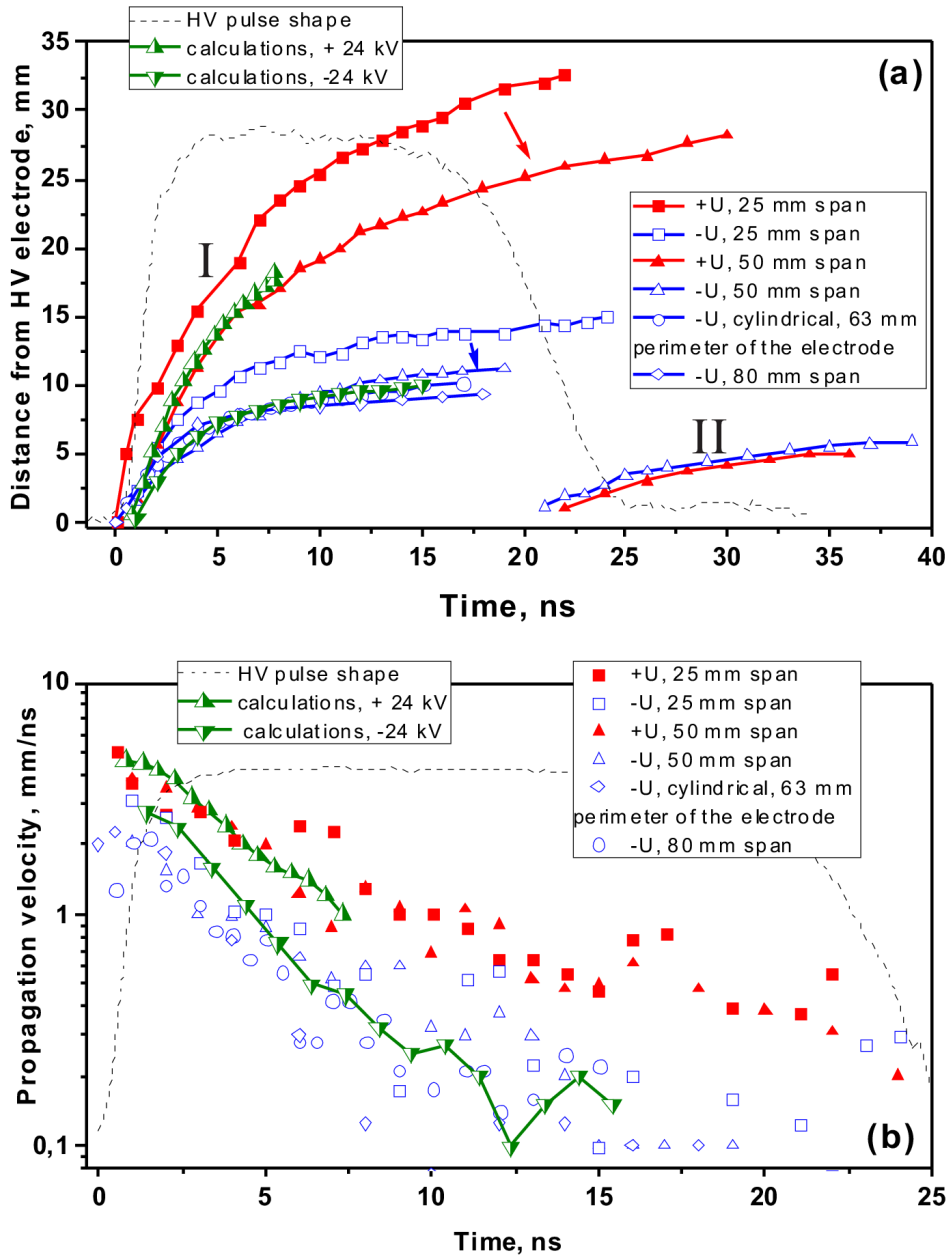


Figure 6.3: Experimentally obtained and calculated dynamics of the nSDBD propagation. (a)  $x-t$  diagrams. I and II are for the first and second ionization fronts, the waveform of the voltage pulse is given by dashed line; (b) velocity of the discharge front as a function of time. The synchronized with the data shape of the high-voltage pulse (a.u.) is indicated with a dashed line. Filled symbols are for positive polarity discharge; open symbols are for negative polarity discharge. Half-filled triangles are for numerical modeling. Data for different spans of the electrode system are marked by different symbols (see the legend).

positive polarity streamers, described in a number of publications [57, 110, 135, 137]. The head of the surface streamer and the nearest region behind the head represent a complex structure combining the features of the volumetric streamers (photoionization and ionization by electron impact) and presence of the dielectric surface (charge deposition on the dielectric with consequent enhancement of the electric field near the surface). When the length of the surface streamer exceeds a few millimeters, the head and the “channel” are clearly distinguished. We will use the term “channel” to designate a structure of the surface streamer behind the head, although for negative polarity, the electric field in this region is rather diffuse. For both polarities, there is a narrow region of high electric fields near the dielectric. For negative polarity streamers, it is reported to be a few micrometers while for positive polarity, it comprises tens of micrometers [57, 108]. So, the channel consists of a thin zone of very high electric field and low electron density and of the “body” of the channel, described by contours of the electron density.

The most principal difference in propagation is explained by structure of streamer head [57]. In the negative polarity streamer, the electrons produced in cathode layer near the high-voltage electrode, move to the surface, producing a negative charge surplus; finally, the electron density and the electric fields are “sticked” to the surface comparing to the positive polarity discharge. In the positive polarity discharge, on the contrary, the electrons go from the surface, the ions practically do not move, and as a result, the structure of the field and of the electron density pattern is different, the electric fields in and below the streamer head are very high and the propagation of positive streamer is faster. Another important point is that the conductivity of the negative polarity streamer is lower. The drop of potential along the O-X axis consists of near electrode drop (cathode or anode fall), potential drop along the channel and potential drop in the streamer head. Lower conductivity of the channel of negative streamer results in higher longitudinal electric field in the channel, lower electric field in the head and, as a consequence, lower propagation velocity.

The described difference is clearly illustrated in [110] where the ionization sources, electron densities, and electric field in the vicinity of the streamer head of negative and positive polarity are calculated.

A simple estimate made in [229] for a negative polarity streamer, was based on the idea that when the streamer stops, the electrical field in the streamer head is close to zero. Assuming that the voltage on the cathode layer [?] is small comparing to the potential of the cathode, it is possible to calculate the reduced electric field  $(E/N)_{ch}$  in the channel of the negative polarity streamer. For  $U = -24$  kV and for  $L_{max} \approx 10$  mm, at  $P = 1$  bar and  $T = 300$  K the value  $(E/N)_{ch} \approx 100$  Td. As far as positive polarity streamer propagates at much longer distances, it is reasonable to assume that the longitudinal electric field in the streamer “body” is lower than in

the case of the negative polarity discharge.

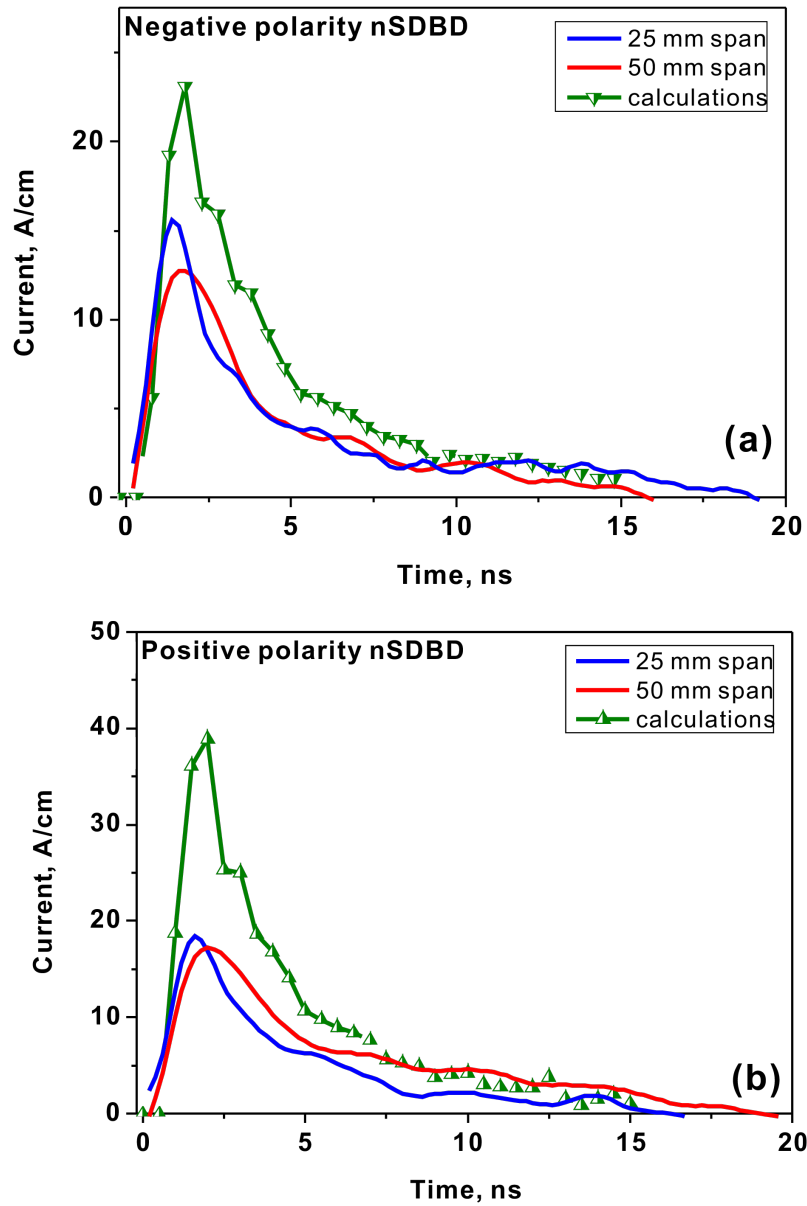


Figure 6.4: Discharge electrical current per unit length for negative (a) and positive (b) polarity nSDBD. The current was measured for two spans of the electrode system,  $W = 25$  mm and  $W = 50$  mm. Half-filled triangles are for numerical modeling.

To analyze the influence of possible edge effects, the experiments with two different spans were selected to measure electrical current:  $W = 25$  mm and  $W = 50$  mm. Figure 6.4 presents experimentally measured total electrical current through the discharge divided by the span of the electrode system and numerical results for the current per unit length. It is important to note that the electrical current corresponding to charging of the electrode system in absence of the discharge was subtracted when treating the data. In numerical modelling, the current was calculated as an integral

of fluxes of negative and positive charges through the surface of the high-voltage electrode.

The agreement is rather qualitative for both polarities. For discharge of negative polarity (Figure 7 a), the current peaks at 16 A/cm for 25 mm span, and at 13 A/cm for 50 mm span. The result obtained by numerical modeling for the same conditions is 23 A/cm, with secondary emission coefficient on the electrode being  $\gamma = 0.1$  and ion mobility ranging between 1.4 and 2.5 cm<sup>2</sup>/V·s according to [230]. For the discharge of positive polarity (Figure 7 b), the current through the electrode is mainly the current of electrons; experiments give almost the same peak current value for 25 mm and 50 mm span, 18 A/cm and 19 A/cm. Result in numerical simulation gives 2 times higher peak current value in first 5 ns (40 A/cm), and a decaying current that behaves similar as experimental ones.

Despite the difference in the peak current values, a good agreement is observed for measured and calculated absolute values of the current after the peak; qualitative behaviour of the current as a function of time is also well reproduced. Detailed description of the shape of the pulse of the current linked to the phases of the development of the negative polarity discharge can be found in [137]. According to [137], the first peak of the current (20 – 40 A/cm in Figure 7 a) is due to the ion current from the cathode layer to the HV electrode. High electron densities and high electric field result in strong charge separation [137] and sharp rise of the current. The electrons produced in the cathode layer drift to the dielectric surface and charge the surface negatively. As a result, the  $y$ -component of the external electric field is shielded and ionization inside the cathode layer decreases. Another feature is the behavior of the current on the plateau of the electrical pulse. This stage with a slowly decreasing electrical current (3 – 15 ns in the Figure 7) is due to the formation of the near-surface plasma layer [137], and is observed in both calculation and measurements. The current in both calculations and experiments and in both polarities, decay progressively to 0 at almost the same rate in the tail.

The formation of the near-surface plasma layer is an issue which is extremely complicated for experimental study. In available numerical calculations [57, 110, 135, 137] the electric field in the case of the negative polarity discharge has a diffuse structure. Although some authors [135], say that “there is no streamers at negative polarity”, we will prefer to keep, similar to [110], terms “negative streamers” and “positive streamers”. In both negative and positive streamers, there is a sheath region near the dielectric. In the sheath, the strong electric field is directed perpendicular to the dielectric surface, and the electron density is low. The thickness of the sheath predicted numerically for atmospheric pressure SDBDs is a few microns for the negative polarity discharge and 40 – 50  $\mu\text{m}$  for the positive polarity discharge.

## 6.4 Electron density and electric field

Two approaches to the nSDBD description, theoretical and experimental, are different, first of all, by the definition of “streamer”. In theory and in numerical calculations, a streamer is represented by isolines of the electron density and/or the electric field. In the experiments, measurements of the electron density are complicated because of relatively low absolute values of  $n_e$  and high demands to spatial resolution. Two wavelength Shack-Hartmann type laser wavefront sensors were successfully used to measure 2D time-resolved electron density in extinguishing atmospheric arc discharges with currents of several tens of amperes [231] but the lower electron densities reported in [231] were on the order of  $10^{17} \text{ cm}^{-3}$ . The measurements of the electric field are limited by measurements of the ratio of emission of two bands with different thresholds integrated over the thickness of the streamer [56,57], as discussed above. A picosecond four-wave mixing can be in perspective adapted for the measurements of the electric field in a surface discharge, but at present only the measurements in volumetric nSDBD are available [232]. As a result, in the experiments the surface streamer is defined as a region corresponding to optical emission in UV and visible range of spectra. The aim of the next two sections is to provide a comparison between two ways to describe a surface streamer.

The evolution of the electron density in the negative and in the positive streamer at 4 successive time moments is shown in Figure 6.5. The time moments are different: 1, 5, 10 and 15 ns for negative polarity and 2, 4, 6 and 8 ns for positive polarity. The point (0, 0) corresponds to the triple point. The scale on the  $X$ -axis is also different: 0 – 10 mm for negative polarity, and 0 – 20 mm for positive polarity. The vertical scale is the same for negative and positive polarity; a represented region takes 1.1 mm above the dielectric electrode. Similar to [110,137], a negative polarity streamer is more diffuse; this can be seen from the 2D plots of the electron density near the high voltage electrode. For both polarities, the electron density increases and then decreases when moving in vertical direction from the dielectric surface. For positive polarity, the thickness of the region of a high electron density is approximately two times higher.

With time, a diffuse “cloud” of the electron density near the high-voltage electrode at negative polarity remains practically unchanged with a typical vertical size about 0.4 mm, in an excellent correlation with calculations of [110]. The size of the streamer head is much smaller than the size of the “cloud”, about  $60 \mu\text{m}$  at 5 ns at a distance of 7.5 mm from the high-voltage electrode, and about  $30 \mu\text{m}$  at a distance of 10 ns at 9.6 mm from the high-voltage electrode. The cross-section of a negative streamer keeps a triangle-like shape with a diffuse “cloud” near the high-voltage electrode and a “needle-like” head during the discharge propagation along the sur-

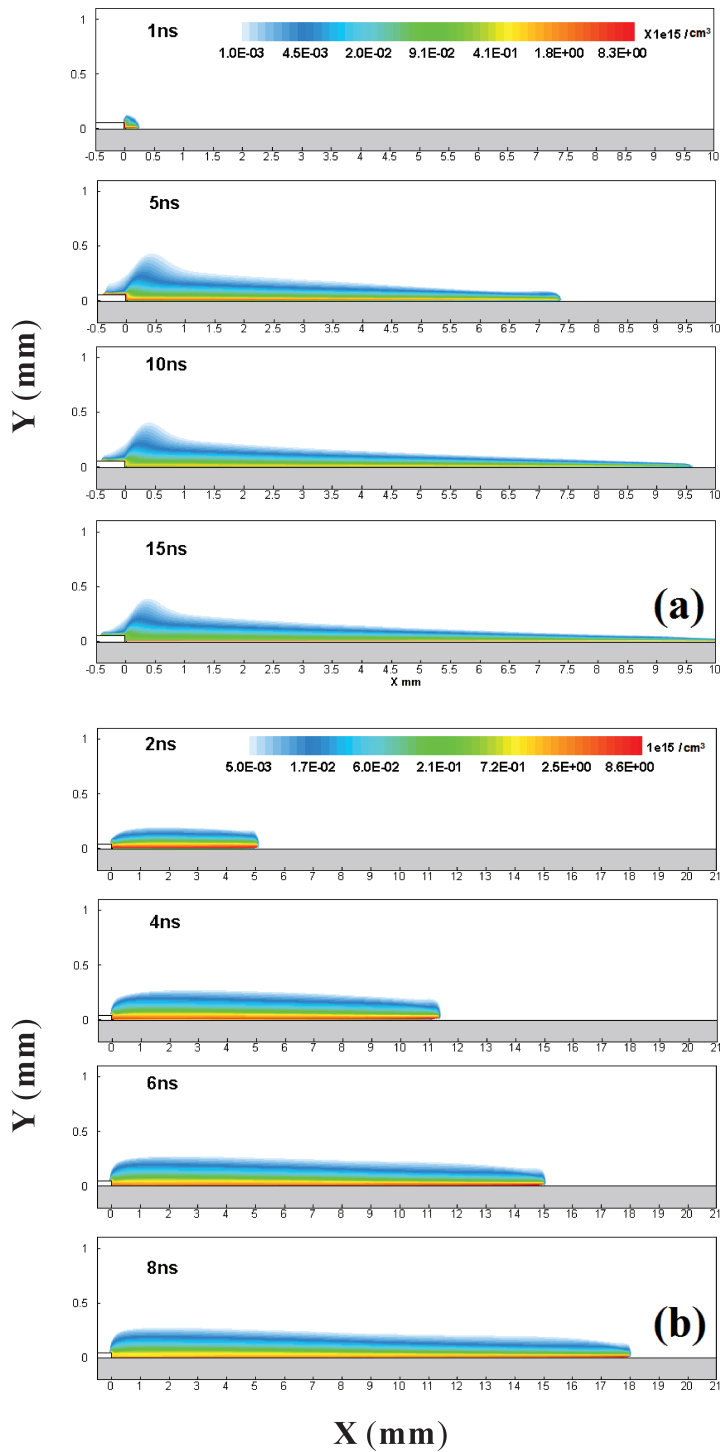


Figure 6.5: The evolution of the electron density for negative (a) and positive (b) streamers. Time instants are 1, 5, 10, 15 ns for negative polarity streamer and 2, 4, 6 and 8 ns for positive polarity streamer. The scale on  $OX$ -axis is 0 – 10 mm for negative polarity streamer and 0 – 20 mm for positive polarity streamer. The scale on  $OY$ -axis and the scale for the electron density are the same for both polarities.

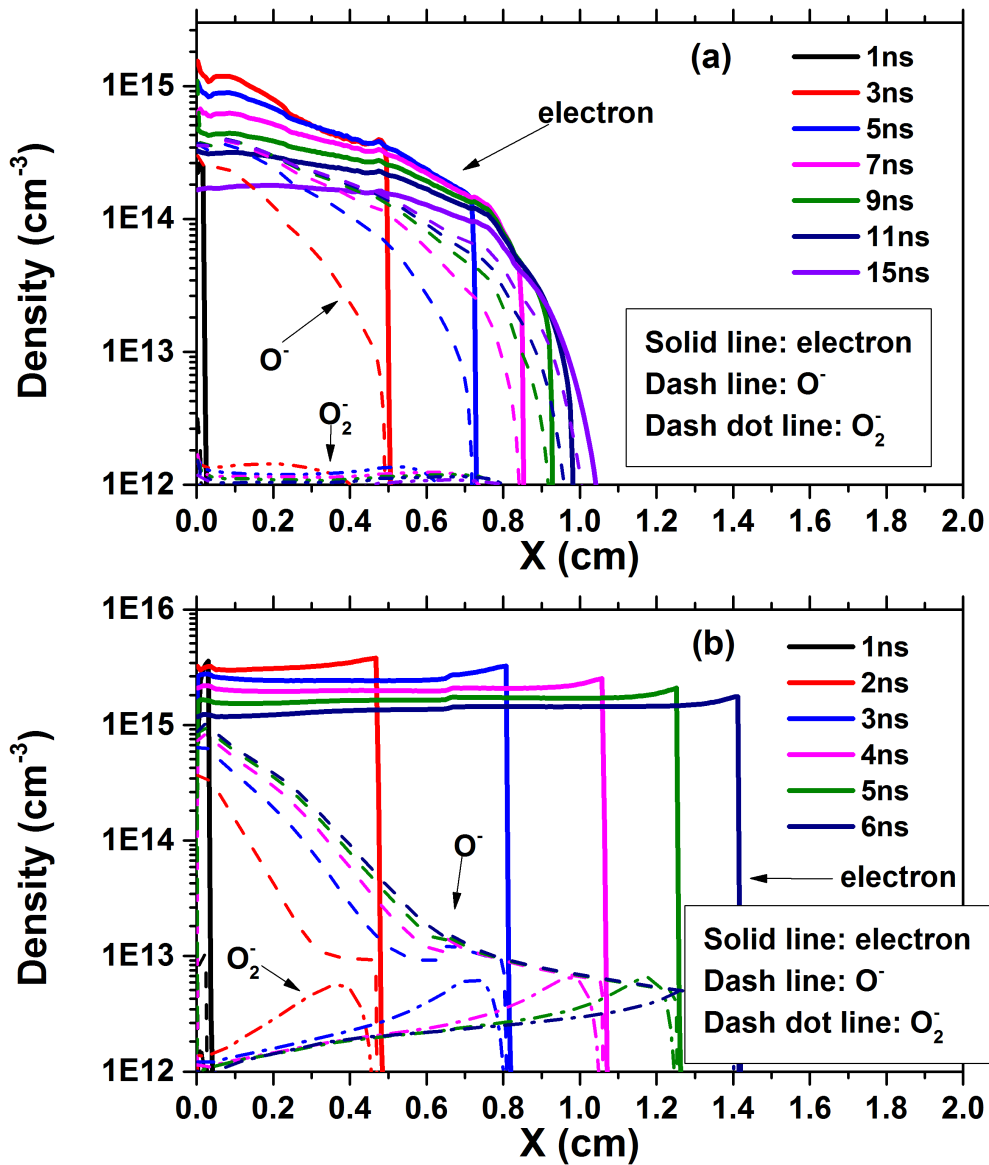


Figure 6.6: The distribution of density of electrons,  $O_2^-$  and  $O^-$  along the line probe 25  $\mu m$  above the dielectric for negative polarity (a) and positive polarity (b).

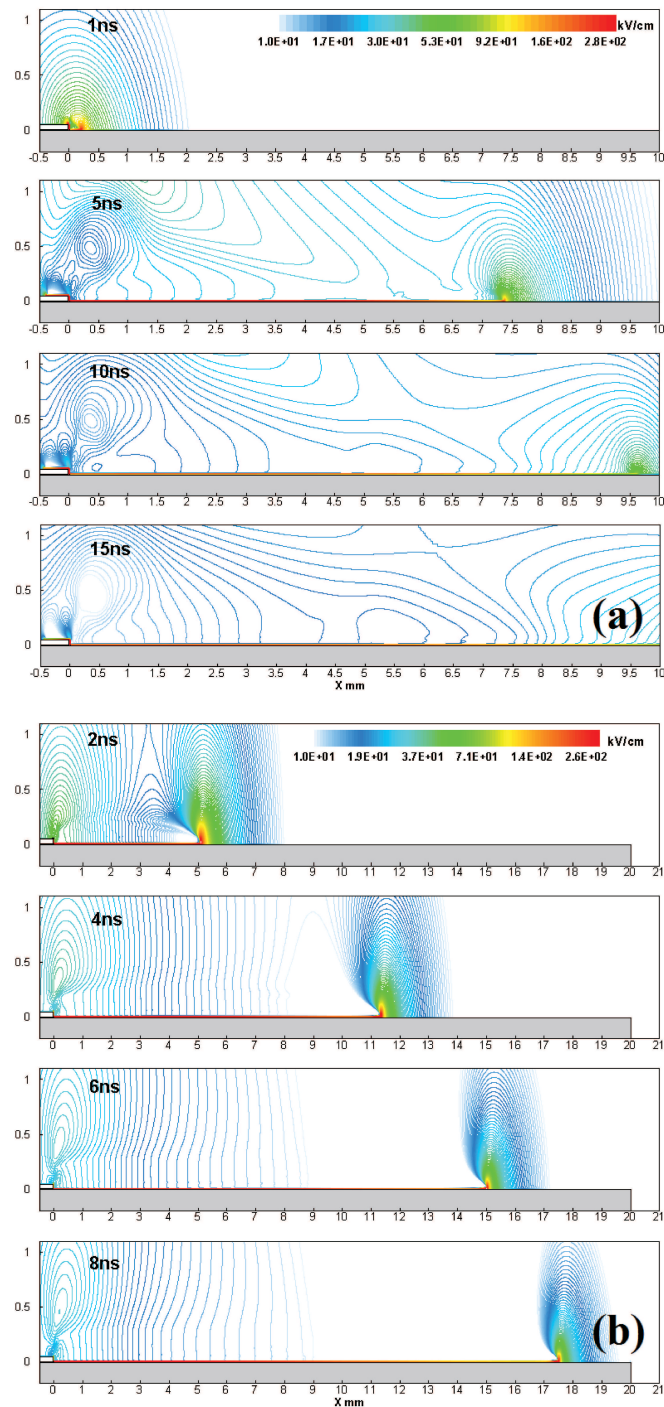


Figure 6.7: The evolution of the absolute value of the electric field for negative (a) and positive (b) streamers. Time instants are 1, 5, 10, 15 ns for negative polarity streamer and 2, 4, 6 and 8 ns for positive polarity streamer. The scale on  $OX$ -axis is 0 – 10 mm for negative polarity streamer and 0 – 20 mm for positive polarity streamer. The scale on  $OY$ -axis and the scale for the electric field are the same for both polarities.

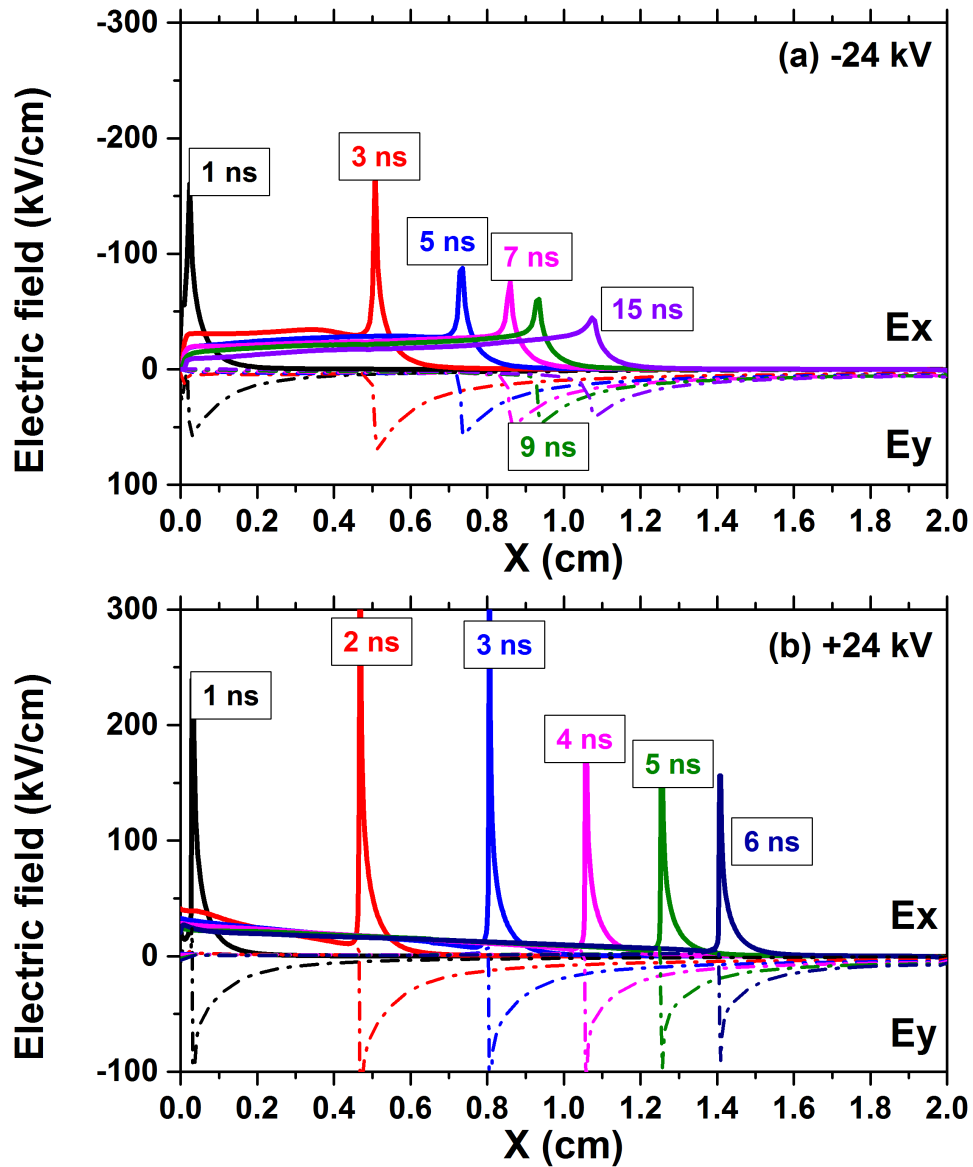


Figure 6.8: The distribution of electric field in X and Y direction along the line probe  $25 \mu m$  above the dielectric for negative polarity (a) and positive polarity (b).

face. For positive polarity, a “sandwich-like” structure is observed for the electron density: the thickness of the layers with a constant electron density changes only slightly along the streamer.

A deeper insight into the streamer channel can be achieved by probing electron density along a line 25  $\mu\text{m}$  above the dielectric surface starting from the edge of HV electrode. The densities of electron for negative polarity in 1-15 ns and for positive polarity in 1-6 ns have been plotted in Figure 6.6 together with densities of other negative charge species. The distributions are well distinguished. At negative polarity the production of electrons is getting lower and lower while ionization front propagates, the maximum density is located near HV electrode, so as  $\text{O}^-$  atoms and  $\text{O}_2^-$  molecules. For positive polarity, electron density keeps almost the same across the channel and decrease in the whole channel temporally. The density of electrons are higher than in negative polarities, but the density of  $\text{O}^-$  atoms caused by dissociative attachment of electrons is lower than negative polarity.

To compare the behavior of emission of a particular molecular band for different polarities, the information about the electron density and about the electric field is needed. The evolution of the absolute value of the electric field in the negative and in the positive streamers at the same time instants that the electron density is shown in Figure 6.7. For both polarities, high values of electric field are observed in the streamer head. Maximum of the color scale presented by Figure 6.7 corresponds to approximately 300 kV/cm (1200 Td at atmospheric pressure) being in a reasonable correlation with [57, 110]. Higher electric fields in the head of a positive polarity streamer at a distance a few cm from the high-voltage electrode comparing to negative polarity are also in correlation with calculation of [110]. To distinguish the electric field distribution in the channel of plasma, Figure 6.8 shows the line probed electric field components at 1-15 ns for negative polarity and 1-6 ns for positive polarity.

A principal difference in behavior of the electric field for negative and positive polarity is that at negative polarity, as can be seen in Figure 6.8 (a), a weak electric field is observed at significant distances from the dielectric in vertical direction, starting from tens of microns to  $y = 1$  mm and more. The absolute value,  $(E/N)^* \leq 20 - 30$  kV/cm, or 80 – 120 Td (light blue color in Figure 6.7), is not enough for efficient ionization, so it is often neglected in a “standard” streamer representation, where the electron density and the ionization source are typically plotted. But these values are efficient for excitation of  $\text{N}_2(\text{C}^3\Pi_u)$ -state of molecular nitrogen. Indeed, in the outer perimeter of the streamer head the electric field is  $(E/N) \approx 50 - 100$  kV/cm, or 200 – 400 Td (green color in Figure 6.7). The ratio of the rates of excitation of  $\text{N}_2(\text{C}^3\Pi_u)$ -state by electron impact and of ionization at  $E/N = 400$  Td is about 3, while at  $E/N = 80$  Td this ratio is equal to 240. As a result, the emission

of the second positive system should be visible not only in the front and near the electrode, but also between them. At positive polarity, the field between the streamer head and the near-electrode region at significant distances,  $y \geq 30 - 50 \mu\text{m}$ , is low according to Figure 6.8 (b),  $E/N \ll (E/N)^*$ . As a result, calculated emission of the second positive system of  $\text{N}_2$  in the case of positive polarity should be visibly concentrated in the streamer head and near the high-voltage electrode.

The aim of the next section is to compare, for both polarities, calculated and measured experimentally 2D time-resolved streamer emission for the second positive system of molecular nitrogen, and so to compare numerical and experimental streamer “appearance” for the same conditions.

## 6.5 Time-resolved emission of excited species

The emission observed by 2D imaging, is mainly (at least with the accuracy of a few percent) the emission of the second positive system of molecular nitrogen. The only “concurrent” of the second positive system in the UV and visible (200-800 nm) range of spectra at short time at high electric fields in air is the first negative system of  $\text{N}_2$ , with a strong  $v' = 0 \rightarrow v'' = 0$  band at  $\lambda = 391.4 \text{ nm}$ , partly overlapped with  $3 \rightarrow 6$ ,  $\lambda = 389.5 \text{ nm}$  and  $2 \rightarrow 5$ ,  $\lambda = 394.3 \text{ nm}$  bands of the second positive system. We performed a set of additional experiments with  $340 \pm 5 \text{ nm}$  and  $390 \pm 5 \text{ nm}$  narrow band filters, trying to separate the emission from the second positive and the first negative system at the front of the discharge with a time resolution of 0.5 ns, and we failed: no one time instant and no spatial zone where the emission of  $\lambda = 391.4 \text{ nm}$  can be clearly distinguished on the background of the  $2^+$  system under the mentioned way of visualization were found. Two conclusions were made from these preliminary experiments: (i) using the photomultiplier tubes with a gain an order of magnitude higher than ICCD camera gate and selecting the emission strictly by molecular bands, it is possible to separate experimentally the first positive and the second negative systems in the nSDBD [57] and to judge about the absolute values of the electric field [58, 59]. The experiments to separate the emission in 2D in time-resolved mode are possible but demand more precautions; (ii) the emission observed experimentally and presented below is the emission of the second positive system of molecular nitrogen.

The emission intensity in any point at any time instant is defined by a product of electron density  $n_e$  and the rate constant of  $\text{N}_2$  excitation by electron impact, which is a function of the reduced electric field  $E/N$ . The density of  $\text{N}_2(\text{C}^3\Pi_u)$  in nSDBD is governed by the following equation:

$$\frac{d[\text{N}_2(\text{C}^3\Pi_u)]}{dt} = k_e(E/N)n_e[\text{N}_2] - \frac{[\text{N}_2(\text{C}^3\Pi_u)]}{\tau_0} - \sum_i k_q^i[\text{N}_2(\text{C}^3\Pi_u)][\text{M}_i], \quad (6.1)$$

where  $k_e(E/N)$  is a rate constant of excitation of  $\text{N}_2(\text{C}^3\Pi_u)$  by electron impact,  $\tau_0$  is the lifetime,  $k_q^i$  and  $[\text{M}_i]$  are the rate constants of quenching and the densities of quenchers respectively, and the emission intensity is proportional to the density of molecules on the upper state:  $I \sim [\text{N}_2(\text{C}^3\Pi_u)]$ .

The calculated 2D map of  $\text{N}_2(\text{C}^3\Pi_u)$  emission at 7 successive time moments is shown in Figure 6.9. The time moments are different: 1, 2, 3, 4, 5, 10 and 15 ns for negative polarity and 1, 2, 3, 4, 5, 6 and 8 ns for positive polarity. The scale on the  $OX$ -axis is 0 – 10 mm for negative polarity, and 0 – 20 mm for positive polarity, similar to Figures 6.5 and 6.7. The vertical scale is the same for negative and positive polarity and twice smaller than for the electron density and electric field: a represented region takes 0.6 mm above the dielectric layer.

At the negative polarity, two distinctive features of calculated profile of emission should be mentioned (Figure 6.9 a): (i) during a few first nanoseconds, the emission reproduces the behaviour of the electron density; (ii) after 10 ns, the emission flattens against the dielectric, and the visible thickness of the discharge decreases by a factor of 4 – 8. Observed gradual flattening of the emission is connected with slow decrease of the absolute value of the electric field in the “body” of the streamer channel, tens and hundreds of micrometers above the dielectric surface.

The evolution of the positive polarity nSDBD (Figure 6.9 b) also reflects the distribution of the electric field in time and space. Two regions of high electric field and relatively high electron density are observed: in the streamer head and near the high voltage electrode. As a result, the emission pattern is divided into two parts (2 – 4 ns) more and more separated in space with time, and finally (6 – 8 ns and more) no optical emission is observed from the streamer “body” between the streamer head and near-electrode region.

Calculated emission presented in Figure 6.9 was compared with measured emission plotted in Figure 6.10. The experimental 2D map of the emission is taken at 0.5, 1, 1.5, 2, 2.5, 8 and 10 ns for both polarities. The synchronization between the calculated and measured picture is present but the initial moment can be shifted by 0.5–1.5 ns: in experiments, the  $t = 0$  instant was defined as a point 0.5 ns before the first image with a visible emission, no special experiments to synchronize electrical and optical measurements or to measure emission at the beginning of the discharge with increased ICCD sensitivity were made. No reverse Abel procedure has been made, but qualitative analysis of the profile of emission in assumption that all the streamers are identical, shows that the maximum of emission is observed inside the

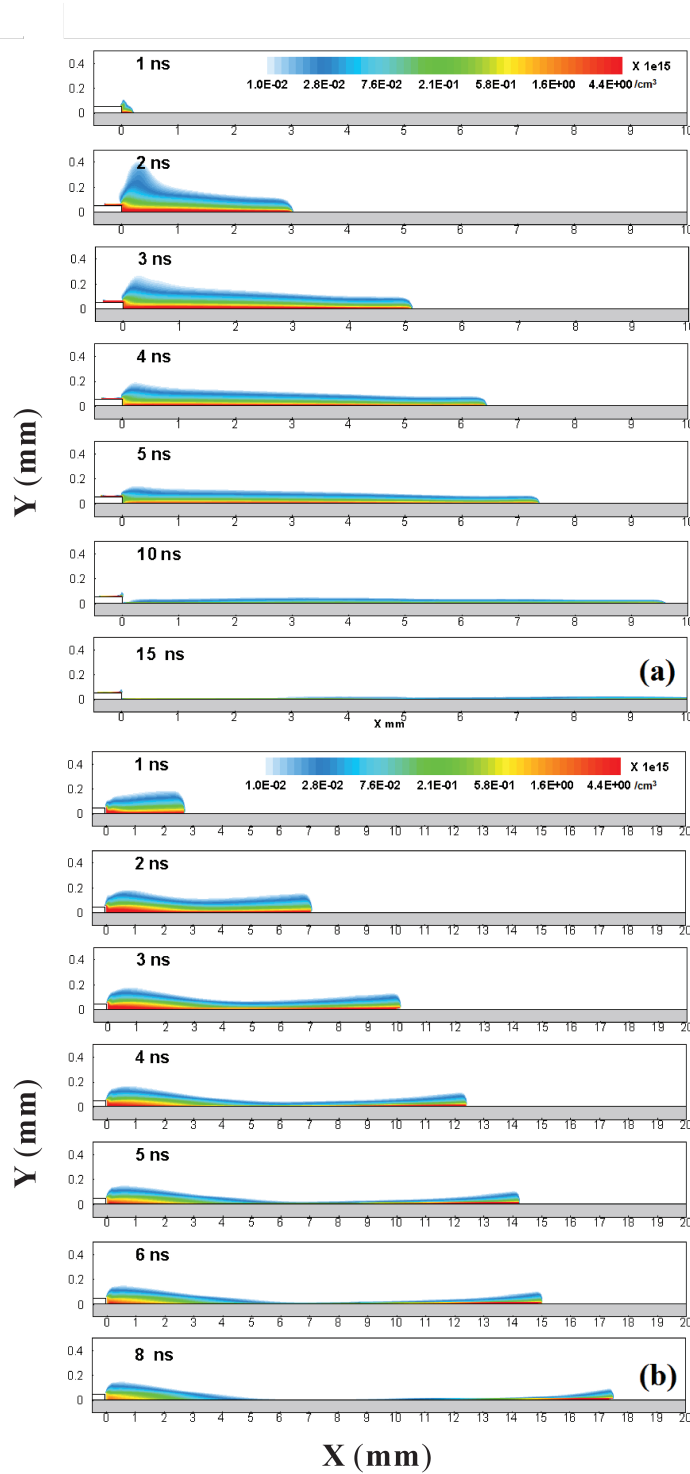


Figure 6.9: The evolution of the calculated  $N_2(C^3\Pi_u)$  density in unit  $\times 10^{15}/cm^3$  for negative (a) and positive (b) streamers. Time instants are 1, 2, 3, 4, 5, 10, 15 ns for negative polarity streamer and 1, 2, 3, 4, 5, 6 and 8 ns for positive polarity streamer. The scale on  $OX$ -axis is 0 – 10 mm for negative polarity streamer and 0 – 20 mm for positive polarity streamer. The scale on  $OY$ -axis and the scale for the  $N_2(C^3\Pi_u)$  density are the same for both polarities.

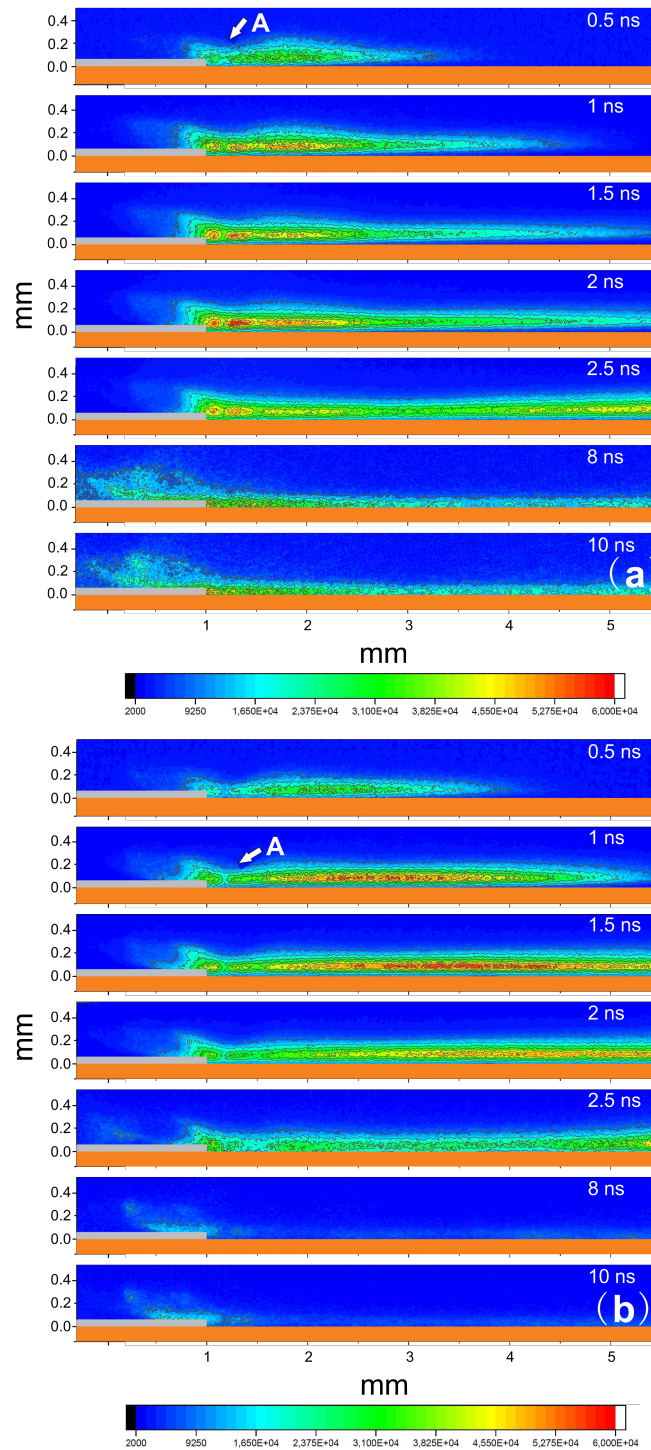


Figure 6.10: The evolution of the measured  $N_2(C^3\Pi_u) \rightarrow N_2(B^3\Pi_g)$  emission intensity (a.u.) for negative (a) and positive (b) streamers. The span of the electrode system is  $W = 25$  mm. The ICCD camera gate is equal to 0.5 ns. Time delays relative to the start of the discharge are 0.5, 1, 1.5, 2, 2.5, 8, 10 ns for both polarities. The scales on  $OX$  and  $OY$ -axes and the sensitivity of the ICCD camera are the same for both polarities. See the text for explanation of point A.

streamer channel, decreasing to the periphery. The picture is not symmetrical, the central “axis” of emission is shifted toward the dielectric. The maximum of emission is observed at a distance about 35 % of the diameter of the total emission channel over the dielectric. It should be noted that the emission intensity near the surface was not corrected for the solid angle: as far as the angle of the light collection decreases when approaching the dielectric, a visible intensity of emission should also decay.

For negative polarity, the shape of the measured emission profile during a few first nanoseconds is similar to the shape of calculated emission and electron density. Similar to the electron density, a vertical cross-section of the negative streamer has a triangle-like shape with a diffuse “cloud” near the high-voltage electrode and a “needle-like” head during the discharge propagation along the surface. After 8 – 10 ns, similar to observed in the calculations, the optical emission flattens and significantly decreases in amplitude.

For positive polarity discharge, the velocity of propagation is much higher starting from the first nanoseconds. At time period 8 – 10 ns and later, no emission is observed behind the front of the streamer. “Separation” of the two regions with decrease of a thickness of the streamer in the central part, is clearly seen at 2.5 ns in Figure 6.10.

A feature which does not exist in numerical modeling, is a “bottleneck” separating a bright near-electrode region 150–200  $\mu\text{m}$  in length and the main streamer channel. The bright region exists from the very beginning of the streamer propagation; it elongates and disappears at 2 – 2.5 ns. The feature is experimentally observed for both polarities of the high-voltage pulse (see point A in Figure 6.10).

It is important to note that the thickness of the region of a well-pronounced  $\text{N}_2(\text{C}^3\Pi_u)$  emission (“the emission zone”) is about 200 – 250  $\mu\text{m}$ , well above the calculated thickness of the near-dielectric region of high electric fields, a few micrometers for negative and tens of micrometers for positive polarity. As far as the threshold of excitation of  $\text{N}_2(\text{C}^3\Pi_u)$ -level is 11.03 eV [233], the emission describes a region where the electric field is still high  $(E/N)^* \sim 80 - 100 \text{ Td}$ , and the electron density is already high enough to provide efficient excitation of electron levels and so, efficient dissociation. The emission zone is the most important zone of the discharge when considering the nSDBD as plasmachemical reactor.

Another important issue is temperature increase due to fast gas heating [37] on tens-hundreds of nanoseconds and further due to VT-relaxation [234] on a microsecond time scale. Local increase of gas temperature can (i) provoke a chemical reaction, when reaction rate is an Arrhenius exponential function of gas temperature; (ii) create a hydrodynamic perturbation and a low density region. The last action is accepted to be the most important factor in gas flow control using nS-

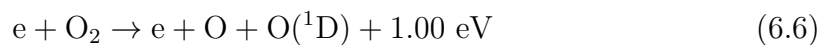
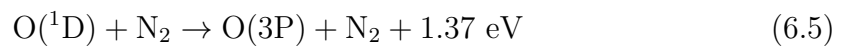
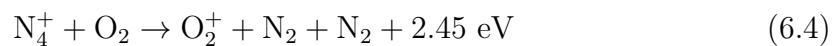
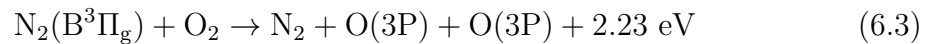
DBDs [235]. This issue will be discussed in next section together with the study of fluid responses.

## 6.6 Fast gas heating and fluid responses

nSDBD is well known as a prospective tool for plasma assisted aerodynamics by the effect of local heating, and for plasma assisted ignition/combustion by production of active species and also local heating. The features of energy release and fast gas heating in nSDBD is an important issue for the community of aerodynamics and combustions.

According to [37], the main processes contributing to fast gas heating in nSDBD can be classified as: (i) quenching of the  $N_2(C^3\Pi_u)$  states by oxygen; (ii) quenching of the  $N_2(B^3\Pi_g)$  states by oxygen; (iii) reactions involving charged particles; (iv) dissociation of  $N_2$  molecules by electron impact followed by quenching of  $N(^2D)$  atoms; (v) quenching of excited  $O(^1D)$  atoms by nitrogen; (vi) dissociation of  $O_2$  molecules by electron impact; and (vii) quenching of the excited molecules  $N_2(A^3\Sigma_u^+)$  and  $N_2(a'^1\Sigma_u^-)$  by oxygen. According to section Figure 6.7 and Figure 6.8 in 6.4, the electric field for nSDBD ranges from 0 to 200 Td in the streamer channel. In the near HV cathode sheath region, the field can reach above 1000 Td. Study based on detailed kinetics [37] has revealed that in the field range in streamer channel, the main processes contributing to fast gas heating are (i), (ii), (v) and (vi), while for higher field region, it is (iii) and (iv) that dominates.

In the calculation of nSDBD by PASSKEY, the main contribution to fast gas heating energy in nSDBD can be summarized as:



The reactions mentioned above agree with well the conclusions given in Ref [37]. To further distinguish the contributing reactions to fast gas heating in spatial scale,

we plot the fractions of contribution from the reactions mentioned above in Figure 6.11 (a) and (b) at both polarities. The total energy density are plotted together with the fractions in the bottom of each sub-figures. The spatial distribution of released energy share several features in common for both polarities: (1) Energy release from quenching reactions (i) and (ii) are dominant in the streamer channel; (2) Reactions of charged species (iii) release energy mainly near the electrode; (3) Total energy density is higher near the electrode and decrease with the grow of distance from HV electrode at both polarities.

Despite the similarities, the difference of the spatial distribution of energy release for negative and positive polarity nSDBD is significant. Near the electrode, there is significant energy density near HV electrode. In the streamer channel, the detailed contribution from reactions concerning fast gas heating is plotted in Figure 6.12 (a) and (b). At negative polarity, the energy fraction is rather uniform across the channel: quenching reactions contribute up to 75% the energy release, dissociation of  $O_2$  molecules contribute 20%, and other reactions involving charged species contribute the rest ( $<5\%$ ). For a positive polarity nSDBD, the constitution of energy release changes: at near electrode region ( $X < 5$  mm) quenching and  $O_2$  dissociation still dominate as in negative polarity, but in streamer channel far from the HV electrode, the fraction of energy release from reactions of charged species increases from 5% to 35%. This change of energy fraction in positive nSDBD is due to the fact that, in positive polarity the electric field is much higher in the ionization head and approximately 0 right after the front, as a result, when positive streamer propagates far away from the HV electrode, the released energy mainly comes from the charged species produced by the rather high electric field.

Hydrodynamic response was calculated using the same mesh as for plasma equations. Unlike widely used mesh mapping or interpolating methods in coupling fluid and plasma code, using the same mesh for both plasma and fluid sacrifices the resolution of fluid problem faraway from the electrode, but enables a possibility to resolve the early response of fluid during and after the discharge in a very short time and very fine spatial scale.

The direct consequence of fast gas heating is the change of temperature in discharge region. The calculated temperature distribution has been presented in Figure 6.13 (a) for negative polarity and (b) for positive polarity from 10 ns in the discharge to 10000 ns in the afterglow. To quantify the differences, we probe the temporal temperature evolution near the electrode and in the channel in Figure 6.14. For both polarities, a heated channel is observed above dielectric layer. Near the electrode, the presence of cathode region at negative polarity leads to intensive heating and temperature rise (to 1400 K), while for positive polarity maximum temperature of 500 K is observed at the edge of electrode. But in the channel, temperature rise

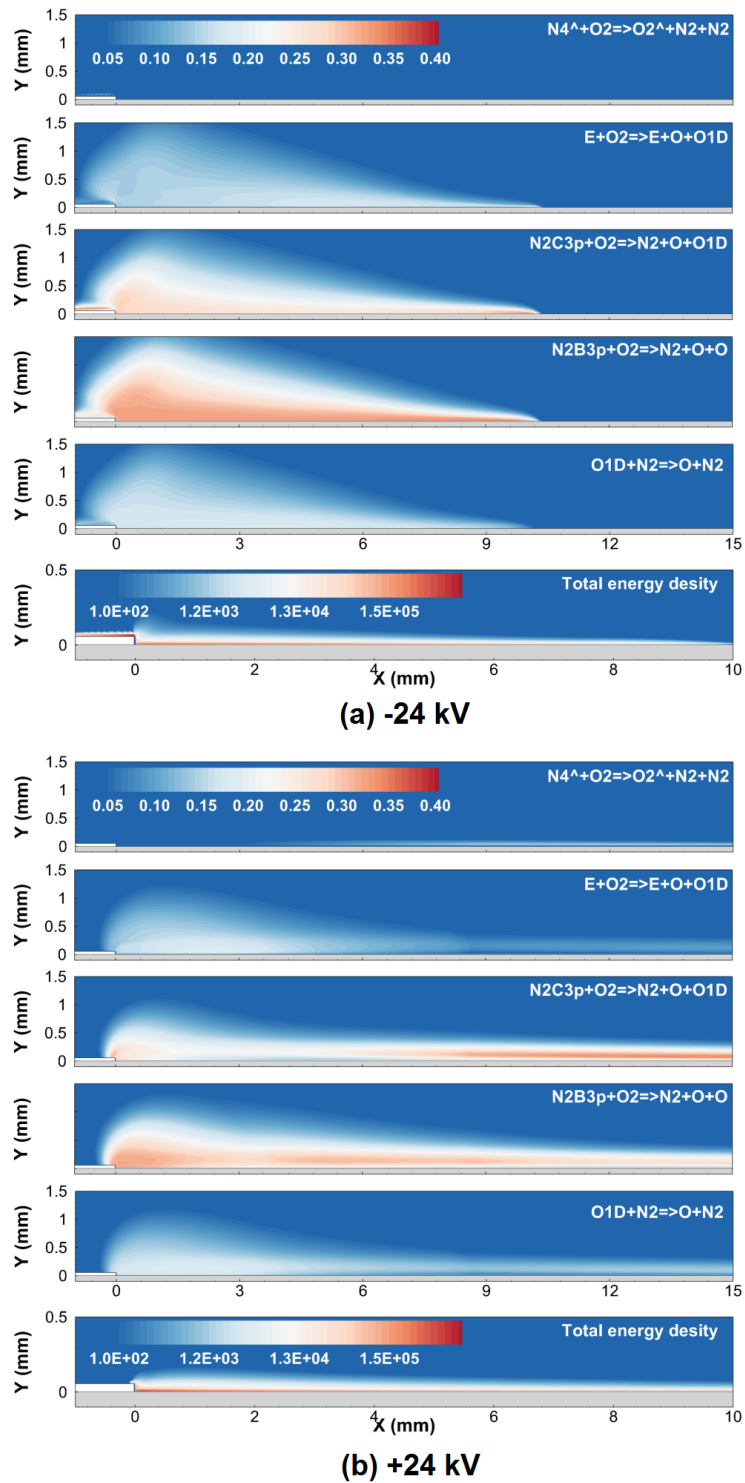


Figure 6.11: The spatial distribution of the fraction of energy from 5 main reactions contributing to fast gas heating for (a) negative polarity and (b) positive polarity. For each group the last figure gives the distribution of absolute energy density (in unit  $J/m^3$ ) that heat the gas.

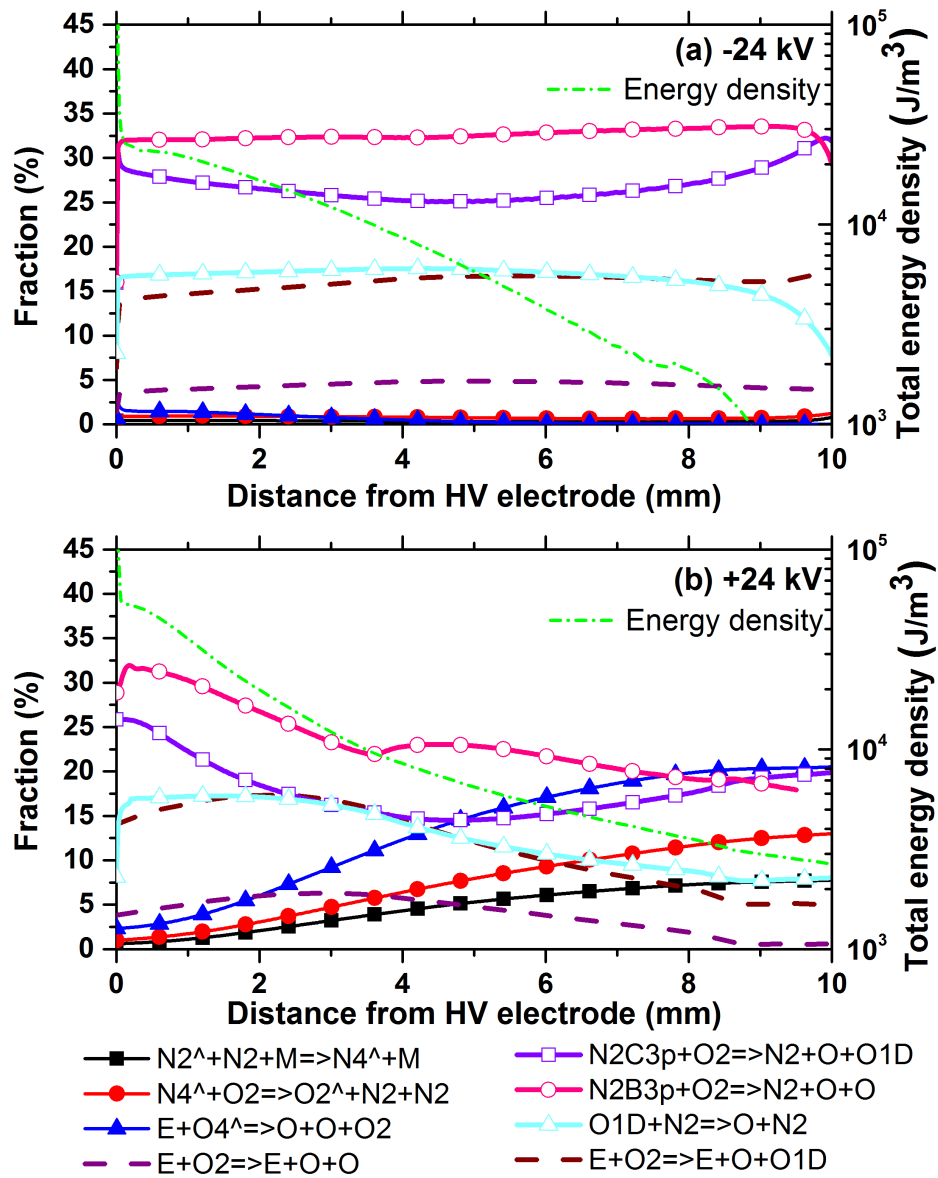


Figure 6.12: Energy density for fast gas heating and the fraction of energy from main reactions contributing to fast gas heating for (a) negative polarity and (b) positive polarity along the line probe  $25 \mu m$  above the dielectric.

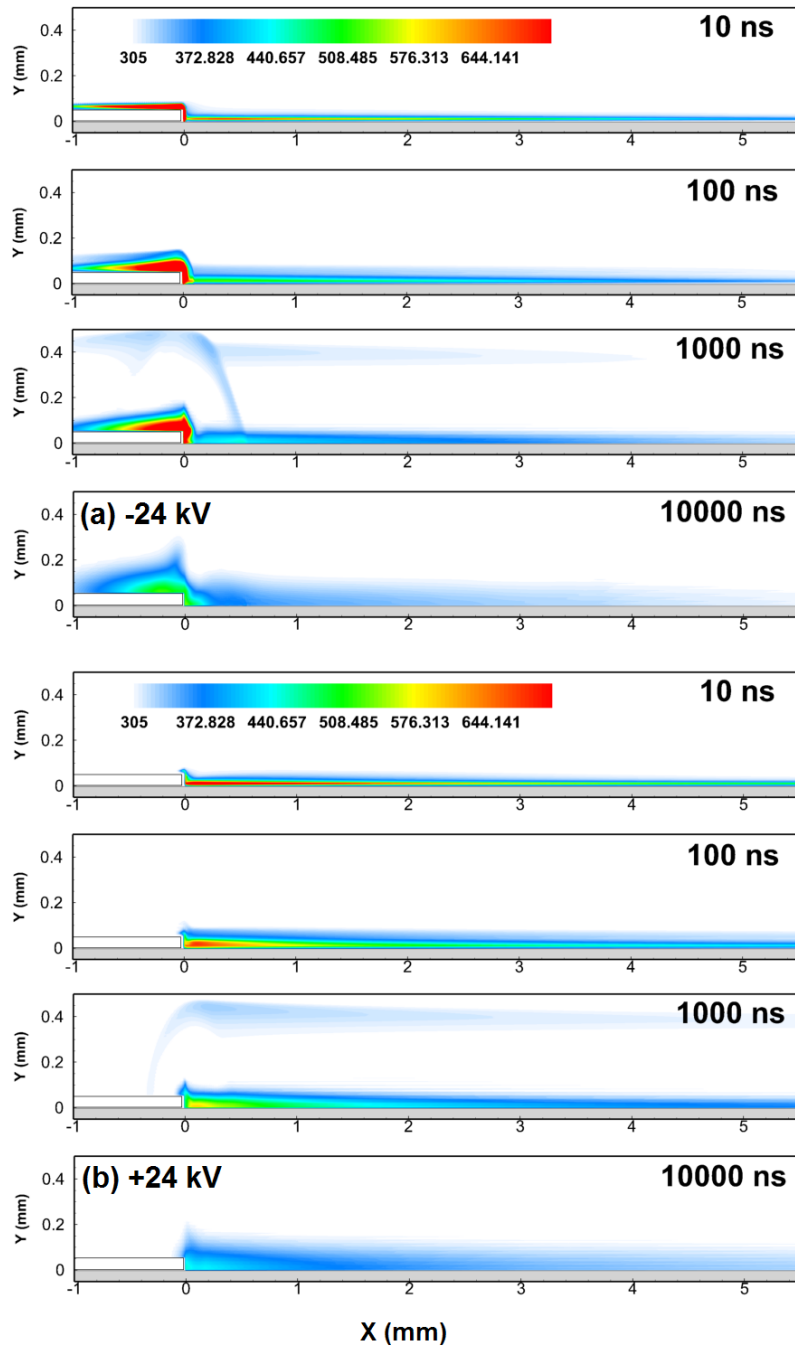


Figure 6.13: The evolution of the calculated temperature distributions (in K) from 10 ns to 10000 ns for (a) negative polarity and (b) positive polarity discharge.

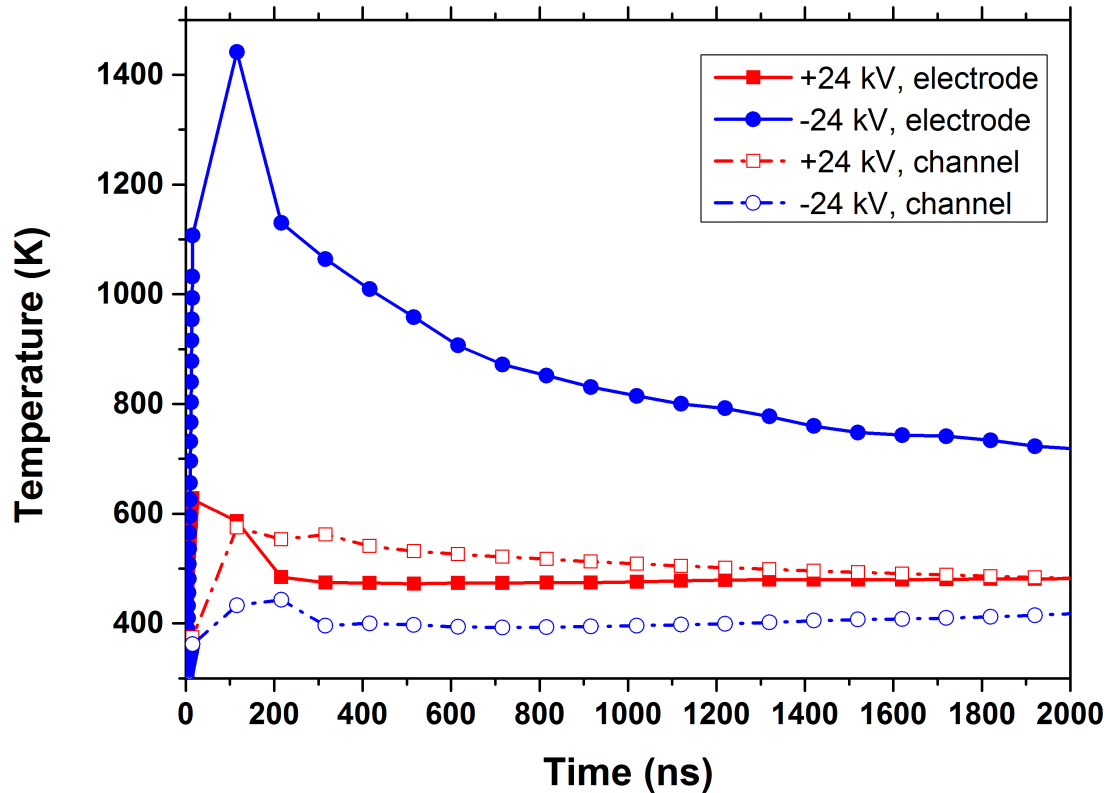


Figure 6.14: The temporal evolution of temperature during and after discharge for discharges in both polarities. Solid scatter line indicates the temperature in the vicinity of HV electrode ( $10\mu\text{m}$  from HV electrode), empty scatter lines indicates the temperature in the streamer channel (1 mm from HV electrode). Red lines refers to positive polarity and blue lines negative polarity.

under positive polarity is higher (to 500 K) than negative polarity (400 K). It has to be noted that, in this work the energy release from vibrational relaxation which is significant in time scale of  $\mu s$  is not calculated, thus the temperature at 10000 ns must have been underestimated. Since the temperature rise caused by vibrational relaxation will affect neither plasma parameters in nanosecond time scale nor pressure perturbations discussed below, this work will not pay more attention to it.

The generation and propagation of compression waves in nanosecond SDBDs is one of the most typical nSDBD phenomena observed both in experiments and simulations [9, 98, 140, 236]. In the present paper, the calculation is focused mainly on formation and propagation of the hydrodynamic perturbation within a small spatial scale at the early stage,  $t < 1 \mu s$ , referred to as the “early stage”. The longer time scale,  $1 < t < 5 \mu s$  is considered mainly for the reference to the majority of available experiments.

Figure 6.15 shows the calculated pressure map after the discharge initiated by positive and negative polarity voltage pulses. In both cases, a strong perturbation of pressure is observed along the dielectric surface (“wave 1” hereinafter) and at the edge of the exposed electrode due to fast and local heat release in chemical reactions (“wave 2”). The waves propagate with approximately constant slightly supersonic velocity at  $t < 2 - 2.5 \mu s$  and then slow down. For negative polarity discharge, waves 1 and 2 are well distinguished and propagate with  $v_1 = 1.2M$  and  $v_2 = 1.5M$  respectively. For positive polarity nSDBD, the wave 1 is more uniformly distributed above the dielectric;  $v_1 = v_2 \approx 1.35M$ . For negative polarity, increased energy release in the near-cathode region is clearly seen (“wave 3”,  $v_3 = 1.5M$ ). The near-cathode layer with elevated specific energy deposition and increased density of dissociated oxygen has been observed in calculations for atmospheric pressure air performed in [237]. A typical size of the layer was about  $10 \mu m$  in  $x$ -direction at 30 ns from the moment of start of the discharge. The authors of [237] concluded that the discharge of negative polarity should ignite the combustible mixtures better due to concentrated energy release and proved this experimentally on the example of  $C_2H_2$ :air mixtures for initial ambient temperatures and initial pressures in the range of 0.6 – 1 atm. Typical shadowgraphy and Schlieren measurements reported for a few microseconds and longer time, do not demonstrate significant difference for different polarities of the discharge [238]. To our knowledge, no direct experimental confirmation of high energy release at the early stage was available before in the literature.

Shadowgraphy images of the nSDBD discharge in the same configuration of the experimental system as described above optical emission images (Figure 6.10) are presented in Figure 6.16. Already at 200 ns, a perturbation, started from the near-dielectric zone along all the streamer channel (wave 1), is clearly seen for both

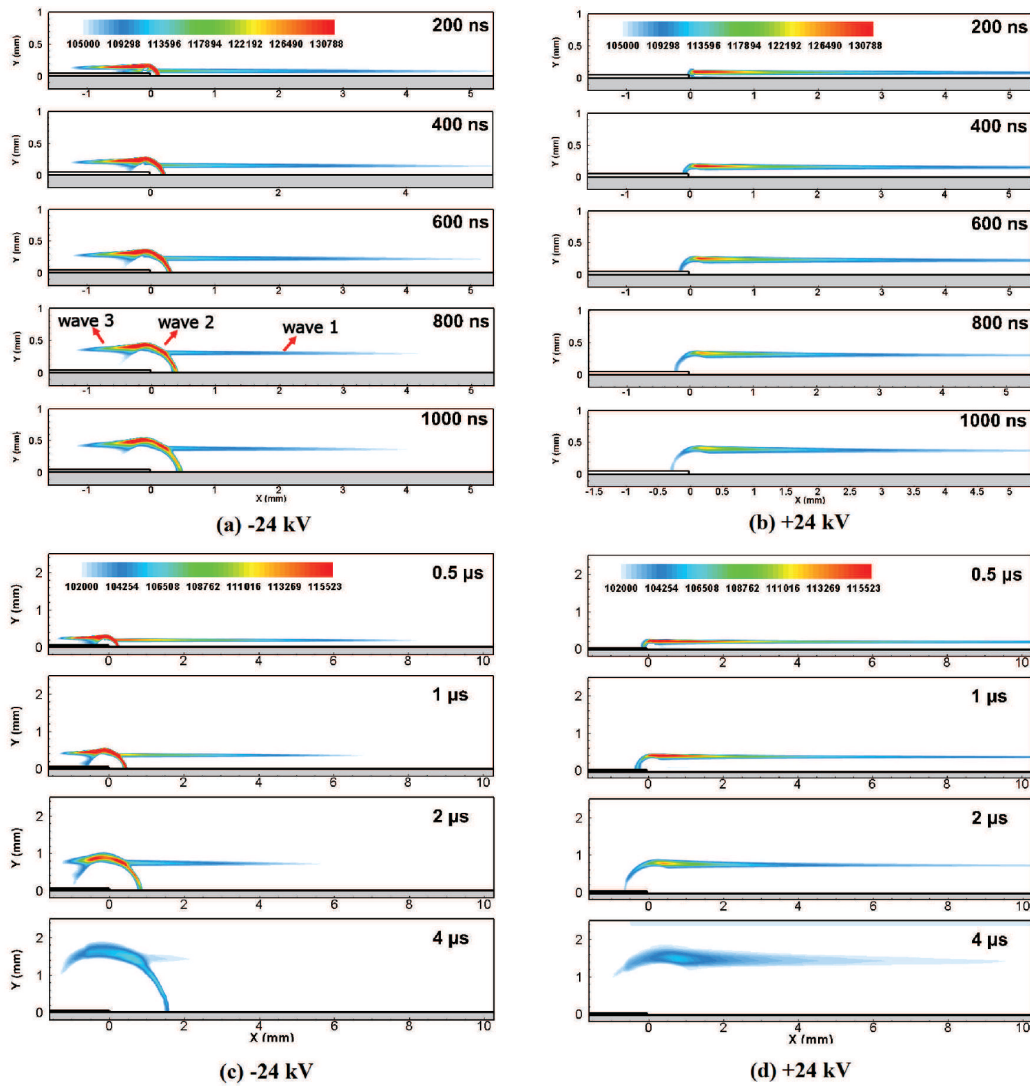


Figure 6.15: The evolution of the calculated pressure perturbations (in Pa): (a),(b) — short time scale,  $0.2 - 1 \mu\text{s}$ , (c),(d) — long time scale,  $0.5 - 4 \mu\text{s}$ ; (a),(c) — negative polarity discharge, (b),(d) — positive polarity discharge. The  $OX$  and  $OY$  scales are kept similar for (a), (b) cases and similar for (c), (d) cases, the short time scale maps are zoomed relative to the long time scale images. Wave 1, 2 and 3 are marked in 800 ns frame (see explanations in the text).

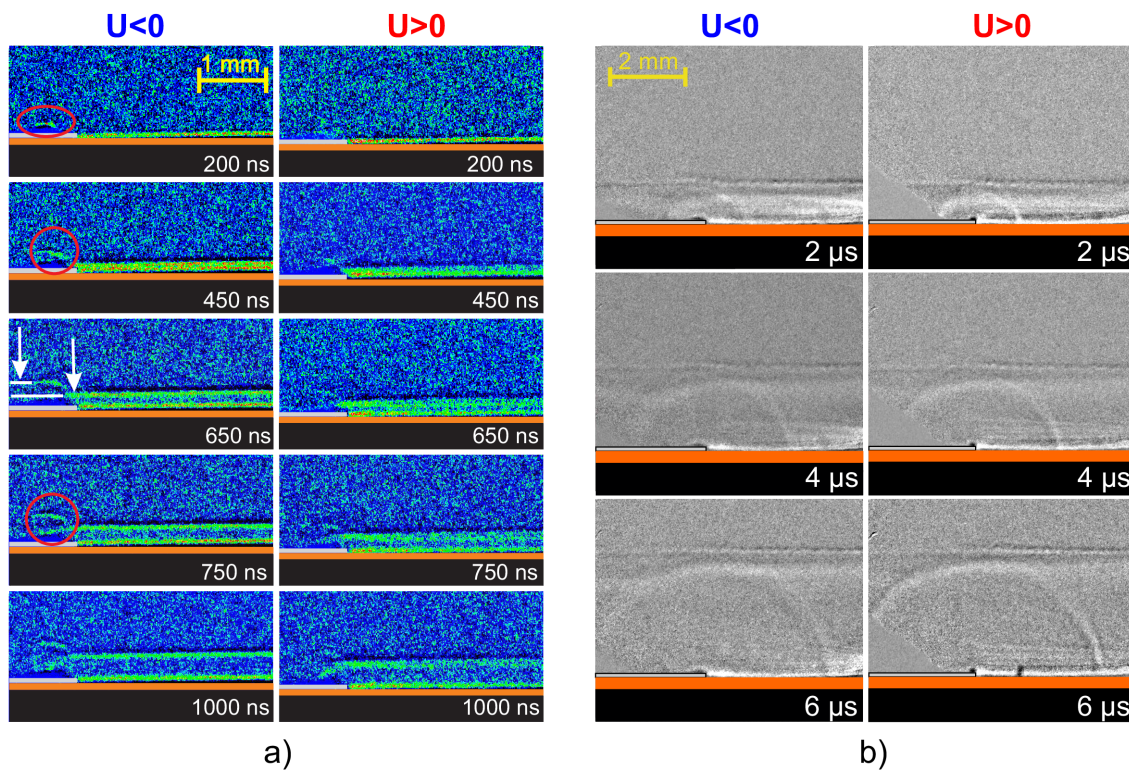


Figure 6.16: Hydrodynamic perturbations observed experimentally by shadowgraphy technique for different polarities of the high-voltage pulse: (a) — short time scale, 0.2 – 1  $\mu\text{s}$ ; (b) — long time scale, 2 – 6  $\mu\text{s}$ .

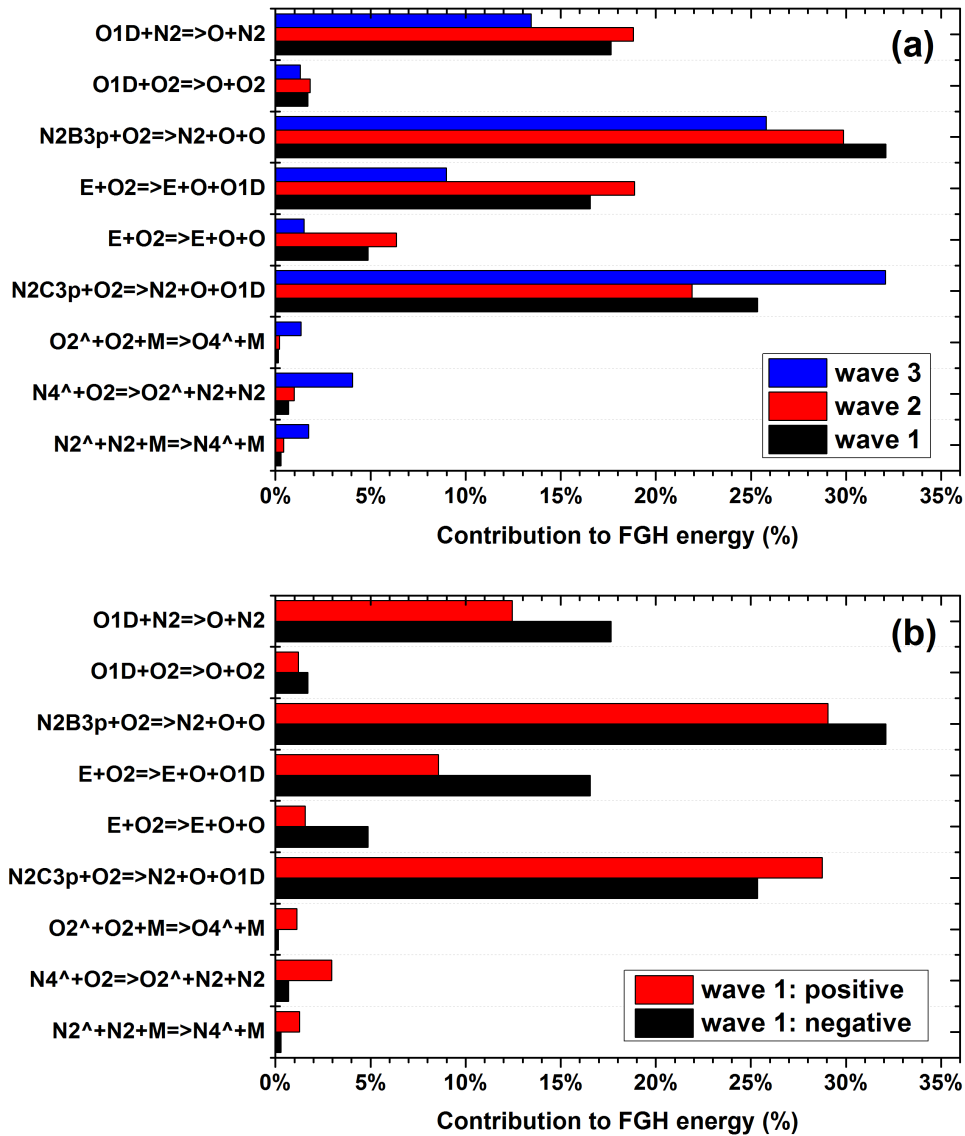


Figure 6.17: The constitution of the energy for fast gas heating. (a) the contribution fraction responsible for the generation of different compressive waves in negative polarity discharge; (b) the contribution fraction in wave 2 for both polarities.

polarities. The perturbation moves up in the vertical direction. At this stage, the perturbation near the high-voltage electrode (mainly above the electrode) can be distinguished only for negative polarity (wave 3). At later time scale,  $t > 1 \mu\text{s}$ , experimental measurements gives quite similar pictures for negative and positive polarity: a cylindrical wave propagating from the edge of the high-voltage electrode (wave 2) and a set of waves, “enveloping” each streamer (wave 1). A qualitative difference between experiments and numerical modeling, is an appearance of these waves. In numerical modeling, the waves 1 and 2 appear simultaneously; the intensity of the wave 2 at negative polarity is stronger, and at positive polarity is comparable to the intensity of the wave 1. In experiments, wave 1 along the streamers appears first. Wave 2, from the edge of the electrode, becomes clearly visible only starting from  $1 \mu\text{s}$ . The intensity of waves 1 enveloping the streamers is visibly higher at the early stage. The intensities of the waves 1 and 2 are nearly equal at  $t > 1 \mu\text{s}$ . The additional perturbation above the high-voltage electrode, wave 3, observed in numerical modeling and in the experiments at the negative polarity, appears at early stage and visible up to a few microsecond in the modeling; appears at early stage and does not exist already at a few microseconds in the experiments.

Numerical simulation make it possible to analyse the formation of wave “1”, “2” and “3” from the view of fast gas heating. A probe to the starting point of each wave results in Figure 6.17, in which the source reactions and their contributions to the formation of each wave are plotted and compared. Results show that different appearance of the wave 3 and the waves 1 and 2 is in correlation with quenching of  $\text{N}_2(\text{C}^3\Pi_u)$  level: at negative polarity,  $\text{N}_2(\text{C}^3\Pi_u)$  is produced in the thin layer over the high-voltage electrode; as a result, the flat wave 3 (see Figure 6.15 a) starts from the electrode. In authors opinion, sensitivity of hydrodynamic perturbation to kinetics can be used in the future to “measure” the input of different classes of reactions in the fast gas heating, comparing experimentally and numerically a fine structure of hydrodynamic perturbations at the early time scale,  $t < 1 \mu\text{s}$ .

## 6.7 Influence of dielectric parameters

Change of the discharge morphology and propagation is directly related to the changes in the deposition of the electrical charge and changes of the electric field in the vicinity of the dielectric. To analyse nSDBD morphology and propagation at different conditions, a parametric study has been performed. Calculations were made for atmospheric pressure air and for the parameters of the high-voltage pulses of the present work for two different cases. The case (A) was calculated for the constant thickness of dielectric,  $D = 0.5 \text{ mm}$ , and for 5 different dielectric permittivities:

$\varepsilon = 4, 8, 16, 40$  and  $80$ . The case (B) considered the constant dielectric permittivity,  $\varepsilon = 4$ , and the thickness of the dielectric changed:  $D = 0.5$  mm,  $0.75$  mm,  $1.0$  mm,  $2.0$  mm and  $5.0$  mm.

Figure 6.18 shows the morphology of discharge at both polarities when the streamer is fully developed. Dielectric permittivity changes nSDBD morphology in both polarities. For negative polarity, already in the baseline case (see Figure 6.5 a) the electron density pattern can be considered as a combination of two distinctive shapes: a diffuse “cloud” near the high-voltage electrode, and a triangle-like narrow pattern, sliding along the surface of the dielectric. With  $\varepsilon$  increase, the “cloud” elongates but the triangle-like narrow pattern shrinks and finally disappears. For positive polarity discharge, with  $\varepsilon$  increase the electric field map stays similar to the baseline case ( $d = 0.5$  mm,  $\varepsilon = 4$ ) with the only difference that the field in the streamer channel increases with  $\varepsilon$ . As a result, (i) the thickness of the electron density pattern increases ( $0.5$  mm at  $\varepsilon_3 = 80$  instead of  $0.1$  mm at  $\varepsilon_1 = 4$ ) transforming to the shape close to  $n_e$  at negative polarity and (ii) combination of high electric fields in the streamer channel and high electron density results in high densities of  $N_2(C^3\Pi_u)$ . With increase of dielectric permittivity, a channel of the positive polarity streamer should become to be “visible” experimentally.

Figure 6.19 presents the x-t diagram of the discharge propagation front for different  $\varepsilon$  values and corresponding electric current values under different  $\varepsilon$ . For both polarities, the propagation velocity decreases at high  $\varepsilon$ , the dynamics of propagation of positive nSDBD at  $\varepsilon = 80$  even copies that of negative nSDBD at  $\varepsilon = 4$ . The electric current increases with  $\varepsilon$ , reaching  $50 - 100$  A/cm for  $\varepsilon_2 = 16$  and  $150 - 200$  A for  $\varepsilon_3 = 80$ .

The following conclusions can be made from numerical calculations: with  $\varepsilon$  increase, the streamer thickness (calculated by electron density) increases significantly, by a factor of 5 at changing  $\varepsilon$  from 4 to 80; the electric fields, for  $\varepsilon > 10$ , should be enough to observe the emission from the streamer channel at both polarities of the high-voltage pulse. A special care should be taken to avoid the breakdown of the dielectric with increasing electrical current.

The influence of dielectric thickness to discharge morphology and propagation was studied following the same methodology as above. Figure 6.20 shows the morphology of discharge at both polarities when the streamer is fully developed. In this case, nSDBD morphology based on electron concentration only slightly changes but not for the optical emission in view of experiment: for negative polarity discharge, the “cloud-like” feature will stay near the high-voltage electrode, and the “needle-like” shape of the electron density will transform to a shape close to the streamer at positive polarity but with lower values of the electron density. The electric field behind the streamer head will drop down, and finally, the emission

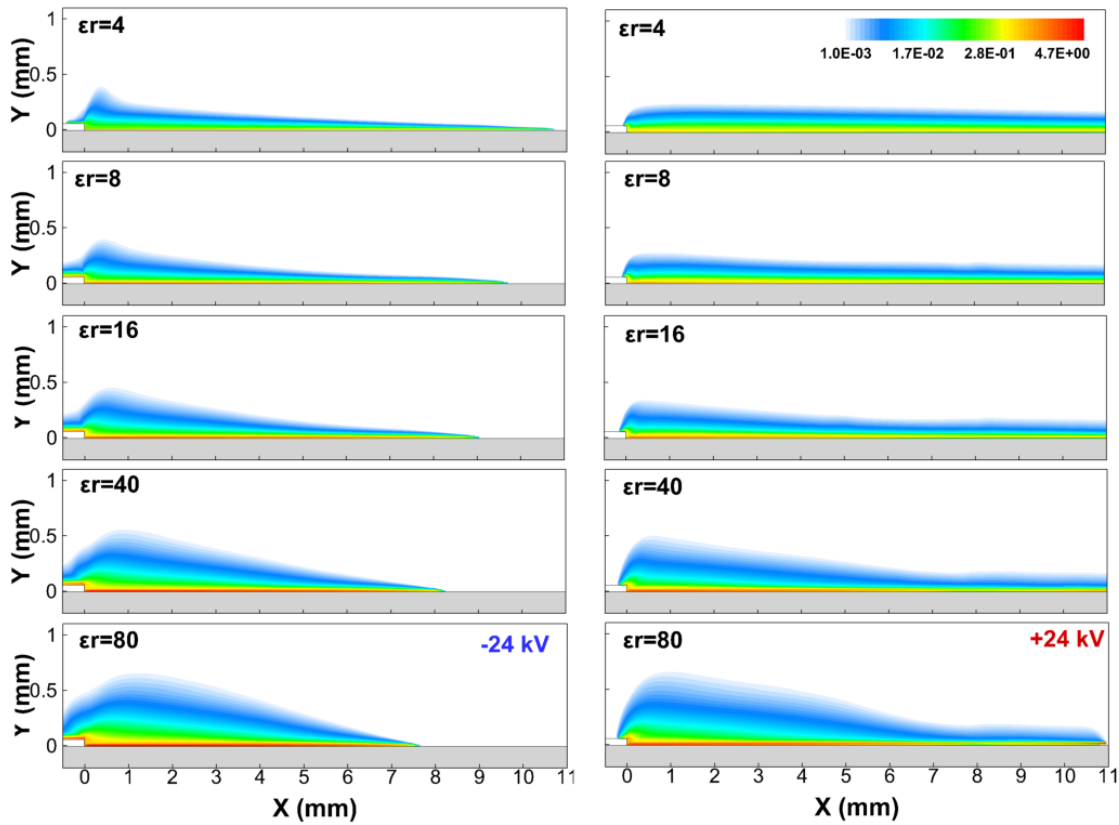


Figure 6.18: Calculated electron density (in unit  $\text{m}^{-3}$ ) under relative dielectric permittivity  $\varepsilon = 4, 8, 16, 40$  and  $80$  under both polarities. The left column is for negative polarity discharges and the right for positive.

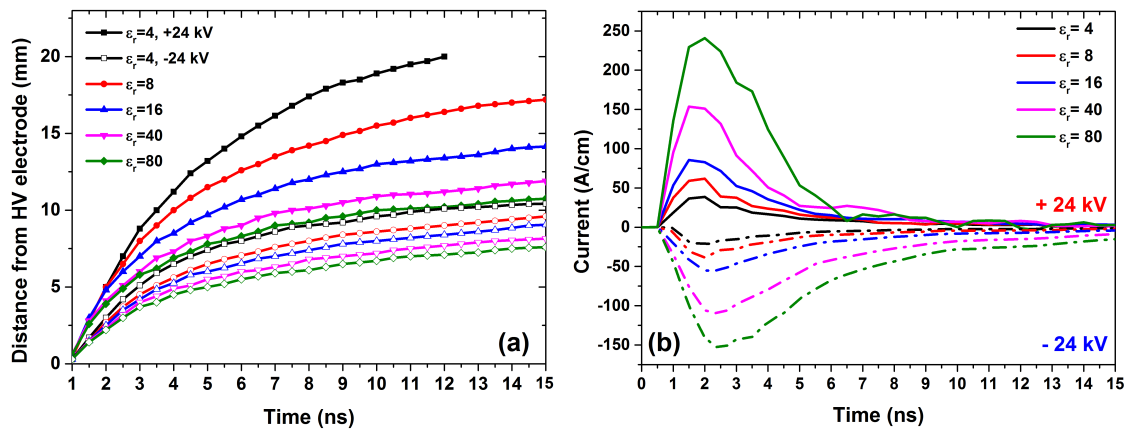


Figure 6.19: The (a)  $x$ - $t$  diagram and (b) current value calculated under relative dielectric permittivity  $\varepsilon = 4, 8, 16, 40$  and  $80$  for both polarities. Solid scatter lines in (a) refer to positive polarity discharges and empty scatter lines refer to negative ones.

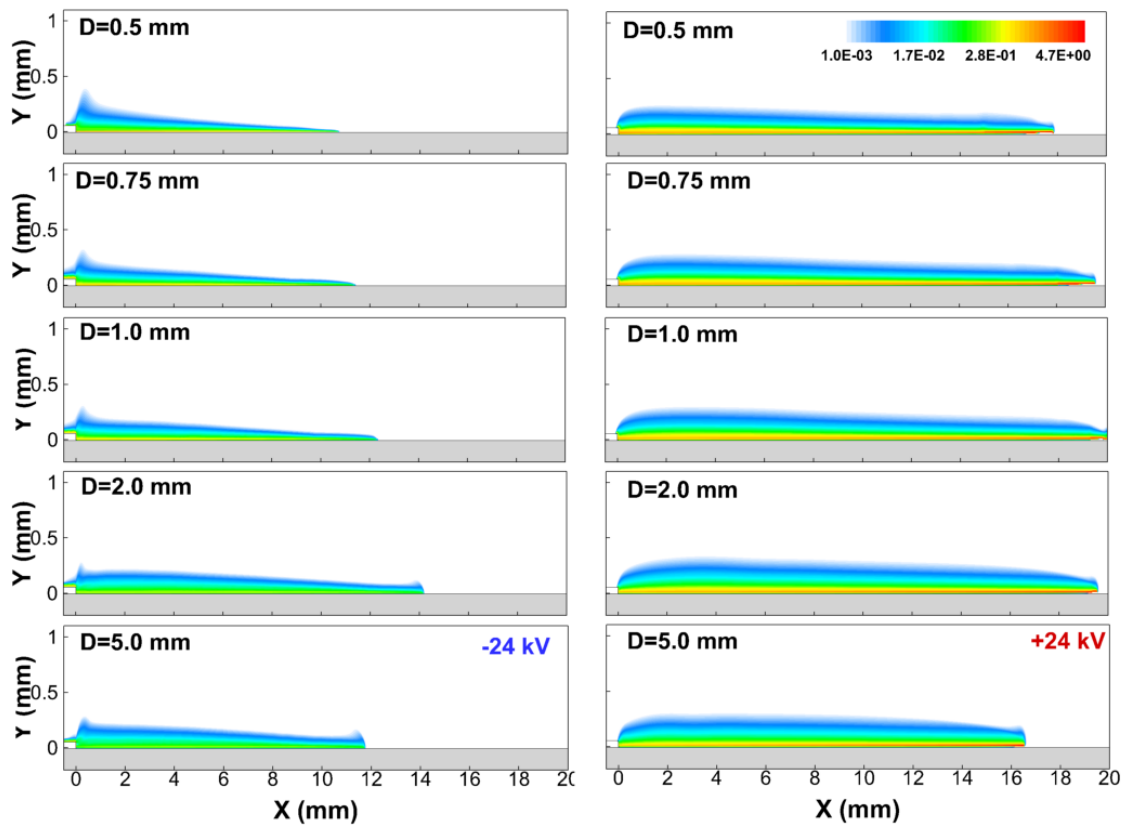


Figure 6.20: Calculated electron density (in unit  $m^{-3}$ ) under dielectric thickness  $D = 0.5$  mm,  $0.75$  mm,  $1.0$  mm,  $2.0$  mm and  $5.0$  mm under both polarities. The left column is for negative polarity discharges and the right for positive.

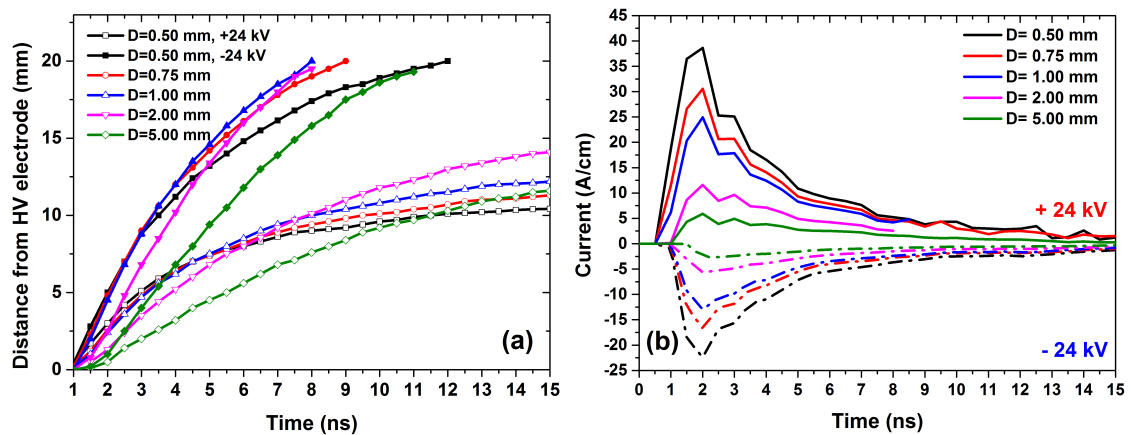


Figure 6.21: The (a) x-t diagram and (b) current value calculated under dielectric thickness  $D = 0.5$  mm,  $0.75$  mm,  $1.0$  mm,  $2.0$  mm and  $5.0$  mm for both polarities. Solid scatter lines in (a) refer to positive polarity discharges and empty scatter lines refer to negative ones.

from the streamer channel will not be detected experimentally. For positive polarity discharge, with dielectric thickness increase the electric field in the channel will be totally concentrated in the narrow, tens of microns, gap near the dielectric, and the electron density layer will not change noticeably. As a consequence, no emission will be seen experimentally from the streamer channel.

Another visibly change is the maximum propagation distance for negative polarity (for positive polarity the streamer will reach the end of the dielectric in this work). With the increase of the dielectric thickness, the maximum propagation distance streamer increases from 10 mm when  $D=0.5$  mm to maximum of 14 mm when  $D= 2.0$  mm, and decrease again. To analyse the physics of the changes in streamer propagation, the x-t diagram of propagation of ionization head in Figure 6.21 (a) together with current values in (b) are used.

When increasing the dielectric thickness slightly from 0.5 mm to 1.0 mm in step of 0.25 mm, it is clearly seen for both polarities, the streamers propagate in almost the same velocity in the initial 4-5 ns, then slow down in different rates. For larger dielectric thickness, the electric field in the ionization head and between streamer channel and dielectric is relatively low, the loss of charges on the dielectric become slower (in other words, the streamer becomes less attached to the dielectric surface), thus the weaken the slowing down of propagation and elongate the propagation distance. Further increase of dielectric thickness from 1.0 mm to 5.0 mm, a significant drop of streamer propagation velocity can be observed starting from the beginning of the discharge, making propagation distance shorten again. Electrical current decreases noticeably with the increase of dielectric thickness: to 12 – 25 A/cm at  $d_2 = 1$  mm and to 3 – 6 A/cm at  $d_3 = 5$  mm.

## 6.8 Influence of ambient pressures

The morphology of the transient discharge is very sensitive to the gas density, composition of gas mixtures and the polarity and/or frequency of applied pulses. It was found recently [57] that at pressure and/or voltage increase, a single-shot nSDBD transforms into a filamentary form. Streamers start from the HV electrode, slow down and stop. At this instant, a few nanosecond after the discharge start, a set of equidistant channels-filaments start from HV electrode as a secondary ionization wave.

Figure 6.22 shows the morphology of nSDBD under atmospheric pressure (a) and elevated pressures (b) and (c). A transition from streamer mode in (b) to filamentary mode in (c) under the same pressure is observed experimentally. More systematic experiments conducted in [57] give the “filamentary curve” in Figure 6.22 (d), below

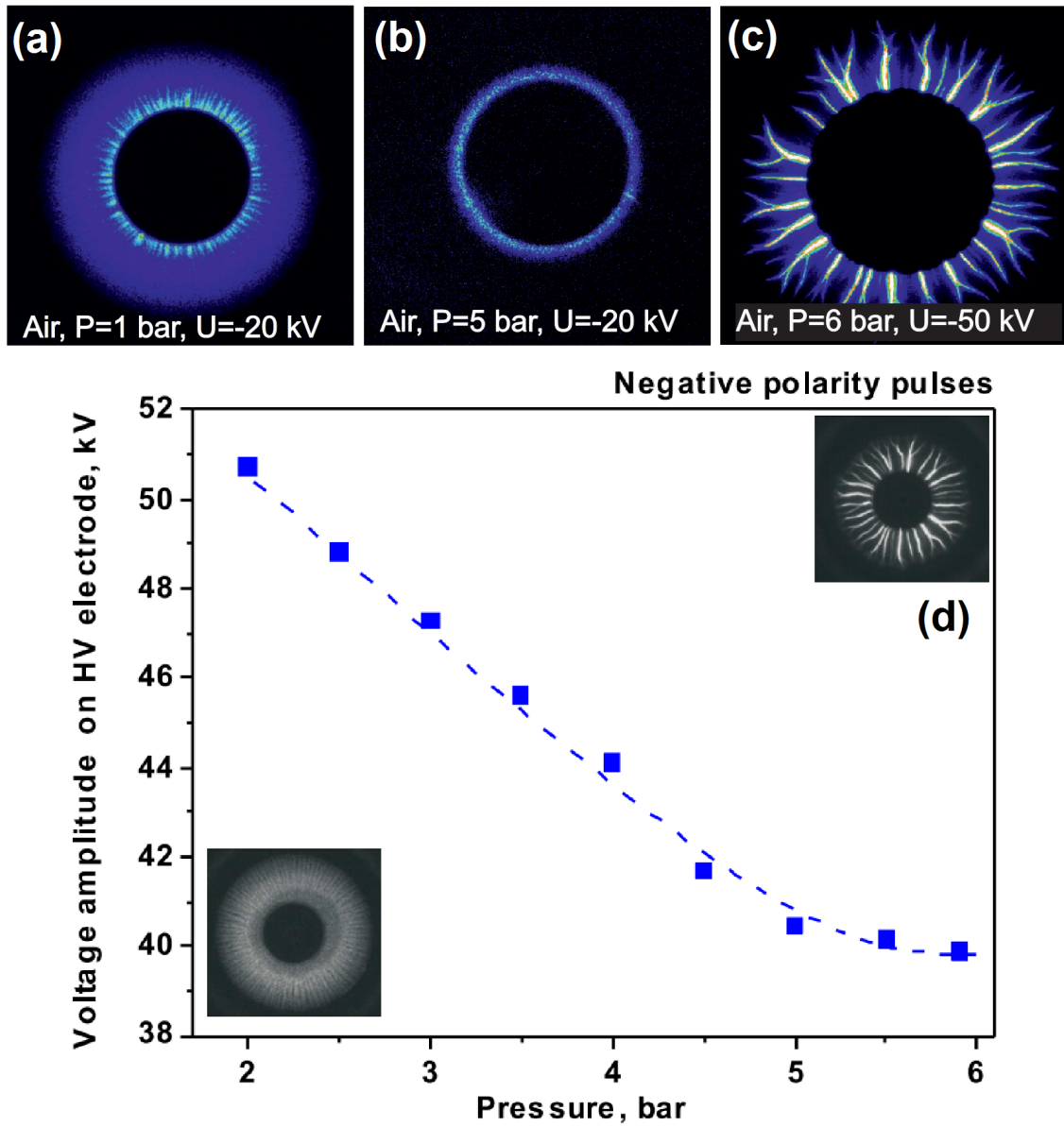


Figure 6.22: Discharge morphology of nSDBD in an asymmetric configuration and filamentary curve. (a) P=1 bar, U=-20 kV, streamer; (b) P=5 bar, U=-20 kV, streamer; (c) P=6 bar, U= -50 kV, filaments.

the curve discharge is in the form of streamer while above is in filament.

Currently no strict explanation of filamentary nSDBD discharge appearance or filaments propagation can be found. Insufficient amount of experimental data does not allow building a complete model. The 3D self-organizing structure and the combination of non-equilibrium and local temperature equilibrium conditions in filamentary discharges also propose severe challenges to the community of numerical simulation.

The two-dimensional PASSKEy code can be used to calculate the behaviours of nSDBD at elevated pressures below the filamentary curve, when the discharge is still in streamer mode and can be described in quansi-2D approximation. Figure 6.23 shows the calculated morphology of nSDBD operated under 1 bar, 3 bar and 5 bar with applied voltage of  $\pm 24$  kV. The streamer channel shrinks in both thickness and length with the increase of ambient pressures, which can also be seen in Figure 6.22 (b).

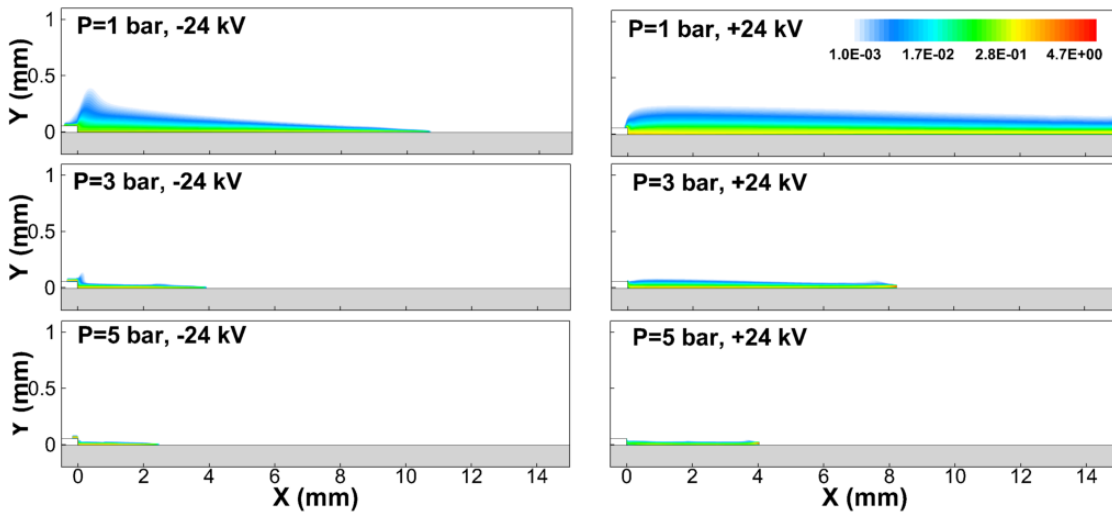


Figure 6.23: Calculated electron density (in unit  $\text{m}^{-3}$ ) under pressure  $P= 1$  bar, 3 bar and 5 bar for both polarities. The left column is for negative polarity discharges and the right for positive.

Despite the fact that no theoretical descriptions for filamentary discharges in nSDBD are available, the calculation of nSDBD at elevated pressures at higher voltages above filamentary curve is still necessary, as it provides the information before the transitions happen, thus to help analysing the possible mechanisms of streamer-to-filament transition. To reduce complexity, we start from a base case without fluid equations coupling, and obtained the morphology of high pressure ( $P= 3$  bar, 5 bar) nSDBD above filamentary curve in Figure 6.24.

The increase of applied voltage does not bring principle changes to the discharge

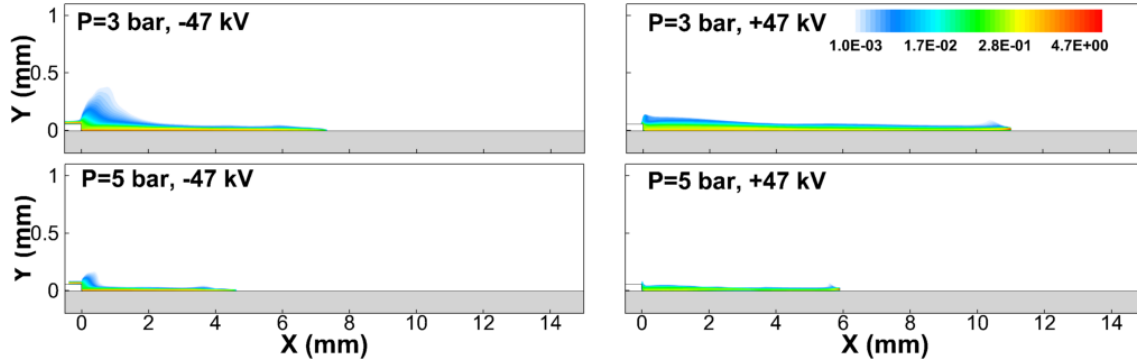


Figure 6.24: Calculated electron density (in unit  $\text{m}^{-3}$ ) under pressure  $P= 3$  bar and 5 bar for both polarities. The left column is for negative polarity discharges and the right for positive. The results are obtained without fluid coupling.

morphology. The “cloud-like” region grows for negative polarity, and the propagation length of streamer at both polarities is elongated. Deeper insight into the high pressure discharge can be achieved by probing the line distribution of electric field and electron density  $20 \mu\text{m}$  above the dielectric under  $P=5$  bar,  $U=-47$  kV in Figure 6.25 (a)-(d). For negative polarity the physics of the streamer channel shown in Figure 6.25 (a) and (c) are similar with that of Figure 6.6 (a) and Figure 6.8 (a), with quickly decay of electron concentration during propagation and relatively high electric field in the channel. For positive polarity, an increase of electric field 2mm after the ionization front is observed in Figure 6.6 (b), leading to a region of higher electron density near the HV electrode.

In atmospheric pressure nSDBD the characteristic time of hydrodynamics responses is longer than the pulse duration thus one can neglect fluid equations in modelling. Under high pressure condition, both characteristic time and spatial scale of discharge reduces. The fast gas heating in the cathode sheath and in streamer channel could further reduce the characteristic time of hydrodynamics in local region, this thermalization of local region could possibly lead to the changes of electric characteristics in nSDBD. This assumption is confirmed by turning on the fluid equations for high pressure conditions. The morphologies of discharge operated under the same conditions as in Figure 6.24 but with fluid equations coupled are shown in Figure 6.26.

Taking into account the influence of hydrodynamics to the model doesn’t change the propagation length of streamers but leads to visible changes in morphology of nSDBD for high pressures under high applied voltage. At negative polarities, similar combination of “cloud-like” discharge near the HV electrode and “triangle” like shape in the channel as in 1 bar case are observed for both 3 bar and 5 bar cases. At positive polarities, higher concentration of electrons is observed near the

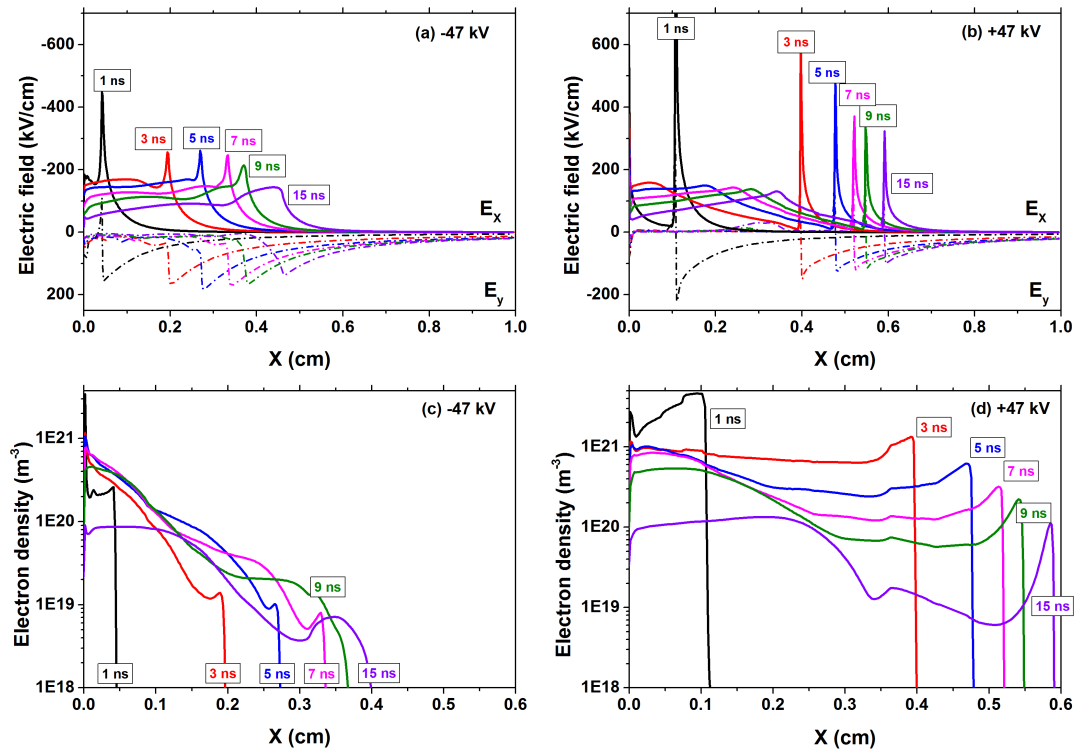


Figure 6.25: The distribution of electric field ((a) and (b)) and electron density ((c) and (d)) along line probe  $25\mu\text{m}$  above dielectric surface at  $P=5$  bar. The results are obtained without fluid coupling.

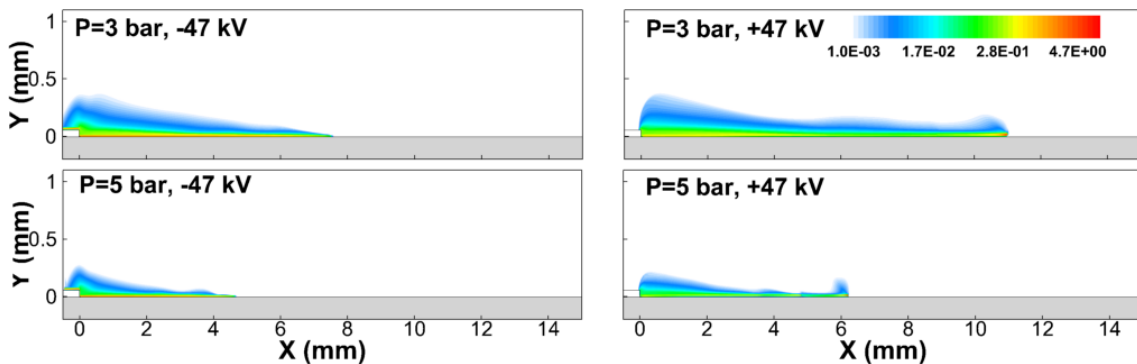


Figure 6.26: Calculated electron density (in unit  $\text{m}^{-3}$ ) under pressure  $P=3$  bar and 5 bar for both polarities. The left column is for negative polarity discharges and the right for positive.

HV electrode. For both polarities, the thickness of streamer channels increase.

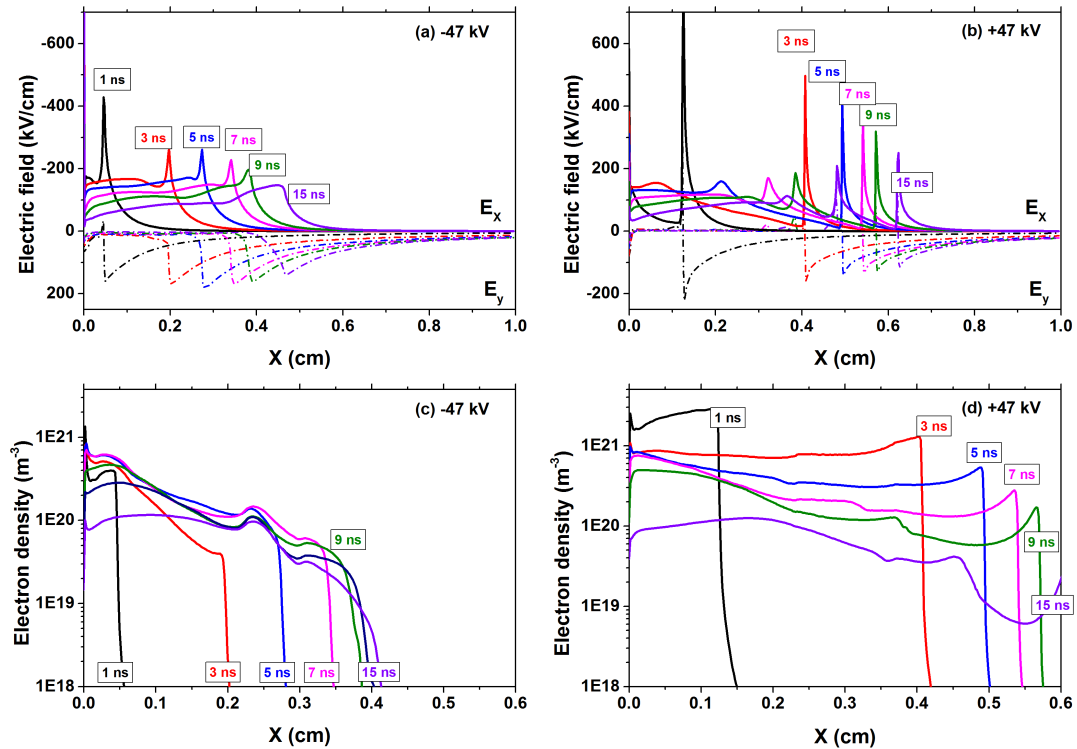


Figure 6.27: The distribution of electric field ((a) and (b)) and electron density ((c) and (d)) along line probe  $25\mu m$  above dielectric surface at  $P=5$  bar.

The changes brought by fluid coupling can be quantified according to the line plot of electric field and electron density shown in Figure 6.27. A comparison between Figure 6.27 and Figure 6.25 helps to clarify the differences and analyse the mechanism of changes: (i) At negative polarity, although there are no obvious changes in electric field distribution, the electron density in the channel can be 5 times higher than the case without fluid coupling. (ii) At positive polarity, there appears a second ionization head at about 1-2 mm behind the first ionization head after 7 ns. The first ionization head continues propagating and leaves a pre-ionized region. Then the high electron concentration region expands with the propagation of the second ionization head. For both polarities, the changes in electron density and electric field distribution in 5 bar condition are caused by combining effects of significant increase of temperature, pressure and slightly decrease of density. Calculated results show that, there is a temperature increase of 700 K for negative polarity near the cathode and 600 K for positive polarity in the channel. Pressure is almost half the ambient pressure. Neutral density of gas varies from  $203 \text{ mol}/\text{m}^3$  to  $198 \text{ mol}/\text{m}^3$ , this approximately 2.5% change of density increases  $E/N$  a bit, and leads to higher ion-

ization rate. It has to be noted that, here in PASSKEy code the Helmholtz model for photo-ionization uses pressure and partial pressure of oxygen as tuning parameters, as there is huge changes of pressure in the discharge region, photo-ionization plays an extremely important role in determining the morphology of discharges.

## 6.9 Conclusion

Two-dimensional parallel PASSKEy (“PARallel Streamer Solver with KinEtics”) code coupling plasma and hydrodynamics has been used to model development of a nanosecond surface dielectric barrier discharge (nSDBD).

Calculations of negative and positive polarity streamer have been performed for atmospheric pressure air, voltage amplitude  $U = \pm 24$  kV on the electrode, dielectric thickness  $d = 0.5$  mm and dielectric permittivity  $\varepsilon = 4$ . The results were compared with experimentally obtained data. Discharge velocity, electrical current, time-resolved structure of 2D emission of the second positive system of molecular nitrogen and hydrodynamic perturbation measured in the time interval  $0.2 - 5 \mu\text{s}$  were the subject of comparison. To our knowledge, this is the first detailed comparison of numerical calculations and experiments performed for the same parameters of the nSDBD. Based on the experimental validated calculations in 1 bar condition, the detailed characteristics of discharges and fast gas heating were obtained. In addition, parametric calculations for  $D = 0.5 - 5$  mm,  $\varepsilon = 4 - 80$  have been done for both polarities. Initial investigations of high pressure nSDBD in streamer mode were also conducted.

It was confirmed that for different geometries of electrodes, the velocity of the discharge front is about  $2 - 3$  mm/ns for negative and  $\sim 5$  mm/ns for positive discharge at the early stage of propagation. It drops down to  $0.1$  mm/ns and less for the negative polarity streamer, while the positive polarity streamer continues to propagate with a velocity progressively decreasing to  $0.4 - 0.5$  mm/ns at the end of the pulse. A good correlation between experimental data and numerical calculations confirm that the model takes into account the main processes responsible for a surface streamer propagation. Measured and calculated electrical current through the discharge are in reasonable correlation, comprising  $20 - 50$  A/cm depending upon conditions.

Two-dimensional maps of the electron density, absolute value of the electric field and  $\text{N}_2(\text{C}^3\Pi_u)$  density were calculated. The existence of narrow zones of high electric field, a few microns for negative polarity discharge and a few tens of microns for positive polarity discharge, has been confirmed numerically. The 2D maps of the emission intensity for two polarities of the nSDBD in the plane perpendicular to the electrode system were obtained experimentally for the first time. The main aim of the calculations was to compare the structure of experimentally measured and calculated  $\text{N}_2(\text{C}^3\Pi_u)$  distribution, and to analyze the emission of the second positive system of molecular nitrogen on the basis of 2D distributions of the electron density and electric field.

Electron density distribution at negative polarity consist of two distinctive zones:

a “cloud-like” diffuse zone near the high-voltage electrode and a “needle-like” zone propagating along the dielectric. Positive polarity streamer produces relatively uniform along the dielectric, a constant thickness pattern of the electron density. The electric field in the bulk of the streamer channel of negative polarity is high, about 100 Td; for the streamer channel of positive polarity the field is low, less than 40 Td. Calculated  $N_2(C^3\Pi_u)$  density repeats the main peculiarities of distributions of electrons and field in time and space. Thickness of the channel of the surface streamer calculated from the distribution of  $N_2(C^3\Pi_u)$  density is about 1.5 times larger than the radius calculated from the electron density in the first 5 ns and then becomes thinner. The most distinctive experimentally observed difference, namely a non-zero level of emission in the developed channel in the negative polarity streamer and absence of emission in the positive polarity streamer is reproduced in the calculations.

The constitution of energy release for fast gas heating differs spatially for negative and positive polarity. At negative polarity, the energy fraction is rather uniform across the channel: quenching reactions contribute up to 75% the energy release, dissociation of  $O_2$  molecules contribute 20%, and other reactions involving charged species contribute the rest (<5%). For a positive polarity nSDBD, the constitution of energy release changes: at near electrode region ( $X < 5$  mm) quenching and  $O_2$  dissociation still dominate as in negative polarity, but in streamer channel far from the HV electrode, the fraction of energy release from reactions of charged species increases from 5% to 35%.

Weak shock waves, appearing around the streamers and near the edge of the high-voltage electrode at sub-microsecond time scale, is a consequence of a fast gas heating in plasmachemical reactions. The main processes responsible for the formation of hydrodynamic perturbation, are reactions of quenching of  $N_2(C^3\Pi_u)$  and  $N_2(B^3\Pi_g)$  by molecular oxygen, and reaction of  $O(^1D)$  quenching by  $O_2$ . A specific zone of energy release corresponding to  $N_2(C^3\Pi_u)$  production, was found numerically and experimentally over the high-voltage electrode for the discharge of the negative polarity.

Parametric calculations provided for 5 different dielectric permittivities ( $\varepsilon=4, 8, 16, 40, 80$ ) and 5 different values of the thickness of the dielectric ( $D = 0.5$  mm, 0.75 mm, 1.0 mm, 2.0 mm and 5.0 mm) show that discharge changes in a quite complex way. In general, electron density and electric current will increase at higher  $\varepsilon$  or lower  $D$ . Discharge propagation length will increase when reducing  $\varepsilon$  or increasing dielectric thickness when  $D \geq 2.0$  mm. The optical thickness of the streamer significantly increases with  $\varepsilon$  and slightly with  $D$ , at high  $\varepsilon$  value, the morphologies of the discharges become similar for both polarities.

Parametric calculations provided for 3 different pressures ( $P= 1, 3$  and 5 bar)

show that streamer will shrink both in length and thickness with the increase of pressures. At high pressures and high voltage condition in which the filamentary discharge is observed experimentally, the calculation of streamer phase nSDBD has to couple directly with fluid equations.

For all calculated cases, there exists a long region of plasma with relatively uniform parameters, a channel, where plasma properties, in spite of the non-uniformity of the surface streamer in the direction perpendicular to the dielectric, can be analyzed on the basis of the electrical current and  $N_2(C^3\Pi_u)$  emission. This region is the most important when analyzing nSDBD as a source of active species.

---

---

# Chapter 7

---

## General conclusions

### 7.1 Contributions of the present work

This work is focused on the numerical study of nanosecond capillary at moderate pressure and surface dielectric barrier discharges at atmospheric pressure. For both discharges, the delivered energy is tens of mJ, but due to the different pressures, the specific delivered energy differs by at least one order of magnitude. The kinetics, transport and fluid response in these two configurations were investigated according to a broad set of experimental results obtained in the same scientific group, allowing detailed analysis of experimental data and validation of developed numerical code.

Detailed 0D kinetics and optical actinometry were the subjects of interest while studying a nanosecond capillary discharge. Density of O-atoms in the discharge and near afterglow was studied in air at 28.5 mbar with 5.3% addition of Ar. O-atoms density reaches as high values as  $6 \times 10^{17} \text{ cm}^{-3}$  in the early afterglow due to the quenching of excited molecular nitrogen. The high dissociation degree of oxygen (50%) indicates that the nanosecond capillary discharge can be suggested as an efficient dissociative tool through quenching of excited species.

A reduced kinetic scheme with 48 reactions has been suggested to describe the consistent behaviours of electrical current, field, density of Ar( $2p_1$ ), O( $3p^3P$ ) and N<sub>2</sub>( $C^3\Pi_u$ ). The scheme is selected on the basis of the kinetics code ZDPLASKin with the help of the of supplementary home-made code for sensitivity analysis.

Based on the reduced scheme, it was found that electron quenching and three-body recombination reactions become significant at the conditions of a high specific

energy deposition. A modification of the “traditional” Ar-based actinometry has been suggested.

The restrictions of a 0D kinetics model is that it needs the experimentally measured  $E/N$  or current waveform. To have a self-consistent description, 2D calculations of nanosecond capillary discharge based on nonPDPsim code have been conducted. The calculations were made for the same pressure and voltage,  $P = 28.5$  mbar and  $U = 20$  kV, respectively. A special attention has been devoted to analysis of changes of kinetics in the afterglow as a function of specific deposited energy.

In the discharge propagation stage, two modes were identified: the fast ionization wave (FIW) mode and the streamer mode. The FIW mode provides higher  $E/N$  in the ionization head and higher electron density in the channel. Both modes give a good uniformity of the parameters along the tube. With decrease of the tube radius, the velocity of ionization front decreases while the shape changes, from a “bulk” shape where electron density is distributed smoothly in the radial direction, to a “hollow” shape where there is a higher electron density near the tube wall, finally to a “bullet” shape when the peaks of the electron density and of  $E/N$  near the wall merge to have higher density and field in the capillary.

In the afterglow stage, the evolution of  $N_2(C^3\Pi_u)$  was used as a marker to evaluate the influence of kinetics on the discharges under different specific energy deposition  $E_{dep}$ . It was found that, starting from  $E_{dep} > 0.3$  eV/mol, the decay rate of  $N_2(C^3\Pi_u)$  will be significantly accelerated by the electron quenching reaction, and the spatial profile of  $N_2(C^3\Pi_u)$  will be changed by kinetics. Further increase of  $E_{dep} > 0.6$  eV/mol leads to decrease of  $N_2(C^3\Pi_u)$  density in plasma channel.

Study of nSDBD development and of the nSDBD influence on chemistry and on fluid reponses in the afterglow stage demands higher spatial resolution and longer time scale calculation. The computational cost will increase dramatically. A two-dimensional parallel PASSKEy (“PARallel Streamer Solver with KinEtics”) code coupling plasma and hydrodynamics has been developed to achieve higher flexibility and performance. For  $10^6$  mesh cells and 38 kinetic reactions, the calculation of a 2 cm surface streamer propagated under the voltage pulse about 24 kV in amplitude takes 8 – 20 hours on a single HPC node (Intel Xeon E5, 2.40 GHz, 16 cores).

Discharge in synthetic air at 1 bar is studied. Calculations of negative and positive polarity nSDBD have been performed with voltage amplitude  $U = \pm 24$  kV on the electrode, dielectric thickness  $d = 0.5$  mm and dielectric permittivity  $\varepsilon = 4$ . The results were compared with experiments for the same parameters of the nSDBD. The characteristics of plasma, parameters of fast gas heating and fluid responses were obtained. To our knowledge, this is the first detailed comparison of numerical calculations and experiments performed for the same parameters of the nSDBD.

2D maps of the electron density and  $E/N$  were calculated. Electron density

distribution at negative polarity consists of a “cloud-like” diffuse zone near the high-voltage electrode and a “needle-like” propagating zone along the dielectric. Positive polarity streamer is produced relatively uniform along the dielectric, with a constant but smaller channel thickness. The different profiles and electron motion manner result in higher electric field in the channel for negative polarity, about 100 Td and lower for positive polarity, less than 40 Td.

The difference in the electron density and the field for different polarities changes the discharge propagation. At the early stage, the streamer velocity is about 2 – 3 mm/ns for the negative discharge, while due to higher field in the ionization head, the value is  $\sim 5$  mm/ns for the positive discharge. At the end of the pulse, the velocity drops down to 0.1 mm/ns and less for the negative polarity streamer, while the positive streamer continues to propagate with a velocity progressively decreasing to 0.4 – 0.5 mm/ns .

The optical emission modelled by  $N_2(C^3\Pi_u)$  profile differs for polarities. The thickness of streamer channel decided from  $N_2(C^3\Pi_u)$  density is about 1.5 times larger than the thickness calculated from the electron density in the beginning of discharge. Once the streamer is developed, a non-zero level of emission exists in the negative polarity streamer channel but is absent under positive polarity. Emission distribution is differed from electron density distribution.

The fast gas heating is analysed. At negative polarity, the quenching reactions contribute up to 75% to the released energy, dissociation of  $O_2$  molecules contribute 20%, and other reactions involving charged species contribute the rest (<5%). At positive polarity nSDBD, quenching and  $O_2$  dissociation dominate only at near electrode region, but the fraction of energy released from reactions of charged species increase significantly in streamer channel far from the HV electrode. A specific zone of higher energy release corresponding to  $N_2(C^3\Pi_u)$  production, was found numerically and experimentally over the high-voltage electrode for negative discharge, leading to an additional shock wave near the edge of HV electrode at sub-microsecond time scale.

Parametric 2D calculations of nSDBD have been performed for a broad range of permittivities ( $\varepsilon=4-80$ ) and thickness ( $D =0.5-5.0$  mm) of the dielectric. The integral discharge parameters (the electron density, the current, the propagation length) were predicted. Discharge propagation length will increase when  $\varepsilon$  decrease or dielectric thickness increase over  $D \geq 2.0$  mm. The optical thickness of the streamer significantly increases with  $\varepsilon$  and slightly with  $D$ , at high  $\varepsilon$  value, the morphology of the discharges become similar for both polarities. Varying the dielectric properties of the electrode is a promising way to obtain a comparison between the theoretical predictions and experimental observations.

## 7.2 Perspectives and future work

The results presented in the thesis provide a description of nanosecond pulsed capillary discharge at relatively low pressure (27 mbar) and of surface dielectric barriers discharge at atmospheric pressure by fluid method. The perspectives and future work will be focused mainly on PASSKEy code and calculations of nSDBD in extended time scale.

Discharges under elevated pressures, 3 and 5 bar, were calculated for a trial in this work. At high pressures and high voltage condition in which the filamentary discharge is observed experimentally, the electron energy equation based on local mean energy approximation (LMEA) should be introduced. Some special boundary conditions, like high energy electron flux from cathode will be used to study nSDBD at elevated pressures. To resolve the cathode region in negative polarity, and to reduce the computational load, the technique of structured adaptive mesh refinement (SAMR) will be introduced. A new data structure based on the framework of SAMR has been finished and tested for PASSKEy, as is shown in Figure 7.1.

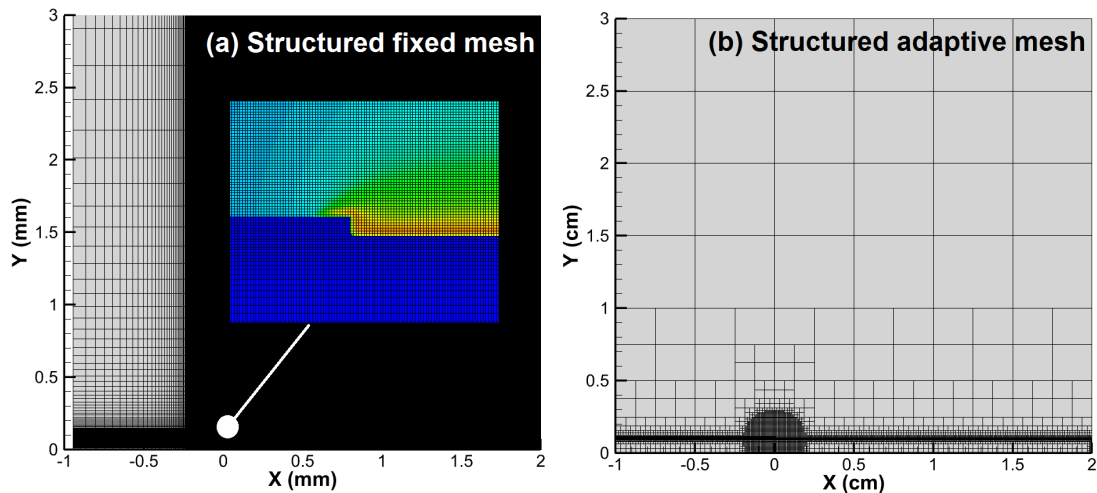


Figure 7.1: Distribution of mesh grid in the framework of (a) structured fixed Cartesian mesh and (b) structured adaptive Cartesian mesh. Significant mesh grids can be saved in the framework of (b)

Responsible reactions of fast gas heating differ in discharge regions. This leads to the possibility of checking kinetics schemes suggested from different groups: we can calculate the shock waves caused by fast gas heating due to different kinetics and compare them to experimental facts, to decide the correct ones. To have higher accuracy, vibrational relaxations of excited species will also be included in the kinetics scheme. Reactions concerning combustion will also be considered to make

PASSKEy able for calculating the ignition processes. A preliminary calculation of hydrodynamics after discharge with/without chemical reactions for combustion in Figure 7.2 shows present code's potential capability as a tool for studying plasma assisted ignition problems.

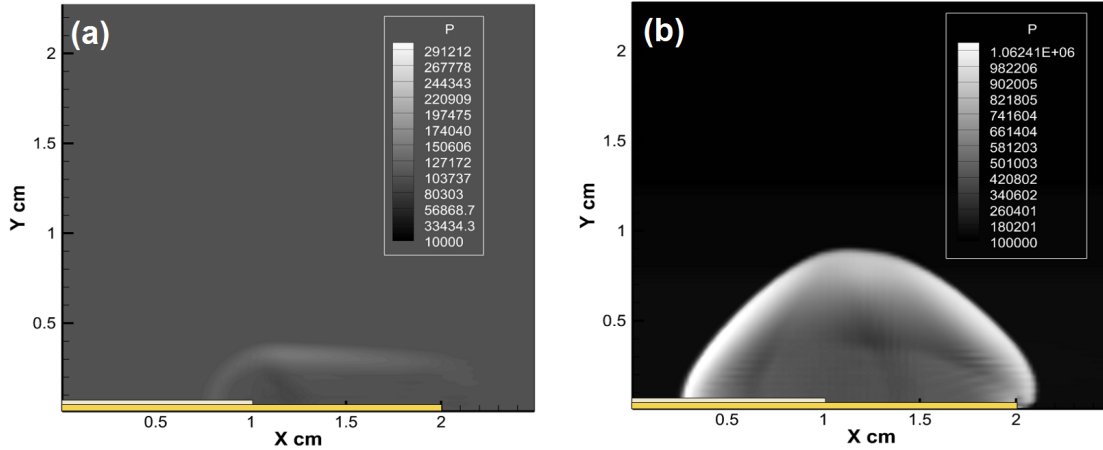


Figure 7.2: Compressive waves in air and in  $\text{H}_2$ :  $\text{O}_2$  mixture after ignition by initial local high temperature (maximum 800K) in a SDBD configuration.

Another point is the calculation of multi-pulse discharges with the help of ambipolar approximation, to understand the accumulation effects of active species, the memory effects from last pulse, and the effects to fluid responses.

Finally, it has to be mentioned that, the codes used in this thesis, are not specifically for nCD or nSDBD. The kinetics model and sensitivity module is also capable for analysing discharges in other  $E/N$  and  $E_{dep}$  values. The 2D nonPDPsim code and PASSKEy code, can also be used for studying discharges in other conditions that satisfy the approximations of a fluid model.

# Bibliography

---

- [1] B. Eliasson and U. Kogelschatz, "Nonequilibrium volume plasma chemical processing," *IEEE transactions on plasma science*, vol. 19, no. 6, pp. 1063–1077, 1991.
- [2] H. Biederman, *Plasma polymer films*. World Scientific, 2004.
- [3] V. E. Gusev and A. A. Karabutov, "Laser optoacoustics," *NASA STI/Recon Technical Report A*, vol. 93, 1991.
- [4] H.-H. Kim, "Nonthermal plasma processing for air-pollution control: a historical review, current issues, and future prospects," *Plasma Processes and Polymers*, vol. 1, no. 2, pp. 91–110, 2004.
- [5] G. Pilla, D. Galley, D. A. Lacoste, F. Lacas, D. Veynante, and C. O. Laux, "Stabilization of a turbulent premixed flame using a nanosecond repetitively pulsed plasma," *IEEE Transactions on Plasma Science*, vol. 34, no. 6, pp. 2471–2477, 2006.
- [6] F. Massines, P. Segur, N. Gherardi, C. Khamphan, and A. Ricard, "Physics and chemistry in a glow dielectric barrier discharge at atmospheric pressure: diagnostics and modelling," *Surface and Coatings Technology*, vol. 174, pp. 8–14, 2003.
- [7] A. Fridman, A. Chirokov, and A. Gutsol, "Non-thermal atmospheric pressure discharges," *Journal of Physics D: Applied Physics*, vol. 38, no. 2, p. R1, 2005.
- [8] A. Starikovskiy, N. Aleksandrov, and A. Rakitin, "Plasma-assisted ignition and deflagration-to-detonation transition," *Phil. Trans. R. Soc. A*, vol. 370, no. 1960, pp. 740–773, 2012.
- [9] A. Y. Starikovskii, A. Nikipelov, M. Nudnova, and D. Roupasov, "SDBD plasma actuator with nanosecond pulse-periodic discharge," *Plasma Sources Science and Technology*, vol. 18, no. 3, p. 034015, 2009.

- 
- 
- [10] K. Takashima, Z. Yin, and I. V. Adamovich, “Measurements and kinetic modeling of energy coupling in volume and surface nanosecond pulse discharges,” *Plasma Sources Science and Technology*, vol. 22, no. 1, p. 015013, 2012.
- [11] D. Rusterholtz, D. Lacoste, G. Stancu, D. Pai, and C. Laux, “Ultrafast heating and oxygen dissociation in atmospheric pressure air by nanosecond repetitively pulsed discharges,” *Journal of Physics D: Applied Physics*, vol. 46, no. 46, p. 464010, 2013.
- [12] E. Mintousov, S. Pendleton, F. Gerbault, N. Popov, and S. Starikovskaia, “Fast gas heating in nitrogen–oxygen discharge plasma: Ii. energy exchange in the afterglow of a volume nanosecond discharge at moderate pressures,” *Journal of Physics D: Applied Physics*, vol. 44, no. 28, p. 285202, 2011.
- [13] Y. Zhu, Y. Wu, W. Cui, Y. Li, and M. Jia, “Numerical investigation of energy transfer for fast gas heating in an atmospheric nanosecond-pulsed DBD under different negative slopes,” *Journal of Physics D: Applied Physics*, vol. 46, no. 49, p. 495205, 2013.
- [14] I. Kossyi, A. Y. Kostinsky, A. Matveyev, and V. Silakov, “Kinetic scheme of the non-equilibrium discharge in nitrogen-oxygen mixtures,” *Plasma Sources Science and Technology*, vol. 1, no. 3, p. 207, 1992.
- [15] G. Stancu, F. Kaddouri, D. Lacoste, and C. Laux, “Atmospheric pressure plasma diagnostics by OES, CRDS and TALIF,” *Journal of Physics D: Applied Physics*, vol. 43, no. 12, p. 124002, 2010.
- [16] G. Fridman, G. Friedman, A. Gutsol, A. B. Shekhter, V. N. Vasilets, and A. Fridman, “Applied plasma medicine,” *Plasma Processes and Polymers*, vol. 5, no. 6, pp. 503–533, 2008.
- [17] M. G. Kong, G. Kroesen, G. Morfill, T. Nosenko, T. Shimizu, J. Van Dijk, and J. Zimmermann, “Plasma medicine: an introductory review,” *new Journal of Physics*, vol. 11, no. 11, p. 115012, 2009.
- [18] D. Dobrynin, G. Fridman, G. Friedman, and A. Fridman, “Physical and biological mechanisms of direct plasma interaction with living tissue,” *New Journal of Physics*, vol. 11, no. 11, p. 115020, 2009.
- [19] J. Heinlin, G. Morfill, M. Landthaler, W. Stolz, G. Isbary, J. L. Zimmermann, T. Shimizu, and S. Karrer, “Plasma medicine: possible applications in dermatology,” *JDDG: Journal der Deutschen Dermatologischen Gesellschaft*, vol. 8, no. 12, pp. 968–976, 2010.

- 
- 
- [20] M. Laroussi, “From killing bacteria to destroying cancer cells: 20 years of plasma medicine,” *Plasma Processes and Polymers*, vol. 11, no. 12, pp. 1138–1141, 2014.
- [21] D. B. Graves, “Low temperature plasma biomedicine: A tutorial review a,” *Physics of Plasmas*, vol. 21, no. 8, p. 080901, 2014.
- [22] K. Song, G. Li, and Y. Ma, “A review on the selective apoptotic effect of nonthermal atmospheric-pressure plasma on cancer cells,” *Plasma Medicine*, vol. 4, no. 1-4, 2014.
- [23] D. B. Graves, “Mechanisms of plasma medicine: Coupling plasma physics, biochemistry, and biology,” *IEEE Transactions on Radiation and Plasma Medical Sciences*, vol. 1, no. 4, pp. 281–292, 2017.
- [24] N. Popov, “Fast gas heating initiated by pulsed nanosecond discharge in atmospheric pressure air,” in *51st AIAA Aerospace Sciences Meeting*, AIAA Reston, VA, 2013.
- [25] D. Rusterholtz, D. Pai, G. Stancu, D. Lacoste, and C. Laux, “Ultrafast heating in nanosecond discharges in atmospheric pressure air,” in *50th Aerospace Sciences Meeting*, 2012.
- [26] S. B. Leonov, I. V. Adamovich, and V. R. Soloviev, “Dynamics of near-surface electric discharges and mechanisms of their interaction with the airflow,” *Plasma Sources Science and Technology*, vol. 25, no. 6, p. 063001, 2016.
- [27] D. B. Graves, “Low temperature plasma biomedicine: a tutorial review a,” *Physics of Plasmas*, vol. 21, no. 8, p. 080901, 2014.
- [28] A. Starikovskiy, “Physics and chemistry of plasma-assisted combustion,” 2015.
- [29] Y. Ju and W. Sun, “Plasma assisted combustion: dynamics and chemistry,” *Progress in Energy and Combustion Science*, vol. 48, pp. 21–83, 2015.
- [30] M. Uddi, N. Jiang, E. Mintusov, I. V. Adamovich, and W. R. Lempert, “Atomic oxygen measurements in air and air/fuel nanosecond pulse discharges by two photon laser induced fluorescence,” *Proceedings of the Combustion Institute*, vol. 32, no. 1, pp. 929–936, 2009.
- [31] M. S. Simeni, B. Goldberg, I. Gulko, K. Frederickson, and I. V. Adamovich, “Sub-nanosecond resolution electric field measurements during ns pulse breakdown in ambient air,” *Journal of Physics D: Applied Physics*, vol. 51, no. 1, p. 01LT01, 2017.

- 
- 
- [32] M. Simeni Simeni, B. M. Goldberg, C. Zhang, K. Frederickson, W. R. Lempert, and I. V. Adamovich, "Electric field measurements in a quasi-two-dimensional ns pulse discharge in atmospheric air," in *55th AIAA Aerospace Sciences Meeting*, p. 1811, 2017.
- [33] A. Starikovskiy and N. Aleksandrov, "Plasma-assisted ignition and combustion," *Progress in Energy and Combustion Science*, vol. 39, no. 1, pp. 61–110, 2013.
- [34] N. Popov, "Kinetics of plasma-assisted combustion: effect of non-equilibrium excitation on the ignition and oxidation of combustible mixtures," *Plasma Sources Science and Technology*, vol. 25, no. 4, p. 043002, 2016.
- [35] K. Takashima, I. V. Adamovich, Z. Xiong, M. J. Kushner, S. Starikovskaia, U. Czarnetzki, and D. Luggenhölscher, "Experimental and modeling analysis of fast ionization wave discharge propagation in a rectangular geometry," *Physics of Plasmas*, vol. 18, no. 8, p. 083505, 2011.
- [36] A. Klochko, J. Lemainque, J. Booth, and S. Starikovskaia, "TALIF measurements of oxygen atom density in the afterglow of a capillary nanosecond discharge," *Plasma Sources Science and Technology*, vol. 24, no. 2, p. 025010, 2015.
- [37] N. Popov, "Fast gas heating in a nitrogen–oxygen discharge plasma: I. kinetic mechanism," *Journal of Physics D: Applied Physics*, vol. 44, no. 28, p. 285201, 2011.
- [38] N. B. Anikin, N. A. Zavialova, S. M. Starikovskaia, and A. Y. Starikovskii, "Nanosecond-discharge development in long tubes," *IEEE Transactions on Plasma Science*, vol. 36, no. 4, pp. 902–903, 2008.
- [39] A. V. Klochko, A. Salmon, J. Lemainque, N. A. Popov, J.-P. Booth, Z. Xiong, M. J. Kushner, and S. M. Starikovskaia, "Experimental and numerical study of fast gas heating and O atom production in a capillary nanosecond discharge," in *Proc. 52nd AIAA Aerospace Science Meeting (National Harbor, MD)*, 2014.
- [40] N. Anikin, S. Starikovskaia, and A. Y. Starikovskii, "Study of the oxidation of alkanes in their mixtures with oxygen and air under the action of a pulsed volume nanosecond discharge," *Plasma Physics Reports*, vol. 30, no. 12, pp. 1028–1042, 2004.
- [41] N. Fuller, M. Malyshev, V. Donnelly, and I. P. Herman, "Characterization of transformer coupled oxygen plasmas by trace rare gases-optical emission

- spectroscopy and langmuir probe analysis,” *Plasma Sources Science and Technology*, vol. 9, no. 2, p. 116, 2000.
- [42] W. Harshbarger, R. Porter, T. A. Miller, and P. Norton, “A study of the optical emission from an RF plasma during semiconductor etching,” *Applied Spectroscopy*, vol. 31, no. 3, pp. 201–207, 1977.
- [43] J. Coburn and M. Chen, “Optical emission spectroscopy of reactive plasmas: A method for correlating emission intensities to reactive particle density,” *Journal of applied physics*, vol. 51, no. 6, pp. 3134–3136, 1980.
- [44] R. d’Agostino, F. Cramarossa, S. De Benedictis, and G. Ferraro, “Spectroscopic diagnostics of  $\text{CF}_4\text{-O}_2$  plasmas during si and  $\text{SiO}_2$  etching processes,” *Journal of applied physics*, vol. 52, no. 3, pp. 1259–1265, 1981.
- [45] R. d’Agostino, V. Colaprico, and F. Cramarossa, “The use of actinometer gases in optical diagnostics of plasma etching mixtures:  $\text{SF}_6\text{-O}_2$ ,” *Plasma Chemistry and Plasma Processing*, vol. 1, no. 4, pp. 365–375, 1981.
- [46] R. Walkup, K. Saenger, and G. Selwyn, “Studies of atomic oxygen in  $\text{O}_2\text{+CF}_4$  RF discharges by two-photon laser-induced fluorescence and optical emission spectroscopy,” *The Journal of chemical physics*, vol. 84, no. 5, pp. 2668–2674, 1986.
- [47] D. Pagnon, J. Amorim, J. Nahorny, M. Touzeau, and M. Vialle, “On the use of actinometry to measure the dissociation in  $\text{O}_2$  DC glow discharges: determination of the wall recombination probability,” *Journal of Physics D: Applied Physics*, vol. 28, no. 9, p. 1856, 1995.
- [48] J. R. Roth, D. M. Sherman, and S. P. Wilkinson, “Electrohydrodynamic flow control with a glow-discharge surface plasma,” *AIAA journal*, vol. 38, no. 7, pp. 1166–1172, 2000.
- [49] J. R. Roth, “Aerodynamic flow acceleration using paraelectric and peristaltic electrohydrodynamic effects of a one atmosphere uniform glow discharge plasma,” *Physics of plasmas*, vol. 10, no. 5, pp. 2117–2126, 2003.
- [50] C. Enloe, T. E. McLaughlin, R. D. VanDyken, K. Kachner, E. J. Jumper, T. C. Corke, M. Post, and O. Haddad, “Mechanisms and responses of a single dielectric barrier plasma actuator: geometric effects,” *AIAA journal*, vol. 42, no. 3, pp. 595–604, 2004.

- [51] C. Enloe, M. McHarg, and T. E. McLaughlin, “Time-correlated force production measurements of the dielectric barrier discharge plasma aerodynamic actuator,” *Journal of applied physics*, vol. 103, no. 7, p. 073302, 2008.
- [52] J. Boeuf, Y. Lagmich, and L. Pitchford, “Contribution of positive and negative ions to the electrohydrodynamic force in a dielectric barrier discharge plasma actuator operating in air,” *Journal of applied physics*, vol. 106, no. 2, p. 023115, 2009.
- [53] Y. Lagmich, T. Callegari, L. Pitchford, and J. Boeuf, “Model description of surface dielectric barrier discharges for flow control,” *Journal of Physics D: Applied Physics*, vol. 41, no. 9, p. 095205, 2008.
- [54] M. Sokolova, K. Kozlov, S. Krivov, V. Samoilovich, and P. Tatarenko, “Studying emission from a surface discharge in dry air,” *Technical Physics Letters*, vol. 35, no. 3, pp. 207–210, 2009.
- [55] T. Hoder, R. Brandenburg, R. Basner, K. Weltmann, K. Kozlov, and H. Wagner, “A comparative study of three different types of barrier discharges in air at atmospheric pressure by cross-correlation spectroscopy,” *Journal of Physics D: Applied Physics*, vol. 43, no. 12, p. 124009, 2010.
- [56] M. Nudnova, N. Aleksandrov, and A. Y. Starikovskii, “Influence of the voltage polarity on the properties of a nanosecond surface barrier discharge in atmospheric-pressure air,” *Plasma Physics Reports*, vol. 36, no. 1, pp. 90–98, 2010.
- [57] S. Stepanyan, V. Soloviev, and S. Starikovskaia, “An electric field in nanosecond surface dielectric barrier discharge at different polarities of the high voltage pulse: spectroscopy measurements and numerical modeling,” *Journal of Physics D: Applied Physics*, vol. 47, no. 48, p. 485201, 2014.
- [58] P. Paris, M. Aints, F. Valk, T. Plank, A. Haljaste, K. Kozlov, and H. Wagner, “Intensity ratio of spectral bands of nitrogen as a measure of electric field strength in plasmas,” *Journal of Physics D: Applied Physics*, vol. 38, no. 21, p. 3894, 2005.
- [59] P. Paris, M. Aints, and F. Valk, “Collisional quenching rates of  $N_2^+(B^2\Sigma_g^+, v = 0)$ ,” in *Book of contributed papers of 17th Symposium on Application of Plasma Processes and Visegrad Workshop on Research of Plasma Physics*, (Slovakia), pp. 227–228, jan 2009.

- 
- 
- [60] D. Arnaud-Cormos, S. Kohler, D. Bessières, R. P. O'Connor, J. Paillol, and P. Leveque, "Electrical measurements for nanosecond repetitive pulsed discharges," *IEEE Transactions on Plasma Science*, vol. 42, no. 7, pp. 1909–1916, 2014.
- [61] S. B. Leonov, V. Petrishchev, and I. V. Adamovich, "Dynamics of energy coupling and thermalization in barrier discharges over dielectric and weakly conducting surfaces on  $\mu\text{s}$  to ms time scales," *Journal of Physics D: Applied Physics*, vol. 47, no. 46, p. 465201, 2014.
- [62] D. Opaits, D. Roupassov, S. Starikovskaia, A. Y. Starikovskii, I. Zavalov, and S. Saddoughi, "Plasma control of boundary layer using low-temperature non-equilibrium plasma of gas discharge," *AIAA paper*, vol. 1180, p. 2005, 2005.
- [63] S. Leonov, D. Opaits, R. Miles, and V. Soloviev, "Time-resolved measurements of plasma-induced momentum in air and nitrogen under dielectric barrier discharge actuation," *Physics of Plasmas*, vol. 17, no. 11, p. 113505, 2010.
- [64] C. Rethmel, J. Little, K. Takashima, A. Sinha, I. Adamovich, and M. Samimy, "Flow separation control using nanosecond pulse driven DBD plasma actuators," *International Journal of Flow Control*, vol. 3, no. 4, 2011.
- [65] N. J. Bisek, J. Poggie, M. Nishihara, and I. Adamovich, "Hypersonic flow over a cylinder with a nanosecond pulse electrical discharge," *Journal of Thermophysics and Heat Transfer*, 2014.
- [66] K. Bayoda, N. Benard, and E. Moreau, "Nanosecond pulsed sliding dielectric barrier discharge plasma actuator for airflow control: Electrical, optical, and mechanical characteristics," *Journal of Applied Physics*, vol. 118, no. 6, p. 063301, 2015.
- [67] D. V. Roupassov and A. Y. Starikovskii, "Development of nanosecond surface discharge in "actuator" geometry," *IEEE Transactions on Plasma Science*, vol. 36, no. 4, pp. 1312–1313, 2008.
- [68] D. Roupassov, A. Nikipelov, M. Nudnova, and A. Y. Starikovskii, "Flow separation control by plasma actuator with nanosecond pulse periodic discharge," in *Gas Discharges and Their Applications, 2008. GD 2008. 17th International Conference on*, pp. 609–612, IEEE, 2008.
- [69] I. Kosarev, V. Khorunzhenko, E. Mintousov, P. Sagulenko, N. Popov, and S. Starikovskaia, "A nanosecond surface dielectric barrier discharge at elevated

- pressures: time-resolved electric field and efficiency of initiation of combustion,” *Plasma Sources Science and Technology*, vol. 21, no. 4, p. 045012, 2012.
- [70] S. Starikovskaia, K. Allegraud, O. Guaitella, I. Kosarev, E. Mintusov, S. J. Pendleton, N. Popov, P. Sagulenko, and A. Rousseau, “Surface discharges: possible applications for plasma-assisted ignition and electric field measurements,” in *48th AIAA Aerospace Sciences Meeting including The New Horizons Forum and Aerospace Exposition*, 2010.
- [71] F. Tholin, D. A. Lacoste, and A. Bourdon, “Influence of fast-heating processes and o atom production by a nanosecond spark discharge on the ignition of a lean h<sub>2</sub>–air premixed flame,” *Combustion and Flame*, vol. 161, no. 5, pp. 1235–1246, 2014.
- [72] M. Capitelli, C. M. Ferreira, B. F. Gordiets, and A. I. Osipov, *Plasma kinetics in atmospheric gases*, vol. 31. Springer Science & Business Media, 2001.
- [73] L. W. Sieck, J. T. Heron, and D. S. Green, “Chemical kinetics database and predictive schemes for humid air plasma chemistry. part i: Positive ion–molecule reactions,” *Plasma Chemistry and Plasma Processing*, vol. 20, no. 2, pp. 235–258, 2000.
- [74] J. T. Herron and D. S. Green, “Chemical kinetics database and predictive schemes for nonthermal humid air plasma chemistry. part ii. neutral species reactions,” *Plasma Chemistry and Plasma Processing*, vol. 21, no. 3, pp. 459–481, 2001.
- [75] A. Fridman, *Plasma chemistry*. Cambridge university press, 2008.
- [76] “<http://www.zdplaskin.laplace.univ-tlse.fr/n2-o2-mixtures/>.”
- [77] N. Popov, “Associative ionization reactions involving excited atoms in nitrogen plasma,” *Plasma Physics Reports*, vol. 35, no. 5, pp. 436–449, 2009.
- [78] N. Popov, “Dissociation of nitrogen in a pulse-periodic dielectric barrier discharge at atmospheric pressure,” *Plasma Physics Reports*, vol. 39, no. 5, pp. 420–424, 2013.
- [79] N. Lepikhin, A. Klochko, N. Popov, and S. Starikovskaia, “Long-lived plasma and fast quenching of N<sub>2</sub>(C<sup>3</sup>Π<sub>u</sub>) by electrons in the afterglow of a nanosecond capillary discharge in nitrogen,” *Plasma Sources Science and Technology*, vol. 25, no. 4, p. 045003, 2016.

- 
- 
- [80] H. P. Le, A. R. Karagozian, and J.-L. Cambier, “Complexity reduction of collisional-radiative kinetics for atomic plasma,” *Physics of Plasmas*, vol. 20, no. 12, p. 123304, 2013.
- [81] T. E. Magin, M. Panesi, A. Bourdon, R. L. Jaffe, and D. W. Schwenke, “Coarse-grain model for internal energy excitation and dissociation of molecular nitrogen,” *Chemical Physics*, vol. 398, pp. 90–95, 2012.
- [82] R. Lehmann, “An algorithm for the determination of all significant pathways in chemical reaction systems,” *Journal of atmospheric chemistry*, vol. 47, no. 1, pp. 45–78, 2004.
- [83] A. H. Markosyan, A. Luque, F. J. Gordillo-Vázquez, and U. Ebert, “Pumpkin: A tool to find principal pathways in plasma chemical models,” *Computer Physics Communications*, vol. 185, no. 10, pp. 2697–2702, 2014.
- [84] K. Peerenboom, A. Parente, T. Kozák, A. Bogaerts, and G. Degrez, “Dimension reduction of non-equilibrium plasma kinetic models using principal component analysis,” *Plasma Sources Science and Technology*, vol. 24, no. 2, p. 025004, 2015.
- [85] S. Pancheshnyi, M. Nudnova, and A. Starikovskii, “Development of a cathode-directed streamer discharge in air at different pressures: experiment and comparison with direct numerical simulation,” *Physical Review E*, vol. 71, no. 1, p. 016407, 2005.
- [86] M. S. Bak and M. A. Cappelli, “A reduced set of air plasma reactions for nanosecond pulsed plasmas,” *IEEE Transactions on Plasma Science*, vol. 43, no. 4, pp. 995–1001, 2015.
- [87] J. Poggie, I. Adamovich, N. Bisek, and M. Nishihara, “Numerical simulation of nanosecond-pulse electrical discharges,” *Plasma Sources Science and Technology*, vol. 22, no. 1, p. 015001, 2012.
- [88] N. Aleksandrov, S. Kindysheva, M. Nudnova, and A. Y. Starikovskiy, “Mechanism of ultra-fast heating in a non-equilibrium weakly ionized air discharge plasma in high electric fields,” *Journal of Physics D: Applied Physics*, vol. 43, no. 25, p. 255201, 2010.
- [89] R. Morrow and J. Lowke, “Streamer propagation in air,” *Journal of Physics D: Applied Physics*, vol. 30, no. 4, p. 614, 1997.
- [90] A. Kulikovskiy, “Positive streamer in a weak field in air: A moving avalanche-to-streamer transition,” *Physical Review E*, vol. 57, no. 6, p. 7066, 1998.

- [91] F. Pechereau, J. Jánskỳ, and A. Bourdon, "Simulation of the reignition of a discharge behind a dielectric layer in air at atmospheric pressure," *Plasma Sources Science and Technology*, vol. 21, no. 5, p. 055011, 2012.
- [92] J.-P. Boeuf and L. C. Pitchford, "Pseudospark discharges via computer simulation," *IEEE Transactions on Plasma Science*, vol. 19, no. 2, pp. 286–296, 1991.
- [93] A. Fiala, L. Pitchford, and J. Boeuf, "Two-dimensional, hybrid model of low-pressure glow discharges," *Physical Review E*, vol. 49, no. 6, p. 5607, 1994.
- [94] N. Y. Babaeva and G. Naidis, "Two-dimensional modelling of positive streamer dynamics in non-uniform electric fields in air," *Journal of Physics D: Applied Physics*, vol. 29, no. 9, p. 2423, 1996.
- [95] N. Y. Babaeva and G. V. Naidis, "Dynamics of positive and negative streamers in air in weak uniform electric fields," *IEEE transactions on plasma science*, vol. 25, no. 2, pp. 375–379, 1997.
- [96] S. Rauf and M. J. Kushner, "Dynamics of a coplanar-electrode plasma display panel cell. i. basic operation," *Journal of applied physics*, vol. 85, no. 7, pp. 3460–3469, 1999.
- [97] S. Pancheshnyi, P. Ségur, J. Capeillère, and A. Bourdon, "Numerical simulation of filamentary discharges with parallel adaptive mesh refinement," *Journal of Computational Physics*, vol. 227, no. 13, pp. 6574–6590, 2008.
- [98] T. Unfer and J. Boeuf, "Modelling of a nanosecond surface discharge actuator," *Journal of physics D: applied physics*, vol. 42, no. 19, p. 194017, 2009.
- [99] P. L. Ventzek, R. J. Hoekstra, and M. J. Kushner, "Two-dimensional modeling of high plasma density inductively coupled sources for materials processing," *Journal of Vacuum Science & Technology B: Microelectronics and Nanometer Structures Processing, Measurement, and Phenomena*, vol. 12, no. 1, pp. 461–477, 1994.
- [100] G. Hagelaar and G. Kroesen, "Speeding up fluid models for gas discharges by implicit treatment of the electron energy source term," *Journal of Computational Physics*, vol. 159, no. 1, pp. 1–12, 2000.
- [101] K.-M. Lin, C.-T. Hung, F.-N. Hwang, M. R. Smith, Y.-W. Yang, and J.-S. Wu, "Development of a parallel semi-implicit two-dimensional plasma fluid modeling code using finite-volume method," *Computer Physics Communications*, vol. 183, no. 6, pp. 1225–1236, 2012.

- 
- 
- [102] T. Unfer, J.-P. Boeuf, F. Rogier, and F. Thivet, “An asynchronous scheme with local time stepping for multi-scale transport problems: Application to gas discharges,” *Journal of Computational Physics*, vol. 227, no. 2, pp. 898–918, 2007.
- [103] C. Li, J. Teunissen, M. Nool, W. Hundsdorfer, and U. Ebert, “A comparison of 3d particle, fluid and hybrid simulations for negative streamers,” *Plasma Sources Science and Technology*, vol. 21, no. 5, p. 055019, 2012.
- [104] N. Y. Babaeva and M. J. Kushner, “Effect of inhomogeneities on streamer propagation: I. intersection with isolated bubbles and particles,” *Plasma Sources Science and Technology*, vol. 18, no. 3, p. 035009, 2009.
- [105] D. Levko and L. L. Raja, “Fluid versus global model approach for the modeling of active species production by streamer discharge,” *Plasma Sources Science and Technology*, vol. 26, no. 3, p. 035003, 2017.
- [106] G. Naidis, “Effects of nonlocality on the dynamics of streamers in positive corona discharges,” *Technical Physics Letters*, vol. 23, no. 6, pp. 493–494, 1997.
- [107] C. Li, U. Ebert, and W. Hundsdorfer, “Spatially hybrid computations for streamer discharges with generic features of pulled fronts: I. planar fronts,” *Journal of Computational Physics*, vol. 229, no. 1, pp. 200–220, 2010.
- [108] V. Soloviev and V. Krivtsov, “Surface barrier discharge modelling for aerodynamic applications,” *Journal of Physics D: Applied Physics*, vol. 42, no. 12, p. 125208, 2009.
- [109] O. Chanrion, Z. Bonaventura, D. Cinar, A. Bourdon, and T. Neubert, “Run-away electrons from a ‘beam-bulk’ model of streamer: application to tgfs,” *Environmental Research Letters*, vol. 9, no. 5, p. 055003, 2014.
- [110] N. Y. Babaeva, D. V. Tereshonok, and G. V. Naidis, “Fluid and hybrid modeling of nanosecond surface discharges: effect of polarity and secondary electrons emission,” *Plasma Sources Science and Technology*, vol. 25, no. 4, p. 044008, 2016.
- [111] S. Rauf, A. Balakrishna, A. Agarwal, L. Dorf, K. Collins, D. R. Boris, and S. G. Walton, “Three-dimensional model of electron beam generated plasma,” *Plasma Sources Science and Technology*, vol. 26, no. 6, p. 065006, 2017.

- 
- 
- [112] N. Y. Babaeva, C. Zhang, J. Qiu, X. Hou, V. F. Tarasenko, and T. Shao, “The role of fast electrons in diffuse discharge formation: Monte carlo simulation,” *Plasma Sources Science and Technology*, vol. 26, no. 8, p. 085008, 2017.
- [113] O. Chanrion and T. Neubert, “A pic-mcc code for simulation of streamer propagation in air,” *Journal of Computational Physics*, vol. 227, no. 15, pp. 7222–7245, 2008.
- [114] D. Levko, S. Yatom, V. Vekselman, J. Gleizer, V. T. Gurovich, and Y. E. Krasik, “Numerical simulations of runaway electron generation in pressurized gases,” *Journal of Applied Physics*, vol. 111, no. 1, p. 013303, 2012.
- [115] C. MacLachlan, H. Potts, and D. Diver, “Simulation of transient energy distributions in sub-ns streamer formation,” *Plasma Sources Science and Technology*, vol. 22, no. 1, p. 015025, 2013.
- [116] J. Teunissen and U. Ebert, “3d pic-mcc simulations of discharge inception around a sharp anode in nitrogen/oxygen mixtures,” *Plasma Sources Science and Technology*, vol. 25, no. 4, p. 044005, 2016.
- [117] F. Tholin and A. Bourdon, “Simulation of the hydrodynamic expansion following a nanosecond pulsed spark discharge in air at atmospheric pressure,” *Journal of Physics D: Applied Physics*, vol. 46, no. 36, p. 365205, 2013.
- [118] A. M. Lietz, E. Johnsen, and M. J. Kushner, “Plasma-induced flow instabilities in atmospheric pressure plasma jets,” *Applied Physics Letters*, vol. 111, no. 11, p. 114101, 2017.
- [119] D. Z. Pai, D. A. Lacoste, and C. O. Laux, “Nanosecond repetitively pulsed discharges in air at atmospheric pressure in the spark regime,” *Plasma Sources Science and Technology*, vol. 19, no. 6, p. 065015, 2010.
- [120] N. Popov, “Pulsed nanosecond discharge in air at high specific deposited energy: fast gas heating and active particle production,” *Plasma Sources Science and Technology*, vol. 25, no. 4, p. 044003, 2016.
- [121] G. Naidis, “Modelling of streamer propagation in atmospheric-pressure helium plasma jets,” *Journal of Physics D: Applied Physics*, vol. 43, no. 40, p. 402001, 2010.
- [122] G. Naidis, “Modelling of plasma bullet propagation along a helium jet in ambient air,” *Journal of Physics D: Applied Physics*, vol. 44, no. 21, p. 215203, 2011.

- 
- 
- [123] D. Breden, K. Miki, and L. Raja, "Self-consistent two-dimensional modeling of cold atmospheric-pressure plasma jets/bullets," *Plasma Sources Science and Technology*, vol. 21, no. 3, p. 034011, 2012.
- [124] N. Y. Babaeva and M. J. Kushner, "Interaction of multiple atmospheric-pressure micro-plasma jets in small arrays: He/o<sub>2</sub> into humid air," *Plasma Sources Science and Technology*, vol. 23, no. 1, p. 015007, 2014.
- [125] S. A. Norberg, E. Johnsen, and M. J. Kushner, "Formation of reactive oxygen and nitrogen species by repetitive negatively pulsed helium atmospheric pressure plasma jets propagating into humid air," *Plasma Sources Science and Technology*, vol. 24, no. 3, p. 035026, 2015.
- [126] Z. Xiong, E. Robert, V. Sarron, J.-M. Povesle, and M. J. Kushner, "Dynamics of ionization wave splitting and merging of atmospheric-pressure plasmas in branched dielectric tubes and channels," *Journal of Physics D: Applied Physics*, vol. 45, no. 27, p. 275201, 2012.
- [127] J. Jánskỳ, F. Tholin, Z. Bonaventura, and A. Bourdon, "Simulation of the discharge propagation in a capillary tube in air at atmospheric pressure," *Journal of Physics D: Applied Physics*, vol. 43, no. 39, p. 395201, 2010.
- [128] A. V. Klochko, S. M. Starikovskaia, Z. Xiong, and M. J. Kushner, "Investigation of capillary nanosecond discharges in air at moderate pressure: comparison of experiments and 2D numerical modelling," *Journal of Physics D: Applied Physics*, vol. 47, no. 36, p. 365202, 2014.
- [129] A. V. Likhanskii, M. N. Shneider, S. O. Macheret, and R. B. Miles, "Modeling of dielectric barrier discharge plasma actuators driven by repetitive nanosecond pulses," *Physics of plasmas*, vol. 14, no. 7, p. 073501, 2007.
- [130] D. Gaitonde, M. Sahin, K. Shaler, B. Glaz, S. Dinavahi, and P. Aberdeen, "High-fidelity simulations of ns-dbd-based control of a stalled naca0015 airfoil," *AIAA Paper*, vol. 1118, 2013.
- [131] K. Takashima, Z. Yin, and I. V. Adamovich, "Measurements and kinetic modeling of energy coupling in volume and surface nanosecond pulse discharges," *Plasma Sources Science and Technology*, vol. 22, no. 1, p. 015013, 2012.
- [132] J. Zheng, Z. Zhao, J. Li, Y. Cui, B. Khoo, *et al.*, "Numerical simulation of nanosecond pulsed dielectric barrier discharge actuator for flow control," in *APS Meeting Abstracts*, 2013.

- 
- 
- [133] Z. Chen, L. Hao, and B. Zhang, “A model for nanosecond pulsed dielectric barrier discharge (nsdbd) actuator and its investigation on the mechanisms of separation control over an airfoil,” *Science China Technological Sciences*, vol. 56, no. 5, pp. 1055–1065, 2013.
- [134] J. Zheng, Z. Zhao, J. Li, Y. Cui, and B. Khoo, “Numerical simulation of nanosecond pulsed dielectric barrier discharge actuator in a quiescent flow,” *Physics of Fluids*, vol. 26, no. 3, p. 036102, 2014.
- [135] V. Solov'ev, A. Konchakov, V. Krivtsov, and N. Aleksandrov, “Numerical simulation of a surface barrier discharge in air,” *Plasma Physics Reports*, vol. 34, no. 7, pp. 594–608, 2008.
- [136] V. Soloviev and V. Krivtsov, “Mechanism of streamer stopping in a surface dielectric barrier discharge,” *Plasma Physics Reports*, vol. 40, no. 1, pp. 65–77, 2014.
- [137] V. Soloviev, V. Krivtsov, S. Shcherbaney, and S. Starikovskaia, “Evolution of nanosecond surface dielectric barrier discharge for negative polarity of a voltage pulse,” *Plasma Sources Science and Technology*, vol. 26, no. 1, p. 014001, 2016.
- [138] M. Abdollahzadeh, J. C. Páscoa, and P. J. Oliveira, “Two-dimensional numerical modeling of interaction of micro-shock wave generated by nanosecond plasma actuators and transonic flow,” *Journal of Computational and Applied Mathematics*, vol. 270, pp. 401–416, 2014.
- [139] M. Abdollahzadeh, J. Pascoa, and P. Oliveira, “Implementation of the classical plasma–fluid model for simulation of dielectric barrier discharge (dbd) actuators in openfoam,” *Computers & Fluids*, vol. 128, pp. 77–90, 2016.
- [140] Y. Zhu, Y. Wu, W. Cui, Y. Li, and M. Jia, “Modelling of plasma aerodynamic actuation driven by nanosecond SDBD discharge,” *Journal of Physics D: Applied Physics*, vol. 46, no. 35, p. 355205, 2013.
- [141] S. Xu, J. Cai, Z. Zhang, and S. Tang, “Investigation of the electrode surface geometry effects driven by nanosecond-pulsed surface dielectric barrier discharge,” *Journal of Physics D: Applied Physics*, vol. 50, no. 18, p. 185201, 2017.
- [142] S. Xu, J. Cai, and J. Li, “Modeling and simulation of plasma gas flow driven by a single nanosecond-pulsed dielectric barrier discharge,” *Physics of Plasmas*, vol. 23, no. 10, p. 103510, 2016.

- 
- 
- [143] S. Pancheshnyi, B. Eismann, G. Hagelaar, and L. Pitchford, “Computer code ziplaskin, university of toulouse, laplace,” tech. rep., CNRS-UPS-INP, Toulouse, France, [www. ziplaskin. laplace. univ-tlse. fr](http://www.ziplaskin.laplace.univ-tlse.fr), 2008.
- [144] P. Chabert and N. Braithwaite, *Physics of radio-frequency plasmas*. Cambridge University Press, 2011.
- [145] G. Hagelaar and L. Pitchford, “Solving the boltzmann equation to obtain electron transport coefficients and rate coefficients for fluid models,” *Plasma Sources Science and Technology*, vol. 14, no. 4, p. 722, 2005.
- [146] L. Frost and A. Phelps, “Rotational excitation and momentum transfer cross sections for electrons in  $h\ 2$  and  $n\ 2$  from transport coefficients,” *Physical Review*, vol. 127, no. 5, p. 1621, 1962.
- [147] L. Pitchford, S. O’Neil, and J. Rumble Jr, “Extended boltzmann analysis of electron swarm experiments,” *Physical Review A*, vol. 23, no. 1, p. 294, 1981.
- [148] T. Holstein, “Energy distribution of electrons in high frequency gas discharges,” *Physical Review*, vol. 70, no. 5-6, p. 367, 1946.
- [149] W. Allis, “Handbuch der physik, vol. 21,” *Electron-Emission Gas Discharges I*, Flügge S eds. (Berlin: Springer-Verlag) pp, pp. 383–444, 1956.
- [150] W. P. Allis, “Semidivergence of the legendre expansion of the boltzmann equation,” *Physical Review A*, vol. 26, no. 3, p. 1704, 1982.
- [151] P. N. Brown, G. D. Byrne, and A. C. Hindmarsh, “Vode: A variable-coefficient ode solver,” *SIAM journal on scientific and statistical computing*, vol. 10, no. 5, pp. 1038–1051, 1989.
- [152] R. T. Haftka and Z. Mróz, “First-and second-order sensitivity analysis of linear and nonlinear structures,” *AIAA journal*, vol. 24, no. 7, pp. 1187–1192, 1986.
- [153] M. Mitchner and C. H. Kruger, “Partially ionized gases,” 1973.
- [154] J. Gallagher, C. Brion, J. Samson, and P. Langhoff, “Absolute cross sections for molecular photoabsorption, partial photoionization, and ionic photofragmentation processes,” *Journal of physical and chemical reference data*, vol. 17, no. 1, pp. 9–153, 1988.
- [155] B. Lay, R. S. Moss, S. Rauf, and M. J. Kushner, “Breakdown processes in metal halide lamps,” *Plasma Sources Science and Technology*, vol. 12, no. 1, p. 8, 2002.

- 
- 
- [156] D. L. Scharfetter and H. K. Gummel, "Large-signal analysis of a silicon read diode oscillator," *IEEE Transactions on electron devices*, vol. 16, no. 1, pp. 64–77, 1969.
- [157] A. Phelps and L. Pitchford, "Anisotropic scattering of electrons by N<sub>2</sub> and its effect on electron transport," *Physical Review A*, vol. 31, no. 5, p. 2932, 1985.
- [158] J. Dutton, "A survey of electron swarm data," *Journal of Physical and Chemical Reference Data*, vol. 4, no. 3, pp. 577–856, 1975.
- [159] H. Kucukarpaci and J. Lucas, "Simulation of electron swarm parameters in carbon dioxide and nitrogen for high  $e/n$ ," *Journal of Physics D: Applied Physics*, vol. 12, no. 12, p. 2123, 1979.
- [160] J. Fletcher and I. Reid, "The transport parameters of an electron swarm in nitrogen at elevated  $e/n$ ," *Journal of Physics D: Applied Physics*, vol. 13, no. 12, p. 2275, 1980.
- [161] C. R. Rao and G. G. Raju, "Growth of ionization currents in dry air at high values of  $e/n$ ," *Journal of Physics D: Applied Physics*, vol. 4, no. 4, p. 494, 1971.
- [162] J. Moruzzi and D. Price, "Ionization, attachment and detachment in air and air-CO<sub>2</sub> mixtures," *Journal of Physics D: Applied Physics*, vol. 7, no. 10, p. 1434, 1974.
- [163] J. Bacri and A. Medani, "Electron diatomic molecule weighted total cross section calculation: Iii. main inelastic processes for N<sub>2</sub> and N<sub>2</sub><sup>+</sup>," *Physica B*, vol. 112, no. 1, pp. 101–118, 1982.
- [164] M. Zhelezniak, A. K. Mnatsakanian, and S. V. Sizykh, "Photoionization of nitrogen and oxygen mixtures by radiation from a gas discharge," *High Temperature Science*, vol. 20, pp. 423–428, 1982.
- [165] A. Bourdon, V. Pasko, N. Liu, S. Célestin, P. Ségur, and E. Marode, "Efficient models for photoionization produced by non-thermal gas discharges in air based on radiative transfer and the Helmholtz equations," *Plasma Sources Science and Technology*, vol. 16, no. 3, p. 656, 2007.
- [166] A. Luque, U. Ebert, C. Montijn, and W. Hundsdorfer, "Photoionization in negative streamers: Fast computations and two propagation modes," *Applied physics letters*, vol. 90, no. 8, p. 081501, 2007.

- [167] A. Kulikovskiy, “A more accurate scharfetter-gummel algorithm of electron transport for semiconductor and gas discharge simulation,” *Journal of computational physics*, vol. 119, no. 1, pp. 149–155, 1995.
- [168] A. Kulikovskiy, “Two-dimensional simulation of the positive streamer in n<sub>2</sub> between parallel-plate electrodes,” *Journal of Physics D: Applied Physics*, vol. 28, no. 12, p. 2483, 1995.
- [169] A. Kulikovskiy, “Positive streamer between parallel plate electrodes in atmospheric pressure air,” *Journal of physics D: Applied physics*, vol. 30, no. 3, p. 441, 1997.
- [170] A. A. Kulikovskiy, “Production of chemically active species in the air by a single positive streamer in a nonuniform field,” *IEEE transactions on plasma science*, vol. 25, no. 3, pp. 439–446, 1997.
- [171] A. A. Kulikovskiy, “The efficiency of radicals production by positive streamer in air: The role of laplacian field,” *IEEE Transactions on plasma science*, vol. 29, no. 2, pp. 313–317, 2001.
- [172] N. Liu and V. Pasko, “Effects of photoionization on similarity properties of streamers at various pressures in air,” *Journal of Physics D: Applied Physics*, vol. 39, no. 2, p. 327, 2006.
- [173] M. Steffen, “A simple method for monotonic interpolation in one dimension,” *Astronomy and Astrophysics*, vol. 239, p. 443, 1990.
- [174] J.-G. Li, “Upstream nonoscillatory advection schemes,” *Monthly Weather Review*, vol. 136, no. 12, pp. 4709–4729, 2008.
- [175] G.-C. Zha and E. Bilgen, “Numerical solutions of euler equations by using a new flux vector splitting scheme,” *International Journal for Numerical Methods in Fluids*, vol. 17, no. 2, pp. 115–144, 1993.
- [176] F. Tholin, *Numerical simulation of nanosecond repetitively pulsed discharges in air at atmospheric pressure: Application to plasma-assisted combustion*. PhD thesis, Ecole Centrale Paris, 2012.
- [177] B. Van Leer, “Towards the ultimate conservative difference scheme. v. a second-order sequel to godunov’s method,” *Journal of computational Physics*, vol. 32, no. 1, pp. 101–136, 1979.

- [178] F. Pechereau, *Numerical simulation of the interaction of atmospheric pressure plasma discharges with dielectric surfaces*. PhD thesis, Châtenay-Malabry, Ecole centrale de Paris, 2013.
- [179] J. G. Verwer, B. P. Sommeijer, and W. Hundsdorfer, “RKC time-stepping for advection–diffusion–reaction problems,” *Journal of Computational Physics*, vol. 201, no. 1, pp. 61–79, 2004.
- [180] P. Vitello, B. Penetrante, and J. Bardsley, “Simulation of negative-streamer dynamics in nitrogen,” *Physical Review E*, vol. 49, no. 6, p. 5574, 1994.
- [181] N. Aleksandrov and I. Kochetov, “Electron rate coefficients in gases under non-uniform field and electron density conditions,” *Journal of Physics D: Applied Physics*, vol. 29, no. 6, p. 1476, 1996.
- [182] C. Li, W. Brok, U. Ebert, and J. Van der Mullen, “Deviations from the local field approximation in negative streamer heads,” *Journal of applied physics*, vol. 101, no. 12, p. 123305, 2007.
- [183] N. Liu and V. P. Pasko, “Effects of photoionization on propagation and branching of positive and negative streamers in sprites,” *Journal of Geophysical Research: Space Physics*, vol. 109, no. A4, 2004.
- [184] P. Tardiveau, N. Moreau, S. Bentaleb, C. Postel, and S. Pasquiers, “Diffuse mode and diffuse-to-filamentary transition in a high pressure nanosecond scale corona discharge under high voltage,” *Journal of Physics D: Applied Physics*, vol. 42, no. 17, p. 175202, 2009.
- [185] V. I. Gibalov and G. J. Pietsch, “Dynamics of dielectric barrier discharges in different arrangements,” *Plasma Sources Science and Technology*, vol. 21, no. 2, p. 024010, 2012.
- [186] M. V. Pachuilo, F. Stefani, R. D. Bengtson, R. Srivastava, L. L. Raja, *et al.*, “Dynamics of surface streamer plasmas at atmospheric pressure: Mixtures of Argon and Methane,” *IEEE Transactions on Plasma Science*, 2017.
- [187] A. Dubinova, D. Trienekens, U. Ebert, S. Nijdam, and T. Christen, “Pulsed positive discharges in air at moderate pressures near a dielectric rod,” *Plasma Sources Science and Technology*, vol. 25, no. 5, p. 055021, 2016.
- [188] F. Pechereau, J. Jánský, and A. Bourdon, “Simulation of the reignition of a discharge behind a dielectric layer in air at atmospheric pressure,” *Plasma Sources Science and Technology*, vol. 21, no. 5, p. 055011, 2012.

- [189] G. A. Sod, "A survey of several finite difference methods for systems of nonlinear hyperbolic conservation laws," *Journal of computational physics*, vol. 27, no. 1, pp. 1–31, 1978.
- [190] E. F. Toro, *Riemann solvers and numerical methods for fluid dynamics: a practical introduction*. Springer Science & Business Media, 2013.
- [191] R. Codina, E. Oñate, and M. Cervera, "The intrinsic time for the streamline upwind/petrov-galerkin formulation using quadratic elements," *Computer Methods in Applied Mechanics and Engineering*, vol. 94, no. 2, pp. 239–262, 1992.
- [192] R. Codina, "Comparison of some finite element methods for solving the diffusion-convection-reaction equation," *Computer Methods in Applied Mechanics and Engineering*, vol. 156, no. 1-4, pp. 185–210, 1998.
- [193] R. Codina, "On stabilized finite element methods for linear systems of convection–diffusion–reaction equations," *Computer Methods in Applied Mechanics and Engineering*, vol. 188, no. 1, pp. 61–82, 2000.
- [194] V. John and E. Schmeier, "Finite element methods for time-dependent convection–diffusion–reaction equations with small diffusion," *Computer methods in applied mechanics and engineering*, vol. 198, no. 3, pp. 475–494, 2008.
- [195] R. Codina, "Finite element approximation of the convection-diffusion equation: subgrid-scale spaces, local instabilities and anisotropic space-time discretizations," in *BAIL 2010-Boundary and Interior Layers, Computational and Asymptotic Methods*, pp. 85–97, Springer, 2011.
- [196] F. Pechereau, P. Le Delliou, J. Jánský, P. Tardiveau, S. Pasquiers, and A. Bourdon, "Large conical discharge structure of an air discharge at atmospheric pressure in a point-to-plane geometry," *IEEE Transactions on Plasma Science*, vol. 42, no. 10, pp. 2346–2347, 2014.
- [197] L. M. Vasilyak, S. Kostyuchenko, N. N. Kudryavtsev, and I. Filyugin, "Fast ionisation waves under electrical breakdown conditions," *Physics-Uspekhi*, vol. 37, no. 3, p. 247, 1994.
- [198] S. Starikovskaia, A. Y. Starikovskii, and D. Zatsépin, "Hydrogen oxidation in a stoichiometric hydrogen-air mixture in the fast ionization wave," *Combustion Theory and Modelling*, vol. 5, no. 1, pp. 97–129, 2001.

- [199] S. Pancheshnyi, S. Starikovskaia, and A. Y. Starikovskii, "Collisional deactivation of  $N_2(C^3\Pi_u, v = 0, 1, 2, 3)$  states by  $N_2$ ,  $O_2$ ,  $H_2$  and  $H_2O$  molecules," *Chemical Physics*, vol. 262, no. 2, pp. 349–357, 2000.
- [200] A. Flitti and S. Pancheshnyi, "Gas heating in fast pulsed discharges in  $N_2 - O_2$  mixtures," *Journal of Applied Probability*, vol. 45, no. 02, p. 21001, 2009.
- [201] "<http://www.zdplaskin.laplace.univ-tlse.fr/n2-o2-mixtures/>."
- [202] S. Lawton and A. Phelps, "Excitation of the  $b\ 1\sigma_g^+$  state of  $o_2$  by low energy electrons," *The Journal of Chemical Physics*, vol. 69, no. 3, pp. 1055–1068, 1978.
- [203] C. Yamabe, S. Buckman, and A. Phelps, "Measurement of free-free emission from low-energy-electron collisions with Ar," *Physical Review A*, vol. 27, no. 3, p. 1345, 1983.
- [204] W. Van Gaens and A. Bogaerts, "Kinetic modelling for an atmospheric pressure argon plasma jet in humid air," *Journal of Physics D: Applied Physics*, vol. 46, no. 27, p. 275201, 2013.
- [205] N. Kang, F. Gaboriau, S.-g. Oh, and A. Ricard, "Modeling and experimental study of pulse modulated ICP discharge: production of Ar highly excited states," *Plasma Sources Science and Technology*, vol. 20, no. 3, p. 035002, 2011.
- [206] A. Bogaerts, R. Gijbels, and G. P. Jackson, "Modeling of a millisecond pulsed glow discharge: Investigation of the afterpeak," *Journal of Analytical Atomic Spectrometry*, vol. 18, no. 6, pp. 533–548, 2003.
- [207] M. B. Schulman, F. A. Sharpton, S. Chung, C. C. Lin, and L. Anderson, "Emission from oxygen atoms produced by electron-impact dissociative excitation of oxygen molecules," *Physical review A*, vol. 32, no. 4, p. 2100, 1985.
- [208] R. R. Laher and F. R. Gilmore, "Updated excitation and ionization cross sections for electron impact on atomic oxygen," *Journal of Physical and Chemical Reference Data*, vol. 19, no. 1, pp. 277–305, 1990.
- [209] O. Zatsarinny and S. Tayal, "Electron collisional excitation rates for OI using the B-spline R-matrix approach," *The Astrophysical Journal Supplement Series*, vol. 148, no. 2, p. 575, 2003.

- [210] H. Cherkani-Hassani, D. Belic, J. Jureta, and P. Defrance, "Absolute cross sections for electron impact ionization and dissociation of  $\text{O}_2^+$ ," *Journal of Physics B: Atomic, Molecular and Optical Physics*, vol. 39, no. 24, p. 5105, 2006.
- [211] C. Park and N.-E. H. Aerothermodynamics, "A wiley-interscience publication," *New York*, pp. 255–268, 1990.
- [212] A. Bourdon, Y. Térésiaik, and P. Vervisch, "Ionization and recombination rates of atomic oxygen in high-temperature air plasma flows," *Physical Review E*, vol. 57, no. 4, p. 4684, 1998.
- [213] N. Sadeghi, D. Setser, A. Francis, U. Czarnetzki, and H. Döbele, "Quenching rate constants for reactions of Ar( $4p'[1/2]0$ ,  $4p[1/2]0$ ,  $4p[3/2]2$ , and  $4p[5/2]2$ ) atoms with 22 reagent gases," *The Journal of Chemical Physics*, vol. 115, no. 7, pp. 3144–3154, 2001.
- [214] L. G. Piper, "Electronic energy transfer between metastable argon atoms and ground-state oxygen atoms," *Chemical Physics Letters*, vol. 28, no. 2, pp. 276–279, 1974.
- [215] J. Deschamps and A. Ricard, "Transfert d'excitation dans les melanges argon-azote," *Le Journal de Physique Colloques*, vol. 34, no. C2, pp. C2–123, 1973.
- [216] J. Balamuta and M. F. Golde, "Formation of electronically excited oxygen atoms in the reactions of argon ( $3P0$ , 2) and xenon ( $3P2$ ) atoms with oxygen molecules," *The Journal of Physical Chemistry*, vol. 86, no. 14, pp. 2765–2769, 1982.
- [217] K. Niemi, V. Schulz-Von Der Gathen, and H. Döbele, "Absolute atomic oxygen density measurements by two-photon absorption laser-induced fluorescence spectroscopy in an RF-excited atmospheric pressure plasma jet," *Plasma Sources Science and Technology*, vol. 14, no. 2, p. 375, 2005.
- [218] G. Dilecce, M. Vigliotti, and S. De Benedictis, "A TALIF calibration method for quantitative oxygen atom density measurement in plasma jets," *Journal of Physics D: Applied Physics*, vol. 33, no. 6, p. 53, 2000.
- [219] D. P. Lymberopoulos and D. J. Economou, "Fluid simulations of glow discharges: Effect of metastable atoms in argon," *Journal of applied physics*, vol. 73, no. 8, pp. 3668–3679, 1993.
- [220] T. Sato and T. Makabe, "A numerical investigation of atomic oxygen density in an inductively coupled plasma in  $\text{O}_2/\text{Ar}$  mixture," *Journal of Physics D: Applied Physics*, vol. 41, no. 3, p. 035211, 2008.

- [221] “Phelps database database (www.lxcat.net).”
- [222] V. Puech and L. Torchin, “Collision cross sections and electron swarm parameters in argon,” *Journal of Physics D: Applied Physics*, vol. 19, no. 12, p. 2309, 1986.
- [223] “Puech database database (www.lxcat.net).”
- [224] J. E. Chilton, J. B. Boffard, R. S. Schappe, and C. C. Lin, “Measurement of electron-impact excitation into the  $3p^54p$  levels of argon using Fourier-transform spectroscopy,” *Physical Review A*, vol. 57, no. 1, p. 267, 1998.
- [225] R. Gangwar, L. Sharma, R. Srivastava, and A. Stauffer, “Argon plasma modeling with detailed fine-structure cross sections,” *Journal of Applied Physics*, vol. 111, no. 5, p. 053307, 2012.
- [226] “ngfsrdw database database (www.lxcat.net).”
- [227] Y. Zhu, S. Shcherbanev, B. Baron, and S. Starikovskaia, “Nanosecond surface dielectric barrier discharge in atmospheric pressure air: I. measurements and 2d modeling of morphology, propagation and hydrodynamic perturbations,” *Plasma Sources Science and Technology*, vol. 26, no. 12, p. 125004, 2017.
- [228] S. Pancheshnyi, S. Starikovskaia, and A. Y. Starikovskii, “Measurements of rate constants of the  $N_2(C^3\Pi_u, v = 0)$  and  $N_2^+(B^2\Sigma_g^+, v = 0)$  deactivation by  $N_2$ ,  $O_2$ ,  $H_2$ ,  $CO$  and  $H_2O$  molecules in afterglow of the nanosecond discharge,” *Chemical physics letters*, vol. 294, no. 6, pp. 523–527, 1998.
- [229] S. Stepanyan, A. Y. Starikovskiy, N. Popov, and S. Starikovskaia, “A nanosecond surface dielectric barrier discharge in air at high pressures and different polarities of applied pulses: transition to filamentary mode,” *Plasma Sources Science and Technology*, vol. 23, no. 4, p. 045003, 2014.
- [230] L. Viehland and E. Mason, “Transport properties of gaseous ions over a wide energy range, iv,” *Atomic Data and Nuclear Data Tables*, vol. 60, no. 1, pp. 37–95, 1995.
- [231] Y. Inada, S. Matsuoka, A. Kumada, H. Ikeda, and K. Hidaka, “Shack–hartmann type laser wavefront sensor for measuring two-dimensional electron density distribution over extinguishing arc discharge,” *Journal of Physics D: Applied Physics*, vol. 45, no. 43, p. 435202, 2012.
- [232] M. S. Simeni, B. M. Goldberg, C. Zhang, K. Frederickson, W. R. Lempert, and I. V. Adamovich, “Electric field measurements in a nanosecond pulse discharge

- in atmospheric air,” *Journal of Physics D: Applied Physics*, vol. 50, no. 18, p. 184002, 2017.
- [233] A. Radtsig and B. Smirnov, “Handbook on atomic and molecular physics,” *Atomizdat, Moscow*, p. 240, 1980.
- [234] B. Gordiets, A. I. Osipov, E. Stupochenko, and L. A. Shelepin, “Vibrational relaxation in gases and molecular lasers,” *Physics-Uspokhi*, vol. 15, no. 6, pp. 759–785, 1973.
- [235] D. Gaitonde and M. McCrink, “A semi-empirical model of a nanosecond pulsed plasma actuator for flow control simulations with LES,” *AIAA paper*, vol. 184, p. 2012, 2012.
- [236] K. Takashima, Y. Zuzeev, W. R. Lempert, and I. V. Adamovich, “Characterization of a surface dielectric barrier discharge plasma sustained by repetitive nanosecond pulses,” *Plasma Sources Science and Technology*, vol. 20, no. 5, p. 055009, 2011.
- [237] E. Anokhin, D. Kuzmenko, S. Kindysheva, V. Soloviev, and N. Aleksandrov, “Ignition of hydrocarbon: air mixtures by a nanosecond surface dielectric barrier discharge,” *Plasma Sources Science and Technology*, vol. 24, no. 4, p. 045014, 2015.
- [238] N. Benard, N. Zouzou, A. Claverie, J. Sotton, and E. Moreau, “Optical visualization and electrical characterization of fast-rising pulsed dielectric barrier discharge for airflow control applications,” *Journal of Applied Physics*, vol. 111, no. 3, p. 033303, 2012.

**Titre :** Étude numérique dans une décharge capillaire nanoseconde et dans la décharge contrôlée par barrière diélectrique surfacique: cinétiques, transport et réponses de fluide

**Mots clés :** décharge, nSDBD, capillaire, modélisation, cinétiques, hydrodynamique

**Résumé :** Les décharges pulsées nanoseconde sont l'énergie électronique de quelques eV à quelques dizaines eV et la déposition d'énergie spécifique de  $10^{-3}$  eV/mol à quelques eV/mol. Les électrons énergétiques peuvent générer des espèces chimiques actives efficacement, à fin de chauffer le gaz plus rapidement. Ce type de décharge est largement utilisé dans certaines applications pratiques. Deux configurations particulières sont étudiées dans ce travail: (i) décharge capillaire nanoseconde (nCD) et décharge contrôlée par barrière diélectrique surfacique de nanoseconde (nSDBD).

Le travail dans le manuscrit est organisé en trois parties. Dans la première partie, la modélisation numérique et les expérimentations de l'actinométrie basée sur argon sont utilisées pour étudier la densité de l'oxygène atomique dans nCD. Un schéma cinétique décrivant le comportement cohérent de l'ensemble des données expérimentales est développé. La densité des O-atomes des atomes d'oxygène en état fondamental est obtenue par les calculs.

La deuxième partie est consacrée à étudier, analy-

ser et prévoir des caractéristiques de la décharge et de la post-décharge de nCD sous différents énergies spécifiques de la déposition, basées sur un code auto cohérent bidimensionnel, nonPDPsim. La propagation de la décharge a été modélisée. Le taux de décroissance et la distribution radiale des électrons et de  $N_2(C^3\Pi_u)$  dans la post-décharge sont étudiés en respectant l'énergie spécifique de la déposition.

Finalement, un modèle parallèle bidimensionnel PASSKEy (PARallel Streamer Solver with KinEtics) a été développé et validé pour modéliser le nSDBD. Une série de calculs numériques pour un seul pulse de nSDBD, les résultats ont été comparés avec des résultats expérimentaux dans les mêmes conditions. L'effet des différents processus cinétiques dans la distribution 2D de la chaleur est étudié. Les données sont présentées et analysées pour la polarité de tension négative et positive. Un ensemble de calculs paramétriques avec différentes permittivité diélectrique, différent épaisseur des diélectriques et différente pression ambiantes sont présentés.

**Title :** Numerical study of nanosecond capillary and surface dielectric barrier discharges: kinetics, transport and fluid responses

**Keywords :** discharge, nSDBD, capillary, model, kinetics, hydrodynamics

**Abstract :** Nanosecond pulsed discharges have characteristic electron energies of a few to tens of eV and specific energy deposition ranging from  $10^{-3}$  eV/mol to a few eV/mol. The energetic electrons can efficiently generate chemical active species, lead to fast gas heating. These discharges are found in a growing list of successful practical applications. Two particular configurations are studied in present work: (i) nanosecond capillary discharge (nCD), and (ii) nanosecond surface dielectric barrier discharge (nSDBD).

The results in the thesis are presented in 3 parts. In the first part, numerical modelling and experiment of Ar-based actinometry are used to study the atomic oxygen density in nanosecond capillary discharge. The main processes responsible for population and decay of the three species of interest are selected on the basis of sensitivity and rate analysis. Density of O-atoms in the ground state is obtained from the calculations.

The second part is devoted to study, analyse and predict the features of the discharge and afterglow of

nCD under different specific energy deposition based on a two-dimensional self-consistent code, nonPDPsim. Propagation of the discharge have been modelled. The decay rate and radial distribution of electrons and  $N_2(C^3\Pi_u)$  in the afterglow are studied with respect to specific energy deposition.

Finally, a two-dimensional parallel PASSKEy ("PARallel Streamer Solver with KinEtics") code coupling plasma and hydrodynamics has been developed and validated to model nSDBD. The results were compared with experiments in the same conditions. Calculated and measured velocity of the discharge front, electrical current, 2D map of emission of  $N_2(C^3\Pi_u) \rightarrow N_2(B^3\Pi_g)$ , and hydrodynamic perturbations caused by the discharge on the time scale  $0.2 - 5 \mu s$  are analysed. The effect of different kinetics processes in 2D distribution of heat release is studied. The data are presented and analyzed for negative and positive polarity of voltages. A set of parametric calculations with different dielectric permittivity, the thickness of dielectric and ambient pressures are presented.

